

Development of a peripheral neuroprosthesis to elicit fine hand movements in primates

Présentée le 29 janvier 2021

Faculté des sciences et techniques de l'ingénieur
Chaire Fondation Bertarelli en neuro-ingénierie translationnelle
Programme doctoral en génie électrique

pour l'obtention du grade de Docteur ès Sciences

par

Marion Aimée Geneviève BADI-DUBOIS

Acceptée sur proposition du jury

Prof. D. N. A. Van De Ville, président du jury
Prof. S. Micera, directeur de thèse
Prof. D. Farina, rapporteur
Prof. C. Chestek, rapporteuse
Prof. D. Ghezzi, rapporteur

A sense of wonder is desperately important
— Jane Godall

Acknowledgements

I would like to express my deep and sincere gratitude to my research supervisor, Prof. Silvestro Micera, for giving me the opportunity to pursue my PhD thesis in his lab, for trusting me on a challenging and exciting project, and for providing thoughtful scientific guidance and support over those past four years. My sincere thanks go to Prof. Eric Rouiller, for warmly welcoming me in his lab in Fribourg, and guiding me through the intricate world of primate research with patience and empathy, for always being trustful and encouraging despite the scientific difficulties. I would like to sincerely thank Prof. Marco Capogrosso, for being such an inspiring mentor in science as in life, and for all the support he provided me over these four years. His sharp mind and never-ending optimism always pushed me to give the best of myself. I wish him all the best in Pittsburgh.

I had the chance to work with talented teams and be surrounded by incredible people. Among all the many persons that contributed to the accomplishment of this thesis, I would like to especially thank Ilaria Scarpato for her unconditional help and support, for the many hours spent on programming the TDT together, and for being such a talented engineer and invaluable friend. I also would like to thank Evgenia Roussinova for her critical insights on the brain-controlled experiments, for her impressive work on the data analysis, and her constant motivation and good humor. Thank you to Elena for joining the team, helping us with the experiments and analysis, and taking on the exciting project of translating our technology to humans. I thank Dr. Andrew Bogaard for his help in designing a fully-automated experimental setup, the interesting discussions on experimental design, and the organization of our trip to Seattle. I also thank Dr. Sophie Wurth for her implication throughout the project. My warm and grateful thanks to Maude Delacombaz for her dedication and patience in training the animals. I also thank Dr. Paul Cvančara for providing us with many TIME implants and addressing every single design problem with brilliant ideas. Thank you to Dr. Florian Fallegger for his critical help in the design of the cuff implant. Warm thanks to Beatrice Barra, for her support with many technical aspects of my work, for sharing her expertise, and for being an inspiring scientist and friend. I would like to thank all the labmates for all their encouragement, support, and for the great moments spent together: Nicolò Macellari, Aaron Brändli, Dr. Sara Conti, Dr. Nathan Greiner, Dr. Matthew G. Perich, Dr. Shiqi Sun, Dr. Elvira Pirondini, Andreas

Rowald, Fanny Demon, Dr. Florian Lanz, Dr. Eric Schmidlin, Dr. Katie Zhuang, and all the TNE labmates. I also thank Laurent Bossy, Véronique Moret, André Gaillard, Andrea Francovich, Christine Roulin, David Michel, Laurent Monney, Jacques Maillard, Dr. Andrina Zbinden, Yann Dixon, Katia Galan, Dr. Quentin Barraud, and Dr. Laura Batti for providing all the technical support. Thanks to Dr. David Su for his availability and his professionalism in performing complex chronic implantations. I also thank Prof. Grégoire Courtine, Prof. Jocelyne Bloch, and Dr. Georges Kohut for performing acute surgical interventions. Special thanks go to Alexandra M. Hickey for her support, her critical input on this work, and her irreplaceable friendship. I also heartily thank Dr. Ismael Saenez, my tennis partner, and a great scientific advisor. Many thanks to all my students: Gaia Carparelli, Giovanna Aiello, Aurelien Touzain, and Sebastian Savidan.

I thank Prof. Cynthia Chestek, Prof. Dario Farina, Prof. Diego Ghezzi, and Prof Dimitri Van de Ville, for reading and revising this work as members of my thesis examination committee. Thank you to Silvestro, Simon, Evgenia and Marco for their feedback on parts of this work.

I am infinitely grateful to my mom, for her support, her unconditional love, and for being a model of virtue and strength guiding me through life. Thank you with all hearts to my sisters, and my grandparents for their support and infinite affection. I also would like to wholeheartedly thank all my friends, the Capibabar's team, Manon, Vincent, and all the others, for making these four years much more fun, for bringing me joy, support, and laughs. Finally, I express my greatest love and gratitude to Simon, for your sincere and unconditional support, for being my scientific partner, my best friend, for being the anchor of my life. I cannot wait for our next scientific and life adventure.

PS: Thank you to Lou, Jo, Arya, Olenna, Melina and Lionel - The more we learn of the true nature of non-human animals, especially those with complex brains, the more we cherish what they offer us.

Fribourg, 11 Novembre 2020

Abstract

Neurological disorders such as spinal cord lesion and stroke disturb sensorimotor pathways and result in severe motor deficits that can dreadfully impact the quality of life of affected individuals. Strategies aiming at restoring hand function after upper-limb paralysis have relied on functional electrical stimulation (FES) of the remnant muscles but have shown limited functional benefits. Other electrical stimulation approaches have employed peripheral nerve electrodes to engage multiple distal muscles from a single proximal location on the nerve. Interestingly, intrafascicular interfaces penetrating the nerve have shown impressive capabilities for the restoration of specific somatosensory percepts in humans following limb amputation. In this thesis, I developed a peripheral neuroprosthesis based on intrafascicular implants for the restoration of fine hand movements in the pre-clinical primate model. The first part of this work focuses on building an adaptable technological platform for the design of arm and hand sensorimotor tasks in monkeys. I demonstrated the significance of our platform for fundamental and translational studies by studying a rich collection of physiological signals during unconstrained reaching and grasping tasks. In the second part of this work, I mobilized this experimental framework for the functional evaluation of intrafascicular stimulation paradigms in monkeys. More specifically, I used complementary neuroanatomical and computational analyses to tailor an intrafascicular interface to the arm motor nerves of monkeys. I then demonstrated that intrafascicular stimulation promotes selective hand muscle activation, evokes a large diversity of functional hand movements, and generates sustained and controllable levels of force. Finally, I coupled intrafascicular stimulation to motor cortical signals to enable a temporarily paralyzed monkey to perform a functional grasping task. The last part of this thesis is dedicated to a pilot study investigating the use of low-dimensional cortical dynamics for the direct control of a neuroprosthetic device. It provides exploratory routes for the design of an adaptive brain-control paradigm to drive peripheral implants using robust, voluntary commands. This thesis brings evidence of the high selectivity and functionality of intraneural implants for motor applications, and demonstrates their potential for eliciting precise hand movements. These findings open promising perspectives for the development of peripheral intraneural neuroprosthetic systems to restore functional and dexterous hand control after paralysis.

Key words: peripheral nerve, electrical stimulation, intraneural electrodes, intrafascicular, fine hand control, grasping, movement restoration after paralysis, cortical control.

Résumé

Les troubles neurologiques tels que les lésions de la moelle épinière et les accidents vasculaires cérébraux perturbent les voies sensorimotrices et entraînent de graves déficits moteurs. Les stratégies visant à restaurer la fonction de la main après une paralysie des membres supérieurs se sont appuyées sur la stimulation électrique fonctionnelle des muscles, mais ont jusque là montré des avantages limités. D'autres approches de stimulation ont utilisé des électrodes nerveuses périphériques pour engager plusieurs muscles distaux à partir d'un seul emplacement proximal. Fait intéressant, les interfaces intrafasciculaires ont démontré des propriétés inédites pour la restauration de percepts somatosensoriels après l'amputation d'un membre. Dans cette thèse, je décris le développement d'une neuroprothèse périphérique basée sur les implants intrafasciculaires, pour la restauration des mouvements fins de la main chez le primate. La première partie de ce travail se concentre sur la construction d'une plateforme technologique permettant le design de tâches sensorimotrices chez le singe. J'y démontre l'importance de notre plateforme pour les études fondamentales et translationnelles grâce à l'étude de nombreux signaux physiologiques dans des tâches de préhension. Dans la seconde partie de ce travail, j'utilise cette plateforme pour l'évaluation fonctionnelle de la stimulation intrafasciculaire chez le singe. J'emploie des analyses neuroanatomiques et computationnelles pour adapter une interface intrafasciculaire aux nerfs moteurs du bras des singes. Je démontre ensuite que la stimulation intrafasciculaire favorise l'activation sélective des muscles des doigts et du poignet, évoque une grande diversité de mouvements fonctionnels de la main et génère des niveaux de force soutenus. La dernière partie de cette thèse est consacrée à une étude pilote portant sur l'utilisation de dynamiques corticales pour le contrôle direct d'un dispositif neuroprosthétique. Elle fournit des pistes d'exploration pour la conception d'un paradigme de contrôle cérébral visant à piloter des implants périphériques de manière robuste et volontaire. Cette thèse apporte la preuve de la sélectivité et de la fonctionnalité élevées des implants intraneuraux pour les applications motrices et démontre leur potentiel à générer des mouvements précis de la main. Ces résultats ouvrent des perspectives prometteuses pour le développement de neurprothèses intraneurales périphériques pour restaurer le contrôle fonctionnel et fin de la main après une paralysie.

Mots clefs : nerf périphérique, stimulation électrique, électrodes intraneurales, intrafasciculaire, contrôle fin de la main, préhension, restauration du mouvement après paralysie, contrôle cortical.

Contents

Acknowledgements	v
Abstract (English/Français)	i
List of Figures	ix
List of Tables	xi
1 Introduction	1
1.1 Fine hand control and related disorders	3
1.1.1 Neuromuscular organization of the hand and forearm	3
1.1.2 Sensorimotor hand disorders	4
1.2 Restorative technologies for the recovery of hand motor control	6
1.2.1 Functional electrical stimulation of the muscles	7
1.2.2 Electrical stimulation of the peripheral nerves	9
1.3 Interaction between electrical stimulation and peripheral nerves	11
1.3.1 The anatomical structure of the somatic peripheral nervous system . .	12
1.3.2 Mechanisms of neural fiber recruitment	13
1.3.3 Refinement strategies for peripheral neuromodulation	18
1.4 Voluntary control of a prosthesis restoring hand function	19
1.4.1 Peripheral body commands to drive the prosthesis	19
1.4.2 Brain-controlled prosthetic devices	20
1.5 Thesis Outline	24
2 Adaptive behavioral platform for the study of upper-limb movements in monkeys	27
2.1 Abstract	28
2.2 Introduction	29
2.3 Methods	30
2.3.1 Robotic Platform	30
2.3.2 Animals involved in this study	34
2.3.3 Multimodal recordings	36
2.3.4 Data Analysis	37
2.3.5 Statistics	43
2.3.6 Data and software availability	43

2.4	Results	43
2.4.1	System performance	43
2.4.2	Applications to basic and translational studies	46
2.4.3	Arm and hand dynamics during natural reaching and grasping	47
2.4.4	Sensorimotor neural dynamics during natural reaching and pulling	52
2.4.5	Single unit encoding of multimodal motor and sensory information	53
2.4.6	Discrete and Continuous decoding of movement kinematics	55
2.5	Discussion	58
2.5.1	A versatile framework for multimodal characterization of three-dimensional arm movements	58
2.5.2	Applications in the study of three-dimensional movement dynamics	59
2.5.3	Applications in the study of neural sensorimotor processes	59
2.5.4	Applications in neuroengineering and brain computer interfaces	60
2.6	Limitations	60
2.7	Conclusion	61
2.8	Contributions	61
2.9	General Conclusion	61
3	Intrafascicular stimulation elicits dexterous hand movements in primates	63
3.1	Abstract	65
3.2	Introduction	66
3.3	Methods	67
3.3.1	Animals involved in this study	67
3.3.2	Anatomical characterization of the monkey's arm nerves	67
3.3.3	Peripheral implants design and manufacturing	71
3.3.4	Surgical procedures	75
3.3.5	Computational model	77
3.3.6	Electrophysiology	79
3.3.7	Data acquisition	80
3.3.8	Selectivity of muscle recruitment	80
3.3.9	Functional hand movements characterization	81
3.3.10	Design and analysis of brain activity-driven TIME stimulation	83
3.3.11	Lidocaine microfluidic system characterization	90
3.3.12	Statistics	90
3.4	Results	91
3.4.1	Design of a tailored intrafascicular interface for arm nerves in monkeys	91
3.4.2	Intrafascicular stimulation selectively recruits hand muscles	96
3.4.3	Intrafascicular stimulation elicits a variety of functional grips	99
3.4.4	Cortically driven TIME modulation during a functional grasping task: a proof-of-concept	105
3.5	Discussion	109
3.6	Contributions	110

3.7	General Conclusion	111
4	Low-dimensional manifold-based direct cortical control strategy	113
4.1	Abstract	114
4.2	Introduction	115
4.3	Methods	116
4.3.1	Animal involved in this study	116
4.3.2	Surgical procedures	116
4.3.3	Experimental paradigm	117
4.3.4	Data acquisition	120
4.3.5	Direct brain control of peripheral nerve stimulation	122
4.3.6	Data analysis	123
4.4	Results	125
4.4.1	Calibration of a direct cortical control space based on neural manifold directions	125
4.4.2	Rapid learning of a one-dimensional direct control through neural mode activation	126
4.4.3	Progressive adaptation to a second degree of freedom of direct cortical control	127
4.4.4	Successful independent and simultaneous modulation of two degrees of freedom	129
4.4.5	Evolving strategies for the activation of two degrees of freedom via fixed cortical mapping	130
4.4.6	Direct low-dimensional control of peripheral nerve stimulation: a demonstration	133
4.5	Discussion	135
4.5.1	Controllability of neural dynamics based direct-control	135
4.5.2	Functionality of neural dynamics based direct-control	136
4.5.3	Long-term stability of neural dynamics-based direct control	137
4.5.4	Limitations and perspectives	138
4.6	General Conclusion	139
5	Perspectives on the translation of intraneural prostheses to restore hand movements	141
5.1	Functional and technical considerations for the clinical application of intrafascicular stimulation targeting motor functions	142
5.1.1	Clinical application for hand paralysis: challenges and prospects . . .	142
5.1.2	Development of tailored experimental paradigms in humans	143
5.1.3	Technical prospects for the clinical use of intrafascicular implants . . .	144
5.2	Opportunities for the refinement of peripheral nerve stimulation	147
5.2.1	Realistic computational frameworks for the design and optimization of stimulation strategies	147
5.2.2	Machine learning approaches to improve parameter search	150

5.3	Merging motor and somatosensory restoration for the recovery of fine hand function	153
6	General conclusion	155
A	Appendix	157
A.1	Animals involved in the study	157
A.2	Computational models tensor values	158
A.3	Detailed muscular implants	158
A.4	Kinematic features characterizing hand movements in 2D	160
A.5	Data specifications	162
A.6	Supplementary videos captions	163
	Bibliography	195
	Glossary of abbreviations	197
	Curriculum Vitae	199

List of Figures

1.1	Robotic framework for the study of reaching and grasping	4
1.2	Levels of cervical spinal cord injury	6
1.3	Muscular functional electrical stimulation (FES)	8
1.4	Relationship between selectivity and invasiveness of peripheral nerve interfaces	11
1.5	Anatomical structure of the peripheral nerve	14
1.6	Extraneural stimulation of a myelinated peripheral nerve fiber	16
2.1	Robotic framework for the study of reaching and grasping	31
2.2	Experimental primate chair and robot workspace	32
2.3	Scheme of the robotic arm control and design of the grip pressure sensor . . .	34
2.4	Evaluation of the system performances	45
2.5	Multimodal electrophysiology during unconstrained reaching and grasping .	47
2.6	Arm and hand dynamics during natural reaching and grasping	48
2.7	Arm and hand dynamics during natural reaching and grasping - supplementary	51
2.8	Sensorimotor neural dynamics during unconstrained reaching and pulling . .	52
2.9	Kinematics, kinetics and neural dynamics in Mk-OI	53
2.10	Single unit encoding of multimodal motor and sensory information	55
2.11	Discrete and Continuous decoding of movement dynamics	56
3.1	Methodology for the neuroanatomical study of the monkey arm nerves	70
3.2	Design, fabrication and implantation of the peripheral nerve interface	73
3.3	Microfluidic cuff design for the selective paralysis of movement	74
3.4	Design of a realistic model of intraneural stimulation in the monkey median nerve	78
3.5	Experimental paradigm for the brain-controlled stimulation of the radial nerve	85
3.6	Experimental setup for brain controlled-stimulation of the peripheral nerve .	88
3.7	Development of an intraneural implant for selective arm nerve stimulation in monkey	92
3.8	Detailed neuroanatomical organization of the median and radial nerves in fascicularis macaques	93
3.9	Simulation results of a realistic model of intraneural stimulation in the monkey median nerve	95
3.10	Selective hand muscles recruitment using intraneural stimulation	97
3.11	Selective hand muscles recruitment in additional animals	98

3.12	Functional grip movements and extension gestures achieved with the TIME	100
3.13	Reproducible grips and hand extension movements elicited by intraneural stimulation	102
3.14	Intraneural stimulation can be modulated to produce functional force levels	104
3.15	Microfluidic cuff characterization for the selective paralysis of movement	106
3.16	Intraneural stimulation restores hand extension during functional reaching task	107
3.17	Performance during behavioral task and neural manifold characteristics	109
4.1	Training of two-dimensional cortical control using neural manifolds	120
4.2	Hand muscular activity during direct control	122
4.3	Choice of control space and baseline activity drift	126
4.4	Learning of one-dimensional control of the cursor	127
4.5	Progressive adaptation to a second degree of freedom of cortical control	128
4.6	Successful simultaneous modulation of two degrees of freedom	130
4.7	Evolving control strategies relying on fixed cortical mapping	132
4.8	Direct low-dimensional control of peripheral nerve stimulation	134
5.1	Experimental setup for the clinical testing of intrafascicular stimulation	145
5.2	Bipolar intrafascicular stimulation increases muscular selectivity	149
5.3	Gaussian process-based Bayesian Optimization algorithm for intraneural stimulation paradigms	152

List of Tables

1.1	Types of fibers in mammalian nerves	13
A.1	Animals used for neuro-anatomy	157
A.2	Animals used for acute electrophysiology	157
A.3	Animals used for chronic electrophysiology	157
A.4	Veterinary license numbers	158
A.5	Modelled electrical conductivities	158
A.6	Implanted muscles and nerves for electrophysiology	159
A.7	Flexion movements kinematic features	160
A.8	Extension movements kinematic features	161
A.9	Data specifications for Figure 3.12	162
A.10	Data specifications for Figure 3.16	163

1 Introduction

In 2019, collaborators from the “Global Burden of Disease” initiative published a systematic study on the burden of neurological disorders worldwide. By screening 15 neurological disorders in 195 countries from 1990 to 2016, they estimated that neurological disorders were the leading cause for the number of years lived with disability, and the second leading cause of death globally (Feigin et al., 2019). As populations continue to grow and age, the prevalence of neurological disorders such as stroke, Parkinson’s disease, Alzheimer’s disease, and many others dramatically increases. In parallel, health systems are facing increasing demands for treatment, rehabilitation, and assisted nursing services to support patients suffering from neurological deficits. In 2013, the Christopher & Dana Reeve Foundation unveiled startling statistics based on research into the prevalence of paralysis across the U.S. Their analysis revealed that approximately 1.7% of the U.S population reported living with some form of paralysis of the upper or lower limbs (Dana Reeve Foundation, 2020). The leading causes were determined to be stroke (33.7%), followed by spinal cord injury (SCI) (27.3%), and multiple sclerosis (18.6%). To say nothing of the the human tragedy they represent, neurological disorders have major financial implications for victims’ families, caregivers, and health care providers. The increasing trend of spinal cord injuries in the U.S has resulted in an annual cost of 40.5 billion dollars, i.e. more than 3 times higher than in 1998. In Europe, the economic burden caused by neurological disease was estimated to be 139 billion euros in 2004 (Andlin-Sobocki et al., 2005). The financial and societal implications of neurological disorders are serious and require the urgent implementation of prevention strategies and the development of viable therapeutic solutions.

Temporary or permanent paralysis resulting from neurological disorders can have a tremendous impact on patients’ lives, as they potentially affect all body systems. Severe debilitating effects include loss of motor function, sensory deprivation, breathing issues, problems in regulating blood flow, difficulty articulating during speech, and malfunction of the bladder and sexual organs. Consequently, affected individuals suffer from strong physical and psychological burdens, reducing their independence and overall quality of life. Manifestations of the paralysis strongly depend on the nature of the afflicting disorder and can translate

to motor disabilities, spasticity, skin ulcers, neuropathic pain, etc. The desire for functional recovery in individuals affected by neurological dysfunction is conditioned by the type of paralysis, the severity of the injury, and the amount of pain they endure. In two different studies conducted in 2004, researchers evaluated the largest priority for functional recovery in individuals suffering from SCI. Both surveys reported that for tetraplegic patients, the greatest desire was the recovery of hand and arm function, followed by sexual functions, trunk stability, and urinary function (Anderson, 2004; Snoek et al., 2004). Similarly, the restoration of reaching and grasping movements was voiced as a high priority rehabilitative goal in subjects affected by stroke, as they are critical to performing activities of daily living (Timmermans et al., 2009; Turton et al., 2013). Because these two neurological conditions originate from the disruption of very different systems, i.e the interruption of the corticospinal tract in individuals with SCI and the cell death in cortical or subcortical brain areas in stroke victims, therapeutic strategies must be tailored to the specific needs of the patient.

The most common medical treatments for individuals affected by upper limb paralysis consist of rehabilitative therapies and clinical management. Approaches to regain a certain degree of motor function include supportive devices such as braces, arm supports, and exoskeletons. Concurrently, assistive communication tools have been engineered to return some autonomy to disabled subjects. Brain-computer-interfaces (BCIs) have allowed the direct operation of tablet devices, returning the ability to type text, surf on the web, and even play the digital piano (Nuyujukian et al., 2018). Sophisticated decoding algorithms have been developed to convert user inputs extracted from the body periphery (kinematics from healthy limbs, residual EMG), or directly from the brain, into external commands to control a large variety of devices (Ajiboye et al., 2017; Fonseca et al., 2019; Hochberg et al., 2006; Seáñez-González et al., 2016; Thorp et al., 2016). While these strategies allow the deficient neural pathways to be bypassed and some independence to be regained, they do not recover the lost functions, *per se*, and are often not perceived as natural or intuitive solutions.

An alternative means of addressing the disabling consequences of neurological disorders consists of re-activating the paralyzed limbs through artificial inputs, such as electrical stimulation. This approach has previously been used to restore latent circuits in rehabilitation paradigms and substitute efferent central nervous commands below the level of the injury. Functional electrical stimulation (FES) applied on the spine, peripheral nerves, or residual muscles has unveiled an immense potential for the recovery of upper-limb motor function in persons suffering from neurological trauma. Importantly, while non-invasiveness represents one of the essential device requirements for individuals affected by SCI, a study revealed that most of the subjects would consider invasive surgery if it helped them regain functions critical for daily life (Collinger, Boninger, et al., 2013).

In recent decades, significant technological advances in the development of electronic devices for the rehabilitation of paralyzed patients have been made. Implantable interfaces have been engineered to modulate the activity of remnant neuro-muscular structures and produce functional and sustainable levels of forces. New tools have been employed to read commands

broadcasted from the brain and steer the activation of electronic implants or devices. However, the optimization of these technologies and their transfer towards practical applications still present substantial challenges. Today, a joint effort of scientists, clinicians, and engineers is needed to refine these therapeutic approaches, and eventually translate them to the clinic, where they could significantly improve the independence and quality of life of the users.

1.1. Fine hand control and related disorders

1.1.1. Neuromuscular organization of the hand and forearm

The hand plays an important role in our interaction with the environment, whether it is to grasp and manipulate objects, to communicate through body language, or to represent complex cognitive concepts. Indeed, the ten digits of our two hands have given rise to our current number systems and many of our calculation techniques.

The healthy human hand is composed of five fingers, the index finger, middle finger, ring finger, pinkie finger, and thumb. In humans, the thumb is powerful and well developed, and its opposable characteristic is unique to our species. It has separated from other the fingers and developed a specific musculature through successive stages of evolution. The skeleton of the human hand is composed of 27 bones, organized in a way that allows the fingers to articulate around the metacarpal (MCP) joints, the proximal interphalangeal (PIP) joints, and the distal interphalangeal joints.

The muscles actuating the hand are divided into intrinsic and extrinsic muscles (**Figure 1.1**). The intrinsic muscles of the hand include the thenar and hypothenar muscles controlling the thumb and pinkie fingers, respectively; the interosseous muscles, which are responsible for the abduction and adduction of the fingers; and the lumbrical muscles that flex the metacarpophalangeal joints and extend the interphalangeal joints. The extrinsic muscles are composed of long flexors and extensors, located in the anterior and posterior compartments of the forearm, respectively. Among the long flexor muscles, the flexor digitorum superficialis and profundus allow for the bending of the fingers; the flexor pollicis longus facilitates the closing of the thumb; and the flexor carpi radialis, ulnaris, and palmaris longus promote the flexion and adduction of the wrist (**Figure 1.1**). Intrinsic hand flexors responsible for the flexion and opposition of the thumb include the opponens pollicis, abductor pollicis brevis, and flexor pollicis brevis (**Figure 1.1**). Conversely, the extensors' primary function is to straighten the digits and open the hand. The thumb possesses three extensors in the forearm: the abductor pollicis longus, the extensor pollicis longus, and the extensor pollicis brevis. The fingers are mainly extended by the contraction of the extensor digitorum communis. The extensor carpi radialis (longus and brevis) and ulnaris control the extension and adduction of the wrist, respectively (**Figure 1.1**).

Regarding the innervation of the hand muscles, the radial nerve supplies the wrist and finger extensors, and the abductor pollicis longus (**Figure 1.1**). It is thus responsible for most of the

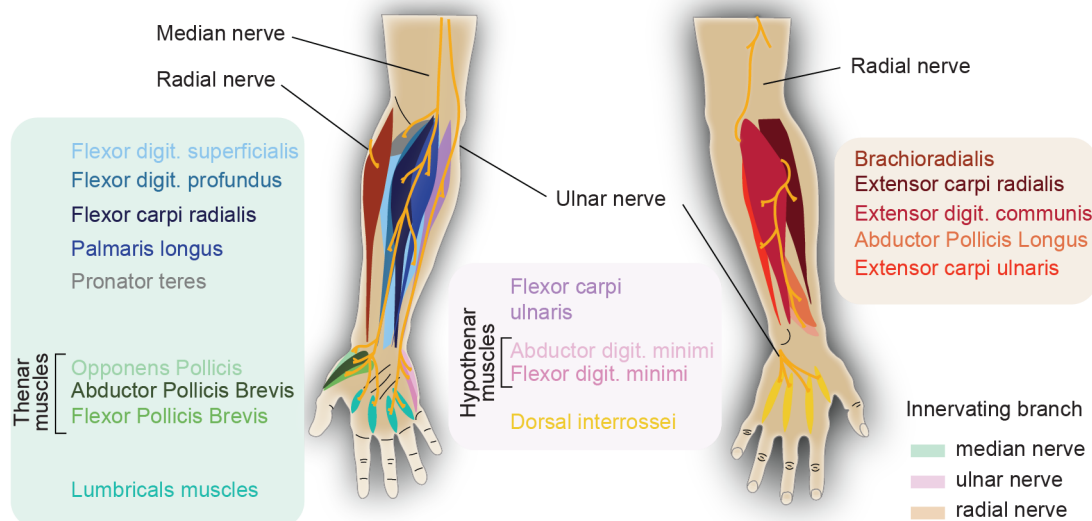


Figure 1.1 – Neuromuscular anatomy of the human hand. Most prominent hand muscles are represented together with their innervating nerve branches. The median and ulnar nerves are composed of a mix of afferent and efferent neural fibers, and thereby convey both motor and cutaneous information to the distal part of the forearm and hand. The radial nerve divides into a superficial sensory branch and a deep motor branch at the elbow level. The superficial branch supplies sensory information to the dorsal aspect of the hand, while the deep branch carries efferent signals to the extensor muscles of the hand.

extension and abduction of the hand. The median nerve innervates the flexors of the wrist, digits, the abductor pollicis brevis, and opponens of the thumb (thenar eminence), as well as the first and second lumbricals, responsible for moving the index finger (Rea, 2016) (**Figure 1.1**). The median nerve controls most of the flexion of the hand and plays an important role in the opposition between the thumb and the index finger. Finally, branches emerging from the ulnar nerve target the flexor carpi ulnaris and the medial half of the flexor digitorum profundus in humans, as well as the hypothenar muscles, the interossei, the abductor pollicis, the flexor pollicis brevis, the palmaris brevis, and the remaining lumbrical muscles (**Figure 1.1**). The ulnar nerve is known as the “musician nerve” as it controls the abduction of the fingers and the wrist, and is responsible for fine hand movements.

1.1.2. Sensorimotor hand disorders

The number of people living with lower or upper-limb paralysis in the U.S. is estimated to be 5.5 million. Among these individuals, 1.6 million people are stroke survivors, 1.2 million suffer from SCI, and over 900,000 live with Multiple Sclerosis (Armour et al., 2016). Paralysis can translate to a complete inability to move, or may only affect some parts of the body. As a result, most of the stroke victims and patients who endured SCI do not retain the ability to move the upper-limb and hand. Indeed, upper limb functions are altered in about 80% of stroke survivors (Glen E. Gresham, 2004) and 60% of SCI cases result in tetraplegia with

cervical levels being the most common injury sites (National Spinal Cord Injury Statistical Center, 2020).

Stroke lesions

Stroke lesions occur after brain areas are deprived of oxygen due to the blockage of brain blood vessels (ischemic stroke), or subsequently to a brain artery leakage or rupture (hemorrhagic stroke). Following stroke events, patients often experience a reduced ability to control fine hand movements due to the loss of muscle strength, somatosensation, and poor selectivity in muscular recruitment (Buma et al., 2013). Additionally, neuromechanical changes progressively appear in the form of increased stiffness and spasticity, influencing the coordination of multi-joint arm and hand movement (Buma et al., 2013; Cirstea et al., 2003). Studies involving patients affected by ischemic events reported that despite early rehabilitative intervention, subjects were still unable to reliably use their affected arm or hand for simple daily activities six months after the injury (Dobkin, 2005). Besides, researchers have shown that compensatory mechanisms arising in the subacute phase of the disease potentially reproduced gross arm movements but frequently left fine finger movements impaired (Krakauer and Carmichael, 2017; Raghavan et al., 2006; Twitchell, 1951; Xu et al., 2017).

Spinal cord injury

In the case of cervical SCI, the degree of remaining upper-limb function depends on the level of the lesion along the cord, and the extent of spinal tissue damage. Garrett and colleagues (Garrett et al., 1964) classified cervical SCI in four distinct levels of disability: i) loss of intrinsic hand muscles, ii) loss of all hand musculature, iii) loss of triceps, and latissimus dorsi, and iv) loss of wrist extension and poor arm control. At the lowest level of SCI, spinal segment T1 to C8, intrinsic muscles of the hand are weakened, the opening of the hand is impaired, and finger flexion is impeded (**Figure 1.2**). Around the C6 level, the elbow flexion and wrist extension are lost, making the grasp much less effective, and reducing dexterity (**Figure 1.2**). At the C4-C5 level and above, the affected individuals cannot flex the elbow or biceps, shoulder functions are weakened or absent, and external power is needed to elicit prehension (**Figure 1.2**).

Many tetraplegic patients rely on the use of the remaining extensor muscles to mimic natural grasping movements. Such grasping is generally poor and imprecise compared to active voluntary closure and opposition (Garrett et al., 1964). Spasticity and tightness of the fingers enable increased strength levels but simultaneously impede the relaxation and opening of the hand, thereby limiting controlled pre-shaping of the hand and adjustment of grip pressure.

As of today, individuals affected by cervical lesions still lack acceptable solutions for the recovery of fine hand motion, and only partially benefit from rehabilitation strategies (Mangold et al., 2005; M. R. Popovic et al., 2006).

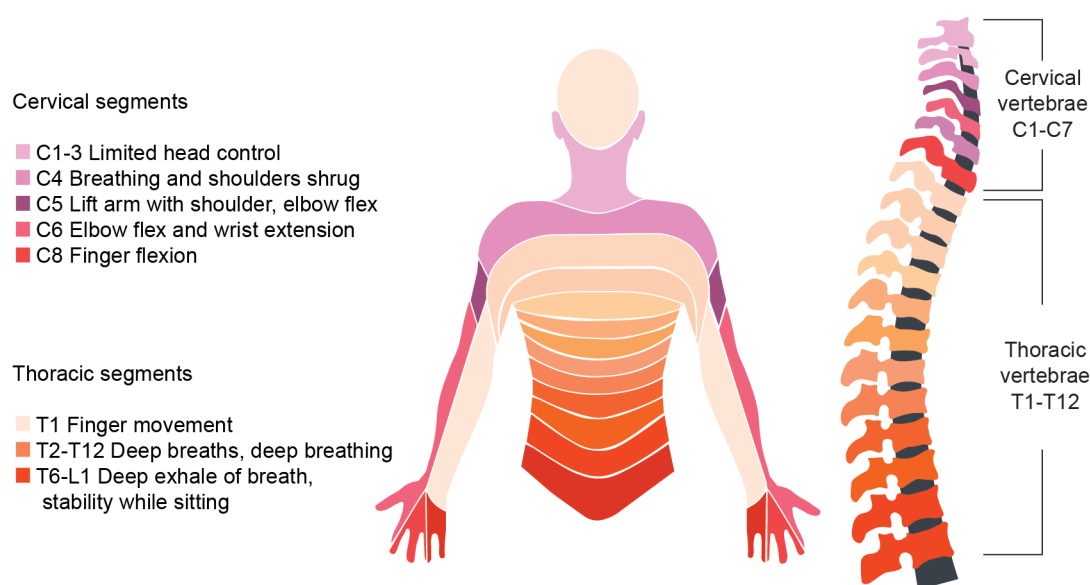


Figure 1.2 – Levels of cervical spinal cord injury. The level of SCI determines extent of upper-limb paralysis.

In most neurological disorders in which hand movements are impeded, upper-limb muscles and peripheral nerves remain intact. The interruption of the descending commands at the level of cortical, subcortical, or spinal structures prevents the communication between the brain and underlying muscles, and the actuation of the limb. Although no therapeutic approach has yet demonstrated the ability to fully restore fine hand control in individuals affected by stroke or SCI, many promising rehabilitative technologies have been developed, and incremental progress has been made to improve arm and hand function in paralyzed individuals.

1.2. Restorative technologies for the recovery of hand motor control

In the past decades, electrical stimulation has been extensively employed, either as a means to progressively strengthen and reanimate the paretic muscles, or to artificially reproduce the lost function of the limb. Alternative treatments to electrical stimulation consist of: i) surgical interventions that rely on the transfer of tendons and muscles to substitute the activity of the paralyzed muscle, ii) restorative therapies that involve long-term rehabilitative training and aim at awakening the remnant neural circuitries, iii) regenerative approaches in which cellular grafts are used to reconstruct damaged neuronal tissues. While these strategies suggest promising therapeutic outcomes, they leave significant gaps in the requirements for functional restoration. FES, on the other hand, has provided functionally relevant gain in hand function and has so far surpassed other available techniques. In particular, neurotechnologies interfacing the peripheral neuromuscular system have successfully been able to modulate the

activity of healthy structures and improve functional recovery of upper-limb movements.

1.2.1. Functional electrical stimulation of the muscles

FES applications for the recovery of motor functions rely either on the direct recruitment of skeletal muscular fibers through targeted stimulation of specific muscles, or on the engagement of neuromuscular junctions, where motor neurons connect to muscle fibrils. The latter is generally more easily achieved due to the lower threshold charge required to produce action potentials in neurons compared to muscle fibers (Gilman and Arbor, 1983; P. H. Peckham and Knutson, 2005). Neuromuscular stimulation may be delivered at the surface of the skin (transcutaneous), using percutaneous wires, or via implantable systems.

Numerous strategies have been devised to enhance hand and arm function through FES. Some have already reached the clinical testing stage of development, and others are now commercially available. The first attempt to develop an arm neuroprosthesis dates back to the 1960s. It consisted of surface electrical stimulation applied on the forearm to open and close the hand (Long, 1963; Vodovnik et al., 1965). This proof-of-concept motivated the development and clinical evaluation of surface (M. Popovic et al., 2001; Prochazka et al., 1997; Saxena, 1995; Snoek et al., 2000; Thorsen et al., 1999), percutaneous (Ajiboye et al., 2017; Handa and Hoshimiya, 1987; P. H. Peckham et al., 1980) and implantable systems (P. H. Peckham et al., 2001; P. Peckham et al., 2002) aimed at reanimating grasping. **Figure 1.2** illustrates the different modes of muscular stimulation and presents examples of successfully used FES devices for the restoration of upper-limb movement. Among them, the Handmaster system (NESS H200®, Bioness, LiveOn™), is a commercial device that reproduced hand movements in individuals affected by tetraplegia at the C5 level, or by stroke-induced hemiplegia (Snoek et al., 2000). A stiff forearm orthosis supports the wrist and hand, and surface electrodes deliver current upon actuation of a handheld control unit (**Figure 1.2 a**). Based on a similar stimulation approach, Prochazka and colleagues developed the Bionic glove (Prochazka et al., 1997), in which a soft sleeve, worn on the forearm and hand, covered transcutaneous stimulation electrodes placed on the finger flexors and extensor muscles. In their study, kinematic wrist angles were measured using a displacement transducer, and wrist flexion and extension movements activated the electrodes responsible for opening and closing the hand, respectively. A more invasive device, the percutaneous system FESMate (NEC Medical Systems, Tokyo, Japan), was commercialized in Japan and employed to stimulate up to 30 muscles of the hand, arm, and shoulder by sucking and puffing on a mouthpiece controller (Handa et al., 1998). Interestingly, stimulation sequences delivered through the FESMate were derived from natural muscular activation patterns recorded in healthy subjects performing grasping tasks. The system was tested in individuals with SCI and hemiplegia, but no quantitative evaluation of the performance has been reported. The FreeHand device developed at Case Western Reserve University (CWRU) and the Cleveland VA Medical Center (D. M. Taylor et al., 2002), consisted of a fully implantable device that elicits stereotypic palmar and lateral grips in persons with tetraplegia (**Figure 1.2 b**). The first version, which received FDA approval in 1967,

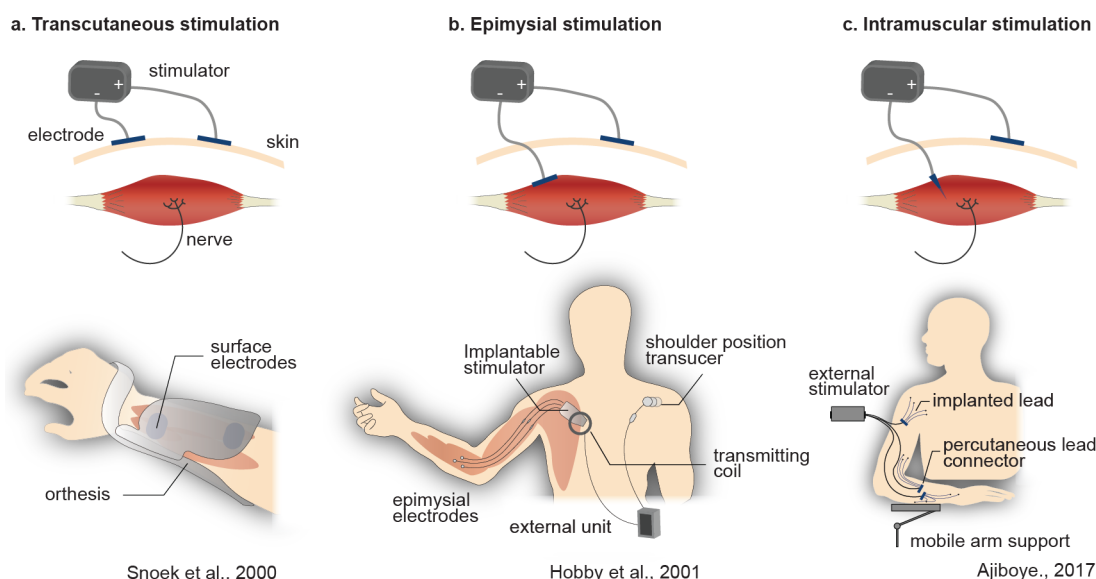


Figure 1.3 – Muscular functional electrical stimulation (FES). Various modes of muscular FES and examples of clinical applications.

was composed of a stimulator and receiver unit, implanted in the chest, which controlled eight epimysial or intramuscular electrodes implanted at the neuromuscular junction of the hand and forearm muscles. Stimulation was commanded through movements of the contralateral shoulder and provided graded control on hand opening and closing. The system was evaluated in 250 people (Carroll et al., 2000; Cornwall and Hausman, 2004; Hobby et al., 2001; Mulcahey et al., 1997; P. H. Peckham et al., 2001). Reports demonstrated that the FreeHand favored independence in activities of daily life, and was widely well accepted within equipped patients. A more sophisticated version of the system was engineered by the same group, which featured an implantable joint angle transducer to control the stimulation based on ipsilateral wrist motion (Bhadra et al., 2002), as well as a myoelectric closed-loop controller to drive stimulation commands based on the contraction of residual muscles (R. Hart et al., 1998). A more recent study published by Ajiboye and colleagues (Ajiboye et al., 2017) successfully used percutaneous intramuscular electrodes inserted in the arm and forearm muscles to stimulate reaching and grasping movements in a tetraplegic subject (**Figure 1.2 c**). Mobile arm support was used to reinforce the paralyzed arm against gravity, and multiple joint movements were triggered based on cortical inputs.

Despite these encouraging proof-of-concept studies showing that FES improves the autonomy of paralyzed individuals by producing simple yet functionally relevant grips, several issues have hindered their application in the clinic. For instance, the cumulative effect of repeated stimuli necessary for the smooth contraction of the limb increases the rate of muscle fatigue. Importantly, the large skin resistance of surface electrodes requires the use of high current amplitude accelerating the exhaustion of muscle fibers (P. H. Peckham and Knutson, 2005). Additionally, epimysial and intramuscular stimulation fails to homogeneously recruit the

muscular units, resulting in a focal activation of the fibers that promotes the rapid fatigue of the skeletal muscles (Binder-Macleod and Snyder-Mackler, 1993). High stimulation current delivered transdermally, especially on the small intrinsic muscles of the hand, can cause discomfort, irritation, and pain (Chae and Hart, 1998). Other challenges encountered in these surface and implanted systems include the difficulty to reliably place the electrodes, the need for cumbersome electronics, the management of short-life batteries, the demand for a large number of stimulation sites to recruit each muscle, and the implementation of complex control strategies to activate muscles in a natural, synergistic manner.

To address some of these issues, researchers investigated the targeting of efferent peripheral nerve fibers as an alternative muscle recruitment strategy.

1.2.2. Electrical stimulation of the peripheral nerves

Peripheral nerve stimulation represents an interesting substitute to functional electrical stimulation of the muscles as it engages most of the distal end effectors from a single proximal location. Moreover, the electrical currents required to activate motor fibers are ten to one hundred times lower than those needed to activate skeletal fibers. Exploiting these interesting properties, several neurotechnologies have been developed in the recent decades to interface with the peripheral nerves. **Figure 1.4**, presents the trade-off of different of neural interfaces in terms of selectivity and invasiveness (Micera et al., 2008).

The least invasive and most widely used approach is extraneural stimulation. This technique often relies on a cuff implant composed of a soft structure wrapped around the nerve (**Figure 1.4 a**). Electrodes distributed inside the cuff are placed in close contact with the nerve's most superficial layer, the epineurium, and deliver current through its outer surface (Loeb and Peck, 1996; Rodríguez et al., 2000; Schiefer et al., 2008). This device has successfully been used to treat incontinence (Hohenfellner et al., 1998; Tanagho et al., 1989) and to partially restore arm and hand movements in non-human primates (NHPs) (Brill et al., 2018) and humans (Memberg et al., 2014; Tigra et al., 2020). Cuff systems present significant advantages compared to muscular stimulation in terms of fatigue, skin discomfort, and control complexity. However, standard monopolar epineural stimulation does not selectively recruit motor axons distributed deep within the nerve structure, and fails to reproduce fine and controlled movements. To solve this problem, Tyler and Durand developed a revised version of the cuff, that flattened the nerve and redistributed the fascicles linearly to gain access to the deepest compartments (Tyler and Durand, 2002). While it increased selectivity, this approach presented the disadvantage of reshaping the nerve, potentially compressing and damaging the fragile intraneural structures. Another interesting technique, used at the University of Montpellier, was to derive multipolar cuff stimulation paradigms from computational models to selectively engage the peripheral nerves of the arm (Tigra et al., 2020). Their results, collected in anesthetized tetraplegic patients, showed promising evidence for the restoration of precise grasping movements using complex 3D stimulation patterns. Yet, to date, epineural cuff stimulation for the restoration of

upper-limb functions has only been tested experimentally, and none of the aforementioned implants is widely available in the clinic.

An alternative way to stimulate peripheral nerves hinges on the use of intraneural implants. For instance, interfascicular electrodes penetrating the epineurium can be positioned in between the fascicles that innervate the muscles of interest (D. Tyler and Durand, 1993; D. Tyler and Durand, 1997) (**Figure 1.4 b**). Interfascicular devices recruit axonal components by stimulating nerve fibers from the external surface of the perineurium. Despite being more invasive than cuff electrodes and lying closer to the efferent axons, these technologies have shown very limited functional outcomes for the elicitation of movements.

On the other hand, the high-density silicone-based slanted multi-electrode array (**Figure 1.4 d**) provides a very large degree of specificity by inserting up to 96 stimulating shafts within the nerve (Branner et al., 2004; Branner et al., 2001; Davis et al., 2016; Wark et al., 2014). Such high-density intrafascicular arrays have shown the ability to selectively recruit afferent and efferent peripheral nerve fibers in animal models and humans. Interestingly, Ledbetter and colleagues demonstrated that slanted Utah arrays implanted in the arm nerves elicit selective muscle responses and grasping movements in anesthetized monkeys (Ledbetter et al., 2013). However, silicon electrode tips are rigid elements, and histological assessment in animal models revealed a large compression of the nerve at the insertion point of the arrays, together with a severe disruption of the epineurium (Branner et al., 2004). The quantitative assessment of the device imprint within the cat sciatic nerve revealed the formation of a thick connective tissue around the arrays, resulting from the foreign body inflammatory response (Christensen et al., 2014). Collectively, these results indicate that despite providing an increased specificity; high-density microelectrode arrays are particularly invasive and apply strong mechanical stress on the neural tissues. The electrode substrate, shafts, and wires are composed of rigid material that imposes strenuous tensile strength when chronically implanted.

Alternatively, softer polyimide-based intrafascicular multichannel electrode arrays (**Figure 1.4 c**) offer an interesting compromise between reduced invasiveness and increased selectivity. These implants consist of linearly organized stimulation channels disposed on a shaft that transversally penetrates the epineurium and perineurium compartments of the nerve (Badia et al., 2011; Badia et al., 2016; Boretius et al., 2012). Once inserted, this design brings the active sites in close vicinity of the fibers of interest. A refined version of this implant incorporates deployable wings for a three-dimensional positioning of the stimulation contacts within the fascicle (Cutrone et al., 2015). Transverse intrafascicular implants have demonstrated very promising results for the recruitment of afferent and efferent fibers in humans and animal models (Gaillet et al., 2020; Oddo et al., 2016; Raspopovic et al., 2012; Raspopovic et al., 2014; Wurth et al., 2017). Moreover, these technologies manifested long-term stability and functionality in rats and amputee subjects (Petrini, Valle, Strauss, et al., 2019; Wurth et al., 2017).

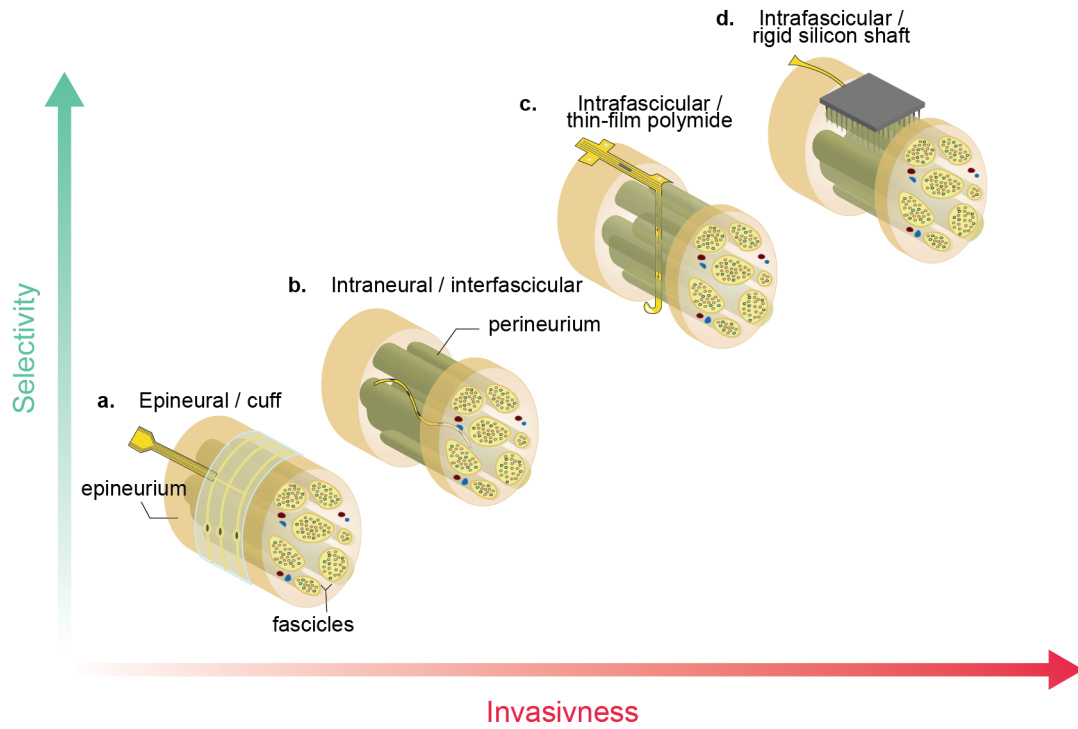


Figure 1.4 – Relationship between selectivity and invasiveness of peripheral nerve interfaces. Four examples of implants are presented: **a.** the epineural cuff implant (Loeb and Peck, 1996; Rodríguez et al., 2000), **b.** the interfascicular longitudinal implant (D. Tyler and Durand, 1997), **c.** the transverse intrafascicular multichannel electrode (Boretius et al., 2012; Raspovic et al., 2014), **d.** the silicon-based Utah array (Branner et al., 2001; Ledbetter et al., 2013).

In this work, we identified the transverse intrafascicular multichannel electrode (TIME) as the optimal candidate to restore precise grasping function through peripheral nerve stimulation (Boretius et al., 2012). We argue that this implant offers a reasonable trade-off between selectivity and invasiveness, allowing, on the one hand, the elicitation of precise grasping movements and, on the other hand, reducing the impact on the nerve and favoring chronic integration and stability.

1.3. Interaction between electrical stimulation and peripheral nerves

Peripheral nerve neuromodulation promotes the generation of powerful yet precise movements by injecting electrical current in the proximity of neural fibers. In this section, we develop the mechanisms underlying the activation of efferent and afferent fibers through electrical stimulation, and the techniques that have been applied to improve axonal recruitment.

1.3.1. The anatomical structure of the somatic peripheral nervous system

The peripheral nervous system (PNS) is composed of cranial nerves originating from the brain, and spinal nerves emerging from the spinal cord. The somatic nervous system relates to the part of the peripheral nervous system associated with voluntary control of body movements. It comprises afferent nerve fibers relaying somatosensory information, and efferent nerve fibers that convey motor commands from the central nervous system to the skeletal muscles. Efferent signals originating from upper motor neurons in the brain travel down the cortical spinal tract, to the ventral horn of the spinal cord, where they are transmitted to the lower motor neurons innervating the musculature. The ensemble, composed of each motor fiber and its target muscle fiber, is called a motor unit. A smooth muscle contraction is the result of the coordinated activation of its motor units. Conversely, peripheral somatosensory neuronal cell bodies reside in the dorsal horn of the spinal cord. Somatosensory and motor fibers are arranged, in a mixed or segregated manner, in parallel bundles, called fascicles (**Figure 1.5**).

Three scaffolding structures (**Figure 1.5**) support the peripheral nerve (Ushiki and Ide, 1990). The innermost tissue, the endoneurium, incorporates axons and their supportive cells, such as Schwann cells, the collagen matrix, fibroblasts, capillaries, and resident macrophages (Liu et al., 2019). These cellular and structural components reside in the fascicular endoneurial fluid. The endoneurium is wrapped in a second protective sheet, the perineurium. This insulating layer, composed of interlacing perineurial cells and collagen fibrils, blocks blood flow and limits the spread of current. The outermost envelope covering the nerve is called the epineurium, and is constituted by relatively compact connective tissue and blood vessels. This fibrous coat provides both resilience and tensile strength to the peripheral nerves (Varga and Mravec, 2015).

The most common morphological classification of nerve fibers distinguishes them into unmyelinated and myelinated fibers. Myelination refers to the superimposition of myelin sheets around the axons (**Figure 1.5**). It significantly increases the speed of signal transmission along the fibers, compared to unmyelinated axons, which run in invaginations along the surface of Schwann cells. Indeed, action potentials propagate along myelinated fibers via saltatory conduction between the nodes of Ranvier. At this location, a rich density of voltage-gated Na^+ and K^+ channels allows the spread of current through the fiber membrane, resulting in the depolarization of the axons. The current travels from one node of Ranvier to the next in a jumping-fashion. Motor fibers connecting to muscle spindles are fast myelinated axons, while sensory fibers can either be myelinated or unmyelinated. In unmyelinated fibers, signal transduction speed is not critical, and action potentials are conducted via passive propagation (Noback et al., 2005; Varga and Mravec, 2015). Most peripheral nerves present a mixed population of myelinated and unmyelinated fibers. Other characteristics differing between nerve fibers are the diameter, the function, and the conduction velocity. Researchers have classified sensory and motor nerve fibers into types A, B, and C, summarized in **Table 1.1**.

In this work, we are interested in the recruitment of skeletal muscles either via the direct

1.3 Interaction between electrical stimulation and peripheral nerves

Table 1.1 – Types of fibers in mammalian nerves modified according to (Ganong, 2013; Terzis et al., 1991)

Fiber Type (μm)	Subtype	Functions	-	Radius (μm)	Conductance Velocity (m/s)
A	α	Myelinated somatic afferent and efferent	Proprioception, somatomotor	12-20	70-120
	β		Touch, pressure	5-12	30-70
	γ		Motor for muscle spindles	3-6	15-30
	δ		Pain, cold, touch	2-5	12-30
B		Myelinated preganglionic autonomic		<3	3-15
C	Dorsal horns	Unmyelinated somatic afferent	Pain, temperature mechanoreception reflex response	0.5-2	0.5-2
	Sympathetic	Unmyelinated autonomic postganglionic	Pain, Pilomotor sudomotor vasomotor	0.7-2.3	0.7-2.3

excitation of efferent fibers or via the elicitation of spinal reflexes through the stimulation of afferent fibers. In both cases, the positioning of the stimulating interface with respect to the targeted fiber population plays a crucial role in the efficacy of the excitation.

1.3.2. Mechanisms of neural fiber recruitment

Numerous studies have documented the mechanisms governing the excitation of neural fibers following the delivery of an electrical stimulus (McIntyre and Grill, 2000, 2002; Rattay, 1986). In particular, researchers have implemented neural models to study the response of fibers to various stimuli, in a simplified and controllable manner. These models usually consist of a series of resistors and capacitors wired in parallel to represent the various types of ion channels responsible for the exchange of electrical charges through the membrane (Richardson et al., 2000). The lipidic double-layer membrane has been modeled as a single capacitor accumulating charge on either side. Through the use of these models, scientists have shown that depolarization and hyperpolarization mechanisms depend on multiple factors, such as the degree of myelination, the distance between the fiber and the excitation source, the diameter of the fibers, the conductivity of the neural structures and the shape of the stimulation pulse.

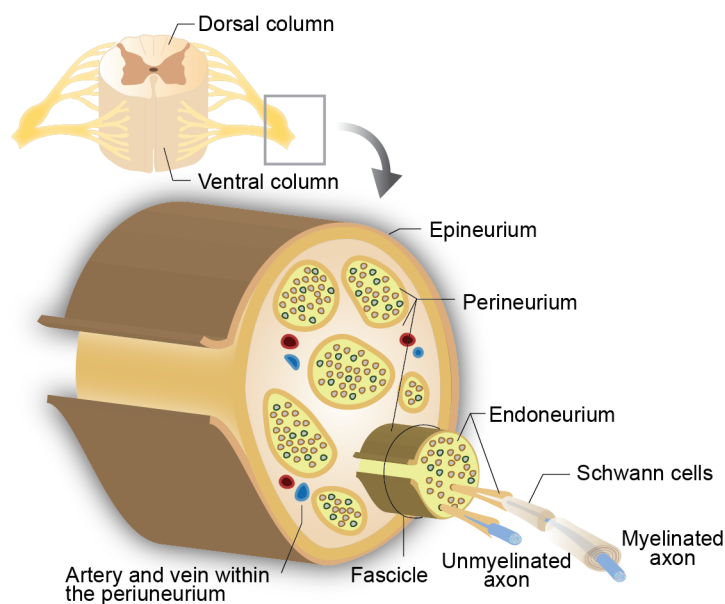


Figure 1.5 – Anatomical structure of the peripheral nerve.

Influence of the myelination

Myelination is known to play an important role in the conduction velocity of an action potential along the nerve fiber (Waxman, 1980). However, studies also demonstrated the importance of the multilamellar myelin sheath in transitory changes of electrical potential following electrical stimulation (Barrett and Barrett, 1982; Blight and Someya, 1985). In particular, Barrett and colleagues have demonstrated the role of myelin in the creation of depolarizing after-potential effects. Their findings suggest that, rather than completely inhibiting current flow, the membrane of myelinated nerve fibers discharges via an internodal leakage pathway under the myelin sheath, resulting in a prolonged super-excitable period following an action potential (Barrett and Barrett, 1982).

Consequently, the representation of myelin has varied among neural models depending on whether it was considered as a perfect insulator (McNNeal, 1976; Sweeney et al., 1987), imperfect barrier (Fitzhugh, 1962; Frijns and ten Kate, 1994; Goldman and Albus, 1968; J. W. Moore et al., 1978; Rubinstein, 1991), or a more complex structure playing a role in depolarizing voltages (Blight and Someya, 1985; Bostock et al., 1991; Halter and Clark, 1991; Stephanova and Bostock, 1995). In 2000, Richardson, McIntyre, and Grill computationally compared three different representations of myelin (Richardson et al., 2000). They demonstrated that partially conductive models resulted in higher activation threshold currents than myelin representations which assumed complete insulation. Their imperfect myelin insulator model was found to recapitulate experimental ranges of conduction velocities, while their most complex myelin representation was the only one to produce the depolarizing after-potentials observed in nature. These examples highlight how sophisticated axon electrical models that incorporate complex physiological processes can help understand the importance of myelin

in the excitatory properties of neural fibers.

Influence of neural tissue electrical properties

Every biological nerve tissue has specific electrical properties. The intrafascicular endoneurium medium presents anisotropic conductivity properties due to the presence of conductive axons running in parallel. Its longitudinal and transversal conductivity values have been measured to be 0.571 S/m and 0.0826 S/m, respectively (Ranck and BeMent, 1965). The resistivity of the epineurium envelope surrounding the nerve is not known but is generally assumed to be equal to the transverse resistivity of the endoneurium, due to the high similarity between these two connective tissues (Choi et al., 2001). The perineurium layer acts as a strong insulator, and therefore possesses a low conductivity value (~ 0.0021 S/m). It was experimentally derived from frog experiments (Weerasuriya et al., 1984) and extrapolated to larger perineurium thicknesses (Choi et al., 2001; Raspopovic et al., 2017; Schiefer et al., 2008). These electrical properties considerably influence the distribution of voltage upon electrical stimulation within the nerve. Namely, the low conductivity of the perineurium limits the current flow inside the fascicle and generates an “all-or-nothing” activation of the fibers once the amplitude becomes large enough to overcome its resistivity. Similarly, the epineurium behaves as an insulating barrier, impeding the crossing of current from the extraneural space to the intraneural space. These properties partially explain why intrafascicular stimulation results in a more graded, and therefore more selective, engagement of the neural fibers than extraneural stimulation (Badia et al., 2011).

Influence of the distance from the excitation source

In 1986, Rattay derived the "activating function", predicting the reaction of an axon stimulated by extracellular electrodes (Rattay, 1986). This function represents the second derivative of the extracellular electrical potential, V_e . In his work, V_e is described as the voltage variation resulting from the monopolar excitation of a point source electrode located at a distance r from the voltage measurement point. He formulated V_e as:

$$V_e = \frac{\rho_e I_e}{4\pi r} \quad (1.1)$$

where ρ_e is the resistivity of the homogenous extracellular milieu, and I_e is the current flowing from the electrode. In **formula 1.1**, the voltage variation is inversely proportional to the distance between the excitation current source and the neural fiber, i.e. voltage values are higher in the vicinity of the electrode. The "activating function" is responsible for the excitation of the fiber and relates to the likelihood of activation. **Figure 1.6** illustrates the displacement of electrical charges in an axon following extracellular stimulation, together with the variations in the voltage and "activating function". The extracellular injection of negative current in the proximity of the fiber creates an accumulation of positive charges at the center of the axon due to the capacitive property of the membrane (**Figure 1.6 a**). This effect increases

the likelihood of depolarizing the membrane and eliciting an action potential. Conversely, a positive extracellular excitation results in the accumulation of negative molecules at the center of the fiber, which repels positive ions on the sides, increasing the probability of triggering an action potential in the areas surrounding the center (**Figure 1.6 b**). However, because positive ion concentrations are lower in the case of anodic stimulation, positive peaks in the "activating function" are reduced. This explains the higher activation charge thresholds for anodic stimulation. Taken together, these properties of extracellular recruitment reveal that axons located close to the stimulation source require a lower recruitment charge threshold than fibers lying farther away.

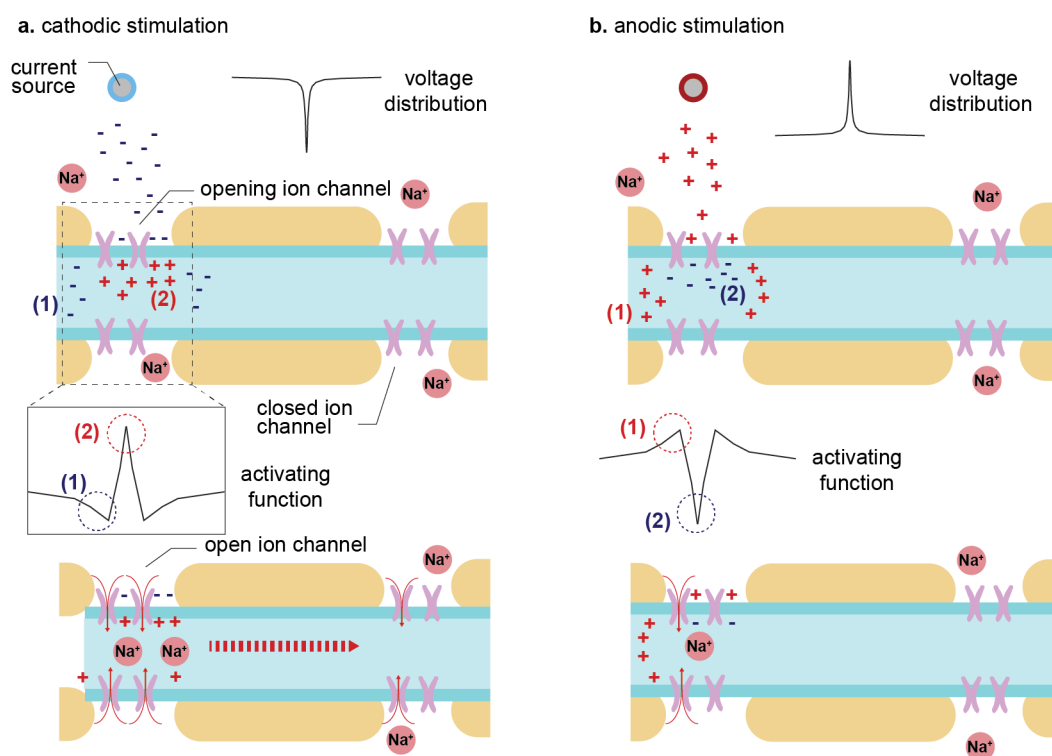


Figure 1.6 – Extraneural stimulation of a myelinated peripheral nerve fiber. a. Cathodic current stimulation results in an extracellular voltage drop and promotes the triggering of an action potential at the center of the stimulated fiber. **b.** Anodic stimulation results in an extracellular voltage rise, reducing the chance of the axon firing at its center, and favoring the elicitation of an action potential in the surrounding areas.

Influence of fiber diameter

The mechanisms underlying the selection of fibers for myelination are not fully understood, but probably relate to the axon diameter. Indeed, by increasing the axon's diameter, the thickness of the myelin sheath increases, as well as the distances between the nodes of Ranvier, creating a larger change in voltage across the fiber membrane. The diameter of the fiber and the length of the internode is thus proportional to the conduction speed of the nerve

impulse (Noback et al., 2005). Concurrently, the likelihood of activation of an axon at a given distance from a current source increases for large-diameter fibers. Extraneural stimulation thus recruits thicker nerve fibers before thin fibers, following an inverse order of recruitment compared to physiological responses (Durand et al., 2004; Henneman, 1985). This unnatural activation of motoneurons constitutes an additional cause for the rapid occurrence of fatigue in neuromuscular FES, since large motor fibers primarily innervate fast-fatiguing motor units.

Such “large-to-small” recruitment order is more critical for extraneural stimulation (percutaneous, surface, cuff) than for intraneural recruitment. Indeed, Veltink’s work based on mathematical models (Veltink, van Veen, et al., 1989) and subsequent experimental validations (Veltink, Alste, et al., 1989; Yoshida and Horch, 1993) showed that for intraneural implants positioned at a small distance from the target axons, the recruitment order was not biased towards large fibers. Similarly, Gaunt and colleagues demonstrated that intraneural stimulation of the dorsal root ganglion of the cat sciatic nerve at low current amplitudes preferentially recruited smaller-diameter afferent fibers than larger ones (Gaunt et al., 2009). Results obtained using polyimide-based intrafascicular electrodes confirmed this response pattern in which the axon diameter has only a limited impact on the order of fiber recruitment (Raspopovic et al., 2012). Hence, by reducing the distance between the electrode and the targeted fiber population, intrafascicular stimulation diminishes the influence of fiber dimensions on the selective recruitment of the axons.

Influence of the stimulation waveform

Other ways to overcome the inverse recruitment of fibers consist of modifying the stimulation paradigms to promote smooth and natural activation of the muscles. Researchers have investigated the effects of trading the simple symmetric squared stimulation waveform for more complex patterns of stimulation, to attenuate the bias towards excitation of large fibers. Early neuromodulation experiments conducted using a tripolar electrode configuration, combined with triangularly shaped pulses, successfully achieved the selective activation of small myelinated delta axons, and the silencing of large beta ones (see **Table 1.1**) (Accornero et al., 1977). Fifteen years later, Fang and colleagues exploited quasitrapezoidal current pulses to block anodal break in large fibers with low current amplitudes, and thereby obtain a small-to-large recruitment order of myelinated fibers (Fang and Mortimer, 1991). Other experimenters extended these results to unmyelinated and myelinated fibers by efficiently inducing anodal block through multipolar epineural stimulation (Fitzpatrick et al., 1991; Rijkhoff et al., 1993).

Overall, the design of effective neurostimulation strategies is crucial to obtain functional, sustainable, and selective excitation of the targeted neural structures. All the aforementioned aspects play an important role in the restoration of motor function, and in particular hand function, via neuromodulation. Neuromuscular stimulation paradigms must therefore be thoroughly thought through and optimized in order to one day be efficiently translated to the clinic.

1.3.3. Refinement strategies for peripheral neuromodulation

The past 20 years have seen a surge in the development of electronic devices for neurological clinical applications. Experimental proof-of-concept studies, together with the manufacturing of miniaturized, wireless, and low-power consumption electronic components, fostered the engineering of more and more sophisticated neurostimulation techniques. However, despite the increasing therapeutic demand and the energetic pace at which neurotechnologies are progressing, critical thinking and rigorous scientific approaches are needed to guide the development of translational tools (Capogrosso and Lempka, 2020). More specifically, the implementation and marketing of novel neural interfaces must be driven by our understanding of how electrical stimulation interacts with the underlying neuronal circuitries. Yet, to date, most neurological systems are largely undetermined, and the characterization of the neuronal targets of electrical stimulation remains insufficient (Capogrosso and Lempka, 2020).

Computational models offer an unprecedented opportunity to base the implementation of neuromodulation devices on reasonable and enlightened estimates of their efficacy *in vivo*. On the one hand, they provide a way to evaluate the gaps in our understanding of neural systems and the experiments we should conduct to fill them (Markram et al., 2015). On the other hand, they constitute powerful *in-silico* testing platforms in which stimulation paradigms can be explored and refined to derive optimal ways of interacting with the neural architecture (Mcintyre and Foutz, 2013).

Computational modeling has successfully been applied to motor control applications in animal models (Capogrosso, Gandar, et al., 2018; Greiner et al., 2020; Raspopovic et al., 2011) and in humans (Raspovic et al., 2017; Tigra et al., 2020). For instance, Capogrosso and colleagues combined electromagnetic models and model-driven experiments to understand the effects of epidural stimulation of the spinal cord (Capogrosso et al., 2013; Capogrosso, Gandar, et al., 2018) and identify its primary recruited neuronal targets. They experimentally confirmed that electrical stimulation of the spinal cord preferentially recruited peripheral sensory circuits, without directly exciting the grey matter neurons, to produce coordinated locomotion after a spinal lesion, as previously suggested (Edgerton et al., 2008). Follow-up studies have extended electromagnetic models of the lumbar spinal cord and combined them with an artificial representation of the complex spinal networks and biomechanical leg models (Formento et al., 2018; Moraud et al., 2016). These frameworks unveiled the existence of disrupting antidromic action potentials in sensory afferents following epidural stimulation in humans, explaining the absence of proprioceptive percepts in patients implanted with epidural stimulators. Interestingly, these deleterious effects were not present in rats, owing to the differences in anatomical dimensions and conduction velocities of neural fibers compared to humans. In peripheral nerve stimulation applications, computational models have shown the benefits of using intrafascicular interfaces over extraneural implants to promote the natural recruitment of motor axons (Raspovic et al., 2012). Volume conductor models based on realistic histological data demonstrated the potential of intrafascicular bipolar stimulation to steer the current towards fascicles that do not intersect with the active sites (Raspovic et al.,

2017).

Besides completing our understanding of neuromodulation mechanisms, modeling approaches can guide the design and placement of stimulating interfaces. Computational modeling of epidural stimulation in the cervical segments in monkeys highlighted the importance of positioning the stimulating contacts on the dorsal roots rather than on the dorsal column to improve recruitment specificity (Greiner et al., 2020). Similarly, Dali et al., used *in-silico* testing to optimize the current distribution of an extraneural implant in the vagus nerve (Dali et al., 2018). They implemented a way to identify optimal multipolar configurations without *a priori* knowledge of the nerve anatomy, and used this method to elicit specific finger movements in anesthetized patients suffering from cervical SCI (Tigra et al., 2020).

Ultimately, computational methods provide a way to take advantage of the extensive amount of data gathered from previous scientific experiments. They give us a better understanding of the mechanisms underlying the modulation of our nervous system and help us optimize neurostimulation devices using evidence-based approaches rather than heuristic incremental research (Capogrosso and Lempka, 2020).

1.4. Voluntary control of a prosthesis restoring hand function

For a restorative electrical therapy to be pertinent and successfully applied in paralyzed individuals, stimulation must ultimately be driven by incoming user commands. In particular, neurotechnologies aiming at replacing upper-limb movements need to integrate more or less complex motor inputs, and afford the control of a sufficient number of degrees of freedom. Numerous challenges undermine the implementation of these control paradigms, such as the precise decoding of motor signals, the encoding of instructions into stimulation patterns evoking specific movements (i.e. single digit motion, grips...), the degree of cognitive load for the user, the multi-dimensional control of several stimulation channels, etc... With the development of modern neuroprosthetic devices, a vast diversity of control strategies has been developed to integrate voluntary commands into the operation loop. These decoding protocols rely on peripheral body signals or incoming cortical inputs and have been extensively used in the design of brain-machine interfaces (BMI) for clinical applications.

1.4.1. Peripheral body commands to drive the prosthesis

A direct and simple way to control electrical stimulation is to rely on peripheral commands from the user's body. The advantage of this approach rests on the use of pre-processed efferent signals that reflect low-dimensional characteristics of the movement. The control signal usually requires little post-processing, and translates intelligible user commands such as muscle contraction, limb movement, eye saccade, etc... Some assistive devices have been operating on substitutive signals such as "sip-and-puff" actions (Handa et al., 1998), or contralateral limb movements (Hobby et al., 2001). Nevertheless, these strategies provide only a small reper-

toire of commands, can be unintuitive, and constrain the user to relearn previously acquired motor tasks. Besides, systems that depend on healthy limb movements or contractions to trigger the stimulation interfere with healthy motor functions, further reducing the mobility of the patient. More importantly, by minimizing body motion and neglecting the dynamics of neurological lesions, stimulation approaches that fail to promote the use of remnant neural and muscular components may contribute to the overall loss of mobility. Indeed, studies have shown that in individuals affected by SCI, the active solicitation of residual neuromuscular structures may reduce collateral effects of paralysis and improve motor functions (Chen et al., 1998; Hesse et al., 2003; Levy et al., 1990; Topka et al., 1991).

Numerous studies have explored the use of remaining muscular or kinematic activity to drive the operation of neuroprostheses. In paralyzed individuals retaining some volitional muscle contraction of the upper-limb or neck, electromyograms (EMG) have been used to provide natural and intuitive control over functional neuromuscular stimulation (Fonseca et al., 2019; Keith et al., 1996; Kilgore et al., 2008; Memberg et al., 2014).

Alternatively, Prochazka and colleagues modulated the transcutaneous excitation of hand muscles based on residual wrist movements (Prochazka et al., 1997). However, the generation of precise hand movements based on peripheral signals is a much more daunting issue in fully-paralyzed individuals. Indeed, kinematic and myoelectric control provide only a few command options and poorly extend to coordinated, multi-joint movements.

Control strategies based on cortical activity offer an intuitive and spontaneous access to motor outputs, and include high dimensional motor features. The complex representation of movements, in particular, finger motion, at the cortical level offers the opportunity to extract multiple control variables and potentially actuate several joints simultaneously.

1.4.2. Brain-controlled prosthetic devices

BMIs, also referred as Brain-computer interfaces (BCIs), describe the complete technological framework, including the software and hardware, that can be used to communicate brain commands to various artificial devices (communication device, robot, prosthesis...). Donoghue and colleagues defined BMIs as systems aiming to provide a cortical command signal to control disabled limbs or physical devices (Donoghue, 2002). Similarly, Schwartz et al. described the BMI technology as “Microelectrodes embedded chronically in the cerebral cortex [that] hold promise for using neural activity to control devices with enough speed and agility to replace natural, animated movements in paralyzed individuals” (Schwartz, 2004). The term BMI encompasses a wide variety of schemes, ranging from non-invasive electroencephalograms (EEG), subdural implants (ECoG), intracortical penetrating arrays, and the operation of multiple external devices (computers, robotic arms, FES...). In this chapter, we focus on BMI protocols relying on intracortical electrode arrays, as these implants have shown extended ability to decode signals in fine upper-limb motor tasks (Collinger, Boninger, et al., 2013; Irwin et al., 2017; Vaskov et al., 2018), high stability (Chestek et al., 2011) and longevity *in*

1.4 Voluntary control of a prosthesis restoring hand function

vivo (Branner et al., 2004), and safe clinical use. Here we discuss the two main approaches researchers have investigated so far for the control of prostheses, in particular, for driving the stimulation of the arm and hand and alleviating upper-limb paralysis. Namely, we describe how continuous cortical decoding can transform complex task-related commands into patterns of stimulation to reanimate muscles. We then further discuss the possibility of artificially mapping brain outputs into a control variable to actuate paralyzed limbs.

Continuous decoding for graded hand movements

BMI systems relying on intracortical continuous decoders have successfully been used in monkeys (Carmena et al., 2003; Lebedev et al., 2005; Serruya et al., 2002; Velliste et al., 2008), and in paralyzed individuals (Aflalo et al., 2015; Collinger, Boninger, et al., 2013; Hochberg et al., 2012; Hochberg et al., 2006), to control the displacement of a cursor on a screen, or the reaching and grasping movements of multi-joint robotic arms. Building upon the seminal work performed in primates, recent clinical studies have achieved online cortical control of haptic robots in a high number of degrees of freedom (Collinger, Boninger, et al., 2013; Wodlinger et al., 2015) and demonstrated the possibility of controlling different robotic grip patterns (Wodlinger et al., 2015).

Regarding electrical stimulation control, temporarily paralyzed monkeys have efficiently employed BCI to drive the stimulation of implanted FES systems, or intraspinal arrays, to elicit wrist and grasping movements (Ethier et al., 2012; Zimmermann and Jackson, 2014). In two successive studies, Bouton and colleagues linked intracortical signals with high-density surface FES to generate graded hand closure in an individual with cervical SCI (Bouton et al., 2016; Friedenberg et al., 2017). Using a similar stimulation approach, a more recent paradigm achieved the dexterous control of seven functional grips using frequency-based neural features and classifying the desired movements with a nonlinear support vector machine (Colachis et al., 2018). Ajiboye and his team employed a more invasive stimulation strategy and coupled an intracortical BMI system with percutaneous FES to restore multi-joint coordinated reaching and grasping movements in a C5/C6 tetraplegic patient (Ajiboye et al., 2017).

Although these results provide impressive proofs-of-concept, most of these stimulation protocols presented simple all-or-nothing hand opening or closing, were limited to a few discrete postures, and elicited relatively gross movements. Two major challenges currently undermine the development of sophisticated neural prostheses for the restoration of dexterous hand movements. First, the reliable decoding and simultaneous control of a large number of degrees of freedom by the user. Second, the encoding of these numerous control variables into stimulation patterns, and the modulation of stimulation parameters to recapitulate smooth and natural hand motion.

Most modern decoders for continuous predictions of upper-limb kinematics rely on linear transformation functions such as Kalman (Ajiboye et al., 2017), or Wiener filters (Carmena et al., 2003; Velliste et al., 2008). These algorithms demonstrated the ability to decode multiple

joint movements and control up to three virtual degrees of freedom simultaneously (Ajiboye et al., 2017). Other neural decoders are based on models linearly coupling the neural firing rate to movement velocity (Collinger, Boninger, et al., 2013; Georgopoulos et al., 1986; Wodlinger et al., 2015). Although these models demonstrated improved levels of performance for numerous degrees of freedom, they have so far been limited to the decoding of reach movements.

Transfer functions such as linear filter methods provide an intuitive control and natural coupling between the cortical inputs and the desired kinematic outputs. However, most are supervised algorithms that must be trained on cortical and kinematic datasets, rarely available in paralyzed individuals. The need for healthy data in studies recruiting disabled subjects has skillfully been bypassed using virtual reality training (Ajiboye et al., 2017; Bouton et al., 2016). Additionally, while being extremely accurate and stable over a few weeks or months (Nuyujukian et al., 2014), continuous decoders still require re-calibration to account for the slight changes in cortical population activity. Recent studies have developed promising techniques to render BMI decoders more robust to neural variability (Degenhart et al., 2020; Gallego, Perich, Chowdhury, et al., 2018; Sussillo et al., 2015). Ultimately, the implementation of these strategies in user-friendly devices for a simplified calibration of the algorithms at home holds promises for the autonomous operation of BMI systems. Continuous decoding strategies for fine and dexterous hand tasks have been less extensively studied than for reaching, but recent work has shown encouraging evidence for the accurate prediction of single-digit movement based on cortical data. Indeed, following the demonstration of Irwin and colleagues on the continuous decoding of finger position in monkeys (Irwin et al., 2017), researchers have refined the calibration of linear decoders and successfully predicted individual index and middle finger motion with largely improved performance (Vaskov et al., 2018).

Altogether, these methods offer interesting perspectives for the specific and reliable decoding of hand movements in clinical paradigms. Conversely, the mapping from sophisticated decoded commands to functional patterns of stimulation for restoring hand control has been far less investigated.

Functional electrical stimulation of the hand muscles based on cortical commands poses a dimensionality control problem. Namely, a large number of electrodes recruiting different muscles needs to be controlled simultaneously and independently through a reduced number of control variables. Continuous intracortical decoding can be used to predict muscular activity or kinematic features. Although the decoding of muscle activation provides quantifiable measures that can be directly linked to the electrical stimulation outputs, virtual reality training on EMG activation is impossible. Instead, this approach likely requires the implementation of complex biomechanical models, none of which are widely available for the hand at this time. In BMI studies predicting kinematic features of the hand, stimulation patterns have so far been identified manually (Ajiboye et al., 2017; Colachis et al., 2018). However, such implementation has either reproduced all-or-nothing grasping movements based on discrete classification results (Colachis et al., 2018), or enabled the activation of several electrode contacts using up to two simultaneous commands (Ajiboye et al., 2017). Although these studies presented major

1.4 Voluntary control of a prosthesis restoring hand function

advances in the field, they were limited in terms of variety and range of hand movements the user could control without excessive cognitive load.

The development of simpler stimulation strategies providing a comprehensive activation of hand muscles through a small number of electrodes would likely improve the control of the prosthesis and yield functionally relevant outputs, without imposing extra mental burden to the user.

Direct control strategy

A less intuitive, yet more straightforward way to drive the stimulation of paralyzed muscles is by using direct cortical control. This technique consists of the direct artificial coupling between neural features, usually neuron firing rate, to a controlled variable, for instance, the amplitude of stimulation. The direct control approach holds the advantage of not requiring training kinematic data for calibrating the predictive algorithm. Besides, cortical commands can theoretically be extracted from structures of the brain that do not necessarily relate to movement, making this strategy applicable for patients with cortical damage, such as stroke victims. Direct control has been used in monkeys to control FES stimulation of the wrist, and elicit bidirectional single-joint movements (Moritz et al., 2008). This approach permitted a fine, graded flexion and extension of the paralyzed wrist muscles, coincident to the respective increase and decrease of a neuron firing rate. The authors reported that the tuning of motor cortical cells during healthy wrist movements was not predictive of the ability of these cells to modulate the stimulation. Hence, cortical modulation was not intrinsically linked to the hand movement. Interestingly, researchers showed that the monkey successfully learned to modulate pairs of neurons independently from each other, and separately control the stimulation of flexor and extensor muscles. In parallel, Taylor and colleagues demonstrated the feasibility of controlling external devices along three-dimensions using direct cortical control (Helms Tillery et al., 2003; D. M. Taylor et al., 2002). These findings have important implications for the command of electrical stimulation using brain control. By providing a direct bridge between cortical outputs and motor activity, this strategy could promote innate motor learning mechanisms to optimize the control over the prosthesis. Namely, a graded, independent control of stimulation channels recruiting different finger muscles could restore dexterous movements in which the timing and co-activation patterns of the stimulation would be regulated by the user. This method relies on the capacity of the brain to adapt to new, but robust, sensorimotor possibilities (Shadmehr and Mussa-Ivaldi, 1994; Thach, 1978) and to rapidly learn new motor skills (Gandolfo et al., 2000; Nudo et al., 1996). Yet, one drawback of previous direct control approaches resides in the use of single-unit activity as control signals. Because single-cell activity has been shown to vary over time (Perge et al., 2013) in intracortical recordings, previous direct control algorithms needed to be re-calibrated. Alternatively, the use of more conserved cortical dynamics for control variables could be explored to ensure the stability of direct commands over time (Gallego, Perich, Chowdhury, et al., 2018) (Gallego et al., 2020, 2018). One could imagine using low-dimensional cortical dynamics to drive three

different kinematic joints and readjusting the decoder space through linear mathematical transformations, for example (Gallego et al., 2020).

Overall, numerous challenges remain for the efficient translation of user commands into dexterous evoked hand movements, such as the need to decode a large range of kinematic features. The effective integration of new motor control modalities into the natural sensory-motor schemes of the user also needs to be investigated. Ultimately, a device able to engage synergistic muscles using simple stimulation strategies would create promising opportunities for the intuitive control of the hand through a reduced number of instructing commands.

1.5. Thesis Outline

This introduction provides a general overview of electrical stimulation therapies in the context of neurological disorders affecting the upper-limb and hand. It introduces the theory underlying the recruitment of muscles through neuromuscular stimulation, and provides a methodological and conceptual framework for the design and control of stimulation devices aiming at restoring hand function after paralysis.

As described in this chapter, functional neuromuscular electrical stimulation, based on the direct excitation of muscles, has previously been used to restore hand or arm control after SCI or stroke. Transcutaneous or invasive muscle recruitment techniques have shown encouraging evidence for the reanimation of hand function, but still face numerous challenges in terms of specificity, technical complexity, and in their ability to generate functional and sustainable movements.

In this thesis, I present a novel and highly-promising approach for the restoration of dexterous hand movements using peripheral electrical stimulation. I argue that intrafascicular thin-film electrodes represent an ideal candidate for the restoration of precise and functional hand movements after paralysis. The optimization and the testing of intrafascicular stimulation paradigms in a pre-clinical animal model allow for a thorough characterization of the technology and provides the basic building blocks to efficiently translate it to the clinic. This hypothesis was tested in a non-human primate model, namely in fascicularis macaques, on account of their close similarity to human anatomy and their ability to perform sophisticated hand motor tasks.

In chapter 2, I present a versatile robotic platform incorporating multiple physiological signals, which I designed for the study of upper-limb movements in monkeys.

In chapter 3, I demonstrate the potential of transverse intrafascicular multichannel electrodes (TIMEs) to specifically activate hand muscles in monkeys and to generate a rich repertoire of wrist and finger movements. I show that tailored intrafascicular stimulation of the arm median and radial nerves allows a selective, functional, and controllable activation of flexors and extensors of the hand. Additionally, I provide a simple proof-of-concept that TIME stimulation

can be driven through motor intracortical signals to enable a transiently paralyzed monkey to perform a functional grasping task.

In chapter 4, I present preliminary results highlighting the possibility of controlling a 2-dimensional cursor based on low-dimensional cortical dynamics. I demonstrate that a monkey can progressively adapt to a fixed linear transfer function, and that coupling intrafascicular stimulation to the modulation of cortical dynamics does not perturb this control.

These developments may have important implications for the functional restoration of hand dexterity in individuals affected by neurological disorders. The rich collection of movements provided by intrafascicular stimulation and the controllability achieved through neuromodulation offer encouraging perspectives for the autonomous and voluntary command of the interface. In this framework, and building upon this thesis work, I discuss the necessity to optimize intrafascicular stimulation for motor recovery of hand function and open the discussion on the next critical steps for a successful translation of this technology to the clinic.

2 Adaptative behavioral platform for the study of upper-limb movements in monkeys

Monkeys represent a valuable model for the pre-clinical testing of experimental therapies targeting neurological disorders. To translate such solution to the clinic, I believe it is crucial to achieve a comprehensive characterization of the sensorimotor components underlying limb movements in primates. In this work, I present a modular behavioral setup for the study of reaching and grasping movements in monkeys. Together with my colleague Beatrice Barra, we implemented a robotic platform, integrating kinetic, kinematic, and electrophysiological signals, for the monitoring of upper-limb state. I describe the robotic platform we engineered, and the sensing devices we customized for the monitoring of grip force. I show that this setup permits the study of multiple joints kinematics and interaction forces, together with their encoding in sensorimotor cortical areas. I also demonstrate the utility of our platform for the implementation of brain decoding algorithms to predict kinematic features of reaching and grasping movements. With this work, I illustrate the potential of our versatile setup for the design of a large collection of tasks, and the benefits it holds for fundamental studies or translational applications of motor control.

The content of this chapter is adapted from the manuscript Barra, Badi et al., “A versatile robotic platform for the design of natural, three-dimensional reaching and grasping tasks in monkeys” published in the journal *Journal of Neural Engineering*, Volume 17, Number 1, December 2019.

Personal contributions: Beatrice Barra (co-first author) and I conceived the study, conducted the experiments, trained the animals, processed the data, performed the data analysis, prepared the figures, wrote the manuscript. I designed and implemented the integrated sensors hardware and software. Beatrice Barra designed and implemented the robotic framework hardware and software modules. Extended authors contributions are reported at the end of the chapter.

A versatile robotic platform for the design of natural, three-dimensional reaching and grasping tasks in monkeys

Barra B^{*1}, **Badi M**^{*2}, Perich MG³, Conti S^{1,4}, Mirrazavi Salehian SS⁵, Moreillon F⁶, Bogaard A^{1,2}, Wurth S², Kaeser M¹, Passeraub P⁶, Milekovic T³, Billard A⁵, Micera S^{**2,4} and Capogrosso M^{**1}

¹ Department of Neuroscience and Movement Science, Platform of Translational Neurosciences, University of Fribourg, Switzerland

² Translational Neuroengineering, Center for Neuroprosthetics and Institute of Bioengineering, École Polytechnique Fédérale de Lausanne (EPFL), Lausanne, Switzerland

³ Department of Fundamental Neuroscience, Faculty of Medicine, University of Geneva, Geneva, Switzerland

⁴ The Biorobotics Institute, Scuola Superiore Sant'Anna, Pisa, Italy

⁵ Learning algorithms and Systems Laboratory, École Polytechnique Fédérale de Lausanne (EPFL), Lausanne, Switzerland

⁶ University of Applied Sciences and Arts Western Switzerland (HES-SO), Geneva, Switzerland

* Co-first authors, ** Co-senior authors

2.1. Abstract

Objective: Translational studies on motor control and neurological disorders require detailed monitoring of sensorimotor components of natural limb movements in relevant animal models. However, available experimental tools do not provide a sufficiently rich repertoire of behavioral signals. Here, we developed a robotic platform that enables the monitoring of kinematics, interaction forces, and neurophysiological signals during user-defined upper limb tasks for monkeys.

Approach: We configured the platform to position instrumented objects in a three-dimensional workspace and provide an interactive dynamic force-field.

Main results: We show the relevance of our platform for fundamental and translational studies with three example applications. First, we study the kinematics of natural grasp in response to variable interaction forces. We then show simultaneous and independent encoding of kinematic and forces in single unit intra-cortical recordings from sensorimotor cortical areas. Lastly, we demonstrate the relevance of our platform to develop clinically relevant brain computer interfaces in a kinematically unconstrained motor task.

Significance: Our versatile control structure does not depend on the specific robotic arm used and allows for the design and implementation of a variety of tasks that can support both fundamental and translational studies of motor control.

2.2. Introduction

Modern approaches to system neuroscience as well as the study of motor recovery in clinical applications require detailed characterization of sensorimotor neural activity underlying natural, three-dimensional movements rather than artificially constrained behaviors. In this context, an ideal experimental set-up should provide 1) flexible and instrumented workspaces to allow natural, but reproducible motor behaviors and 2) the integration of multimodal electrophysiology recordings and behavioral signals.

However, to date, no experimental set-up allows the integration of electrophysiological recordings with extrinsic signals quantifying natural interactions with the environment.

Indeed, several groups developed sophisticated experimental platforms capable of characterizing unconstrained kinematics but did not provide information on interaction forces (Churchland et al., 2012; Hu et al., 2018; Schaffelhofer and Scherberger, 2016; Schwartz et al., 1988; Umeda et al., 2019; Vargas-Irwin et al., 2010). Conversely, the study of active force control historically focused on constrained tasks in restricted experimental settings, often employing only 1-degree of freedom movements (Cheney and Fetz, 1980; Ethier et al., 2012; Herter et al., 2009; Moritz et al., 2007; Nishimura et al., 2013; Seki et al., 2003). These limitations arise from the difficulty of pairing unconstrained natural movements (Schwartz et al., 1988) with instrumented workspaces that allow the execution of active motor tasks (Cheney and Fetz, 1980) while measuring force interactions with the surrounding environment.

We believe that functionalized workspaces that promote natural movements could be designed by extending the concept of classical planar robotic tasks (de Haan et al., 2018; London and Miller, 2013; Omrani et al., 2016) to three-dimensional workspaces. Such setup could provide detailed measurement of kinematics and interaction forces throughout actions involving reaching, grasping and manipulation of objects. At the same time, it would enable complete freedom in defining the spatial constraints, force fields and perturbations of tasks that resembles natural, three-dimensional movements.

Here, we present a versatile robotic platform that combines neurophysiological, mechanical, and kinematic measurements within a customizable three-dimensional experimental environment. This platform consists of 1) a seven degrees-of-freedom compliant robotic arm (LBR iiwa, KUKA, Augsburg, Germany) 2) a custom software control package 3) force and grip pressure sensors integrated in the robot and 4) modules for data synchronisation.

To demonstrate the potential of our platform for both basic and translational studies in motor control, we programmed the robotic arm to present instrumented objects to trained monkeys in a three-dimensional workspace and oppose elastic resistance to displacements of the end effector. By pairing this system with intra-cortical neural recordings of sensorimotor areas, we created an instrumented platform that provides a rich portfolio of signals for the investigation of natural motor behavior.

We trained three monkeys to reach for the robot and pull the end effector to receive a food reward. We first demonstrate the performance and safety of our platform. We then use the platform to study the kinematic and dynamic components of movement and how these vary when applying different strength of dynamic elastic resistance to the target object movement. Third, we show that activity of neurons in both the motor and somatosensory areas encode specific components of the task such as force, kinematics or object contact. Fourth, we argue that our framework can be instrumental to neural engineering studies seeking to decode movement information from motor and sensory areas during natural behavior.

Our versatile control structure does not depend on the specific robotic arm used and allows for the design and implementation of a variety of tasks that can support both fundamental and translational studies of motor control.

2.3. Methods

2.3.1. Robotic Platform

Our platform (**Figure 2.1**) consists of 1) a seven-degrees-of-freedom robotic arm (Intelligent Industrial Work Assistant, IIWA - KUKA, Augsburg, Germany), 2) a custom built software package that enables closed-loop control of the robot arm, 3) a synchronized interaction force recording system, 4) a strain-gauge grip pressure sensor, 5) an infrared video tracking system to measure three-dimensional joint kinematics (Vicon, Oxford, UK) and an 6) electrophysiology system (Blackrock Microsystems, Salt Lake City, USA). We assessed the versatility and efficacy of our framework by programming a robotic task for monkeys. We configured the robot to position objects in a three-dimensional workspace and trained monkeys to reach and pull on the objects while kinetic, kinematic and neural signals were simultaneously recorded.

Closed-Loop control infrastructure

The IIWA robotic arm features a large workspace (**Figure 2.2 c**) allowing ranges of motion that are compatible with both human and monkey reaches. Additionally, the robotic arm is able to actively lift up to 7Kg of weight, which makes it robust to manipulation by monkeys.

We developed a software package that implements a real-time closed-loop control (**Figure 2.3 a**, [10.5281/zenodo.3234138](https://zenodo.org/record/3234138)) configured as a finite state machine. This allows fast configuration of tasks that proceed through several phases, where each phase requires a different behavior of the robot.

In our specific example application, at the beginning of an experimental session the robot lies in home position (**Figure 2.3 a**, FS1), in which all joint coordinates are equal to 0 resulting in a straight and vertical robotic arm configuration (**Figure 2.2 c**). The robotic arm maintains its position until the user triggers the start of a new trial by pressing a remote button. This brings the robot in a position control phase (**Figure 2.3 a**, FS2) during which it moves the end

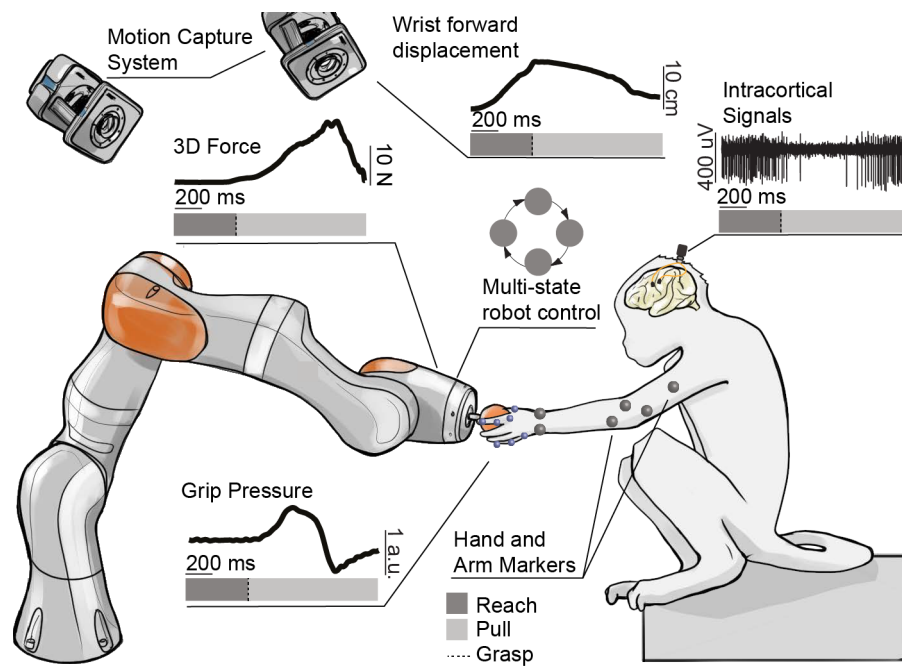


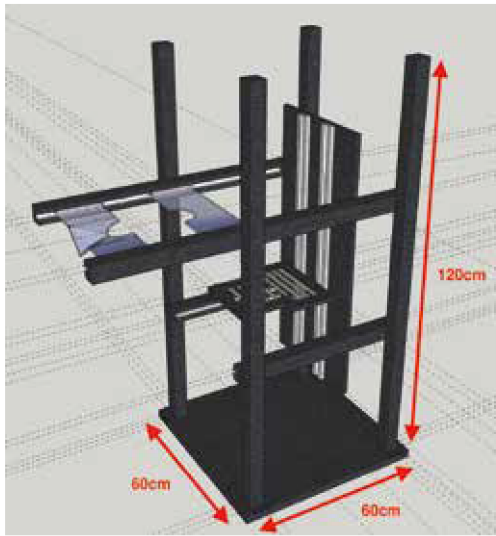
Figure 2.1 – Robotic framework for the study of reaching and grasping. A monkey is implanted with microelectrodes arrays in the arm and hand sensorimotor areas. The arrays are connected to a high-resolution electrophysiology system that records wideband extracellular potentials. A robotic arm presents the target objects to the monkey at different positions within a spherical 3D space (**Figure 2.2**). The animal can interact with the robotic arm by reaching for, grasping and pulling the target objects. A robot control software allows implementation of tasks that proceed through different phases. Each phase can contain different robot behavior. The 3D force applied by the monkey on the robotic joints is measured in real time. The target objects are instrumented with a sensor that measures the applied grip pressure. A motion capture system is used to track the full kinematics of monkey's arm and fingers using reflective markers.

effector to a determined position in space.

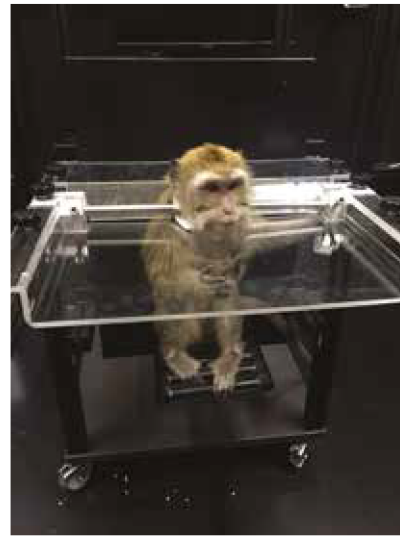
Once the sum of the errors in the positioning of all the joints decreases to a value of 0.01 radians, the robot is considered in target position and the control mode switches to impedance mode (**Figure 2.3 a**, FS3). In this state the robot behaves as a 0°mass-spring-damper system, trying to keep the target position while opposing a dynamic resistance to applied forces. In our specific examples we facilitated smooth movements of the end effector along the x-axis (towards the monkey), by imposing higher stiffnesses and damping parameters along the other orthogonal directions.

To interact with our platform we trained three monkeys to grasp a flexible instrumented object connected to the end effector, and pull it until a user-defined-position along the x-axis is crossed. Upon success, the robot quickly updates the next desired target position and moves towards it (**Figure 2.3 a**, FS4, FS5). If the animal fails to pull the object across the threshold or the trial timeouts, the robot returns to target position. After three failed trials the robot switches to another target.

a Primate chair design



b Primate chair implementation



c KUKA iiwa workspace

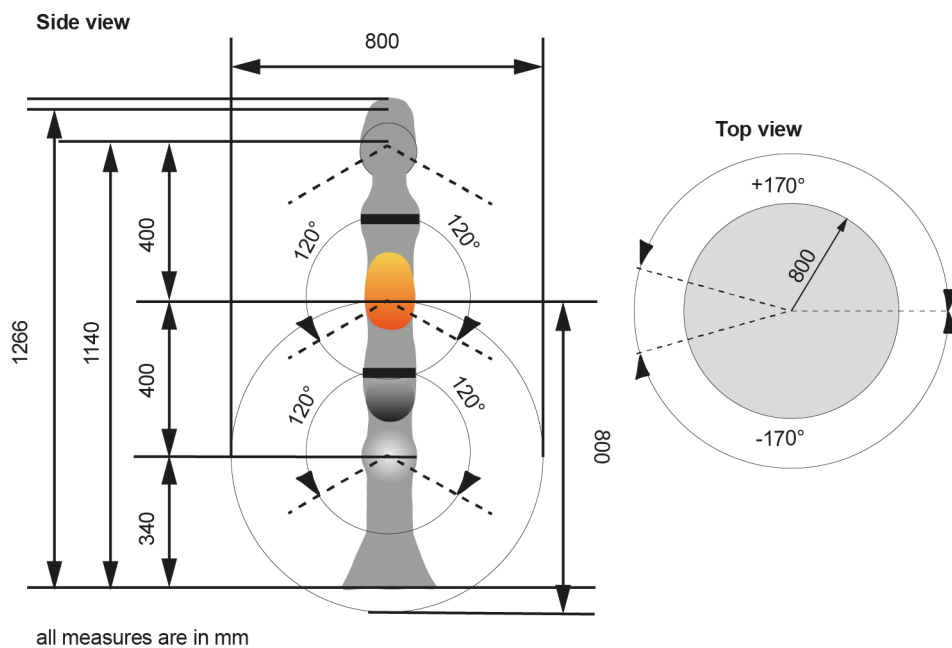


Figure 2.2 – Experimental primate chair and robot workspace (a) Schematic and dimensions of our customized primate chair enabling large ranges of upper limb motion. The height and depth of the seat can be adapted for different animal size. (b) Picture of an animal sitting in the chair. (c) Dimensions and three-dimensional workspace of the robotic arm.

Omnidirectional measurement of grip strength

We designed an air-pressure-based gauge sensor that can measure the applied grip force independently from an object shape in the interval -0.7 kPa to 40 kPa. We 3-D-printed hollow objects of different shape and size (**Figure 2.3 b**) and connected to a steel enclosure hosting the sensor. In this configuration the grip strength is proportional to the air flux produced by compression of the object. We designed a programmable electronic circuit (**Figure 2.3 b**) that digitizes pressure measurements while power and data transfer are provided through connection ports located at the robot end effector thereby limiting external wires at the subject-robot interface.

The pressure sensor circuit converted air pressure into a voltage measurement using strain-gages (1620 measurement SPECIALTIES®) directly connected to a front-end amplifier (FEA - LMP90100) of a full-Wheatstone bridge circuit. The footprint of the electronic circuit was maximally reduced in order to integrate it to the robot (diameter 3.2 cm). The embedded circuit converts the strain-gages signal into an analog output signal bounded between 0 and 4.1 V. The electronic assembly comprises a microcontroller (pic24FV08KM101) for the control of the FEA and the digital-to-analog converter (DAC8551) via a serial peripheral interface (SPI) protocol. Signals were amplified, digitized at 16 bits, and converted in analog signals after noise reduction. A 5 V regulator (EG113NA-5) adjusted the input power supply from 6 V to 9 V and a second regulator (LM4140ACM-4.1) outputted a precise reference voltage of 4.1 V used for signal conversions. Three LEDs indicated the state of the system and three input switches were used to impose gains ranging from 1 to 64. The in-circuit serial programming (ISCP) connector served to re-program the microcontroller. The system was also equipped from an ON/OFF button, a reset button and a power supply connector. The assembly was mechanically and electrically coupled to the flange of the robotic arm.

The objects were printed in a thermoplastic elastomer and were covered with two layers of silicon (DOWSIL™ and Sil-Poxy®) to ensure sealing. All the sensitive elements were characterized using a computer-controlled compression system (Zwick/Roell 1KN D0728165) to derive the internal pressure of each object as a function of the applied force.

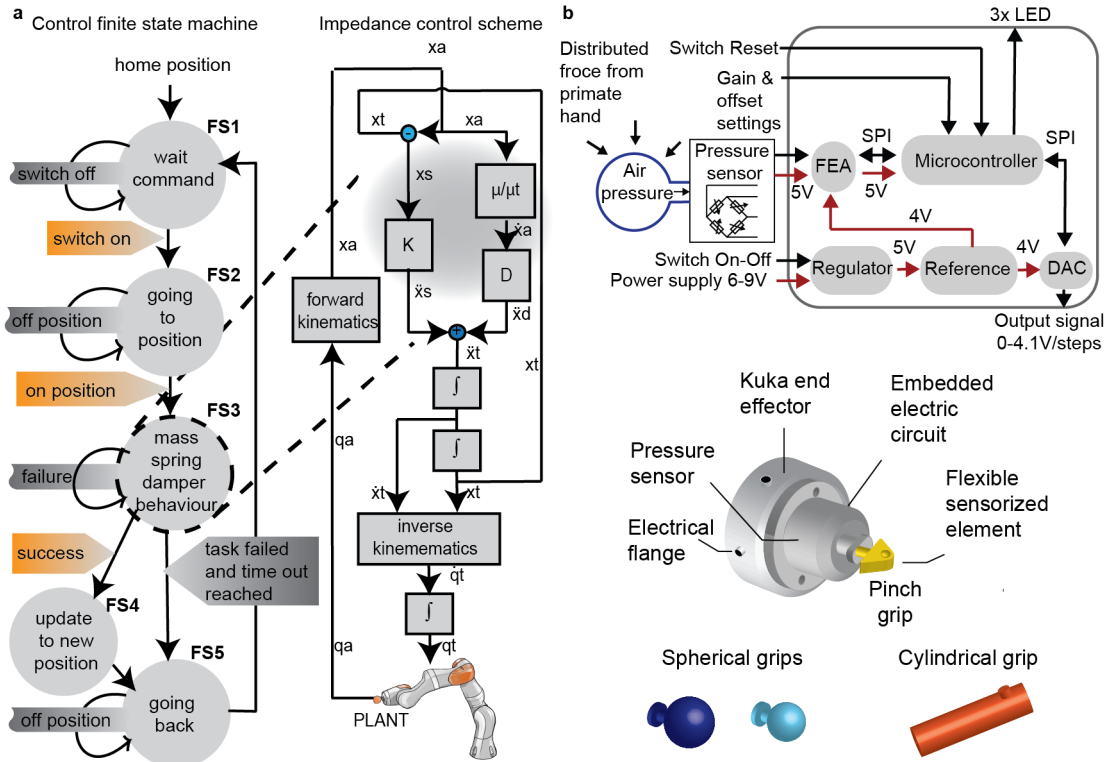


Figure 2.3 – Scheme of the robotic arm control protocol and the design of the grip pressure sensor (a) Finite State Machine of the robotic control protocol during the behavioral task. When a trial starts, the robot moves the end effector to a pre-determined position in space using standard impedance joint control strategy. When the position is reached, the finite state machine switches to a custom impedance control mode to allow interaction with the subject (right panel). In this modality, the end effector behaves like a mass-spring-damper system whose parameters are entirely user-defined and can be easily modified. x_a, \dot{x}_a = measured position and velocity of the end effector in Cartesian coordinates; x_s, \dot{x}_s = derived position and acceleration of the end effector in Cartesian coordinates; \ddot{x}_d = derived damping acceleration in Cartesian coordinates; $x_t, \dot{x}_t, \ddot{x}_t$ = target position, velocity and acceleration in Cartesian coordinates; q_t, \dot{q}_t = target position and velocity in the joint space. (b) Top: pressure sensor electronic circuit design describing the electronic components, the communication protocols and the voltage input values. Bottom: schematic of the pressure sensor assembly fixed at the end effector of the robot with spherical, cylindrical and pinch-like objects shown. DAC: digital-to-analog converter - FEA: front-end amplifier - LED: light-emitting diode - SPI: serial peripheral interface.

2.3.2. Animals involved in this study

Three adult female *Macaca fascicularis* monkeys were trained in this study (Mk-Jo 10 years old, 3.6 kg, Mk-Cs 9 years old 4.0 kg, and Mk-Ol 3 years old 3.0 kg). All procedures were carried out in accordance to the Guide for Care and Use of Laboratory Animals (ISBN 0-309-05377-3; 1996) and the principle of the 3Rs. Protocols were approved by local veterinary authorities (Canton of Fribourg, Switzerland authorizations No 2017_03_FR and 2017_04E_FR) including the ethical assessment by the local (cantonal) Survey Committee on Animal Experimentation and acceptance by the Federal Veterinary Office (BVET, Bern, Switzerland).

Surgical procedures

All the surgical procedures were performed under full anaesthesia induced with midazolam (0.1 mg/kg) and ketamine (10 mg/kg, intramuscular injection) and maintained under continuous intravenous infusion of propofol (5 ml/kg/h) and fentanyl (0.2-1.7 ml/kg/h) using standard aseptic techniques. A certified neurosurgeon (Dr. Jocelyne Bloch, CHUV, Lausanne, Switzerland) supervised all the surgical procedures. We implanted two 64-channel micro-electrode arrays in Mk-Jo and Mk-Cs and two 48-channel microelectrode arrays in Mk-Ol (Blackrock Microsystems, 400 μ m pitch and electrodes tip lengths 1.5 mm and 1 mm for M1 and S1 respectively). Mk-Cs was implanted in M1 and S1 area of the arm, and Mk-Jo and Mk-Ol were implanted in M1 and S1 area of the hand. Functional areas were identified with electrical stimulation delivered as biphasic pulses on the cortex surface at 3 mA and 100 Hz. A 20 mm diameter craniotomy was performed in order to span the brain areas of interest and the dura was incised. Implantation of the arrays was achieved using a pneumatic compressor system (Impactor System, Blackrock Microsystems). The pedestal was fixated to a compliant titanium mesh modelled to fit the skull shape for Mk-Jo and Mk-Cs. The pedestal was fixed directly to the skull in Mk-Ol. Surgical and post-operative care procedure are developed in details in (Capogrosso, Wagner, et al., 2018). Data presented in this paper were collected 3, 8 and 9 weeks post-implantation for Mk-Jo, Mk-Ol and Mk-Cs respectively.

Behavioral tasks

We built a custom primate chair (**Figure 2.2 a-b**) in which only the neck of the animal was fixed with a metallic collar allowing wide range of voluntary arm and hand movements in the three-dimensional space. Two Plexiglas plates were used to restrain the access to the head and a third plate placed around the stomach of the animal served for placing a resting bar and elastic bands to immobilize the right hand. Monkeys were trained to maintain a resting position between trials and place the left hand on the resting bar a few centimetres in the front, at chest level. A trial started when the robot presented a graspable target in front of the animal, at a distance of approximatively 20 cm. As soon as the "go" cue was played (1 sec duration sound), monkeys reached for the target, grasped it, and pulled it towards themselves (x-direction). Once the robot end effector crossed a pre-set virtual spatial threshold (8 cm), a clicker sound played by the experimenter indicated the success of the trial encouraging the animal to release the grip, return to the resting bar and get a food reward. The reward was delivered manually by the experimenter for Mk-Jo and Mk-Cs and automatically for Mk-Ol. The robot returned to its vertical home position at the end of each trial. For Mk-Cs and Mk-Jo, cueing signals during the task were implemented as follow: a go cue was implemented as a high pitch sound coupled to a green light that was played when the robot was in position and reached the impedance control mode; a success cue consisted in a low pitch sound when the monkey crossed the spatial threshold by pulling on the robot. Sounds were played from the application controlling the robot while the light cue was triggered through a synchronisation module (Arduino Due, Arduino, Italy). For Mk-Ol, the visual cues were delivered on a computer

screen. A start cue was displayed as a rectangular box on top of the screen. After 500 ms, the start box disappeared and a cursor was displayed on top of the screen with a rectangular target at the bottom. The cursor moved down vertically towards the target, proportionally to the displacement of the robot end effector towards the pre-set spatial threshold. Auditory cues were delivered automatically and consisted in a high pitch start cue, a medium pitch success cue and a low pitch reward cue. Liquid food was delivered together with the reward sound using a pump (masterflex console drive) triggered externally via the control software. The screen and the reward system were controlled using an in-house application (Matlab Mathworks®) coupled to a synchronization board (National Instruments, US). All cues were identically delivered during training and experimental sessions.

In Task 1, Mk-Jo reached for, grasp and pull objects of different sizes and shapes all presented at the same location. A cylinder (length 8 cm; diameter 1.5 cm), a small sphere (diameter 1.5 cm) and a large sphere (diameter 3 cm) were used to induce cylindrical, small and wide spherical grips respectively. CAD design of these objects are available at (10.5281/zenodo.3234138).

Each of these targets were presented with various levels of resistance applied by the robot impedance controller (joint stiffness 200, 400 and 600 N/m corresponding to “low”, “medium” and “high” stiffness levels). In addition, a small triangular pinch-like object (base 2 cm; height 1.5 cm) was used to prompt a lateral precision grip and was presented with the lowest level of resistance. Each session consisted in 12 to 20 trials per object per level of resistance. Two to four objects were presented during a single session.

In Task 2, Mk-Cs performed 3-dimensional centered-out task where the small spherical object was alternatively and randomly presented in three horizontal positions in the sagittal plane, center, left and right. The object was placed at -40, 0 and 60 mm along the y-axis for the left, center and right position respectively. The z distance was fixed for all conditions at approximately 180 mm above the animal seating height. Each session consisted in approximately 25 trials per position. Mk-Ol performed both Task 1 and Task 2. In Task 2, the left and right targets were placed approximately 3 cm higher than the central target along the z-coordinate. Each session consisted in at least 80 or 70 trials per condition, for position or object respectively.

2.3.3. Multimodal recordings

Kinematic recordings

Three-dimensional spatial coordinates of arm and hand joints during upper limb movements were acquired using a 14-camera motion tracking system (**Figure 2.1**, Vicon Motion Systems, Oxford, UK) at a 100 Hz-frame rate. The video system tracked the Cartesian position of up to 15 infrared reflective markers (6 to 9 mm in diameter each, Vicon Motion Systems, Oxford, UK). For each monkey, one marker was placed directly below the shoulder, three on the elbow (proximal, medial and distal) and two were placed on the wrist (lateral and medial) using elastic bands. For Mk-Jo and Mk-Ol, nine additional markers were positioned on the back of a

customized viscose glove, on the metacarpal (MCP), proximal (PIP) and distal phalanxes (DIP) joints of the thumb, index and little finger (**Figure 2.7 a**). A model of each subject's marker placement was calibrated in Vicon's Nexus software.

Pulling force recordings

The interaction force, measured as the force applied at the robotic joints, was sampled at 500 Hz and synchronized with triggers marking the beginning (go cue) and the end (spatial threshold crossing) of each trial together with the spatial position of the end effector. Values were also streamed in the BlackRock system using the single-board microcontroller. The pressure sensor signal was sampled at 1000 Hz with the VICON and Blackrock systems.

Electrophysiology recordings

Neural signals were acquired with a Neural Signal Processor (Blackrock Microsystems, USA) using the Cereplex-E headstage with a sampling frequency of 30 kHz.

2.3.4. Data Analysis

System performances characterization

We evaluated the safety and usability of the robotic platform accuracy of positioning, stability of position over time and repeatability of behavior across sessions (see section Results). We continuously recorded the three-dimensional position of the robot arm end effector, together with the three-dimensional force exerted on the object. We computed a positioning error, a time for the robot arm to converge on the target position (target positioning time) and a drop error (**Figure 2.4 a**). The precision error was computed as the distance between the targeted end effector position and the reached endpoint position, therefore illustrating the reproducibility of the robotic arm across trials. Since joint stiffness values influence the speed of the motion and the speed of convergence toward the commanded position we evaluated the variation of position error for several joint stiffness values ranging from 200 to 800 N/m. In addition, we enclosed the variation of the time needed for convergence toward the commanded position (time for target positioning). The drop error was computed as the three-dimensional drift of the end effector from the target position during the first 500 ms after placement, illustrating the stability of the robotic arm in holding the object in the target position. Subsequently, we verified the compliance of the robot movement upon interaction with a monkey previously trained to perform Task 2. We recorded three-dimensional coordinates of the joints and then computed a trajectory smoothness index

(Teulings et al., 1997) computed as:

$$S = \sqrt{\frac{T^5}{L^2} \sum_{i=1}^N \left\| \left(\frac{\delta^3 p}{\delta t^3} \right)_i \right\|^2 dt} \quad (2.1)$$

where p is the end effector position, N is the number of samples considered for the measure, t is the time, T and L represents the total duration of the trajectory in seconds and the length of the trajectory in m respectively. We computed a separated smoothness index over the reach and the pull.

We analyzed the movement velocity by computing the maximum wrist speed during the reaching and pulling phase separately. We derived the wrist speed from the wrist kinematics of Mk-Jo using the cylinder for three levels of robotic joint resistances (200 N/m, 400N/m and 600N/m).

All the grip pressure sensor-coupled objects were characterized using a computer-controlled compression system (Zwick/Roell 1KN D0728165) to derive the internal pressure of each object as a function of the applied force in Netwon. Calibration curves were acquired by applying dynamically load ranging from 0 to 10 N on each object.

Analysis of arm and hand dynamics

Post processing of motion capture data was performed to ensure that all joint markers were labelled correctly. We converted the three-dimensional marker position data to rotational degrees of freedom. For Mk-Jo and Mk-OI, we computed 12 joint angles (**Figure 2.7**): index finger PIP flexion/extension, pinkie finger PIP flexion/extension, thumb finger PIP flexion/extension, index finger MCP flexion/extension, pinkie finger MCP flexion/extension, thumb finger MCP flexion/extension, index finger abduction/adduction, pinkie finger abduction/adduction, thumb finger abduction/adduction, thumb opposition, wrist flexion, wrist ulnar deviation. For Mk-Cs, we computed 3 joint angles: shoulder adduction, elbow flexion/extension angle and wrist pronation/supination. Interaction force measurements were synchronized post-hoc to kinematics signals based on triggers marking the start (go cue) and end (threshold crossing) of each trial. For further analysis of arm and hand dynamics during natural reaching and grasping, we averaged the measurements across each condition. Kinematics, force and grip pressure measurements were low-pass filtered at 10 Hz.

Principal Component Analysis (PCA) was performed on joint angle kinematics and kinetic variables to identify which dynamic features (df) accounted for most of the variance in the data. We reconstructed the $Y \times N_{df}$ matrix where N_{df} is the number of joint angles and $Y = [Y_1, Y_2, \dots, Y_N]$ is the concatenated vector of all time points $t = 1, \dots, N$. Average kinematic, force and pressure variables were normalized and mean-centered before singular values

decomposition. The dynamic data projected along the first three eigenvectors in the PC space were averaged over each condition and smoothed using a 5-samples moving average filter before plotting.

Analysis of kinematic synergies

We used PCA, as described in (Santello et al., 1998) to identify kinematic synergies as orthogonal axes of maximal correlated variance in the 3D joint coordinates of the hand. Briefly, the x, y and z joints Cartesian coordinates were first normalized and mean-centered. The principal components (PCs) were then computed from the eigenvalues and eigenvectors of the matrix of the covariance coefficients between each of the joint coordinates waveforms. As each of the 13 markers was represented by three coordinates, the PCA was computed over 39 waveforms. The first PC accounted for at least 70% of the variance. We represented the hand posture corresponding to the first synergy by plotting the 39 coefficients corresponding to the first PC in 3D (Mason et al., 2001) and overlaid a sketch of a monkey hand for the sake of representation. The positions of the ring finger and middle finger were not measured in our experiment but were represented in a realistic inferred position with respect to the thumb index and pinkie to help visualize the hand posture in **Figure 2.7 d**.

Multiunit activity analysis during skilled grasping and 3D reaching

We acquired the multiunit spiking activity from each channel of intracortical neural recordings (2 x 64 channels for Mk-Cs and Mk-Jo, 2 x 48 channels for Mk-Ol) using the Neural Signal Processor (Capogrosso et al., 2016). Specifically, a spiking event was defined on each channel if the band-pass filtered signal (250Hz – 5kHz) exceeded 3.0–3.5 times its root-mean-square value calculated over a period of 5 s. Artefacts removal was achieved by eliminating all the spikes occurring within a time window of 0.5 ms after a spike event in at least 30 channels. We computed the firing rate of each channel as the number of spikes detected over non-overlapping bins of 10 ms.

In order to perform a neural population analysis, we identified a neural manifold (Gallego et al., 2017) by conducting PCA on multi-unit firing rates ranging from movement onset to the end of the pulling phase. Movement onset happened in average 660 ms, 910 ms and 520 ms before the grasp for Mk-Jo, Mk-Cs and Mk-Ol respectively. The pulling phase lasted at least 350 ms, 740 ms and 370 ms for Mk-Jo, Mk-Cs and Mk-Ol respectively. Events marking movement onset, grasp onset and release of the object were identified using video recordings. Neural features for M1 and S1 consisted in the firing rates computed over all intracortical neural channels of each array (64 channels for Mk-Cs and Mk-Jo, 48 channels for Mk-Ol). PCs were computed using at least 15 trials per object and 25 trials per position in Mk-Jo and Mk-Cs respectively (**Figure 2.8**). In Mk-Ol, principal components during the objects-grasping task were computed using 70 trials per object (**Figure 2.9**).

Neural encoding analysis

We manually spike-sorted the recordings from each electrode implanted in M1 and S1. We computed the average firing rate across the entire reach for each neuron to compare the two brain areas (**Figure 2.10 a**). Additionally, we inspected the tuning for each parameter by plotting the firing rate in each bin against the hand velocity and the magnitude of pulling force recorded at each time (**Figure 2.10 b**).

We then constructed encoding models to predict the spiking of each neuron using Generalized Linear Models (GLMs), adapting an analysis previously described by (Lawlor et al., 2018; Perich et al., 2018). First, we counted the number of spikes in non-overlapping 10 ms bins. In brief, GLMs generalize the idea of multilinear regression for non-Gaussian statistical distributions using a nonlinear link function. The neurons were assumed to have Poisson statistics, thus we used an exponential link function (Lawlor et al., 2018). As inputs to the GLMs we provided: 1) full-limb kinematics, including the three-dimensional velocities and accelerations of the shoulder, elbow, and wrist; 2) three-dimensional pulling force applied to the robot by the monkey; 3) the time of the grab event, to capture either motor commands related to hand shaping or sensory feedback from the object contact. For the third input, the grab event was convolved with three raised cosine basis functions (Pillow et al., 2008) spaced evenly up to 300 ms in the past or future for M1 and S1, respectively.

We quantified the performance of the GLMs using a pseudo- R^2 metric, which generalizes the notion of variance explained for the Poisson statistics of the model (Lawlor et al., 2018; Perich et al., 2018). This metric compares the log-likelihood of the tested model fit against a simpler model.

$$pR^2 = 1 - \frac{\log L(n) - \log L(\lambda)}{\log L(n) - \log L(\bar{n})} \quad (2.2)$$

Typically, the simpler model \bar{n} is a mean-fit to the data. However, this formulation also allows us to test the relative contributions of different parameters. We compared the full model with all three types of inputs described above to a reduced model \bar{n} where just one of the inputs is omitted. This relative pseudo- R^2 metric provides insights into how well specific parameters, such as object contact, helps to explain neural activity. We assessed significance for all of these using a Monte Carlo simulation resampling across the available trials. A model fit or parameter was assumed to be significant if the 95% confidence intervals on the parameter fit were greater than zero.

Detection of movement onset and object grasp from the sensorimotor neural activity

We implemented an approach based on a multiclass regularized linear discriminant analysis algorithm (mrLDA) to detect moments of movement onset and object grasp from the

continuous neural recordings from either the motor or somatosensory cortices (Capogrosso et al., 2016; Milekovic, Ball, et al., 2013; Milekovic et al., 2018). In brief, we synchronized the multiunit spike activity with the movement onset and object grasp events. The performance of decoders was evaluated using five-fold cross-validation (Hastie et al., 2009). The movement onset and object grasp events, mo and og , were used to derive the respective classes of neural features, C_{mo} and C_{og} :

$$C_{mo} = \bar{a}_{mo} | \bar{a}_{mo}(i) = \begin{bmatrix} x_1(mo(i) - \Delta t_{mo}) \\ x_1(mo(i) - \Delta t_{mo} - \Delta t) \\ \dots \\ x_1(mo(i) - \Delta t_{mo} - (N_{TP} - 1) \cdot \Delta t) \\ x_2(mo(i) - \Delta t_{mo}) \\ \dots \\ x_{NCH}(mo(i) - \Delta t_{mo}) \end{bmatrix} \quad (2.3)$$

$$C_{og} = \bar{a}_{og} | \bar{a}_{og}(i) = \begin{bmatrix} x_1(og(i) - \Delta t_{og}) \\ x_1(og(i) - \Delta t_{og} - \Delta t) \\ \dots \\ x_1(og(i) - \Delta t_{og} - (N_{TP} - 1) \cdot \Delta t) \\ x_2(og(i) - \Delta t_{og}) \\ \dots \\ x_{NCH}(og(i) - \Delta t_{og}) \end{bmatrix} \quad (2.4)$$

where \bar{a}_{mo} and \bar{a}_{go} are feature vector members of classes C_{mo} and C_{og} , respectively; N_{TP} is the number of multiunit spike rate measurements taken from the same neural channel; Δt is the temporal difference between the two consecutive spike rate measurements taken from the same neural channel; $N_{CH}=64$ is the number of neural channels; and Δt_{mo} and Δt_{og} are the temporal offsets for each type of event. N_{TP} , $N_{TP} \cdot \Delta t$ (history used to sample neural features), Δt_{mo} and Δt_{og} were used as decoder parameters - their values were selected from a following list of values: N_{TP} : 3 and 5; $N_{TP} \cdot \Delta t$: 0.3 s and 0.5 s; Δt_{mo} and Δt_{og} : any value from -200 ms to 200 ms with 0.5 ms steps. We additionally formed another class C_{OTHER} representing states at least 10 ms away from all mo and og events.

We then calibrated a set of mrLDA decoding models using C_{mo} , C_{og} and C_{OTHER} and all possible combinations of parameter values (Capogrosso et al., 2016; Milekovic, Ball, et al., 2013; Milekovic et al., 2018). We used the mrLDA regularization parameter as an additional parameter with values of 0, 0.001, 0.1, 0.3, 0.5, 0.7, 0.9 and 0.99. The performance of each of the models was validated using four-fold crossvalidation on the training dataset as follows. A model was calibrated on three quarters of the training dataset and tested on the remaining

part of the training dataset. For each time point of this remaining part, the mrLDA model calculated the probability of observing neural activity belonging to C_{mo} and C_{og} classes. When one of these two probabilities crossed a threshold of 0.9, the decoder detected movement onset or object grasp, mo_{DET} or og_{DET} , respectively. To reproduce the sparsity of these events, we ignored the probability values of the detected event for 1s after the detection. We pooled the time series of actual and detected events across all four folds and calculated normalized mutual information using a tolerance window of 200 ms (Capogrosso et al., 2016; Milekovic, Ball, et al., 2013; Milekovic et al., 2018). We then calibrated another decoding model on the left-out testing dataset using the parameter values that resulted with the maximum normalized mutual information. This decoder was then used on the testing part of the dataset to detect the mo_{DET} or og_{DET} events. We again pooled actual and detected events across all five testing folds and measured the decoding performance using temporal accuracy – the ratio of actual events that have one and only one event of the same type within the 200 ms neighbourhood. We estimated the standard error of the temporal accuracy using bootstrapping with 10,000 resamples (D. S. Moore et al., 2014).

Time-resolved classification of grasp types and trajectories

We applied a similar approach to classify grasp types (Mk-Jo) and reach target locations (Mk-Cs) using mrLDA from the neural recordings from either the motor or somatosensory cortex (Milekovic et al., 2015). We measured the classification performance using leave-one-out cross-validation (Hastie et al., 2009) – in each validation fold (“e”), a different trial e is selected as a test dataset and all other trials are used as a training dataset to calibrate a mrLDA model. This calibration involves a procedure to select the regularization parameter of the mrLDA model from the values of 0, 0.001, 0.1, 0.3, 0.5, 0.7, 0.9 and 0.99. The training dataset is used to derive the classes of neural features, $C_1(e,t), \dots, C_N(e,t)$ ($N=4$ for four objects in Mk-Jo, and $N=3$ object positions for Mk-Cs) as described above for event timing using leave-one-out validation on the training dataset. We then calibrated a mrLDA classifier on the complete testing dataset using the regularization coefficient that resulted with the maximum decoding accuracy. We pooled the classification outcomes across all folds and measured the decoding accuracy. This procedure resulted in a confusion matrix and decoding accuracy value for every value of the latency t around both movement onset and object grasp events. We estimated the standard error of the decoding accuracy using bootstrapping with 10,000 resamples (D. S. Moore et al., 2014).

Kalman filter decoding

We assessed continuous predictions of limb kinematics using a Kalman Filter (Wu et al., 2006). The Kalman Filter provides a probabilistic framework to predict the state of the limb during the reach and grasp task based on the neural recordings. The output of the filter was the state of the limb. For Mk-Cs, this comprised the position and speed of the elbow and wrist. For Mk-Jo, it comprised the position and speed of the thumb, index and pinkie finger joints

(distal phalanx, PIP joint and MCP joint), as well as of the wrist, elbow and shoulder joints. We computed the limb kinematics and the instantaneous firing rate of each neuron at 50 ms intervals. We used the multiunit firing rate obtained from thresholding on M1 and S1 arrays as inputs to the decoder. The neural signals were shifted relative to the kinematics by a static value of 100 ms in Mk-Cs and 70 ms in Mk-Jo. These lags were determined by testing the models on various delays to optimize the model performance. We trained and tested the models using the leave-one out cross-validation method: we iteratively set aside one trial for testing and trained the model using the remaining trials. We pulled together kinematic and neural data over different objects (small sphere and large sphere) for Mk-Jo and over different positions (left, center and right) for Mk-Cs. The performance was assessed using the coefficient of determination R^2 for which we computed the 95% confidence intervals across all repetitions. 3D static hand posture reconstruction represents hand configuration for the best time point of the fold resulting in the highest average R^2 for both the small sphere and the cylinder objects in Mk-Jo.

2.3.5. Statistics

All computed parameters were quantified and compared between tested groups unless otherwise specified. All data are reported as mean \pm SEM unless specified otherwise. Significance was analysed using non-parametric Monte-Carlo permutation test and Wilcoxon rank-sum test followed by post-hoc correction for multiple comparison.

2.3.6. Data and software availability

The custom-built open-source software application used to control the robotic arm and a step-by-step implementation protocol are available at (10.5281/zenodo.3234138). Further data from this study are available from the corresponding author upon reasonable request.

2.4. Results

2.4.1. System performance

In order to assess the performances of the robotic platform, we ran a series of tests aiming at computing the spatial accuracy of positioning, stability of position over time and repeatability of behavior across sessions (**Figure 2.4 a**, **Video 2.1**).

We evaluated the spatial accuracy by measuring the positioning error - the distance between the target position and the actual position reached by the robot (**Figure 2.4 a**). To evaluate the speed of positioning, we measured the target positioning time – time needed for the robot to move the end effector to the target position. We measured the positioning error and the target positioning time for different joint stiffness values. To evaluate the stability of the robot to hold a specified position over time, we measured the drop error (**Figure 2.4 a**).

For a stiffness of 200 N/m (the typical value used during experimental sessions), the mean positioning errors were 0.186, -0.133 and 0.008 mm for the x, y and z directions with standard deviation of 7, 6 and 13 mm, respectively. We considered these errors acceptable for our experimental demonstrations. Nonetheless, the positioning errors and the target positioning time decreased with increasing stiffness values (**Figure 2.4 b**). This shows that it is possible to obtain a higher positioning precision by accepting a higher joint stiffness during motion. Our analysis revealed no relationship between positioning error and end effector spatial location (**Figure 2.4 c**). Similarly, drop errors (**Figure 2.4 d**) were uniform across space (1.0 ± 1.8 mm, 0.8 ± 2.2 mm and 2.1 ± 0.3 mm for the x, y, and z direction). Measured forces were consistent across sessions (n=2 sessions) (**Figure 2.4 e**).

We next evaluated the robot compliance upon interaction with a monkey. In particular, we verified that passive movements of the end effector did not introduce sudden and unexpected perturbations of the arm kinematic trajectories when pulling on the object.

We measured arm joint kinematics in Mk-Cs performing a reach-and-pull task (**Figure 2.1**) in different directions and computed the smoothness index (Teulings et al., 1997) of arm joints and end effector trajectories during the reaching and the pulling phase separately. The smoothness during the pulling phase was comparable to that computed in the reaching phase suggesting that the robot did not perturbate the dynamics of natural arm movements (**Figure 2.4 f**).

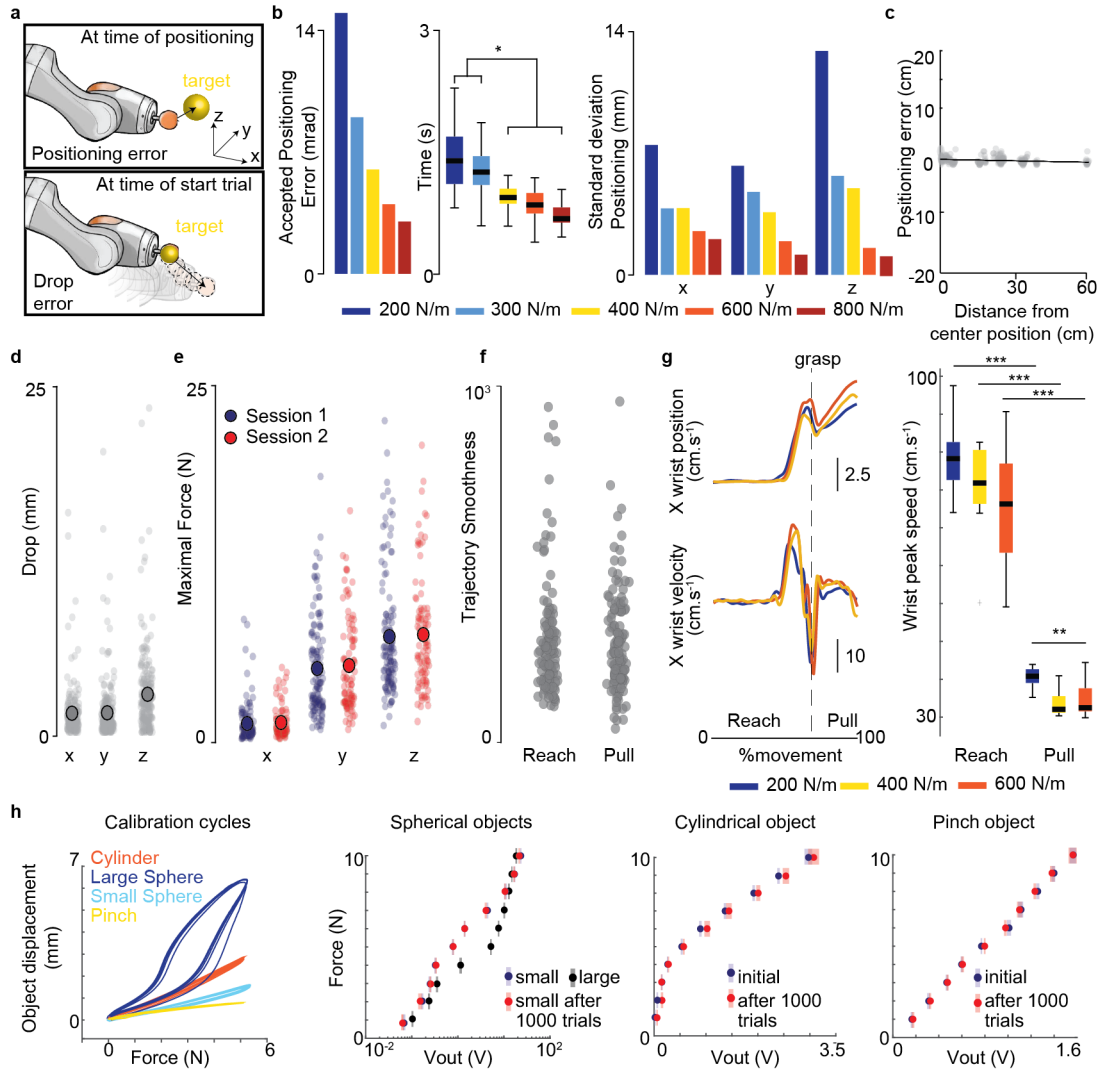


Figure 2.4 – Evaluation of the system performances: (a) Measures of reproducibility of the three-dimensional positioning. The positioning error is the distance between the set and measured robot end effector position; the drop error is the distance between the measured robot end effector position at the cue-time and the measured robot endpoint position 0.5 seconds after the cue-time. (b) Left: accepted positioning tolerance for different values of joint stiffness. Center: time of convergence toward target for different values of joint stiffness ($p < 0.01$); Right: s.t.d of positioning error on the x, y and z dimension for different values of joint stiffness (c) Positioning error values as a function of the distance from the center of the robot workspace. Linear regression $R^2 = -0.009$, RMSE = 0.05. (d) Drop error on the x, y and z dimension. (e) Maximal force exerted on the robot end effector on the x, y and z axis. Comparison across 2 different sessions. (f) Comparison of trajectory smoothness values during the reach (robot not interacting with the subject) and pull (robot interacting with the subject). (2 sessions, $n=100$ trials each). (g) Left: example of Mk-Jo wrist cartesian position and velocity along the x axis for three different levels of robotic joint resistance. Right: maximal wrist speed during the reach and pull phases for three levels of joint resistances ($n=10$ measurements per condition). For each joint resistance, the peak reaching speed was significantly higher than the peak pulling speed. Wilcoxon rank-sum test, $p_{200} = p_{400} = p_{600} = 1.8 \times 10^{-4}$. The pulling peak speed was significantly larger at 200 N/m resistance than at 60 N/m resistance (Kruskal-Wallis test, $\chi^2_{200-600} = 10.72$, $p = 0.005$). (h) Left: example of force-deformation relationship for each object during five calibration rounds at 5 N. Right: Calibration curves describing the voltage to pressure relationship for each object geometry before and after 1000 squeeze movements ($n=3$ measurements per point). Horizontal s.t.d: error on the voltage measurement for forces ranging from 1 to 10 N.

We then computed the maximum wrist speed during the reaching and pulling phase in Mk-Jo performing a reach-and-pull task at different stiffness levels (**Figure 2.4 g**). Our results show that for every stiffness level, the maximal hand speed was significantly lower when interacting with the object than during the reaching phase. In addition, higher stiffness resulted in lower pulling speed. Taken together, these results show that our robotic platform can be used to apply loads while remaining compliant to upper-limb movements.

Finally, we characterized the force-to-voltage relationship of the grip pressure sensor for different object geometries. Calibration curves showed that spherical and cylindrical objects exhibit a non-linear force-to-voltage behavior while the pinch-like geometry displayed a linear behavior (**Figure 2.4 h**). We demonstrated that the force-to-voltage relationship remained stable after 1000 squeezes (**Figure 2.4 h**).

2.4.2. Applications to basic and translational studies

We investigated the kinematic, kinetic and neural components of natural three-dimensional reaching, grasping and pulling behavior in monkeys. Three adult *Macaca fascicularis* female monkeys (Mk-Jo, Mk-Cs and Mk-Ol) were implanted with a pair of microelectrode arrays (Blackrock Microsystems, Salt Lake City, UT, USA). The arrays were placed in the hand and arm area of the right primary motor (M1) and right primary somatosensory (S1, area 1/2) cortices (London and Miller, 2013; Pons et al., 1985) (**Figure 2.5 a**). Brain signals were synchronized to interaction forces, grip pressure and arm and hand kinematics. We implemented two tasks. In both, the animal reached freely towards an object, performed a specific grasp, and compensated for the dynamic resistance applied by the robot to pull the object across a virtual border. In Task 1, the monkey reached for four objects of different shapes: a small sphere, a large sphere, a cylinder, and a “pinch” object. Each object encouraged the animal to use a specific grasp: three finger grip (small sphere), whole hand grip (large sphere), two-finger precision grip (pinch), and power grip (cylinder) (**Figure 2.3 b**, **Figure 2.5 b**). The objects were presented at the same position. The joint impedance varied across “low”, “medium” and “high” level of resistance to object displacement. In Task 2, the monkey reached for the small sphere presented at different positions in space (“central”, “left”, or “right”, **Figure 2.5 c**).

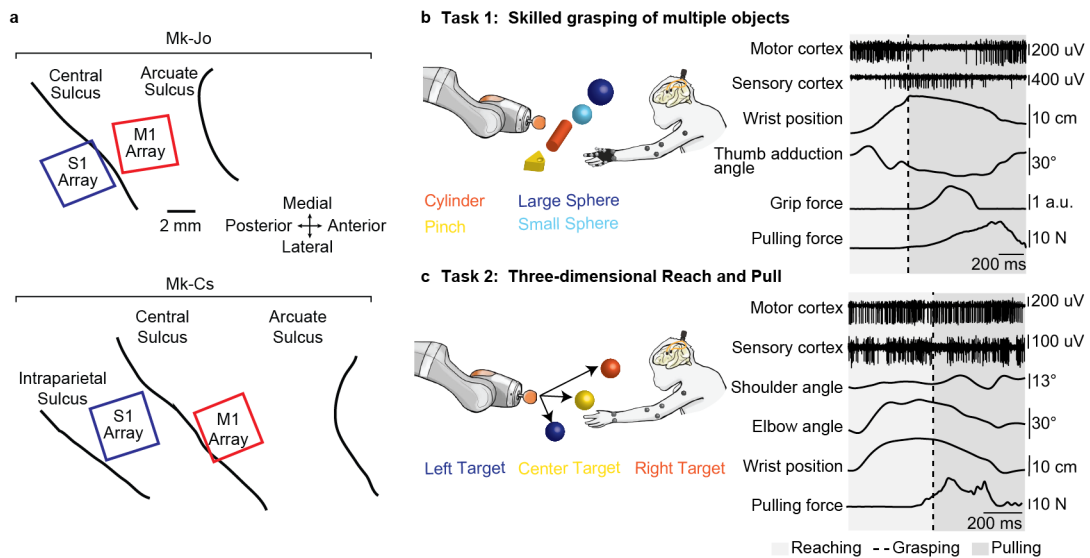
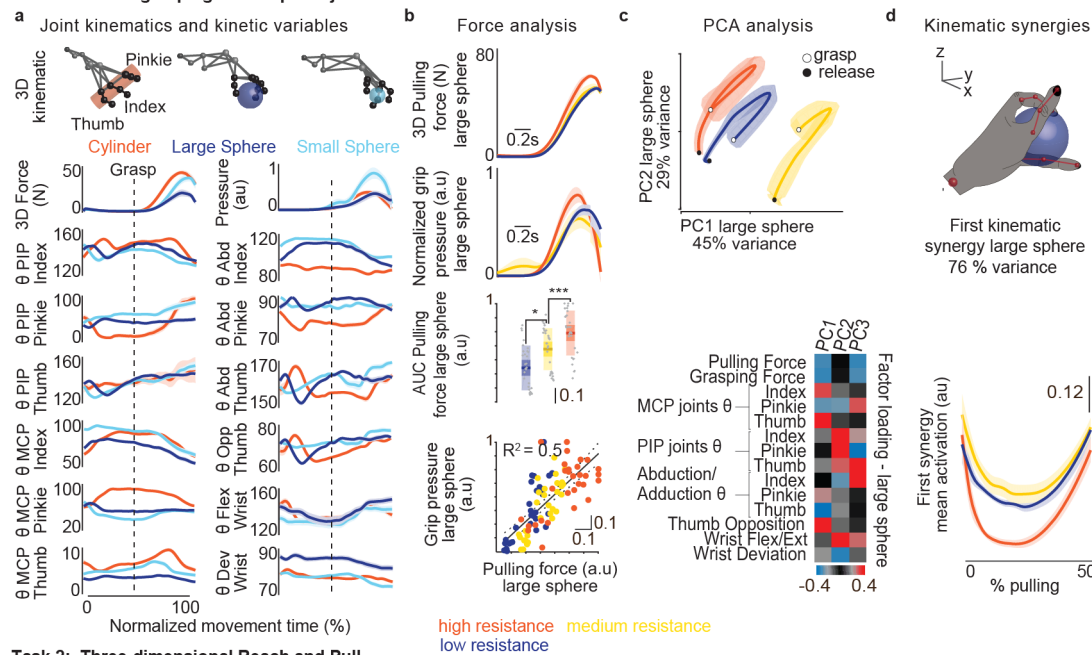


Figure 2.5 – Multimodal electrophysiology during unconstrained reaching and grasping (a) Utah arrays placement for Mk-Jo and Mk-Cs. Each animal received two arrays of 64 channels. M1 hand and arm areas were identified in Mk-Jo and Mk-Cs respectively through intra-operative electrical stimulation. (b) Schematic of a skilled grasping task during which the monkey had to reach for different types of object and pull them towards a pre-determined spatial threshold. (c) Schematic of the 3D reaching task during which the monkey had to reach for an object placed at different positions in space and pull it towards a pre-determined spatial threshold. Examples of synchronous multiunit neural recordings, hand and arm kinematics, grip pressure and pulling force recordings are shown on the right for both tasks.

2.4.3. Arm and hand dynamics during natural reaching and grasping

We first explored how kinematic and kinetic components of movement varied during natural reach and grasp paradigms, and how these evolved under different levels of resistance. The animal adapted the hand configuration according to the selected objects (**Figure 2.6 a** and **Figure 2.9 b**). Fingers joint angles showed closer motor patterns for the small and large sphere than for the cylindrical object. Interestingly, average grip pressure was larger for the small spherical grip than for the other objects, presumably because strong grip was required to compensate for the small surface of hand contact. Grasping pressure and pulling forces increased in response to an increase in resistance (**Figure 2.6 b**, **Figure 2.7 b**), indeed during pulling grip pressure was linearly correlated to pulling force (**Figure 2.6 b**, $R^2 = 0.5$). We performed a principal component analysis (PCA) of kinetic and kinematic features of grasping. This analysis revealed that grasping features evolved over well clustered smooth trajectories for different resistance levels during movement (**Figure 2.6 c**, **Figure 2.7 c**).

Task 1: Skilled grasping of multiple objects



Task 2: Three-dimensional Reach and Pull

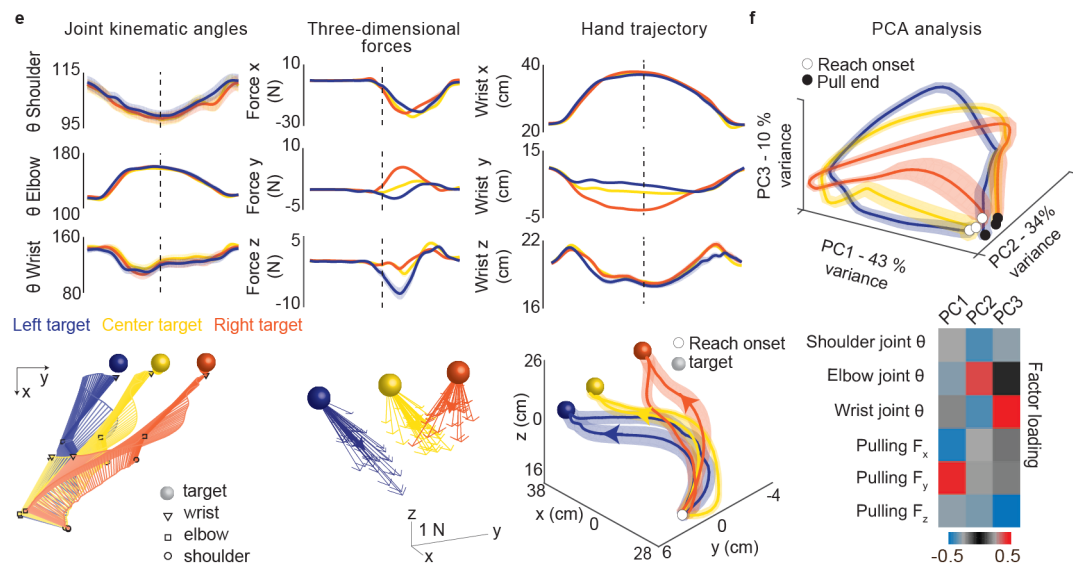


Figure 2.6 – (Continued on the following page.)

Arm and hand dynamics during natural reaching and grasping (a) Examples of kinematic and kinetic variables for three different objects (n=15 trials per object, one recording session). 3D hand configuration is shown on top for each object. **(b)** Example of normalized pulling force and grip pressure obtained for three levels of resistance when pulling on the large spherical object (n=10 trials per resistance condition, one recording session). The box-plots show the median, the 1.96 SEM and the STD of the pulling force area under the curve (AUC) during the movement (n=30 trials per condition, three recording sessions). Data were normalized by the maximal pulling force measured within each session. Increase in resistance had a significant effect on the pulling force impulse (Kruskal-Wallis, $p < 0.001$ with post hoc correction, * $p_{low-med} < 0.05$, *** $p_{low-high} < 0.001$, *** $p_{med-high} < 0.001$). Correlation analysis between the grip pressure and the pulling force impulses (AUC) revealed a linear correlation between these two variables ($R^2 = 0.5$ and $p_{value} = 1.6 \times 10^{-16}$, n=30 trials per condition, three recording sessions). **(c)** Principal component analysis of the kinematic and kinetic components of the movement for the three levels of mechanical resistances (n=10 trials per condition, large sphere object, one recording session). The color-coded representation of factor loadings identifies variables that contributed most to the differences observed between the difference levels of resistance. **(d)** Top panel: postural kinematic synergy defined by the first principal component. Bottom panel: Time course activation of the first PC averaged over trials shows modulation for high level of resistance compared to low and medium resistances, indicating a change in kinematic grasping strategy to overcome increased levels of resistance (n=10 trials per condition, large sphere object, one recording session). **(e)** Examples of kinematic and dynamic variables for 3D reaching towards different spatial targets (n=25 trials per position, one recording session). Joint kinematics angles, three dimensional pulling force and wrist trajectories are shown for the left, center and right position. Stick diagram depicts evolution of the arm joint angles for the three conditions while maxima pulling force is represented as 3D vectors. Thick stroke arrows represents the average maximal force value. Wrist trajectories are also plotted in 3D. **(f)** Principal component analysis of the kinematic and kinetic components of the movement reveals partial overlapping of the movement performed to reach the three different target positions (n=25 trials per position, one recording session). Color-coded representation of factor loadings identifies the x and y components of the pulling force as the most meaningful features for the first PC while the wrist and elbow joints associate with high loadings in the second and third PC respectively. Thicker lines represents the data mean while shaded areas depicts the SEM.

The two leading principal components showed strong correlations to finger joint kinematic features, as well as kinetic features (**Figure 2.6 c**). This suggested that the monkey adapted its kinematic strategy to overcome higher resistances. To verify this hypothesis, we extracted kinematic synergies (Mason et al., 2001; Santello et al., 1998) (**Figure 2.6 d, Figure 2.7 d**). We found that the activation of the main synergy (first component, 70% of variance for all objects (**Figure 2.6 d, Figure 2.7 d**) changed across resistance levels for spherical objects, but not for the cylinder (**Figure 2.6 d, Figure 2.7 d**). This suggests that the monkey adapted the grasping strategy to execute higher force levels. In the case of the cylindrical grip, the monkey overcame large resistance levels by generating stronger pulling torque without substantial change in his grip pattern.

We then inspected kinematic behavior for different spatial targets in Task 2 (**Figure 2.6 e and Figure 2.9 d-e**). Joint angles showed reproducible patterns across trials, even if the animal was not trained to follow a specific strategy and was free to reach the object without time or spatial

constraints. In Mk-Cs, joint angles and hand trajectory along the x and z direction showed a similar trend across the different positions (**Figure 2.6 e**). In Mk-OL, since the lateral targets were located higher than the central target along the z direction, hand trajectories as well as wrist position showed variations along the y and the z coordinate (**Figure 2.9 d**). In both Mk-Cs and Mk-OL, forces along the pulling direction were similar across all the target positions, confirming that the effort needed to pull the robot end effector past the threshold on the x-axis was proportional to the end effector displacement from the target position. Forces along the y-axis were markedly different, suggesting that the monkey always displaced the end effector towards its body center when pulling.

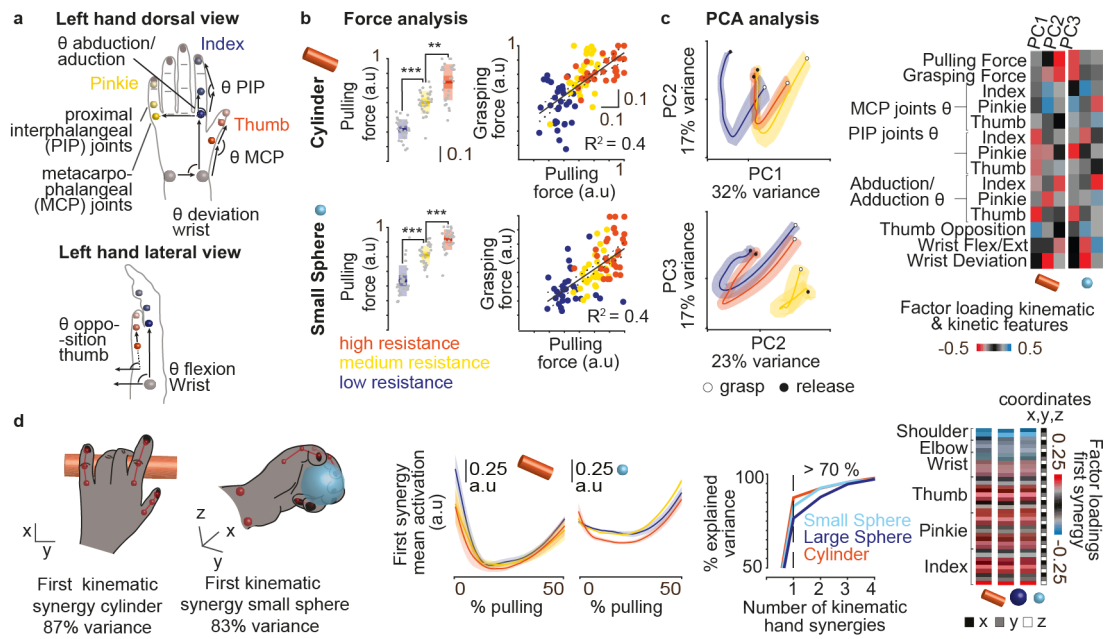


Figure 2.7 – Arm and hand dynamics during natural reaching and grasping (a) Dorsal and lateral view of markers placements and finger joint angles computation for Mk-Jo. (b) The box-plots represent the median, the 1.96 SEM and the STD of the pulling force area under the curve (AUC) during small spherical grip and cylindrical grip (n=30 trials per object per condition, three recording sessions). Data were normalized by the maximal pulling force measured within each session. As for the large spherical grip, increase in resistance had a significant effect on the pulling force impulse (Kruskal-Wallis test, $\chi^2_{cylinder} = 62.36$, $p_{cylinder} = 2.9 \times 10^{-14}$, $\chi^2_{sphere} = 58.48$, $p_{sphere} = 2.0 \times 10^{-13}$ followed by post hoc multiple comparison $p_{low-medcyl} = 2.5 \times 10^{-6}$, $p_{low-highcyl} = 9.6 \times 10^{-10}$, $p_{med-highcyl} = 0.01$ and $p_{low-medsphere} = 2.0 \times 10^{-4}$, $p_{low-highsphere} = 9.6 \times 10^{-10}$, $p_{med-highsphere} = 7.2 \times 10^{-4}$). Correlation analysis between the grip pressure and the pulling force impulses (AUC) revealed a linear correlation between these two variables ($R^2 = 0.4$ and $p_{value} = 5.7 \times 10^{-12}$ for the small sphere and $R^2 = 0.4$ and $p_{value} = 1.2 \times 10^{-12}$ for the cylinder). (c) Principal component analysis of the kinematic and dynamic components of the movement reveals clustering of the three levels of mechanical resistances along the first and second principal components. The color-coded representation of factor loadings identifies variables that contributed most to the differences observed between the difference levels of resistance. (d) Postural kinematic synergy defined by the first principal component. The hand postures represented the hand configuration obtained after applying PCA reduction algorithm to the set of hand cartesian coordinates over all trials and representing the loading coefficients of the first PC. Time course activation of the first PC averaged over trials shows modulation for high level of resistance for the small sphere but not for the cylinder suggesting high resistive loads were overcome by changing grip conformation for the small spherical grip but not for the cylindrical grip. Cumulative variance plotted on the right indicates the first kinematic synergy recapitulated more than 70% of the variance for all the grip types. Factor loadings of the first synergies are color-coded on the right showing higher loadings in the x and z directions than in the y direction.

Projections in the PC space formed smooth and separated trajectories that spanned the three-dimensional manifold defined by first PCs (Figure 2.6 f). Most of the variance was explained by the force exerted in the y direction as suggested by the pulling force profiles (Figure 2.6 e).

2.4.4. Sensorimotor neural dynamics during natural reaching and pulling

We then used our robotic framework to study the neural activity in M1 and S1 during natural reaching and grasping. Nearly all channels showed high modulation of multi-unit firing rates for both sensory and motor areas in all monkeys (**Figure 2.8 a,c** and **Figure 2.9 a,c**). Interestingly, activity arising from the arm somatosensory area (Mk-Cs) was strongly modulated during the whole movement while the largest response in the somatosensory area of the hand (Mk-Jo and Mk-OL) occurred shortly following the grasp (**Figure 2.8 a**).

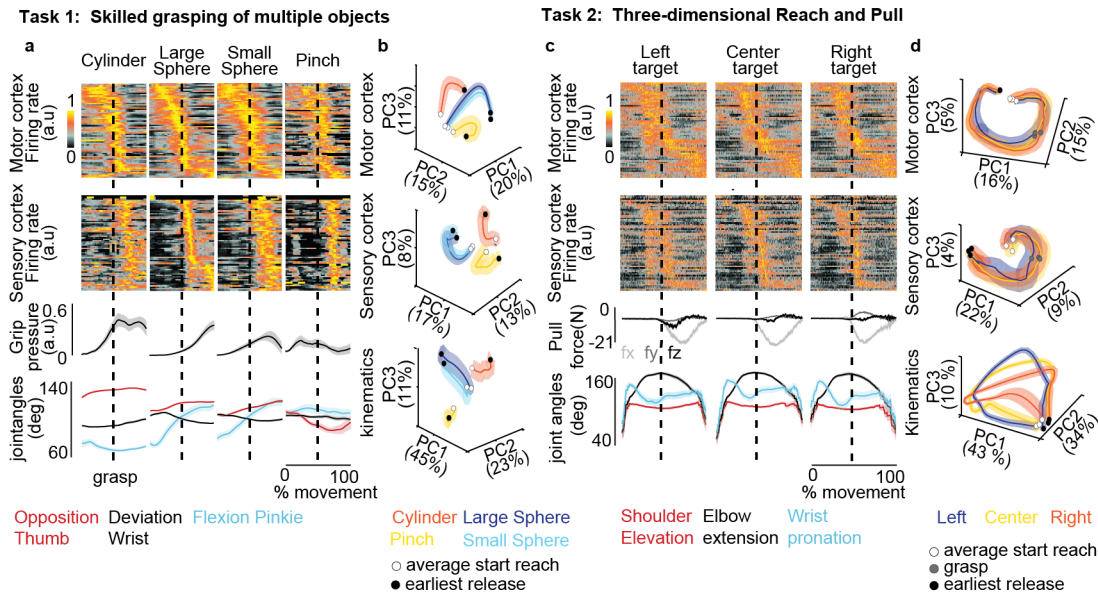


Figure 2.8 – Sensorimotor neural dynamics during unconstrained reaching and pulling (a) Averaged synchronized neural, kinematic and dynamic signals collected during skilled grasping of four different objects (Mk-Jo, n=15 trials per object, one recording session). The dashed line identifies the onset of the grasp. Signals were averaged before the grasp over the mean reaching phase duration and after the grasp up to the minimum pulling phase duration. Brain signals were binned over 10 ms time window, normalized for each channel and sorted in ascending order of time of maximal firing rate. The reference condition for aligning neural signals is the large sphere for Task 1. (b) Principal component analysis of the kinematic, motor and sensory neural components of the movement reveal clustering of the four different types of object geometry along the three first PCs in each the cortical and kinematic PC spaces (Mk-Jo, n=15 trials per object, one recording session). (c) Averaged synchronized neural, dynamic and kinematic signals during the execution of the Task 2 for three different spatial targets. Signals were processed identically to Task 1 (Mk-Cs, n=25 trials per position, one recording session). The reference condition for aligning neural signals is the central target for Task 2 (d) Principal component analysis of the kinematic, motor and sensory neural components of the movement for the three different object positions (Mk-Cs, n=25 trials per position, one recording session) show overlapping trajectories for the three targets in the neural PC space and dissociated trajectories in the kinematics PC space.

We then identified a neural manifold (Gallego et al., 2017) from the multi-unit activity of each brain area and compared the trajectories to those of the kinematics (**Figure 2.8 b, d** and **Figure 2.9 b**). In Task 1, both M1 and S1 showed smooth curves that segregate for different object shapes. The trajectories corresponding to similar objects were found to be very close in the PC space for both kinematic and neural features. In Task 2 instead, trajectories in the kinematic

manifold showed distinct paths for different positions in space (**Figure 2.8 b, d**, and **Figure 2.9 b**), while neural manifolds displayed very similar trajectories for different positions suggesting a common neural basis for reaching and pulling in both motor and sensory areas.

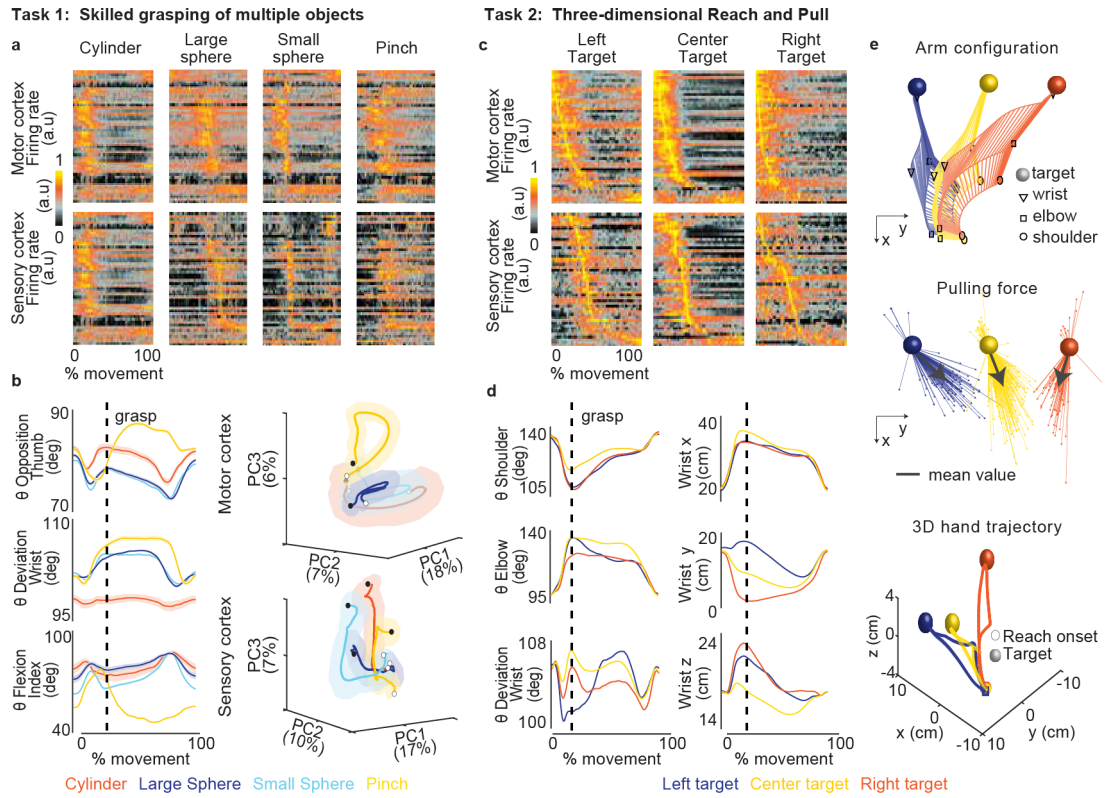


Figure 2.9 – Kinematics, kinetics and neural dynamics in Mk-Ol (a) Averaged synchronized neural signals collected during skilled grasping of four different objects (Mk-Ol, $n=70$ trials per object, one recording session). Signals were interpolated from the start to the end of the movement. Brain signals were binned over 10 ms time window, normalized for each channel and sorted in ascending order of time of maximal firing rate. The reference condition for aligning neural signals is the large sphere for Task 1. (b) Left: Examples of hand kinematic angles along the movement duration when grasping four different objects ($n=70$ trials per object, one recording session). Principal component analysis of the motor and sensory neural components of the movement reveal clustering of the four different types of object geometry along the three first PCs in each the cortical and kinematic PC spaces (Mk-Ol, $n=70$ trials per object, one recording session). (c) Averaged synchronized neural signals collected during the execution of the Task 2 for three different spatial targets. Signals were processed identically to Task 1 (Mk-Ol, at least $n=80$ trials per position, one recording session). The reference condition for aligning neural signals is the central target for Task 2. (d) Joint kinematics angles as well as wrist 3D-cartesian positions are shown for the left, center and right target along the movement. (e) Stick diagram depicts evolution of the arm joint angles for the three conditions while maximum pulling force is represented as multidimensional vectors. 3D Wrist trajectories are shown for the left, center and right position along the movement duration. Thick stroke arrows represents the average maximal force value.

2.4.5. Single unit encoding of multimodal motor and sensory information

We then exploited the capabilities of our framework to dissect the role of kinematic, kinetic or sensory events on the firing patterns of single units. We manually sorted M1 and S1 recordings

to identify well-isolated single units. During the task, firing rates in M1 were typically higher than in S1 (**Figure 2.10 a**). By design, the pulling force applied by the monkey correlated with the negative (towards the body) hand velocity of the pull (**Figure 2.10 b**). We first asked whether this interaction between limb kinematics and object dynamics could be observed at the single neuron level. We then plotted the firing patterns of single neurons against force and velocity variables and observed diverse and complex tuning for hand velocity and pulling force in both M1 (**Figure 2.10 c**) and S1 (**Figure 2.10 d**). While some cells showed apparent tuning for specific features (**Figure 2.10 c** top and **Figure 2.10 d** top likely modulate only with pulling force), others showed a more complex interaction of these features (e.g., **Figure 2.10 d**, bottom, modulates with both hand velocity and pulling force).

We next sought to quantify the influence of these behavioral covariates on each spike train using an encoding model of neural activity. We constructed Generalized Linear Models (GLMs) (Perich et al., 2018; Pillow et al., 2008) to predict the spiking activity of the individual neurons based on numerous behavioral and environment signals including limb kinematics, pulling force, and object contact events reflecting the possibility for cutaneous sensory input (**Figure 2.10 e**) at object contact. The GLMs predicted the probability of observing an individual spike train. We found that the majority of cells in both M1 and S1 could be significantly predicted using this model (**Figure 2.10 f**), with similar performance for both areas. By computing a relative pseudo- R^2 metric, which compares the performance of the full model to a reduced model which omits specific variables (see Methods), we quantified the unique contribution of each specific set of variables on the model performance (**Figure 2.10 g**). We found limb kinematics to be the dominant explanatory variable, reflecting the gross modulation of neural activity throughout the reach. Yet, a significant portion of neural spiking could also be explained by the three-dimensional pulling force or the time of object contact. For both monkeys, approximately 16% of S1 neurons were significantly explained by the precise object contact independently of other variables (**Figure 2.10 h**). Across the population of neurons recorded from the M1 arm area Mk-Cs, 24% of neurons were significantly explained by pulling force, yet we found very little force information in the hand-area M1 neurons recorded from Mk-Jo.

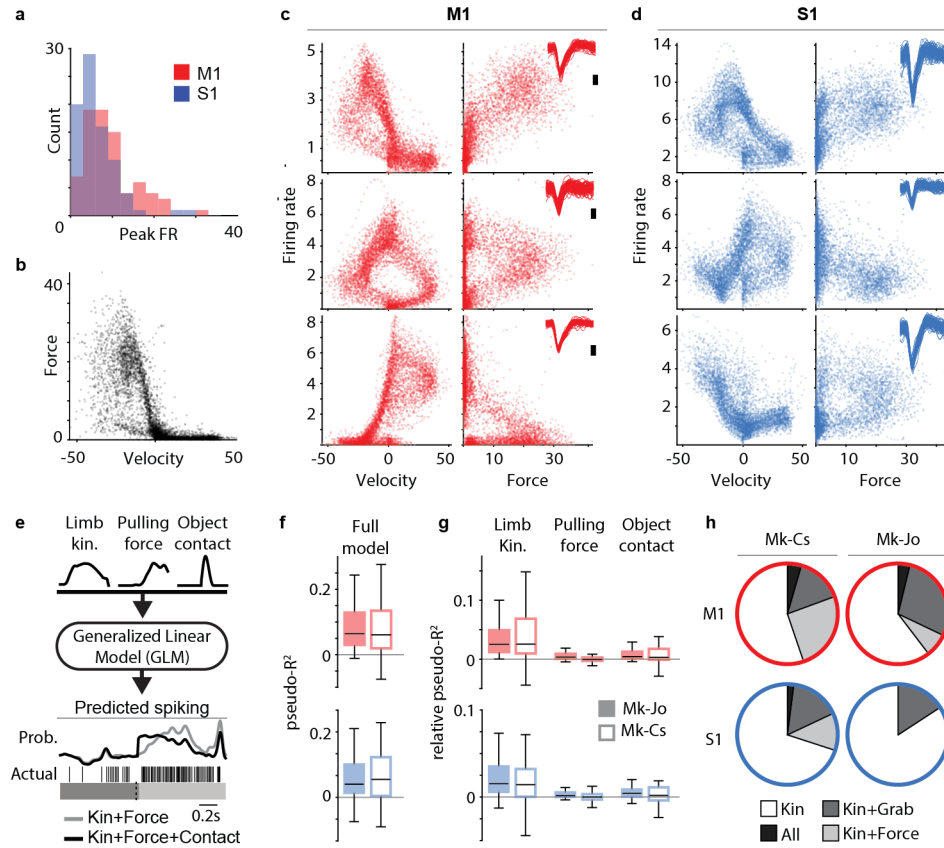


Figure 2.10 – Single unit encoding of multimodal motor and sensory information. (a) Each histogram shows the peak firing rate across all trials (one session per animal) for the populations of sorted neurons from M1 (red) and S1 (blue). On average, M1 firing rates were slightly higher than S1 (9.5 Hz compared to 6.4 Hz; $p < 0.001$, student's t-test). (b) Hand velocity against pulling force for all trials from Mk-Cs. Each dot represents a single time point (sampled at 10 ms intervals). Since the pulling phase was loaded, the pulling force strongly correlates with negative hand velocity. (c) Example tuning for three M1 cells plotting firing rate against the hand velocity (left column) and pulling for (right column). Insets show 100 randomly drawn spike waveforms (scale bar indicates 100 μ V). Due to the interplay between kinematics and force during the object interaction, we observed very complex tuning for the different cells. The top cell, for example, correlates with pulling force, whereas the middle cell appears to correlate with both force and kinematics. (d) Three example cells from S1, presented as in Panel C. (e) We used GLMs to assess whether neural activity is explained by limb kinematics, pulling force, or object contact events. Example predictions for one cell is shown comparing a model with kinematics and force (gray) against the full model (black). The black model better captures the burst of spikes following object contact. (f) The distribution of pseudo- R^2 values for the full model across all M1 and S1 cells in Mk-Cs (solid) and Mk-Jo (hollow). (g) The relative pseudo- R^2 metric captures the contribution of each parameter to the full model fit. Most cells were predominantly explained by limb movements, but there remains a substantial effect of pulling force and object contact. (h) The percentage of cells that were significantly described ($p < 0.05$, bootstrap test; see Methods) by each of the parameters. All cells were significantly predicted by kinematics, though many also were significantly explained by object contact and pulling force.

2.4.6. Discrete and Continuous decoding of movement kinematics

Finally, we sought to demonstrate the relevance of our framework to neural engineering applications. For this, we evaluated the ability to decode discrete and continuous features

of natural movement using tools widely employed in studies of Brain Computer Interfaces (Capogrosso et al., 2016; Ethier et al., 2012; Fitzsimmons et al., 2009; Hu et al., 2018; Nishimura et al., 2013; Vargus-Irwin et al., 2010; Velliste et al., 2008).

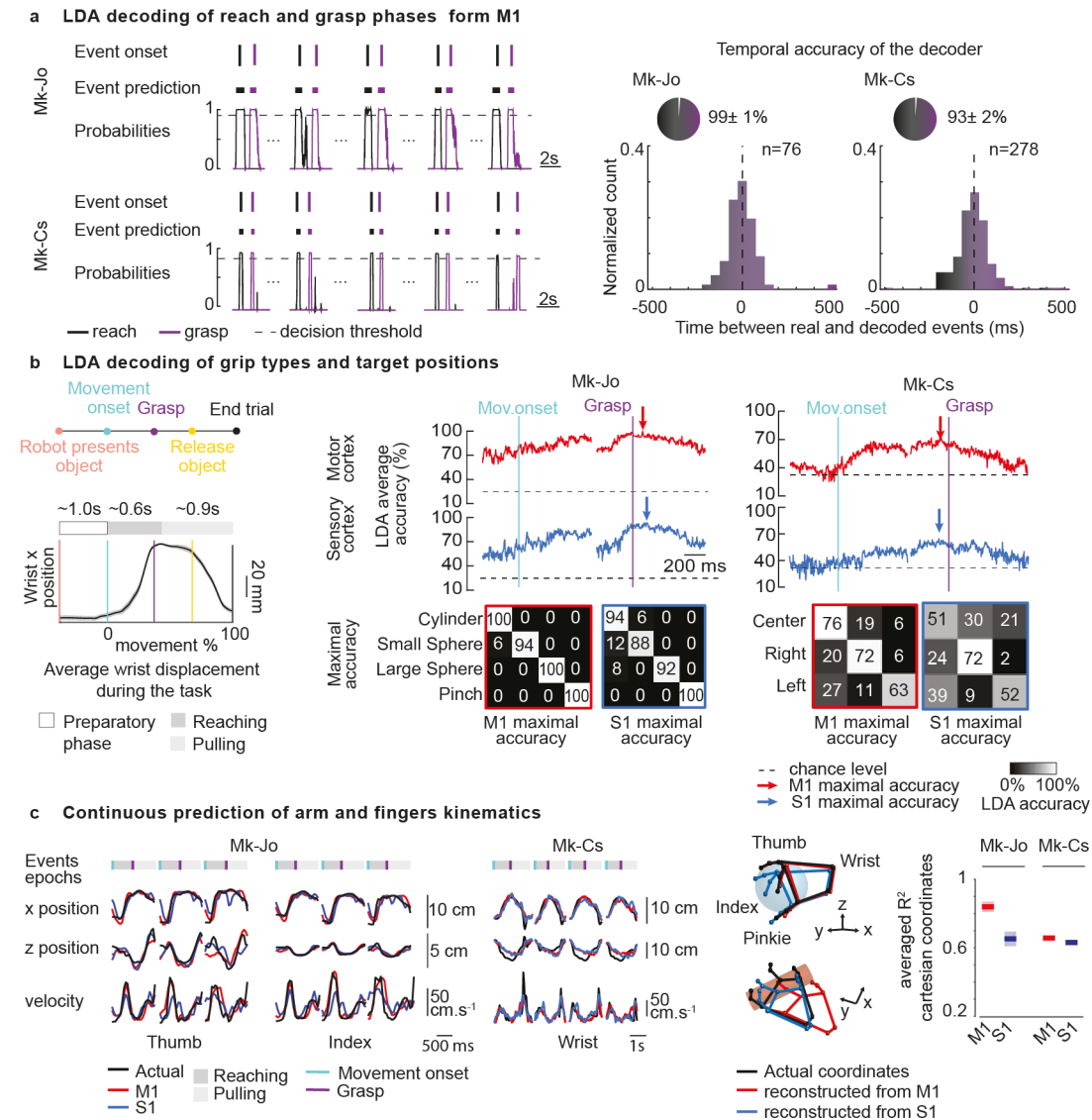


Figure 2.11 – (Continued on the following page.)

We developed a linear discriminant analysis (LDA) decoder that calculated the probability of reaching onset and grasping events using cortical signals from primary motor areas. The decoder accurately predicted these events over extended periods of behavior in both monkeys (**Figure 2.11 a**), with accuracy of up to 99% for Mk-Jo and 93% for Mk-Cs. The median temporal precision was found to be close to zero (median difference: -11.5 ms for reaching onset and 9.5 ms for grasping in Mk-Jo, and -4ms for both events in Mk-Cs).

Discrete and Continuous decoding of movement dynamics. (a) LDA decoding of reach-onset and grasp-onset events from M1 multiunit activity in both monkeys. On the left, four (Mk-Jo) and five (Mk-Cs) successive reach, grasp and pull trials are presented along with the actual event onset identified using video recordings, the detected motor states and the probability of reach-onset and grasp-onset motor states (in black and purple). On the right, histograms show the distribution of the temporal differences between the actual occurrence of reach-onset and grasp-onset events and the decoded occurrence of these motor states for all the recording sessions in the two monkeys (n=76 reach and grasp events for M-Jo, one recording session, and n=278 reach and grasp events for Mk-Cs, one recording session). (b) LDA decoding of grip types and target positions. On the left, we represented the trial structure as well as the average wrist displacement during the task (n=48 trials for Mk-Jo, one recording session). The wrist position does not vary before the movement onset event identified via video recordings. The average reaching phase duration was 650 ms, while the average pulling phase lasted for about 900 ms. On the right, we show the average performance of the offline LDA decoder for each object shapes and each target position in space using multiunit activity recorded from M1 and S1 areas (n=15 trials per objects for Mk-Jo, one recording session and n=25 trials per position for Mk-Cs, one recording session). Confusion matrices report accuracies obtained for the best time window for M1 and S1 signals. (c) Continuous prediction of arm and fingers kinematics using Kalman filtering. Multiunit activity from M1 and S1 areas were used to predict fingers and arm 3D coordinates during the whole reach-and-pull movement. On the left, time traces show prediction of the thumb, index and wrist x, y positions and velocity using neural population activity from M1 and S1 arrays in Mk-Jo and Mk-Cs. Three-dimensional static hand postures were reconstructed by predicting x, y and z coordinates of each fingers and wrist joints in Mk-Jo for the small spherical grip and the cylindrical grip (n=1 trial per object). On the right, performances of the continuous decoders are computed separately for M1 and S1 in both monkeys (cross validation k-folds with k=48 for Mk-Jo, one recording session and k=134 for Mk-Cs, one recording session).

We then used the LDA decoder to classify object type and direction of reaching from both motor and sensory cortices (**Figure 2.11 b**). We repeated the LDA analysis at sliding time windows spanning the entire reach-and-grasp movement. Both M1 and S1 multiunit spiking activity accurately discriminated between different grasps during the grasping phase in Mk-Jo (maximum decoding accuracy: M1: 100%, S1: 94%). Interestingly, multiunit activity from M1 and S1 could be used to differentiate between objects more than 300 ms before movement onset. Yet, we were not able to reliably classify one of the three positions before the movement onset in Mk-Cs (**Figure 2.11 b**). Maximum decoding accuracy was reached around 100 ms before the grasp and was 70% for M1 and 58% for S1.

We finally investigated the possibility to decode continuous arm and fingers kinematics. By fitting a standard Kalman filter (Wu et al., 2006) to each 3D coordinates of the arm and hand joints, we managed to reconstruct time-varying joint coordinates for most of the finger joints, obtaining a median performance of 0.83 and 0.65 for M1 and S1 areas respectively in Mk-Jo (**Figure 2.11 c**). Three-dimensional reconstruction of the wrist and fingers position based on decoded kinematic features is shown in **Figure 2.11 c** for both spherical and cylindrical grips. Hand and arm joint kinematics could also be decoded from Mk-Cs with a median performance of 0.68 and 0.67 for M1 and S1 area respectively. For both monkeys, M1 decoder outperformed S1 decoder.

2.5. Discussion

Here we presented the implementation of a robotic platform for the study of sensorimotor processes underlying upper limb movements in monkeys. We validated this platform by implementing behavioral tasks in monkeys involving natural, three-dimensional reaching, grasping and object manipulation. We discuss our developments and the functionality of our robotic platform in light of three applications: 1) the study of arm/hand kinematics, 2) neural correlates of natural upper limb movements 3) application in Brain Computer Interfaces.

2.5.1. A versatile framework for multimodal characterization of three-dimensional arm movements

In typical neurophysiological experiments with monkeys, experimenters constrain the behavior of monkeys to separate kinematic analysis from the study of dynamic force interactions with the world. Reach to grasp is often studied using static objects (Brochier, 2004; Ethier et al., 2012; Okorokova et al., 2020; Santello et al., 1998; Schaffelhofer and Scherberger, 2016; Vargas-Irwin et al., 2010) or constrained manipulandum (de Haan et al., 2018; London and Miller, 2013; Omrani et al., 2016), while the production of forces is typically investigated under isometric/unidimensional conditions (Ethier et al., 2012; Moritz et al., 2007; Nishimura et al., 2013) or in planar tasks (de Haan et al., 2018; London and Miller, 2013; Omrani et al., 2016). While these constraints are effective to dissect the role of specific neuronal-subpopulation in the control of dynamic movement variables, even simple natural movements present an extraordinary complex patchwork of precision and force-controlled movement actions following unconstrained limb and joint trajectories. Our robotic framework allows the characterization of these natural behaviors while retaining the ability to integrate multimodal recordings of kinetic and kinematic signals.

We devised a platform in which subjects can interact freely with a robotic arm in a large three-dimensional workspace (**Figure 2.2 c**). We showed that interaction with the robot during upper-limb movements was safe and robust and that it did not impose any direct physical constraint on the arm, therefore promoting natural and smooth trajectories (**Figure 2.4 f**). In addition, we instrumented our platform to provide simultaneous recordings of pulling and contact forces. Our robot control strategy can accommodate for simple and straightforward definition of motor tasks and it allows the user to easily adjust robot behavior. The control software package and libraries are made freely accessible and open source on Zenodo (10.5281/zenodo.3234138). These can also be used as a basis to configure other robotic arms for similar tasks using our logic. We finally synchronized kinematics and cortical recordings to both robot behavior and interaction forces measurements to obtain a rich multimodal panel of sensory and motor features characterizing arm and hand movements.

This framework provides with unprecedented means to address scientific questions that require the study of motor actions following unconstrained trajectories of limbs and joints in monkeys, such as the characterization of motor recovery in pre-clinical studies. It can

potentially be used to design complex tasks such as precise control of grip pressure (Ethier et al., 2012), maneuvering of 3D manipulandum, or motion under force-field perturbation. In addition, our platform could serve rehabilitation purposes (Spalletti et al., 2017; Spalletti et al., 2014). For example, deficits and recovery in kinematics or force outputs could be characterized in animal models of disease.

2.5.2. Applications in the study of three-dimensional movement dynamics

Characterization of arm and hand movement dynamics requires the integration of pulling force components, contact forces and kinematics of the joints. In our example, we utilized these features to define a “dynamic” manifold showing the evolution of trajectories in a space that mixes kinematic and forces. We used this tool to study kinematic adaptation to resistance levels and investigate the relationship between kinematics and pulling forces (Santello et al., 1998). Surprisingly, our analysis revealed that kinematic strategies adapted to resistive loads. This suggests that kinematic synergies may vary when stronger forces are perceived. Our results indicate that during functional movements, upper-limb postures, interaction forces, and joint trajectories are continuously adapted together to reach the desired motor output, and perhaps regulated by both central (Santello et al., 1998) or even simple reflex mechanisms (Weiler et al., 2019).

2.5.3. Applications in the study of neural sensorimotor processes

We then sought to demonstrate the efficacy and potential of our framework for applications in the study of neural dynamics during natural movements. We reported that neural activity from both motor and somatosensory cortex show clear modulation with kinematic and dynamic movement variables. Both M1 and S1 activity showed complex modulation throughout the whole movement, with clear and smooth trajectories in the neural manifold (**Figure 2.8** and **Figure 2.9**). This corroborates that somatosensory single cells encode multiple movement components and not only, or mostly, touch-related information (London and Miller, 2013; Prud’homme and Kalaska, 1994). The firing patterns of single units in both M1 and S1 showed strong and complex modulation with respect to multiple movement parameters (**Figure 2.10**). Our unique set up allowed us to investigate how kinematic, forces and contact events could, in combination or independently, explain neuron firing patterns. The majority of neurons in the somatosensory cortex encoded kinematics variables only. The remaining portion of cells encoded either contact events or force in conjunction with kinematics suggesting that important components of movement dynamics are encoded in somatosensory area 2. Availability of such a complex dataset and integrated kinematic signals opens intriguing possibilities for the study of population dynamics during natural behavior.

2.5.4. Applications in neuroengineering and brain computer interfaces

Brain Computer Interfaces have been applied to animal models and humans to control robots (Collinger, Boninger, et al., 2013; Hochberg et al., 2012; Hochberg et al., 2006; Wodlinger et al., 2015), support communication (Gilja et al., 2015; Milekovic, Sarma, et al., 2013; Vansteensel et al., 2016; Wolpaw et al., 2002), and restore motor control (Ajiboye et al., 2017; Bouton et al., 2016; Ethier et al., 2012; Moritz et al., 2007). However clinical applicability is limited by the fact that these devices are tested in restricted laboratory environments and constrained tasks. Instead, the development of future solutions aiming at the recovery of functional movements requires set-ups that replicate and quantify performances of natural motor tasks. Our framework provides with such an opportunity allowing the execution and quantification of three-dimensional arm and hand movements in a relevant animal model.

For example, we showed that it was possible to decode both reach and grasp events as well as target shape or position in space during a natural tasks that did not constrain the execution time or the movement trajectory (**Figure 2.11 a-b**). This type of information could be combined to build simple though robust decoders driving pre-programmed patterns of stimulation of the nervous system in pre-clinical and clinical settings (Capogrosso et al., 2016; Wagner et al., 2018).

Interestingly, even in a task that did not constrain the duration of the movement preparation or execution phase, we were able to predict grasp types from both motor and sensory activity several hundreds of milliseconds before movement onset (**Figure 2.11 b**). We found this result in accordance with several theories around the dynamical interaction and integration of sensory-motor processed during movement, and may even include components such as “efference copy” (Grüsser, 1994).

Finally, we showed that we were able to predict individual fingers kinematics from multiunit activity recorded in motor and somatosensory cortex during whole three-dimensional reaching and grasping movements (**Figure 2.11 c**). These results confirm the findings of Vaskov and colleagues (Vaskov et al., 2018) on M1-based finger motion decoding and extend the findings of Okorokova and colleagues (Okorokova et al., 2020) to multiunit activity and whole arm and hand movements.

2.6. Limitations

Our platform holds some limitations both in terms of performance in the present applications and flexibility towards different experimental uses. First, for our example applications, the monkey interacted with the robotic arm in an impedance-control mode. Impedance control introduces a damping effect on the arm of the animal which slows down the pulling movement. We explicitly chose this control mode, since this dampening effect was a feature of our experimental design. However, this behavior can represent a motor constraint for studies that envision a fully transparent interaction with a robotic device that does not oppose any resis-

tance to manipulation. In this case, direct torque-control strategies offer a good alternative to impedance control. These would allow for transparent interactions by compensation of any force applied on the robot end-effector. However, this control architecture could require additional strategies to compensate for kinematic instabilities. The code structure of our robotic framework provided online allows a custom implementation of direct force control schemes as well as several others, making it compliant to other behavioral requirements.

Second, our platform is built around a robotic arm. Obviously this choice influences not only the experimental performance and constraints, but also the number and type of variables that can be evaluated and compared to neural activity. In our case, we focused on studying upper-limb unconstrained reaching. Therefore, we allowed the monkeys to interact with the robotic arm exclusively at the end effector in order to leave the arm clear from any other constraints. This system is not compatible with studies aiming to manipulate or constrain specific degrees of freedom in the arm joint space, as well as the direct measurements of arm joint torques. In those cases, exoskeletons may offer a valid and more appropriate alternative (Pirondini et al., 2016; Scott, 1999) .

2.7. Conclusion

In summary we have reported and described a platform that can be adapted to study a large variety of tasks that are useful to investigations in motor control and perhaps other related applications. We provided three examples showing the validity of our approach for both basic and applied investigations thus paving the way to more detailed studies investigating sensorimotor processes in both monkeys and humans.

2.8. Contributions

MC, BB and MB conceived the study; BB designed and implemented the robotic framework hardware and the software modules with the support and supervision of SSM and A.Bi. MB designed and implemented the integrated sensors hardware and software with the support and supervision of FM and SSM. BB, MB, SC, MP and SW conducted the experiments; MB, BB, MP and TM performed the data analysis; SC, MB, A.Bo. and MK trained the animals; A.Bo. implemented the automatized training program and reward system and implanted the cortical arrays in Mk-Ol; MB, SC and SW processed the data. MC, MB, BB and MP wrote the manuscript; all authors edited the manuscript; SM and MC supervised the study.

2.9. General Conclusion

In this chapter, I outlined the design and engineering of a modular behavioral recording platform for primate experiments. Throughout a large panel of data analyses, I highlighted some of the potential applications for sensorimotor studies and neuroprostheses development.

Chapter 2 Adaptative behavioral platform for the study of upper-limb movements in monkeys

This work constitutes the first milestone of this thesis. It represents a crucial step in the design and implementation of experimental protocols to test the efficacy and functionality of a peripheral neuroprosthesis in monkeys (see chapter 3). In addition, this versatile behavioral framework aided in the development and characterization of a cortical control paradigm for the driving of the peripheral nerve interface (see chapter 4). More generally, I argue that this platform represents a valuable, flexible, and accessible setup for the study of sensorimotor mechanisms in monkeys.

3 Intrafascicular stimulation elicits dexterous hand movements in primates

Intrafascicular implants have shown the unique ability to selectively recruit peripheral nerve fibers in sensorimotor applications. To demonstrate the clinical viability of intrafascicular electrodes for the restoration of precise hand movements after paralysis, I believe it is critical to assess the functionality and the range of movements elicited with this technology in pre-clinical animal models. In this work, I tailored transverse intrafascicular multichannel electrodes (TIMEs) for the recruitment of arm nerve fibers in monkeys. I characterized the peripheral nerves anatomy in *macaca fascicularis* monkeys and optimized the implantation procedure based on structural neuroanatomical features and computational simulations. I then demonstrate that intrafascicular stimulation of the median and radial nerves engages specific flexor and extensor muscles of the wrist and fingers. Chronically implanted intrafascicular electrodes allow the generation of a large repertoire of hand movements, including specific fine grip patterns, using simple stimulation protocols. Additionally, the modulation of intrafascicular stimulation permits the graded control of hand closure and opening. Ultimately, I demonstrate that intrafascicular stimulation can be modulated to enable a transiently paralyzed monkey to perform a functional grasping task. With this work, I provide a large body of evidence highlighting the potential of intrafascicular interfaces to produce a wide variety of selective, functional, and sustainable wrist and finger movements.

The content of this chapter is adapted from the manuscript Badi et al., “Intrafascicular peripheral nerve stimulation produces fine functional hand movements in primates”, currently in review in the journal Science (November 2020).

Personal contributions: Responsible for the project. I conceived the study, designed and implemented the experimental setup, programmed the electrophysiology and stimulation control software and hardware, implemented the computational model, performed neuroanatomy and histological procedures, and used the results to dimension the intraneural implants. I designed the microfluidic cuff system, trained the animal on the functional task, prepared the surgical procedures and helped performing them. I designed and conducted the experiments, guided and performed the data analysis, pre-processed the data, prepared

the figures, and wrote the manuscript. Sophie Wirth, co-first author of the study, wrote the project's grant and helped conceive the study. She performed neuroanatomy and histological procedures, analyzed the histological data, recruitment curves, and long-term stability data, and prepared the associated figures. She assisted in the surgeries, participated to a part of the experiments, and helped dimension the intraneural implants. She reviewed and edited the manuscript. Extended authors' contributions are reported at the end of the chapter.

Intrafascicular peripheral nerve stimulation produces fine functional hand movements in primates

Badi M*¹, Wurth S^{*1}, Scarpato I¹, Roussinova E¹, Losanno E², Bogaard A³, Delacombaz M³, Borgognon S^{3,4}, Čvančara P⁵, Fallegger F⁶, Su D.K P⁷, Schmidlin E³, Courtine G^{4,8}, Bloch J ^{*8}, Lacour S.P⁶, Stieglitz T⁵, Rouiller E.M³, Capogrosso M ^{3,9}, and Micera S^{1,2}

¹ Bertarelli Foundation Chair in Translational Neuroengineering, Center for Neuroprosthetics and Institute of Bioengineering, École Polytechnique Fédérale de Lausanne (EPFL), Lausanne, Switzerland

² The Biorobotics Institute and Department of Excellent in Robotics and AI, Scuola Superiore Sant'Anna, Pisa, Italy

³ Department of Neuroscience and Movement Sciences, Platform of Translational Neurosciences, Section of Medicine, Faculty of Sciences and Medicine, University of Fribourg, Switzerland

⁴ Center for Neuroprosthetics and BrainMind Institute, School of Life Sciences, École Polytechnique Fédérale de Lausanne (EPFL), Lausanne, Switzerland

⁵ Laboratory for Biomedical Microtechnology, Department of Microsystems Engineering–IMTEK, Bernstein Center Freiburg and BrainLinks-BrainTools Center, University of Freiburg, Freiburg, Germany

⁶ Bertarelli Foundation Chair in Neuroprosthetic Technology. Laboratory for Soft Bioelectronics Interface. Institute of Microengineering, Institute of Bioengineering. Centre for Neuroprosthetics, Geneva, Switzerland

⁷ Neurological Surgery, Harborview Medical Center, Seattle, United States

⁸ Defitech Center for Interventional Neurotherapies (NeuroRestore), Department of Neurosurgery, University Hospital of Lausanne (CHUV) and University of Lausanne (UNIL), Lausanne, Switzerland

⁹ Department of Neurological Surgery, Rehabilitation and Neural Engineering Laboratories, University of Pittsburgh, Pittsburgh, PA.

* Co-first authors,

3.1. Abstract

Regaining hand control is critical for people suffering from upper-limb motor deficits. Neuroprostheses based on direct muscle stimulation have been used to restore hand motor functions (Ajiboye et al., 2017; Ethier et al., 2012; Kapadia et al., 2020; P. Peckham et al., 2002). Due to limited movement specificity, technical complexity, and difficulties to generate sustained levels of force (Micera et al., 2010; Mizrahi, 1997), these solutions have not translated into commonly available clinical neuroprosthesis. An alternative strategy to recruit muscles with electrical stimulation is the use of intrafascicular electrodes inserted into peripheral nerves (George et al., 2019; Petrini, Bumbasirevic, et al., 2019; Raspopovic et al., 2014), but the ability of this approach to generate fine hand movements remains unknown. Here, we demonstrate that a neuroprosthesis featuring only two intrafascicular electrodes produces a rich

repertoire of functional hand movements in monkeys. We tailored transverse intrafascicular multichannel electrodes (Boretius et al., 2010) (TIMEs) to the anatomy of the median and radial nerves of macaque monkeys. These TIMEs achieved the selective recruitment of flexor and extensor muscles mobilizing the wrist and fingers, which translated into a variety of sustained functional grasp and hand opening movements. Finally, we show the possibility to drive TIME stimulation protocols using motor intracortical signals to enable a monkey to perform a functional grasping task with a transiently paralyzed hand. Our findings show that a simplified neuroprosthesis featuring only two TIMEs can be used to generate dexterous hand movements, significantly reducing technical complexity, with important implications for clinical applicability.

3.2. Introduction

Functional neuromuscular electrical stimulation (NMES) delivered via surface electrodes (Popović et al., 1999; Prochazka et al., 1997; Snoek et al., 2000) or epimysial implants (P. Peckham et al., 2002; P. Taylor et al., 2002) has been used for decades to restore grasping after paralysis due to spinal cord injury or stroke. While surface stimulation systems permit the generation of a few pre-determined grasp types, they are limited by high transcutaneous activation currents, poor selectivity, and the difficulty to recruit intrinsic hand muscles. The use of intramuscular electrodes has allowed to target deeper muscular structures and restore additional hand functions in monkeys (Ethier et al., 2012; Moritz et al., 2008; Pohlmeier et al., 2009). Such implantable NMES-based neuroprostheses have been validated in clinical studies (Ajiboye et al., 2017; Colachis et al., 2018; Friedenberg et al., 2017; P. H. Peckham et al., 2001; P. Peckham et al., 2002). However, these systems rely on complicated surgical procedures and the feasibility of upscaling them to a higher number of muscles, and thus functions, remains to be determined. Moreover, all NMES approaches are restricted by the fast generation of muscle fatigue through the unnatural recruitment order of a subset of fast-fatiguing large-diameter muscles (Binder-Macleod and Snyder-Mackler, 1993; McNNeal, 1976; Rattay, 1989; Rattay, 1986).

An alternative strategy to recruit muscles consists of targeting branches of the peripheral nervous system (PNS). The architecture of the peripheral nervous system allows accessing several distal end-effectors from a single proximal location, consequently bypassing the placement of multiple electrodes. For instance, epineural cuff electrodes have been implemented in clinical neuroprostheses aiming at restoring hand function after paralysis (Brill et al., 2018; Memberg et al., 2014; Tigra et al., 2020). Albeit minimally invasive, none of those devices is in wide clinical use due to insufficient selectivity in terms of muscle recruitment, limited functional benefits, and complicated external equipment discouraging daily use (Hugosdottir et al., 2014). Intrafascicular stimulation offers an alternative opportunity to enhance recruitment selectivity (Badia et al., 2011) and thus reduce the onset of fatigue by positioning the implant near efferent axons of different muscles (Bourbeau et al., 2011; Gaunt et al., 2009; Raspopovic et al., 2017; Veltink, van Veen, et al., 1989). For example, penetrating microelectrode arrays

inserted in the arm nerves of anesthetized monkeys have been able to elicit different grasp types (Ledbetter et al., 2013). Despite this important proof-of-concept, to date, no intraneural stimulation based neuroprosthesis for hand functional restoration has been implemented in clinical applications.

Recent studies demonstrated the preeminent potential of transverse intrafascicular multichannel electrodes (Boretius et al., 2010) (TIMES) to elicit selective sensory percepts in subjects with limb amputation with promising results in terms of long-term usability. Moreover, TIME implants have been used to generate specific motor responses and permit a high-fidelity control of evoked movements in rodents (Wurth et al., 2017). Building on these interesting properties, we hypothesized that intraneural stimulation of the median and radial nerves using TIMES would generate a rich collection of fine wrist and finger movements that could be used to improve functionality after hand paralysis.

3.3. Methods

3.3.1. Animals involved in this study

The experiments were conducted on 9 adult macaques (*Macaca fascicularis*) ranging from 5 to 16 years old (weight between 3.1 and 8 kg): (1) six animals for the neuroanatomical analyses (**Appendix Table A.1**); (2) five animals for the acute electrophysiological experiments (**Appendix Table A.2**); and (3) two animals for the chronic electrophysiology (**Appendix Table A.3**). All animals were group-housed in an enriched indoor room where they had access to water and food ad libitum. The experimental protocol was elaborated in compliance with the national law on animal protection and approved by the Federal and local veterinary authorities (authorization number 2017_03_FR 2014_42E FR, 2017_04E_FR, and 2016_09_FR, **Appendix Table A.4**).

3.3.2. Anatomical characterization of the monkey's arm nerves

Cadaver arm dissection for neuroanatomy study

Cadaver arms were harvested after transcardial perfusion with Ringer's solution containing 100000 IU/L heparin and 0.25% NaNO₂ followed by 4% phosphate buffered paraformaldehyde (pH 7.3) containing 5% sucrose. Dissection of the primate arm exposed the muscles of the arm, forearm, and hand, as well as the median, ulnar and radial nerves and their respective branches. From proximal to distal, branches emerging out of the main nerves trunk were followed to their target muscles and identified with pins. The superficial and deep layers of the flexor muscles on the anterior part of the arm and forearm and of the extensor muscles on the posterior side were identified and compared to human anatomy. The complete nerves with their branches were then harvested and pinned down for measurements.

Tissue handling and preprocessing

Samples of about 6 cm proximal to the epicondyle were retained and cut into sub-samples of about 1 cm (**Figure 3.1 a**). The samples were then embedded in paraffin and sectioned in thin cross sections (4 μm thickness) on a microtome (Hyrax M25, Microm, DE). Four tissue sections in a ribbon of 25 were selected and mounted onto coated glass slides (Superfrost Ultra Plus, Thermo Fisher Scientific, MA) yielding tissue slices of approximately every 100 μm between glass slides. Mounted tissue samples were dried overnight at 37°C and then stored at +4°C until use.

Histology

We selected consecutive sections of ~100 μm apart and stained them with hematoxylin and eosin (H&E) using the automatic Tissue-Tek Prisma & Coverslipper HQplus machine (Sakura, NE) to investigate the topographical organization of the fascicles proximal to the elbow.

For immunohistochemistry, slides were first dewaxed and rehydrated and then placed 20 min in a citrate buffer bath (pH 6) at 95°C for antigen retrieval. Slides were then washed (3x in Tris-buffered Saline (TBS) 0.1M), incubated in H₂O₂ 0.3% during 30 minutes (room temperature) to block endogenous peroxidase activity and washed again (3x TBS 0.1M), followed by 1 h blocking of non-specific sites in Bovine Serum Albumin (BSA 10% in TBS 0.1M and Triton 0.3%), also at room temperature. Slides were processed for immunohistochemical labelling against Choline Acetyl Transferase (Goat anti-ChAT 1:50, AB144P Sigma-Aldrich), beta III tubuline (axons, rabbit anti-Tuj 1:200, ab18207), and macrophage/monocytes (mouse anti CD68 1:200, MCA341GA Bio-Rad) by incubation in primary antibody solution for 48h at 4°C. Slides were then rinsed in TBS 0.1M. Slides incubated with ChAT as primary antibody solution were then immersed in biotinylated secondary antibody solution (biotinylated horse anti-Goat IgG (H+L), 1:200, Adipogen SA) during 1 hour at room temperature. After incubation, slides were rinsed (3x in TBS 0.1M), incubated in Avidin/Biotinylated Enzyme complex (Vectastain®ABC system, Vector laboratories, prepared 45 minutes before utilization) for 1 hour at room temperature, and rinsed again (3x TBS 0.1M). Finally, motor axons were revealed using a DAB-Peroxidase (HRP) kit (Vector Laboratories) by incubation of the slices during one minute, followed by abundant washing in PBS 0.1M to stop the reaction and dehydration. The slides were then mounted using Moviol medium (Sigma-Aldrich) and coverslipped for microscopy. Slides incubated with Tuj and CD68 as primary antibodies were immersed in secondary antibody solution containing goat anti-rabbit IgG Alexa488 and goat anti-mouse IgG Alexa555 (both 1:200, ThermoFischerScientific). Finally, those slides were mounted with a Dapi-containing medium (Vectashield, Vector Laboratories) and coverslipped for microscopy.

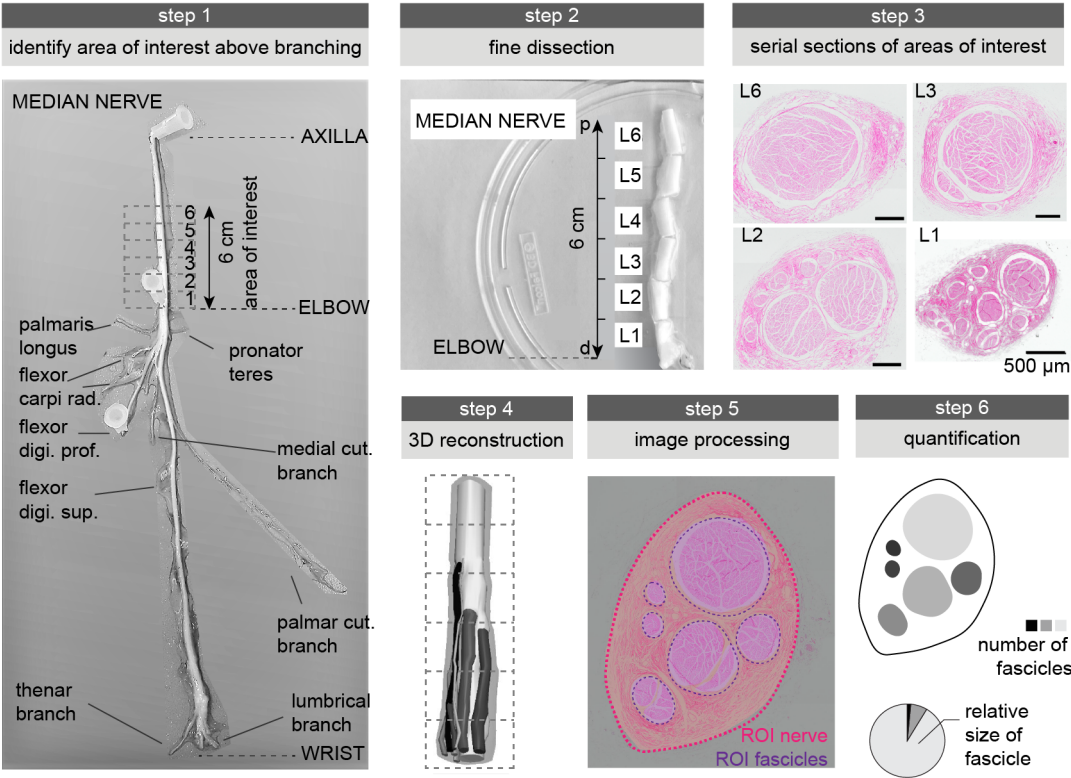
Motor fiber distribution in nerve cross-sections

The distribution of motor fibers across median and radial nerve cross-sections was assessed on immunohistochemically-labelled nerve sections against motor axon component Choline Acetyl Transferase (ChAT). The detailed step by step procedure is illustrated by **Figure 3.1**. Step 1 consisted in manual drawing of the contours of the neural compartments in Fiji. Step 2 consisted in converging the original image to an 8-bit type and applying a Gaussian blur filter (radius = 2 pixels) to reduce noise. Step 3 applied a Fiji in-built thresholding (method “Intermodes”) algorithm to the transformed image to isolate the stained portions of the cross-section. Step 4 applied Fiji-ImageJ’s in-built function “Analyze Particles” (particle size 4 to infinity, circularity 0.25 to 1) to identify the particles corresponding to motor axons in each of the regions of interest, yielding the resulting mask shown in step 4. Step 5 applied of a mean filter (kernel of 100 pixels) to the created mask to nuance the intensity of the particles. In step 6, an image conversion to 32-bit type image allowed to color-code the obtained image with a lookup table to highlight the intensity of the pixels, representing qualitatively the density of motor axons. The final image was constructed by overlaying the color-coded density map to the original image with a transparency of 20% to highlight the areas in the cross-sections with high density of motor axons (step 7).

Fascicles topography

3D reconstructions (Neurolucida 11.0, MBF Biosciences, USA) and fascicular topography analysis along the dissected nerves were performed using evenly spaced H&E stained cross sections (1 slice every 40, Tissue-Tek Prisma Sakura, EU) acquired with an optical microscope (Olympus slide scanner VS120-L100, Olympus Corp., EU) at 10x. Fascicular composition was analysed using open source software Fiji (ImageJ, NIH, USA), (**Figure 3.1 a**).

a Methods neuroanatomical study of NHP arm nerves



b Methods motor neuron distribution density

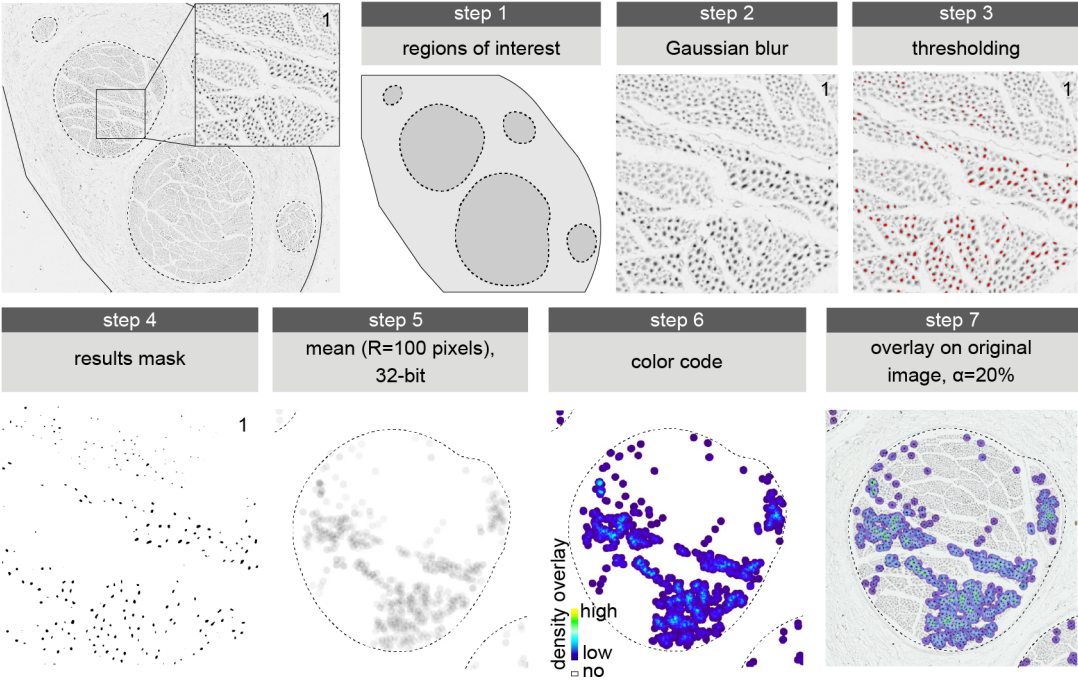


Figure 3.1 – (Continued on the following page.)

Methodology for the neuroanatomical study of the monkey arm nerves (a) Step by step procedure describing the quantification of the neural fascicular content. Step 1: monkey arm nerve dissection and identification of branches. Step 2: fine dissection of segment of interest above epicondyle into six 1 cm long segments for histology. Step 3: H&E staining of transverse nerve cross-sections at different levels along the longitudinal axis. Step 4: 3D reconstruction of fascicular topography above the elbow using Neurolucida software (Neurolucida 11.0, MBF Biosciences, USA). Step 5: Manual drawing and measurement of nerve and fascicle contours using Fiji built-in functions (ImageJ, NIH, USA). Step 6: Quantification of number of identified fascicles per cross-section and their respective cross-sectional area. (b) Protocol for the evaluation of motor fibers distribution in the monkey nerve on immunostained slices revealing the presence of ChAT-positive motor fibers in Fiji Image J. Step 1: Manual contouring of nerve compartments of interest. Step 2: Gaussian blur (radius = 2 pixels) for noise reduction. Step 3: Thresholding to isolate motor axons based on staining. Step 4: Identification of the resulting “particles” using Fiji-ImageJ’s in-built “Analyze Particles” (particle size 4 to infinity, circularity 0.25 to 1). Step 5: Application of a mean filter to nuance the intensity of the particles. Step 6: Image conversion into 32-bit and application of a lookup table to color-code the intensity of the pixels, representing qualitatively the density of motor axons. Step 7: Overlay of color coded density map to original image. Abbreviations: Hemotoxylin & eosin (H&E), Choline acetyltransferase (ChAT)

3.3.3. Peripheral implants design and manufacturing

TIME implant

The TIME implant used in this study was adapted from previously published design (Boretius et al., 2012). It consisted of two polyimide thin-film structures connected with the microflex interconnection technique (Stieglitz et al., 2000) (MFI) via screen-printed ceramics (Boretius et al., 2012) to a 40 cm long cable each. The cables were terminated with a 36-pole Omnetics Nano Strip Connector (A79022-001), which was used to contact the electrodes active sites. A needle (EH7900G) with a loop of suture (Prolene®) was incorporated (diameter 125 µm and suture length 15 cm) within the thin-film electrode (**Figure 3.2** and **Figure 3.7 h-i**). The electrode stimulation and ground contacts were coated with highly porous iridium oxide (sputtered iridium oxide film) to guarantee a high charge injection capacity for nerve applications. The thin-film microelectrode itself was made of a sandwich structure of polyimide-silicon carbide-platinum-iridium oxide-polyimide and had an overall thickness of 11 µm. Polyimide (PI, U-Varnish S, UBE Industries, LTD., Tokyo, Japan) served as substrate and insulation layer, silicon carbide as adhesion promoter (Čvančara et al., 2020), platinum formed the conductive paths, and iridium oxide was used to coat the stimulation and ground contacts. The overall structure was composed of two arms with 16 stimulation contact sites (eight per side and 80 µm in diameter) and two large area ground contacts each. The thin-film layer was folded at the mid-center line during assembly, resulting in a left and a right arm. The ground contacts exhibited 73 circular openings of the same size as the stimulation contacts but were interconnected under the top polyimide layer (Čvančara et al., 2019). Silicone anchoring rings were incorporated on the ceramic adapter to secure it to the surrounding tissue. Three fixation tabs were placed on each side of the polyimide structure and at the entry point to tie the electrode

to the epineurium. A little fixation ring was incorporated at the tip of the active strip to anchor the electrode at the exit point (**Figure 3.2** and **Figure 3.7 h-i**).

Micro-fabrication of the thin-film electrodes was performed in a clean room environment class 4 to 7 (depending on machinery location; according to DIN EN ISO 14644) with standard photolithography and MEMS processes. A 5 μm film of PI was spin-coated onto a 4" -silicon wafer and imidized at 450°C in a nitrogen atmosphere in a furnace (YES-459PB6-2PE-CP, Yield Engineering Systems Inc., San Jose, CA, USA). Afterwards, 1.4 μm of a high-resolution image reversal resist (AZ 5214E, MicroChemicals GmbH, Ulm, Germany) was applied via spin coating. The resist served as deposition mask for the succeeding adhesion layers and track metallization. A 50 nm layer of SiC was deposited using plasma-enhanced chemical vapor deposition (PECVD, PC310 reactor, STS Surface Technology Systems plc, Newport, UK) before evaporation of a 300 nm layer of platinum (Leybold Univex 500, Leybold Vacuum GmbH, Cologne, Germany). A lift-off step with acetone and isopropyl alcohol was performed to remove the resist with the excessive material. The next step was to pattern a further layer of image reversal resist, for the upper 40 nm SiC layer, which had to cover all metallization, for future contact with the top PI layer, but not the stimulation and ground contact sites and MFI structures Stieglitz et al., 2000 for electrical connection. Following a lift-off step, a further image reversal resist defining the stimulation contact sites and ground contacts was spin coated, exposed and developed. 100 nm of iridium and subsequently 800 nm iridium oxide (SIROF) were sputter deposited (Ir, Leybold Univex 500, Leybold Vacuum GmbH, Cologne, Germany), to ensure high charge injection capacities. Following another O₂-plasma surface activation, a second layer of PI with a thickness of approximately 5 μm was spin coated to insulate the metallization. A positive resist (AZ 9260, MicroChemicals GmbH, Ulm, Germany) was utilized as etching mask. The perimeters and openings were realized using RIE in an oxygen plasma. Following the last fabrication step, the thin-film electrodes were pulled off the silicon wafer with a pair of forceps for further assembly of the implants. Previously designed thin-films using same fabrication processes applied in human clinical trials (Čvančara et al., 2020; Petrini, Valle, Strauss, et al., 2019; Petrini, Bumbasirevic, et al., 2019; Petrini, Valle, Bumbasirevic, et al., 2019) were investigated with special cytotoxicity samples (Stieglitz et al., 2011), (run in parallel with the same process) according to the ISO 10993 for cytotoxicity testing. Direct contact and extract tests were performed compliant with the ISO 10993-5 with L929 mouse fibroblasts. Additionally, further direct contact and extract tests were performed with the human nerve cell line Kelly and the human muscle cell line A673. The samples passed the tests and no objections were claimed.

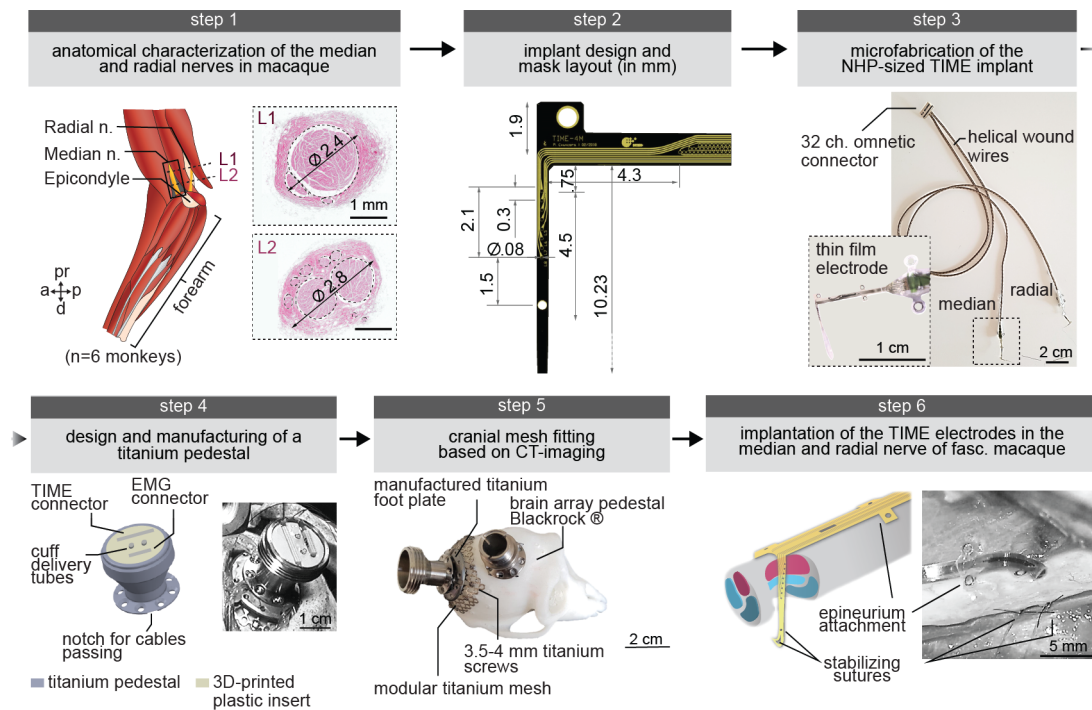


Figure 3.2 – Design, fabrication and implantation of the peripheral nerve interface. Step 1: Determination of the peripheral nerves access in the anterior and posterior compartments of the monkey upper arm (a=anterior; pr=proximal; p=posterior and d=distal). Photographs show transversal cross-sections of the median nerve at two potential implantation sites (L1 and L2 located 3 and 2 cm proximally to the epicondyle respectively). Measurements of the nerve diameter were used to dimension the intraneural implant. Step 2: Mask layout of the TIME electrode re-dimensioned to fit the monkey arm nerves. Modifications from previous design (Boretius et al., 2012) include re-dimensioning (indicated in mm on the picture) and the addition of an anchoring ring on the distal portion of the shaft for a secured attachment to the epineurium post-penetration. Step 3: Microfabrication of the entire TIME assembly containing the two TIME electrodes (median and radial) attached to a 32 channel connector through 40 cm-long helically-wound cables. Inset highlights the structure of the thin-film TIME electrode connected to a ceramic printed circuit and equipped with 5 suturing rings. Step 4: Custom-designed titanium pedestal encapsulating the EMG and TIME connectors, and the silicon tube for lidocaine delivery to the microfluidic cuff (left: schematic, right: photograph of implanted pedestal). Step 5: 3D printed skull (Mk-OLC), illustrating the placement of the pedestals hosting the brain arrays and the peripheral implants connectors. Step 6: Implantation of the TIME in the peripheral nerve. Colored fascicles are penetrated transversally by the electrode. Sutures are used at the entry and exit point to secure the implant to the nerve epineurium

Microfluidic lidocaine-delivery system

The soft cuff was fabricated using two layers of silicone membranes with the channels on one side and openings in the other, which are then bonded together (**Figure 3.3**). In short, first a 100 mm silicon carrier wafer (Siebert Wafer) was oxygen plasma cleaned, then a photopatternable SU8 layer (GM 1070, Gersteltec) was spin-coated at 750 rpm to yield a 100 μm thick layer. The photo-resist was then soft baked, exposed with a Cr mask on a manual aligner (MJB4, Süss Micro), post-exposure baked, developed in PGMEA (Sigma-Aldrich) and hard baked according to the manufacturer's instructions. This created a negative mould of the microchannels. For an easy mould release, the silicon carrier with micro-channels was treated

with a hydrophilic silane (trichloroethane(1H,1H,2H,2H- perfluorooctyl)silane, Sigma-Aldrich) for 1 hour under mild vacuum. Then a 150 μm thick PDMS (polydimethylsiloxane, Sylgard 184 10:1 monomer:cross-linker ratio, Dow Corning) was spin coated at 500rpm, degassed and cured for 2 hours at 75 $^{\circ}\text{C}$ in an oven. Then a thick PDMS handle layer was poured over the wafer after a second silane treatment. After curing, the thin and thick PDMS layers were peeled off the carrier together. For the layer with the channel openings, a 100 μm thick PDMS layer was spin coated over a silicon carrier wafer covered with a thin PDMS layer and a 23 μm PET sheet (Mylar, Lohmann Technologies) cover. After curing, a second PET layer was laminated onto it and the PET/PDMS/PET stack was peeled off the carrier. The channel openings were defined by femtosecond laser microstructuring (Optec). Then the top PET layer is peeled off the stack. Before bonding, the two PDMS layers were oxygen plasma activated (100W, 0.2mbar, 30s, Plasma chamber, Diener), aligned and bonded. A thin silicone tube was inserted at the entrance of the microchannel and then the outline of the device was cut using femtolaser microstructuring. Finally, the thick PDMS handle layer is peeled off. The cuff was attached to a 40 cm long Polyurethane Catheter tube (3.5Fr, Access Technologies, USA). Attachment wings were positioned along the tube to secure the system to the surrounding tissue. Additional substrate material was left on each side of the microfluidic channels to adjust the closing of the cuff around the nerve during implantation (**Figure 3.2** and **Figure 3.3**). The tubing was routed subcutaneously from the arm to the pedestal fixated on the skull and was closed using a hollow stainless steel plug (21G, 1.2cm long, Access Technologies, USA). The tube and cuff were flushed with anti-microbial solution (Taurolidine-citrate catheter solution, Access Technologies, USA) after each use and sealed to prevent infections. **Figure 3.3** describes the developmental and testing steps of the microfluidic-delivery system.

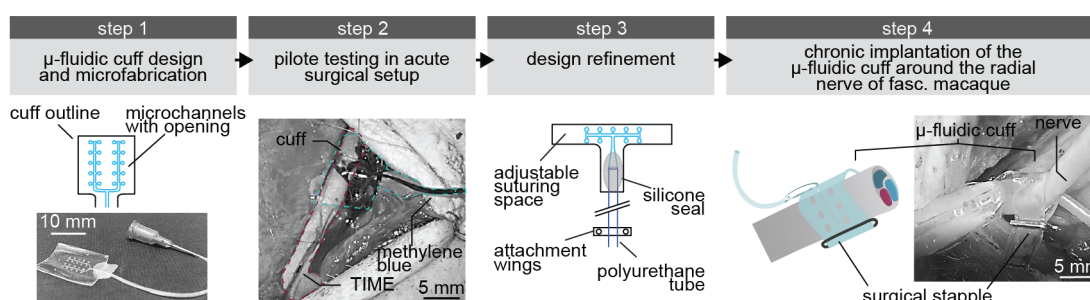


Figure 3.3 – Microfluidic cuff design for the selective paralysis of movement. Microfabrication and testing of a microfluidic cuff for anesthetic nerve delivery in monkey. Step 1: the cuff was microfabricated based on the dimensions of the fascicularis macaque nerves. The core was built in PDMS (polydiméthylsiloxane) to ensure a tight but soft adherence to the nerve and microfluidic channels were printed to provide controlled liquid delivery. Step 2: The cuff was acutely tested in monkey and liquid release was assessed using colored methylene blue liquid. The photograph shows the positioning of the cuff proximally to the TIME implant. Step 3: after initial testing, the implant was rescaled and suturing structures were added to ensure secured attachment to the nerve. Step 4: implantation procedure around the nerve.

Peripheral implants pedestal

A custom-made titanium pedestal was manufactured (EPFL, CH) to receive the TIME, the intramuscular electromyographic leads and the microfluidic system tubing. A plastic insert was design and 3D printed to create positioning holes for the connectors and the lidocaine-delivery tube (**Figure 3.2**). Silicone glue was used to seal the insert and the implants inside the pedestal (Dow Corning 3145 RTV).

3.3.4. Surgical procedures

All surgical procedures were conducted under aseptic conditions and general anaesthesia (Badoud et al., 2017).

Brain array implantation

Mk-OI was implanted with three microelectrode arrays. One array with 48 channels was implanted in the right hemisphere in the M1 hand region (Blackrock Microsystems, USA, 400 μm pitch, 1.5 mm tip length). S1 and PMv areas were also implanted but were not analyzed for this study. A 20 mm diameter craniotomy was performed in order to span the brain areas of interest and the dura was incised. Implantation of the arrays was achieved using a pneumatic compressor system (Impactor System, Blackrock Microsystems). The pedestal was fixed directly to the skull using 6 and 8 mm long screws. Neural data presented in this study were collected up to 8 months post-implantation.

Peripheral implantations surgery

A longitudinal skin incision was made over the skull at the level of fixation of the pedestal and the muscle overlying the skull was scraped off using a periosteal raspator. A second and third skin incision were made at the base of the neck and below the left scapula and the EMG wire electrodes, TIME electrodes, and microfluidic cuffs were subsequently subcutaneously tunneled in two steps from the head towards the shoulder using the Medtronic catheter passer (48409 Medtronic, EU).

Chamber fixation

The connectors for recording from the intramuscular EMG electrodes and for stimulating through the two TIME implants were placed in the custom-designed pedestal. In Mk- Me_c , the pedestal was screwed directly to the skull using eight 6 to 8 mm screws (VOI Europe, FR). In Mk- Ol_c , the pedestal was fixated to a compliant titanium mesh (TiMesh@Medtronic, CH) modelled based on a CT scan to fit the skull shape (**Figure 3.2**). A custom-made titanium foot plate (Buri SA, CH) served as support to the pedestal. The mesh was fixated to the skull using 3.5 mm long self-drilling screws (SCR 9001635 TIMESH, Medtronic, CH). The footplate and

pedestal were secured using custom-made 2mm long screws (Buri SA, CH). Once fixated, the skin was closed around the pedestal using intradermal Vycril 3-0 and external Ethilon 3-0 sutures.

Intramuscular electrode implantation

We implanted two monkeys with 8 pairs of Teflon-coated stainless steel wires to chronically record EMG activity from flexor and extensor muscles of the hand. The detailed implantation procedure is described in (Capogrosso, Wagner, et al., 2018). Acute EMGs recordings were performed using intramuscular subcutaneous needles (Ambu@Neuroline). The muscles implanted in chronic and acute experiments are summarized in **Appendix Table A.6**. Intrinsic hand muscles were implanted acutely.

During the chronic implantation, four pairs of Teflon-coated stainless steel wires were tunneled towards the internal (flexor muscles) and external (extensor muscles) forearm via additional skin incisions in the upper arm and forearm. Each muscle of interest (**Appendix Table A.6**) was carefully freed from adhesions and identified using a bipolar stimulation pen (Fork probe, Inomed, CH) delivering pulses at 1 Hz in the range of one to eight volts. We inserted two 23G needles into the muscle belly to serve as guides for passing the wires. Recording electrodes were created by removing a small notch (~0.1 mm) in the insulation and functionality was verified by pulling the wires inside the muscle belly and delivering pulses. When correctly positioned within the muscle of interest, a single suture (Ethilon 4-0) was positioned around the wires at entry and exit locations from the muscle to secure the recording window in place. The remaining wires were subcutaneously secured in a stress-releasing loop, and the skin was closed using intradermal and external sutures.

Microfluidic system and TIMEs implantation

Microfluidic system and TIME electrode implantation Two custom-made TIME implants were inserted in the median and radial nerves according to previously described methods (Raspopovic et al., 2014; Wurth et al., 2017). The median electrode was placed ~2 cm proximally to the elbow, and the radial electrode was implanted ~2-3 cm proximally to the epicondyle along the humeral bone. Electrophysiological testing was performed intra-operatively to adjust the position of the electrode and verify that a single pulse of stimulation delivered through active sites located at the shaft extremities induced motor responses.

Access to the radial nerve was created through a 3-4 cm skin incision proximal to the elbow and along the humerus bone on the external upper arm at approximately 2 cm medial from the elbow crease. The brachialis and biceps brachii muscles were carefully separated, exposing first a superficial sensory nerve and deeper, below the brachioradialis attachment to the humerus, and adhering to the humerus the radial nerve. The nerve was then carefully freed from surrounding tissue and adhesions to free ~3-4cm of nerve for placement of the proximal microfluidic cuff and distal TIME. Both the cuff and the TIME were then tunneled subcutaneously towards the access of the nerve. The cuff was first folded around the nerve at the

most proximal space and secured in place using a medical grade staple (Premium Surgiclip™, Medtronic, EU) (**Figure 3.3**). The proximal tube was positioned in a small subcutaneous pocket and the device was flushed with saline to verify proper functioning of fluid delivery. Next, the TIME was positioned distally to the cuff. The nerve was carefully lifted using nerve hook and a Prolene 10-0 loop suture guide was used to penetrate the nerve. If more than one fascicle was observed through the slightly transparent epineural envelope of the nerve, care was taken to pierce through those fascicles during the penetration. The entire implant was then pulled through the nerve and fixed to the epineurium via the different fixation holes (**Figure 3.2** and **Figure 3.7 h**). Finally, the ceramic connecting piece was positioned along the nerve and equally sutured to the epineurium via the silicone anchoring wings. The remaining cable was subcutaneously tunneled to the back pocket and secured in place with a loose suture. The muscles were re sutured together and the overlying skin was closed using intradermal and external sutures. Access to the median nerve was created by making a 3-4 cm long skin incision medial to the biceps brachii muscle on the inner side of the upper arm starting at ~2 cm proximal to the elbow. Careful separation of both muscles exposed the deeply lying median nerve. Microfluidic cuff and TIMEs were subcutaneously tunneled to the created opening and implanted and secured as described above for the radial nerve.

3.3.5. Computational model

Implementation of Finite Element and biophysical models

We used histological cross-sections of the median nerve at different implantation levels to build a realistic finite element model (FEM) using previously described methodology (Capogrosso et al., 2013; Raspopovic et al., 2011). Implementation of the FEM model is detailed in **Figure 3.4** and Supplementary Information. Epineurium and fascicles geometries imported into COMSOL (Multiphysics v5.2a COMSOL, Burlington MA) were extruded longitudinally (10 mm). The TIME was modeled as an extruded rectangle (length: 4 mm, width: 120 μm , height: 11 μm) supporting eight cylinders on each side to represent the active sites (diameter: 80 μm , depth: 4 μm , interval: 540 μm). The electrode was placed transversally in the nerve such as to penetrate a maximum number of fascicles. Each structure was assigned with an electrical conductivity tensor value, reported in **Appendix Table A.5**. The finite element method was used to solve the resulting system of differential equations by generating a discrete tridimensional mesh of ~2 million tetrahedral elements. The neurophysiological models of motor fibers were implemented in anaconda 2.7.14 (The Python Software Foundation), using NEURON v7.4 to solve the membrane dynamics. To represent the dynamics of each nerve fiber, we used the McIntyre Richardson Grill model (Capogrosso et al., 2013; Capogrosso, Gandar, et al., 2018; McIntyre and Grill, 2000; McIntyre et al., 2002). The biophysical properties of the fiber compartments were derived from previous work (Raspopovic et al., 2011; Raspopovic et al., 2017; Romeni et al., 2020). Axon diameters were uniformly sampled from a log-norm distribution (Greiner et al., 2020) ($\mu = 14 \mu\text{m}$, $\sigma = 4 \mu\text{m}$). Each fiber of diameter D was composed of 11 Nodes of Ranvier with an intermodal length $L = 100D$. Because the anatomical organization of motor fibers in the

arm nerves is unknown, we hypothesized that fibers innervating the same muscle were placed in close proximity within the nerve. We modelled a total of 11 fibers populations per cross section. Each muscle was innervated by 50 fibers, positioned in a single fascicle, randomly displaced within one of the fascicle quadrants or hemisphere, resulting in partially overlapping distributions (**Figure 3.4** and **Figure 3.7 d**). A small fascicle ($D < 500 \mu\text{m}$) received fibers of one muscle, a medium fascicle ($500 \mu\text{m} < D < 1000 \mu\text{m}$) innervated three different muscles, and a large fascicle contained five efferent fibers populations. The FEM and biophysical model were merged into a hybrid model. Electrical potentials generated inside the FEM structure were interpolated on the positions of the nodes of Ranvier and paranodes compartments.

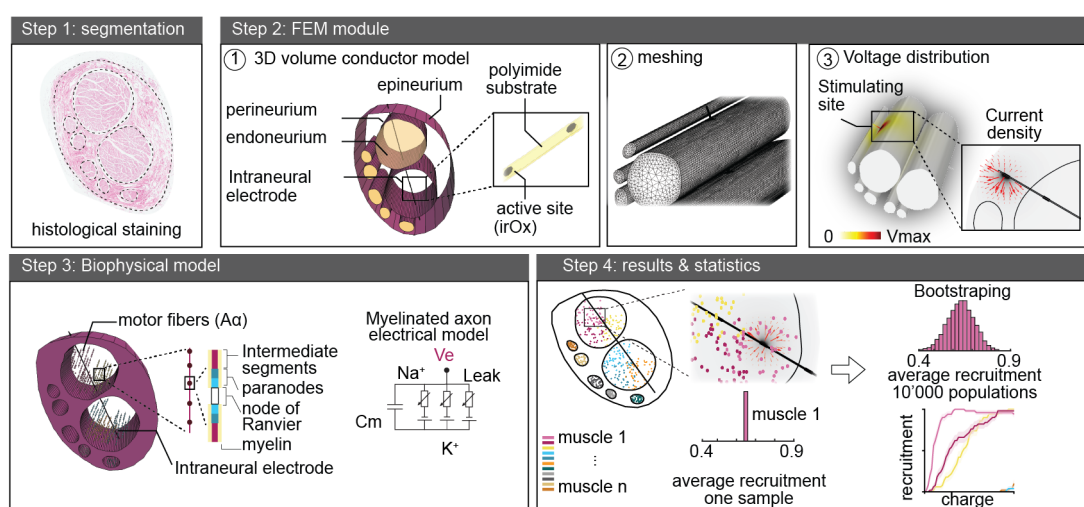


Figure 3.4 – Design of a realistic model of intraneural stimulation in the monkey median nerve Step by step implementation of a hybrid computational model of the monkey median nerve. Step 1: Selection of a histological cross section of the median nerve, segmentation and importation into the modelling software (Multiphysics v5.2a COMSOL, USA). Step 2: (1) Extrusion of the 2D neural geometry and implementation of an anatomically realistic finite element model (FEM) that recapitulates all nerve compartments and TIME elements with their associated dimensions and electrical properties. (2) Meshing of the resulting 3D volume conductor to solve differential equations governing the distribution of electric potential. (3) Modeling of the injected charge ($Q=4 \text{ nC}$) and computation of the resulting voltage variation for each active site of the electrode. Step 3: Implementation of a biophysical model of myelinated axons that simulates α -motor fibers populating the fascicles (see Methods). Step 4: bootstrapping of the fiber populations to apply statistical analysis. Each one of the population innervating the n muscles is resampled with replacement.

Simulated recruitment curves and selectivity analysis

We computed recruitment curves for individual motor fibers during $40 \mu\text{s}$ -long square pulses of monopolar cathodic stimulation at increasing amplitudes. We considered a fiber to be recruited if an action potential travelled along its whole length. Recruitment curves, activation and saturation amplitude, and selectivity indices were computed based on a bootstrap analysis of simulated fibers (Greiner et al., 2020). Resulting boxplot distributions were thus derived from bootstrapped samples ($n= 10'000$ populations per muscle). To compare the specificity of

stimulation at different locations along the nerve, we computed the selectivity index (SI) as:

$$SI_p = REC_p - \frac{\sum_{n \neq p}^P REC_n}{P - 1} \quad (3.1)$$

where p is the muscle of interest, P the total number of innervated muscles, and REC_p and REC_n the normalized recruitment level of muscle p and n , respectively. The SI was computed for every active site, amplitude steps (from 20 μ A to 2 mA, steps of 100 μ A), muscles, and bootstrapped populations. Except when analyzing activation and saturation thresholds or SIs along the electrode, we considered only the channel and current step producing the highest average SI for each muscle.

Simulated recruitment curves were computed as the number of activated fibers normalized by the total number of fibers within the population for each current step. Standard deviations represented the variance over bootstrapped populations for each recruited muscle. The pie charts displayed in **Figure 3.7 d** were constructed by computing the number of muscles recruited with a SI higher than 0.85 for each bootstrapped population and compiling the proportions over the total number of observations (i.e. over 10'000 bootstrapped samples). The distribution of selectivity indices (SIs) for each muscle are summarized in **Figure 3.7 f**. Selectivity polar plots in **Figure 3.9 b** represent the maximum average SI obtained for each muscle at the three implantation levels, L1, L2 and L3. Histograms in **Figure 3.9 c** were derived by taking the mean distribution of SIs over all 11 simulated muscles ($n=10'000$ bootstrapped samples) for each implantation level. The mean intrafascicular selectivity (**Figure 3.9 c**, right) was computed by taking the mean SI of each muscle over all the bootstrapped populations and sub-selecting only the muscles located in a fascicle traversed by an active site. To evaluate the selectivity along the TIME implant, we computed the maximum SI by taking the average SI over the bootstrapped populations for each muscle and then selected the maximum value obtained. Graphs in **Figure 3.9 d** report the results derived for each active site, on the two sides of the implant shaft, at each implantation level. Activation and saturation thresholds were defined as the current amplitudes at which 20% and 75% of the fibers were recruited respectively. They were computed for each muscle at level L2 ($n=10'000$ bootstrapped population per muscle) and plotted in **Figure 3.7 g** and **Figure 3.9 e**.

3.3.6. Electrophysiology

Electrical stimuli were delivered as charge-balanced cathodic-first biphasic pulses through a 32-channels headstage (LP32CH - 32, Tucker Davis Technologies, USA) using a medical grade stimulator (IZ2H, Tucker Davis Technologies, USA). Stimulation waveforms were digitally built within the processor unit (RZ2, Tucker Davis Technologies, USA) using the user programming interface OpenEx suite (Tucker Davis Technologies, USA). Custom-written routines were used to communicate with the controller through matlab (Matlab, The MathWorks Inc, MA) or C++ (Visual Studio®, USA) API.

3.3.7. Data acquisition

During behavioral recordings preceding the TIME implantation and during awake functional TIME mapping experiments, hand and arm kinematics was recorded at 100Hz using a 14-camera motion capture system (Vicon, Oxford, UK). Markers were placed on the elbow, wrist, and on the metacarpophalangeal (MCP), proximal interphalangeal (PIP) and distal interphalangeal (DIP) joints of the thumb, index, middle and pinkie fingers. During anesthetized mapping, kinematics were recorded using up to six high definition cameras covering all the hand angles (25 to 60 Hz). For awake experiments performed after the TIME implantation, kinematics was recorded using three high definition cameras covering the task space (25 to 100 Hz). Bipolar EMG were acquired at 12kHz through the RZ2 processor (RZ2, Tucker David Technologies, USA) after amplification (1000×, PZ5, Tucker David Technologies, USA) using a 16-channels active headstage (LP32CH - 16, Tucker Davis Technologies, USA). Grip pressure was measured for different grip shapes (cylinder, sphere and pinch) using a custom-made sensor⁴⁹, and wrist torque was acquired using a commercial dual-range force sensor¹) (Vernier, EducaTEC AG, CH). Pressure and force signals were saved at 1 kHz. Neural signals were acquired with a Neural Signal Processor (Blackrock Microsystems, USA) using the Cereplex-E headstage with a sampling frequency of 30 kHz. The different acquisition systems were synchronized using stimulation triggers during electrophysiology experiments and through digital triggers marking the different task events during behavioral recordings (see chapter 2 and Barra et al., 2019). **Figure 3.6** illustrates the entire data acquisition and stimulation setup used in the behavioral functional task.

3.3.8. Selectivity of muscle recruitment

Muscles recruitment curves

Recruitment curves (n=5 acute and 2 chronic experiments, **Appendix Table A.6**) were performed by delivering biphasic cathodic-first current pulses (1 Hz) of 40 or 80 μ s duration at increasing current intensities ranging from sub-threshold to saturation of the compound muscle action potential (CMAP) (Raspopovic et al., 2012; Wurth et al., 2017). EMG activity was filtered online (50 Hz Notch, 10–5000 Hz bandpass). For every channel, four repetitions of each current step were performed and the average peak-to-peak amplitude of the evoked CMAP of each muscle was used to analyze the relationship between stimulation-evoked muscle activity and stimulation intensity. The recorded CMAPs were normalized to their maximal amplitude obtained throughout the experiment for each muscle.

¹Dual-Range Force Sensor User Manual – Vernier. <https://www.vernier.com/manuals/DFS-BTA>

In vivo selectivity analysis

The selectivity for every muscle and each charge injection step was assessed by calculating its SI as previously described (Raspopovic et al., 2011):

$$SI_m = CMAP_m - \frac{\sum_{n \neq m}^M CMAP_n}{M - 1} \quad (3.2)$$

where SI_m describes the SI for axonal recruitment of the m^{th} muscle in a set of M different muscles. $CMAP_m$ is the normalized CMAP of the m^{th} muscle for a certain amplitude and pulsewidth. SI_m is comprised between -1 and 1, where 1 corresponds to the complete activation of the m^{th} muscle without any activation of the others; while -1 reflects to complete activation of all the muscle except muscle m .

The final selectivity for each muscle was computed as the maximum selectivity achieved across contacts and range of charges injected. The functional SI was calculated by grouping muscles according to their function, namely wrist flexion (FCR, and PL), wrist extension (ECR, ECU), fingers flexion (FDS, FDP, and FDI), fingers extension (EDC), thumb opposition (APB), and thumb extension (APL) and computing the highest SI within each group.

Electrode stability analysis

We assessed functional stability of the chronic implants by computing the weekly threshold charge as well as the weekly functional SI for each of the six functional muscle groups (see previous paragraph). Implant integrity was assessed by counting the number of functional contacts, defined as contacts eliciting visible movement for a charge inferior to 100 nC, and normalizing them to the first measurement day.

3.3.9. Functional hand movements characterization

Experiments in awake and anesthetized monkeys

Functional and force modulation experiments were performed in awake or anesthetized conditions. In the awake paradigm, the animal was sitting in a chair, slightly sedated (ketamine 3.5 mg kg⁻¹, NaCl 1:1, 0.1mL/15min) while in the anesthetized condition, the animal received an intravenous perfusion of propofol (0.2-1.7 ml/kg/h) and vitals were continuously monitored. In both cases, the forearm was fixed on an arm rest, leaving the hand visible from all directions to record kinematics and/or kinetic signals.

Functional mapping

The characterization of the functional movements elicited through stimulation was done by delivering 500 to 1000 ms bursts (frequency 50 Hz, pulse width 40 or 80 μ s) at different amplitudes. Channels of the median and radial nerves electrodes were mapped individually.

Force modulation

The effects of stimulation amplitude or frequency on the generated wrist force and grip pressure was assessed by modulating one of these two parameters at a time, on individual stimulation channels. Sine-wave modulation was delivered between a minimum and a maximum amplitude or frequency value with a 1 to 2-second period. The amplitude range depended on the active site and the frequency range was set between 40 and 100 Hz. Each trial lasted approximately 10 seconds. Bimodal force modulation was achieved by alternatively stimulating the median and radial nerve with a sinusoidal amplitude wave of 2 seconds-period and a phase shift of 90° (**Figure 3.14**). Fatigue experiments consisted in 20 seconds of tonic bursts at 50 Hz on one single channel.

EMG bursts analysis

EMG signals were band-pass filtered offline (50-500 Hz). In case of stimulation-evoked activity, a Savitzky-Golay filter (2.5 ms smoothing window) was applied to remove stimulation artefacts. The envelope was computed by rectifying the EMG and applying a low-pass filter at 6 Hz. Signals were normalized to the maximal muscle activity obtained across the trials of interest and interpolated when trials differed in length.

Hand kinematics analysis

Post-processing of kinematic data was performed to ensure that joint markers were properly labelled. For movements recorded under anesthetized condition (Mk- Me_a and Mk- Ol_a), 2D kinematics of each finger was extracted manually from single camera frames using a custom-built matlab routine (Matlab, The MathWorks Inc, MA). We converted the 3D marker position data to rotational degrees of freedom and computed joint angles and distances separating fingers during median and radial nerve stimulation (**Appendix Table A.7** and **Appendix Table A.8**). Stimulation intensities eliciting similar range of motion were pooled together. Computation of the kinematic angles from 3D recordings were performed as described in chapter 2. Middle finger kinematic angles were computed as for the index and pinkie fingers. Computations of angles based on 2D video recordings in anesthetized experiments were adapted to account for the position of the hand on the video recordings of interest. Calculations are summarized in **Appendix Table A.7** and **Appendix Table A.8**, and data used for each panel of **Figure 3.12** is specified in **Appendix Table A.9**.

Kinematic features were low-pass filtered at 10Hz and the mean value recorded at maximum movement amplitude (~100 ms window) was subtracted to the value at rest (~100 ms window before stimulation) to derive the scatter plots in **Figure 3.12 c,i** and **Figure 3.13 d**. Outliers falling outside the 25th - 75th percentiles range were excluded. We applied principal component analysis (PCA) on normalized grip kinematic features from all three monkeys and computed the 3D inter- and intra-individual Mahalanobis distance by pooling together the distances obtained between PCA clusters representing different grips of the same animal and identical grips from different animals respectively.

Grip force analysis

Data were low-pass filtered at 5 Hz. To determine the relationship between force and stimulation parameters, force levels elicited at the same amplitude or frequency value were averaged. Amplitude and frequency modulation strategies were compared in terms of i) generated range of force, computed as the peak-to-peak of the force, and ii) induced fatigue, expressed as the difference between the first and the last peaks of the force over 10 seconds of sine-wave stimulation. The difference between the two modulation approaches was examined by pairwise comparing trials with the same force sensor and the same active site. The grip pressure levels corresponding to the maxima of the amplitude sinusoidal wave were compared with natural levels of force exerted by a monkey during a voluntary grasping task (chapter 2 and Barra et al., 2019). Specifically, we compared the force peaks generated by the active site best evoking a certain type of grasp, to the voluntary exerted pressure on the same grip sensor shape (sphere, cylinder or pinch). We quantified the change in selectivity when modulating the stimulation charge by evaluating: i) the charge threshold at which movement was distinguishable, ii) the charge threshold for which we measured functional force levels. For the two conditions we computed the sum of SIs for muscles having a positive SI at condition i). We then subtracted the the sum obtained at condition ii) from the sum obtained at condition i) and performed a one-sample t-test on the total distribution. Voltage values were converted in Newton using calibration curves (Barra et al., 2019, chapter 2, and ²).

The amount of fatigue induced by tonic stimulation was assessed using two measures, namely the difference between the maximal force and the force at the end of the 20 seconds of stimulation normalized to the maximum and the time necessary for the force to decrease of 10

3.3.10. Design and analysis of brain activity-driven TIME stimulation

Neural modes coefficients matrix computation

M1 multiunit activity was recorded in Mk-*Ol_c* performing a reaching and pulling task, as previously described in chapter 2. The task consisted in reaching for, grasping and pulling an object mounted on a haptic robot (KUKA iiwa 7, KUKA AG, DE). In our case, the monkey was

²Dual-Range Force Sensor User Manual – Vernier. <https://www.vernier.com/manuals/DFS-BTA>

presented with cylindrical, spherical and pinch-like objects. Multiunit M1 cortical activity was bandpass-filtered (750 to 5000 Hz) and thresholded ($-6.25 \times \text{root mean square value}$) to extract spike events. The firing rate was computed for each channel from 10 ms bins and principal component (PC) analysis was applied on all channels to derive the "neural modes coefficient matrix" (Gallego et al., 2017) U such as:

$$y = U^T x \quad (3.3)$$

Where U represents the main neural modes, x corresponds to the centered neural firing rates of the 48 M1 channels and y to the representations of x in the principal component space. Firing rates recorded on channels implanted in S1 and PMv area were set to 0 before dimensionality reduction.

We projected the neural activity into the newly derived cortical manifold space to assess cross-correlation with hand kinematics and compute modulation depth along each PC (see PC modulation analysis paragraph, and **Figure 3.17 d**). The "neural modes coefficients matrix" computed over one session (17 weeks before TIME implantation) was kept constant and used as linear transformation between firing rates and cortical activity along the main PCs in subsequent experimental sessions (**Figure 3.5**).

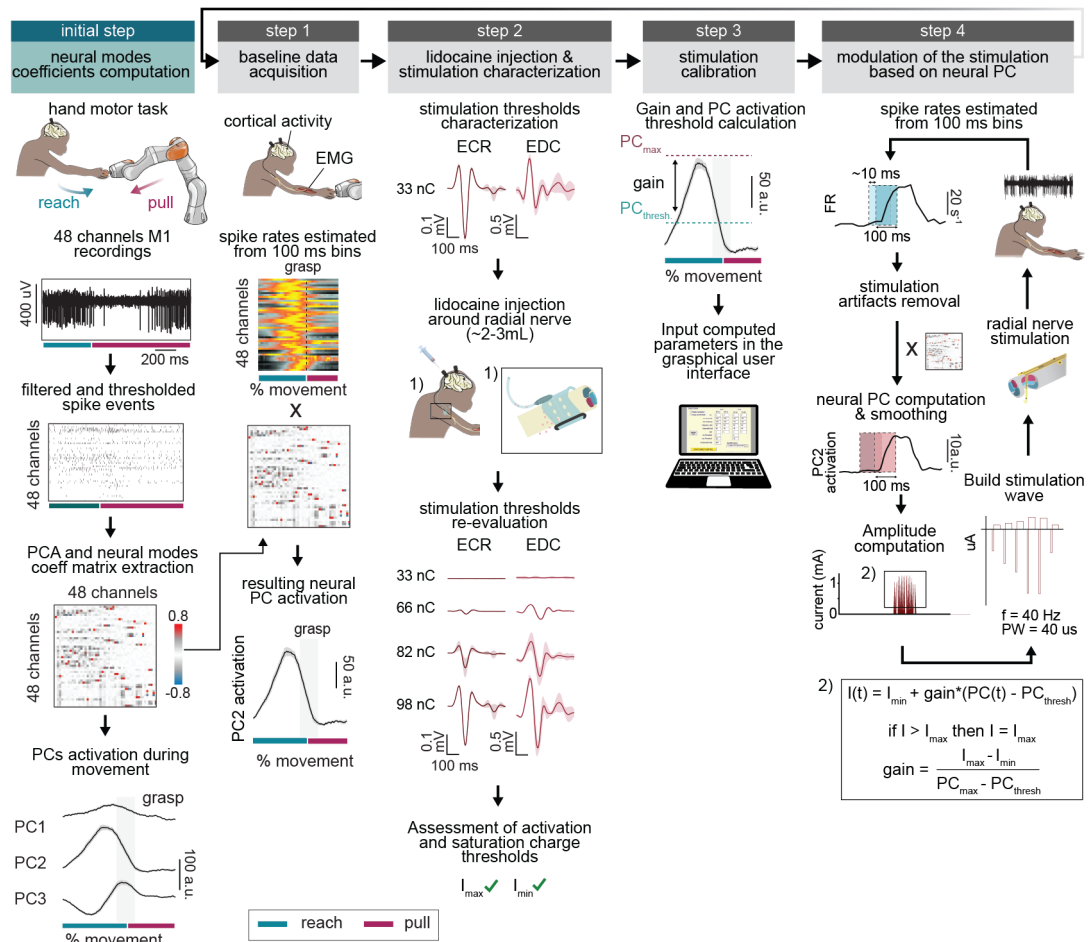


Figure 3.5 – (Continued on the following page.)

Experimental paradigm for the brain-controlled stimulation of the radial nerve. Initial step: This step consisted in computing the neural modes coefficient matrix for behavioral data and was performed only once, prior to TIME implantation (17 weeks before implantation). M1 multiunit activity was recorded while the monkey reached for an object presented by a robotic arm, and pulled it towards a spatial threshold. Cortical activity was bandpass-filtered (750 to 5000 Hz) and thresholded ($-6.25 \times$ root mean square value) to extract spike events. The firing rate was computed for each channel from 10 ms bins and principal component (PC) analysis was applied on all channels to derive the coefficient matrix representing the main neural modes. The average activation along the three first PCs during the movement is shown (Mk- Ol_c n= 54 trials). Reach and pull phase are highlighted in teal and pink colors respectively. The next steps recapitulate the procedure followed for each brain-controlled stimulation experiment. Step 1: during baseline trials, M1 activity was recorded and processed as previously, and the spike rates were estimated from overlapping 100-ms bins, updated every 10 ms. The matrix containing spiking activity from every channel was then projected on to the previously computed neural modes coefficients matrix to derive the neural activation along each PC during the movement. Step 2: stimulation thresholds were assessed by stimulating the radial nerve on a single TIME channel prior to paralysis. A solution of lidocaine was then injected into the microfluidic cuff implanted around the radial nerve to trigger temporary blockage of the nerve conduction. Stimulation thresholds were immediately re-evaluated after injection and new functional amplitude ranges were inferred (I_{min} and I_{max}). Step 3: The average activation along the 2nd PC measured during baseline trials was used together with I_{min} and I_{max} values to calibrate the computation of the amplitude of stimulation. Inset 2) depicts the amplitude calculation based on the minimum and maximum stimulation amplitudes (I_{min} and I_{max}), the maximum PC activation recorded (PC_{max}) and the PC level at which stimulation must be triggered ($PC_{thresh} = \sim 0.2 PC_{max}$). Step 4: This step summarizes the online brain-based control of stimulation during the functional task. Continuous multiunit activity was recorded in the monkey reaching for the object after paralysis of the radial nerve. Spike rates were derived as in previous steps, and projected onto the neural modes coefficient matrix to derive PC activations. PC2 signal was used to drive the stimulation amplitude in real time during the trial duration. Stimulation of the radial nerve electrode was delivered as cathodic charge-balanced pulses at 40 Hz through one channel eliciting wrist and fingers extension. Stimulation artefacts were removed to avoid perturbing the amplitude computation (see Methods). Shaded lines: s.e.m - a.u: arbitrary units. Abbreviations: principal component (PC), principal component analysis (PCA), pulse width (PW) extensor carpi radialis (ECR), extensor digitorum communis (EDC).

Brain-controlled stimulation of extension

Experimental steps are illustrated in **Figure 3.5**. The experiment started with the acquisition of baseline trials in which M1 cortical activity was recorded and processed as described in the previous paragraph. The behavioral task was the same as described above except that only the cylindrical object was used, and was positioned slightly above the animal eye level to promote extension of the hand during the movement. The matrix containing spiking activity from every channel was projected onto the previously computed “neural modes coefficients matrix” to derive the average neural activation along the second principal component (PC2) during the movement. Threshold for intraneural recruitment were assessed by stimulating the radial nerve on a single TIME channel prior to paralysis. A solution of lidocaine (Lidocaine 2% / epinephrine 1:100 00, ~2-5 ml) was then injected into the cuff implanted around the radial

nerve to trigger temporary blockage of the nerve conduction. Stimulation thresholds were immediately re-evaluated after injection and new functional amplitude ranges were inferred, namely I_{min} and I_{max} . The algorithm computing the amplitude of stimulation in real time was calibrated based on the average activation along PC2 measured during baseline trials together with I_{min} and I_{max} values. More precisely, the amplitude at time t was computed as:

$$I(t) = I_{min} + gain * (PC(t) - PC_{thresh})$$

$$gain = \frac{I_{max} - I_{min}}{PC_{max} - PC_{thresh}} \quad (3.4)$$

$$if I > I_{max}, I = I_{max}$$

I_{min} corresponded to the minimum amplitude at which movement twitch appeared, I_{max} was defined as the amplitude at which strong contraction movement was observed, PC_{max} corresponded to the maximum PC2 activation measured during baseline trials and PC_{thresh} represented 20% of PC_{max} .

After the calibration, multiunit activity was recorded continuously in the monkey reaching for the object after paralysis of the radial nerve. Spike rates were derived as in previous steps, and projected onto the “neural modes coefficient matrix” to derive PC activations. PC2 signal was used to drive the stimulation amplitude in real time during the trial duration. Stimulation was disabled upon trial termination (**Figure 3.6**).

Artifact removal

We removed stimulation artifacts in neural recordings by subtracting from each channel the number of spike events recorded in a reference channel found to be silent outside stimulation bursts. Movement artifacts were suppressed by ensuring that if more than 40 channels displayed a firing rate superior to 20 spikes/s, these channels were discarded.

Performance analysis in functional extension task

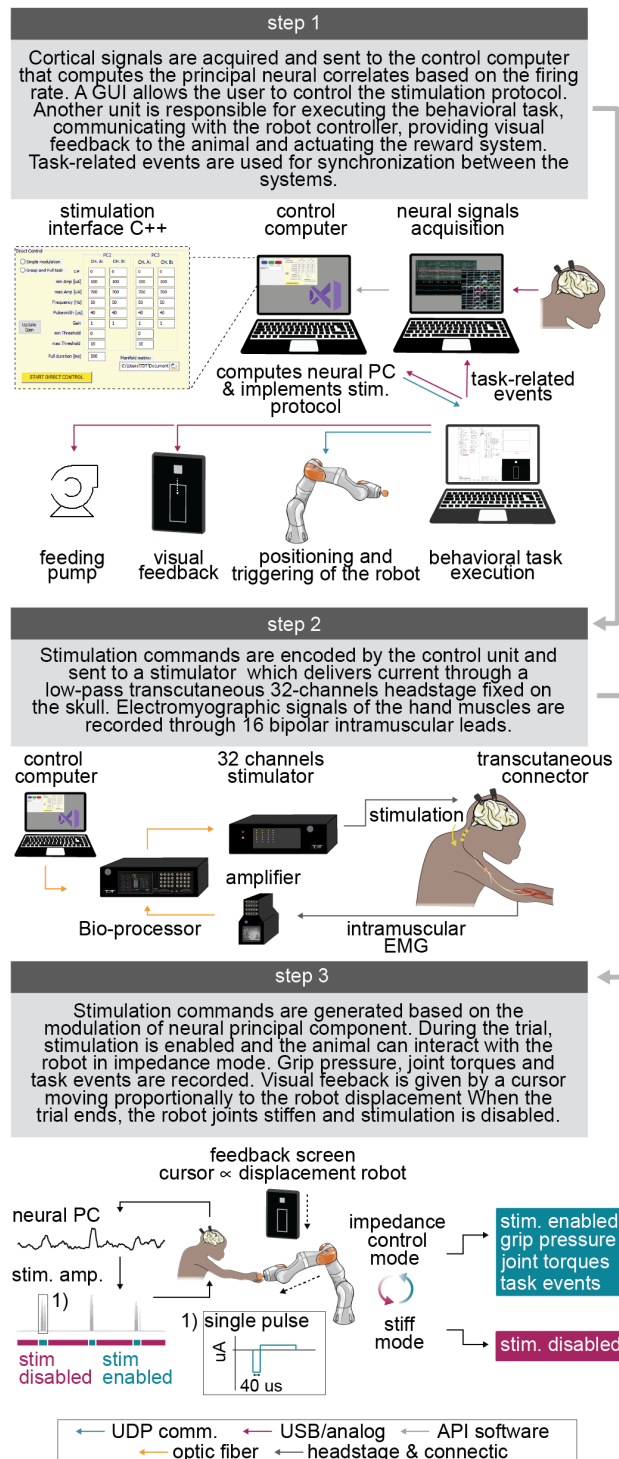
Two experimental sessions were analyzed and trials were counted in three categories: i) dexterous reach, with no disruption of movement, ii) imprecise reach, completed task with bumpy, less smooth trajectory and iii) fail (**Figure 3.17 a** and **Supp. Video 3.3**). Success rates with and without stimulation were compared using bootstrap analysis (100 000 samples, with replacement). Hand kinematics were tracked using the DeepLabCut software (Mathis et al., 2018). Planar shoulder, elbow and wrist coordinates from the top and lateral view were fitted with piecewise cubic Hermite interpolating polynomials to calculate wrist extension and elbow flexion joint angles. Angles were low-pass filtered at 5 Hz and interpolated between the

Figure 3.6 – Experimental setup for brain controlled-stimulation of the peripheral nerve.

Step 1: the cerebus central suite (Blackrock Microsystems, USA) is used to acquire and process neural signals from M1 brain region during the behavioral task. The control computer reads the incoming spike events and computes the neural principal components (PCs) through a C++ custom-written program. It also implements the stimulation protocols based on settings inputted by the experimenter through a graphical user interface. The behavioral task paradigm is controlled through an independent computer program (Matlab, The MathWorks Inc, MA), which instructs the robot positions and actions, provides visual feedback on a screen during the task, and delivers reward through a peristaltic pump (masterflex®consolodrive). Neural PCs calculated by the control computer are sent to the behavioral program and recorded along with task events in the cerebus central suite.

Step 2: The control computer digitally builds stimulation waveforms and send them to a 32-channel stimulator via a bio-processor unit. Stimulation is delivered to the animal through a wired headstage. EMG activity is recorded using intramuscular leads, then amplified (x1000) and stored.

Step 3: The stimulation amplitude is continuously modulated based on the 2nd neural PC activation calculated from the neural firing rate (**Figure 3.5**). The shape of a single charge balanced cathodic pulse is shown in the inset 1). During the trial, the stimulation is enabled and the animal can interact with the robot in impedance control mode. The task consists in reaching and pulling on an object attached to the robotic arm. The cursor displayed on a screen in front of the animal moves proportionally to the displacement of the robot and informs the monkey on the degree of completion of the task. When a trial ends, the robot joints stiffen, the cursor disappears and the stimulation is disabled. Teal and pink colors are used to highlight the intra- and inter-trial periods respectively. Communication protocols between devices are summarized with color-coded arrows (see legend). Screenshots, copyright Blackrock Microsystems©(2020) and Tucker-Davis Technologies©(2020).



start and the end of the reach. These events were automatically detected based on the wrist coordinates. Wrist extension and elbow flexion values over the last 60% of the reaching phase were extracted for the three conditions: baseline, stimulation OFF and stimulation ON, to account for small variations in starting position. Wrist angles and elbow angles falling outside the $[-90^\circ, 90^\circ]$, and $[0^\circ, 180^\circ]$ range respectively, were excluded.

Interjoints coordination was assessed by evaluating the wrist-elbow angles relationship (Cirstea et al., 2003), and compared across conditions by computing the Mahalanobis distance between the baseline distribution of points at time t and the corresponding point in time for another condition. Results were averaged across the movement. EMG envelopes were computed after bandpass-filtering (50-500 Hz), rectifying and low pass filtering (10 Hz) the signals recorded in successful trials (dexterous and imprecise reaches). Envelopes were interpolated between the start and the end of the trial and normalized. Muscles were grouped according to their function, namely wrist extensor (ECR, ECU), and finger extensors (EDC and APL), and the area under the curve was computed.

Neural principal components (PCs) modulation analysis

We projected the multiunit neural activity (firing rates calculated from 10 ms bins) recorded on one day into the fixed cortical manifold space defined by our “neural modes coefficients matrix”. We then assessed the cross-correlation between the cortical activity projected along each neural mode (PC of the space) and the velocity of the wrist. The wrist marker trajectory was smoothed with a moving average window of 100 ms. Then the wrist velocity was computed as the speed of the wrist marker component parallel to the reaching movement. The wrist velocity profile was smoothed (moving average window of 100 ms) and cross-correlated with the activation along the three first principal components (moving average window of 100 ms) between the start and the end of the movement. The cross-correlation was calculated using the matlab (Matlab, The MathWorks Inc, MA) function `xcorr` with the normalization option ‘normalized’. The signals were z-scored before calculating the cross-correlation in order to eliminate effects coming from scale and offset differences. The cross-correlation for lags in the range $[-200 \text{ ms } 0 \text{ ms}]$ (wrist velocity shifted backwards in time with respect to the neural principal component) was analyzed and the maximum cross-correlation index was reported in **Figure 3.17 e-f**.

The modulation depth was also evaluated along each PC component. The PC activation waveform was additionally smoothed with a moving average window of 50 ms and modulation depth was computed as the difference between the maximum value of activation between the start and the end of the trial and the average value measured during the rest period. The latter was defined as the 50 ms window following the start of the trial.

3.3.11. Lidocaine microfluidic system characterization

The acute characterization of the lidocaine microfluidic system (**Figure 3.15**) was done by delivering 3 ml of anesthetic (Lidocaine 2% / epinephrine 1:100 00) around the exposed median nerve (Mk-Lo, anesthetized, **Appendix Table A.4**). CMAPs of the flexor digitorum superficialis (FDS) were measured after delivering bipolar stimulation (frequency 1 Hz, in the range of 1 to 3 volts, pulse width 200 μ s, Micro fork probe, Inomed, CH) at the surface of the nerve proximally and distally to the microfluidic cuff. The TIME activation charge was computed as the charge necessary for the TIME implant inserted proximally to the cuff to recruit 10% of the FDS (1 Hz, 4 repetitions per charge level). Chronic characterization of the microfluidic system implanted on the radial nerve of (Mk- Ol_c) was performed in an awake animal after injection of 2-5 ml of anesthetic and charge was ramped (frequency 50 Hz) until prominent movement could be observed post-injection.

3.3.12. Statistics

All computed parameters were quantified and compared between tested groups unless otherwise specified. All data are reported as mean \pm s.e.m unless specified otherwise. When bootstrap was applied, significance was analyzed using a one sample two-sided t-test on the distribution of mean $\mu = \mu_1 - \mu_2$ and $\sigma = \frac{\sqrt{(\sigma_1 + \sigma_2)}}{2}$ without correcting for sample size. When performing unpaired comparisons, significance was evaluated using non-parametric Kruskal-Wallis test with Bonferroni correction for multiple comparison. For paired comparisons, the Wilcoxon signed-rank test was used.

3.4. Results

3.4.1. Design of a tailored intrafascicular interface for arm nerves in monkeys

Selective TIME stimulation relies on the identification of an optimal intrafascicular implantation site as well as a tailored implant design to target the different fascicles containing motor fibers Delgado-Martínez et al., 2016. Therefore, we performed a detailed anatomical study (**Figure 3.1** and **Figure 3.7 a**) of monkey's median and radial nerves that constitute the main innervation routes for hand flexor and extensor muscles respectively (Brushart, 1991; Marin et al., 2009). Dissection of monkey arms (n=3 animals) enabled us to precisely identify the branching points of the motor fibers innervating these muscles (**Figure 3.7 a** and **Figure 3.8 d**).

In all monkeys, the median and radial ramifications innervating muscles of the wrist and the hand emerged from the main nerve trunk distal to the elbow. To determine the optimal implantation site for the TIME, we quantified the number and cross-sectional area of the fascicles constituting the nerve at different levels proximal to the elbow (n=6 animals, **Figure 3.1** and **Figure 3.7 a**). Our analysis showed the presence of one to two larger-diameter fascicles accompanied by one or several smaller-diameter fascicles in nerve segments harvested 3 cm proximal to the epicondyle (L1 segment). More distal nerve portions, namely L2 and L3, were characterized by a gradually increasing number of progressively smaller fascicles (**Figure 3.7 b** and **Figure 3.8 a,e,f**). Immunohistochemical labeling of ChAT positive motor axons revealed a heterogeneous distribution of efferent fibers within each of the larger fascicles. Motor fibers were found to be organized in patches, dispersed throughout many fascicles and some were located deep within the fascicular compartments (**Figure 3.7 c**). Those anatomical features were generally conserved across animals (**Figure 3.8 b,c,g-i**).

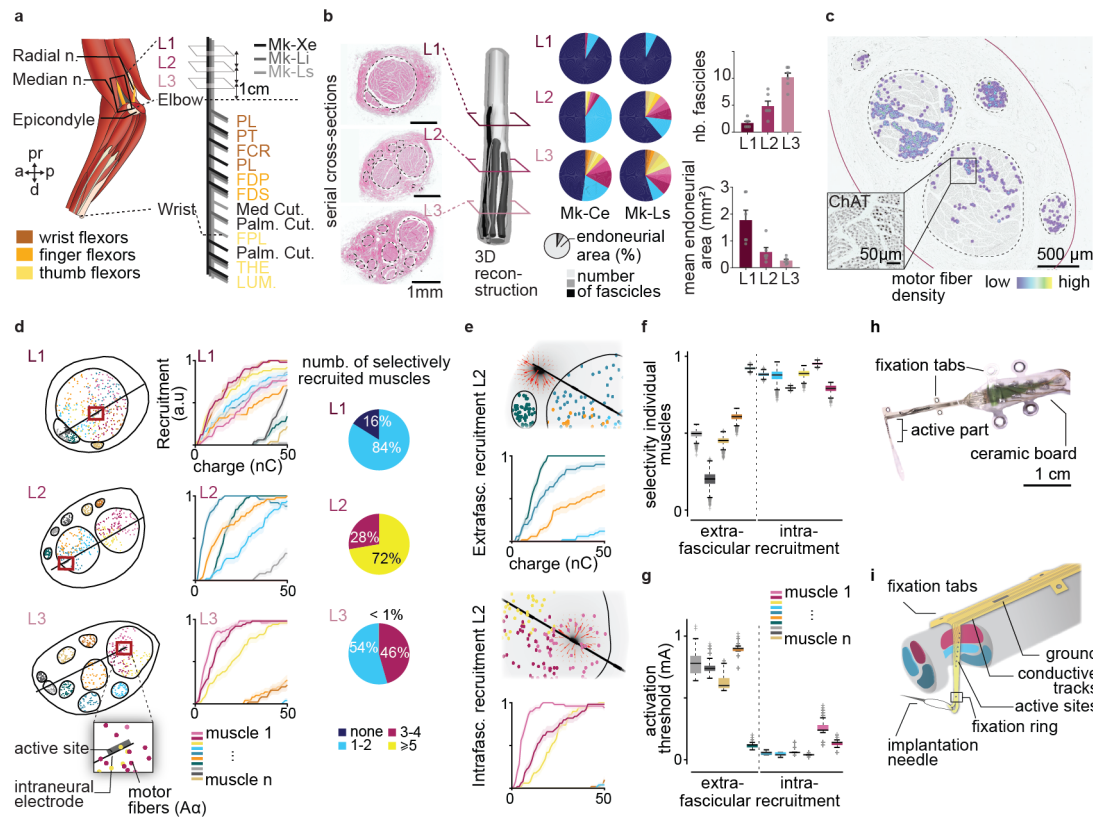


Figure 3.7 – Development of an intraneural implant for selective arm nerve stimulation in monkey. (a) Left: access to median and radial nerves in the upper-arm of the macaque monkey (a=anterior; pr=proximal; p=posterior and d=distal). Right: Tracking of branches originating from the median nerve to target flexor muscles (n=3 animals). (b) Left: Neural fascicular content in serial H&E-stained cross-sections at levels L1, L2, and L3 (3, 2 and 1 cm proximal to the epicondyle) along the nerve and resulting 3D reconstruction of fascicular organization proximal to the elbow (one representative animal). Middle: Number of fascicles and their respective cross-sectional area at each level (two representative animals, different colors represent different fascicles). Right: Quantification of number of fascicles and mean endoneurial area per fascicle at each level (n=6 animals). (c) Example of motor axons distribution in the median nerve, overlaid color map represents motor fibers density over the cross-section. Inset: zoomed-in portion of fascicle with ChAT-labelled motor fibers (black, no overlay). (d) Left: Computationally-modelled motor fiber distributions at levels L1, L2, and L3 of the median nerve; different fiber populations assumed to innervate different muscles are color-coded. Middle: Simulated recruitment of motor fibers for each implantation level. Right: Quantification of number of selectively recruited muscles (SI ≤ 0.85) over the entire simulated fibers dataset. (e) Electric currents and motor fiber recruitment generated by simulated extrafascicular and intrafascicular stimulation at level L2. (f) Maximal SI of individual muscles for simulated extra- and intra- fascicular recruitment of motor fibers at level. (g) Activation threshold (10% recruitment) for simulated extra- and intra- fascicular recruitment. (h) Photograph of a micro-fabricated transverse intraneural multichannel electrode (TIME). (i) Placement of the electrode array transversally inside the nerve. Error bars: s.e.m - Shaded lines: s.t.d - Boxplot distribution: median with 25th and 75th percentiles - a.u.: arbitrary units. Abbreviations: Hemotoxylin & eosin (H&E), Choline acetyltransferase (ChAT), palmaris longus (PL), flexor carpi radialis (FCR), flexor digitorum superficialis (FDS), flexor digitorum profundus (FDP), flexor pollicis longus (FPL), thenar eminence (THE), lumbricals (LUM), median cutaneous branch (Med. cut.), palmar cutaneous branch (Palm. cut.).

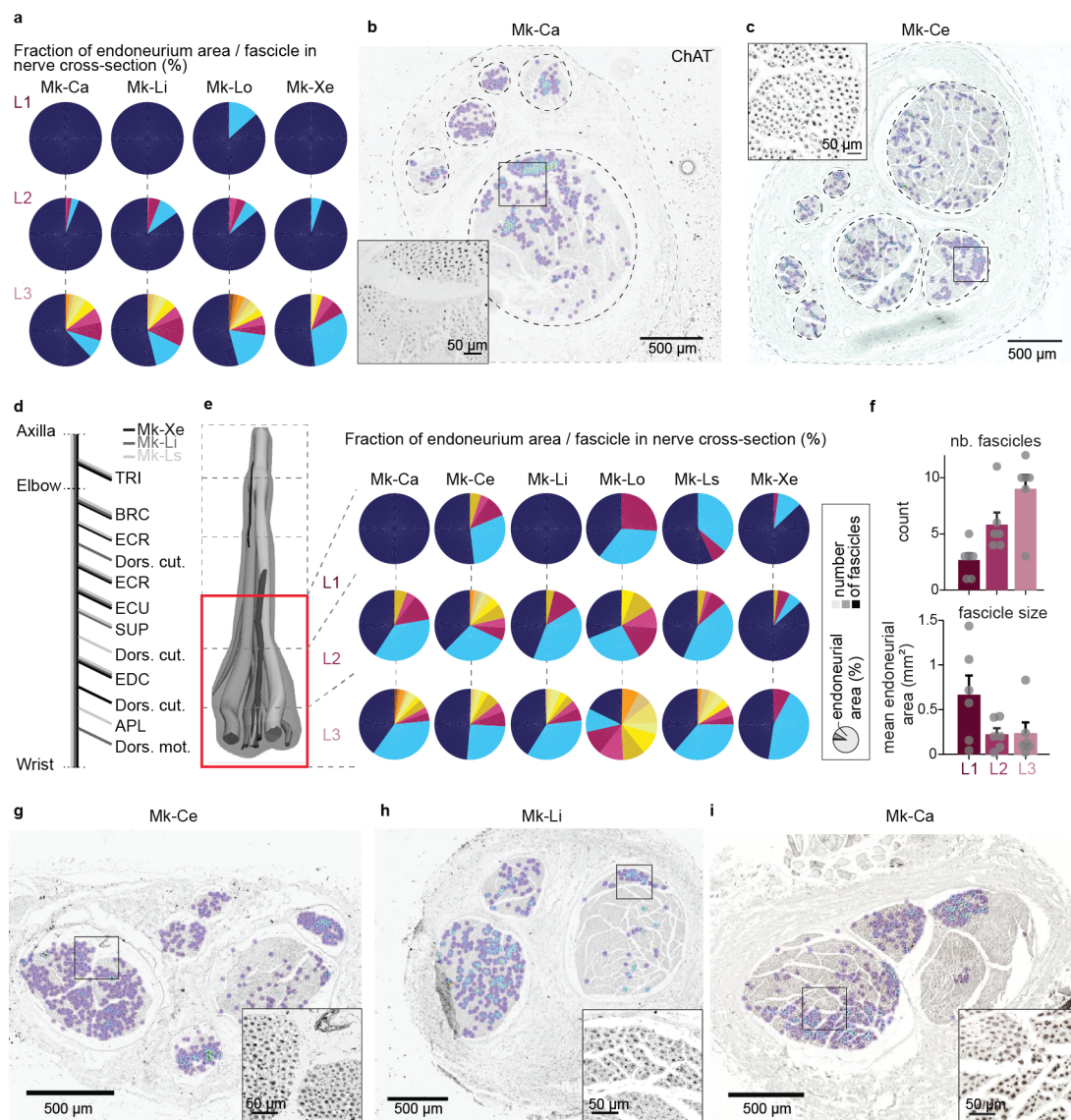


Figure 3.8 – Detailed neuroanatomical organization of the median and radial nerves in fascicularis macaques. (a) Fraction of endoneurium area occupied by each fascicle in the nerve cross-sections of $n=4$ additional animals (see **Figure 3.7 b**). Levels L1 to L3 span 3 cm of nerve segment proximal to the epicondyle (see **Figure 3.1**). (b) and (c) Immunostained cross-sections with motor fibers stained in black (ChAT-labelled) showing the scattered distribution of motor fibers in the median nerve of two animals. Overlaid color-coded map ($\alpha = 0.2$) represents the fibers density. Insets show zoomed-in portions of fascicle without density map overlay. (d) Identification of the muscular and cutaneous targets innervated by the emerging branches of the radial nerve from the axilla to the wrist ($n=3$). (e) Left: 3D reconstruction of the fascicular content of the radial nerve proximally to the elbow for one representative animal. Right: pie charts show the number of fascicles and their respective cross-sectional area at the different nerve levels in $n=6$ animals (as in (a) for the median nerve). (f) Quantification of the number of fascicles and their respective endoneurial area on levels L1, L2 and L3 of the radial nerve across animals ($n=6$). (g), (h) and (i) Motor fibers distribution within the radial nerve above the elbow in $n=3$ animals. Abbreviations: Choline acetyltransferase (ChAT), triceps (TRI), brachioradialis (BRC), extensor carpi radialis (ECR), extensor carpi ulnaris (ECU), supinator (SUP), extensor digitorum communis (EDC), abductor pollicis longus (APL), dorsal cutaneous branch (Dors. cut.).

We used these anatomical findings to implement an anatomically realistic computational model of the nerve (Raspopovic et al., 2011; Raspopovic et al., 2017; Romeni et al., 2020) to simulate the recruitment of axons elicited by intraneural stimulation (**Figure 3.4**). Due to the anatomical similarities observed between the median and radial nerve segments proximal to the elbow (**Figure 3.7 b** and **Figure 3.8**), we designed a single generic model based on median nerve histology. This model combined a volume conductor model of the nerve and a biophysical model of motor fibers (Raspopovic et al., 2011; Raspopovic et al., 2017; Romeni et al., 2020).

First, we calculated voltage distributions elicited by currents injected through single contacts of the TIME. We then estimated which axons were recruited by a given current amplitude (see Methods).

We simulated multiple possible implantation location along the proximal-distal axis of the nerve (L1 to L3) showing that implantation at a location where efferent fibers were segregated in different fascicles led to a more selective recruitment than stimulating densely packed fascicles (**Figure 3.7 d** and **Figure 3.9 a,b**). Indeed, charge injection at the most proximal level, L1, resulted in the simultaneous recruitment of most of the axons and a small number of selectively recruited muscles. Intraneural stimulation delivered at the L2 level engaged the underlying efferent fibers more selectively and led to a higher proportion of selectively recruited muscles (**Figure 3.7 d** and **Figure 3.9 c**). Interestingly, charge injected at the most distal level, L3, did not induce a more specific recruitment of motor fibers than at level L2, despite the muscles being distributed in distinct fascicles (**Figure 3.7 d** and **Figure 3.9 c,d**). This phenomenon results from the linear geometry of the TIME and the limited number of contacts on each side of the active shaft that hinder the recruitment of highly dispersed fibers.

We then compared the essential properties of extra- and intra-fascicular recruitment for the particular level of implantation L2 (**Figure 3.7 e**) and showed that extrafascicular stimulation resulted in a lower selectivity and displayed higher thresholds of activation and saturation than intrafascicular stimulation (**Figure 3.7 f** and **Figure 3.9 e**).

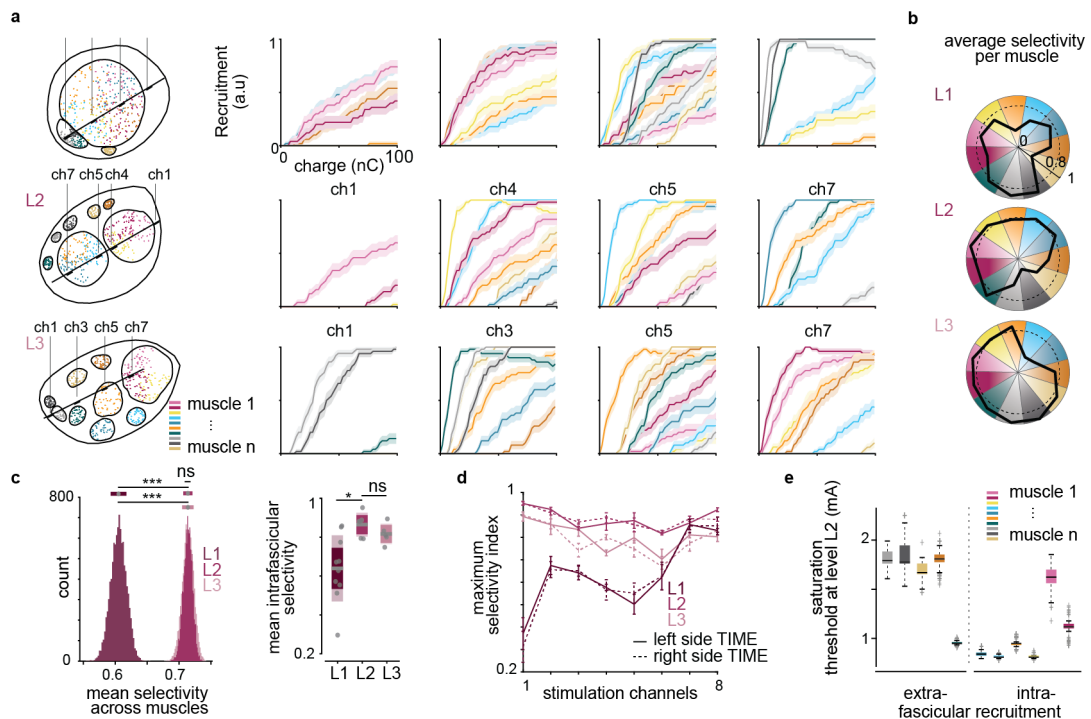


Figure 3.9 – Simulation results of a realistic model of intraneural stimulation in the monkey median nerve. (a) Simulated recruitment curves obtained for different active sites along the shaft of the TIME for three levels of implantation in the nerve, L1, L2 and L3. (b) Selectivity polar plots representing the maximum SI obtained for each muscle at each implantation level (see Methods). (c) Left: histograms representing the mean SI at each implantation ($n=10'000$ bootstrapped samples per level, see methods). Mean and standard deviation are reported above the plot. Right: mean intrafascicular selectivity for each implantation level ($n_{L1}=10$ muscles, $n_{L2}=6$ muscles, $n_{L3}=5$ muscles, see methods). Plots show 95% confidence interval in shaded color, s.t.d in dark color and mean in grey. (d) Maximum SI for each active site along the electrode shaft, at each implantation level ($n=11$ data points per channel, see methods). (e) Saturation thresholds plotted for each muscle at level L2 ($n=10'000$ bootstrapped population per muscle, see methods). * <0.05 , *** $P < 0.001$, non-parametric Kruskal-Wallis test with Bonferroni correction for $n > 2$ or adapted t-test for bootstrapped samples (see Methods). Shaded lines: s.e.m - Error bars: s.e.m - a.u: arbitrary units.

The miscellaneous organization of motor fibers in the median and radial fascicles together with our computational results suggest that an intrafascicular interface penetrating deep neural structures can selectively recruit underlying muscles. Following these findings, we designed and manufactured TIME implants tailored to the dimensions of the monkey nerves (**Figure 3.2** and **Figure 3.7 h-i**) that we implanted approximately 2 cm proximally to the elbow (see Methods). The implant layout presented 16 channels of stimulation: 8 on each flap of the polyimide shaft. Anchoring tabs were placed on the thin-film structure and ceramic adapter, to secure the implant to the epineurium.

3.4.2. Intrafascicular stimulation selectively recruits hand muscles

We inserted two acute TIMEs, one in the median nerve and one in the radial nerve, of five animals (see Methods and **Annexe Table A.2**) to characterize the selectivity of hand muscle recruitment using intraneural stimulation (**Figure 3.10 b**). We recorded electromyographic (EMG) activity using bipolar electrodes implanted in forearm muscles and intrinsic hand muscles (**Figure 3.10 a**). Monopolar stimulation through individual channels activated specific and functional groups of muscles, namely, flexors of the wrist, fingers, and an opponent of the thumb for the median nerve, and extensors of the wrist, fingers, and abductor of the thumb for the radial nerve. Interestingly, the functional selectivity of intrinsic hand muscles, i.e., thumb opponent and first dorsal interosseous, was found to be comparable to the selectivity of extrinsic muscles. Functional selectivity results were reproducible across all monkeys (**Figure 3.10 c-e** and **Figure 3.11**).

Then, we implanted a chronic tailored TIME in the median and radial nerve of two monkeys, together with chronic intramuscular leads in the hand muscles. The TIMEs were routed to connectors on the head through custom-made helically-wound robust and compliant cables. The EMGs and TIMEs connectors were embedded in a custom-designed titanium pedestal fixated to the skull (**Figure 3.2**).

We evaluated chronic electrical, mechanical, and functional stability of two implants (up to 2 months, **Figure 3.10 g-i** and Methods). To evaluate the stability of the electrodes, we measured the activation threshold charge over time and found a progressive increase during the first two weeks post-implantation, possibly in consequence of the body immune response (**Figure 3.10 f**). After this initial period, thresholds remained stable for the rest of the study (**Figure 3.10 g**). Both muscle and functional selectivity remained high and stable (**Figure 3.10 h-i**). These results confirmed previous long-term experiments in rodents (Wurth et al., 2017) humans (Oddo et al., 2016).

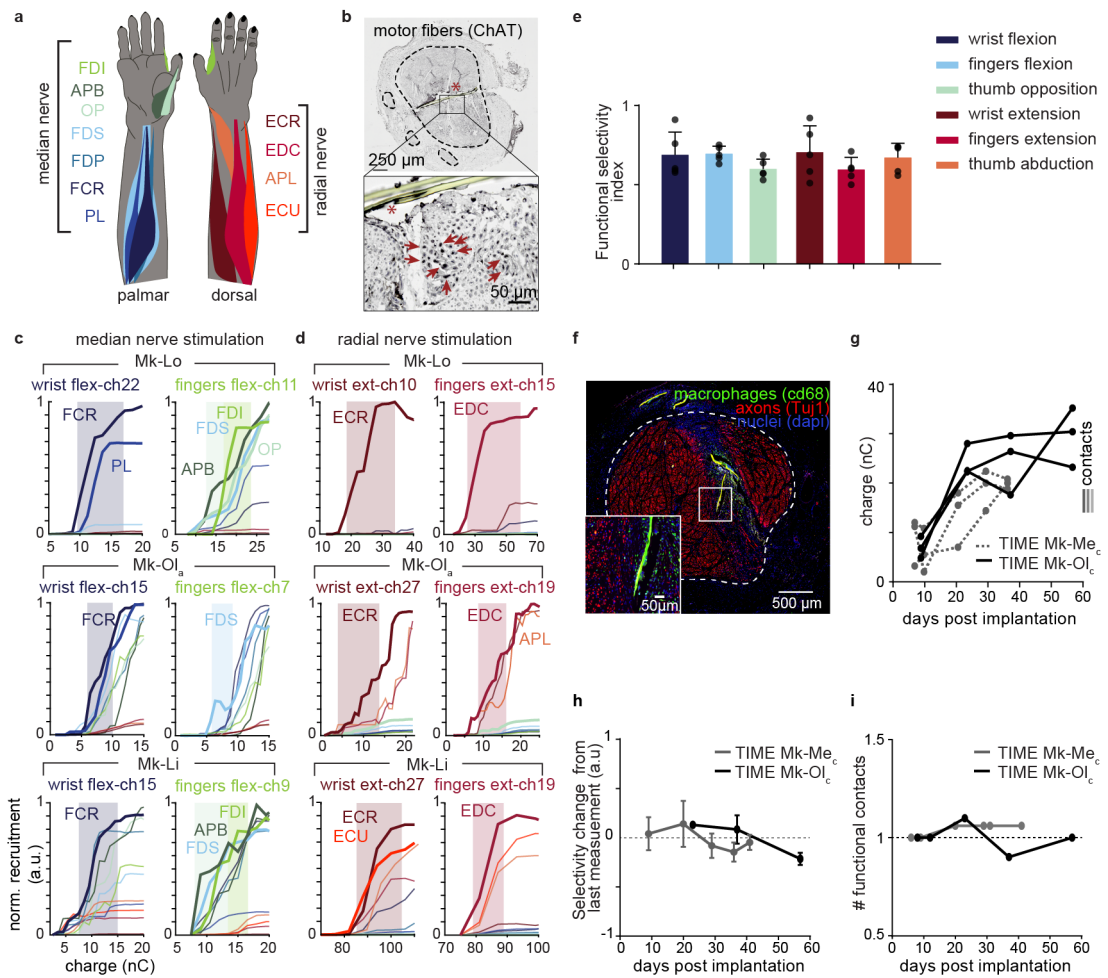


Figure 3.10 – Selective hand muscles recruitment using intraneural stimulation. (a) Anatomical representation of the flexor and extensor muscles of the monkey hand innervated by the median and radial nerve respectively. (b) Cross-section of ChAT labelled, implanted median nerve showing the proximity of the TIME (asterisk) and motor axons (arrows) within a fascicle (Mk-Th, acute). (c) Normalized muscle recruitment obtained by stimulation of the median nerve (n=3 representative animals). (d) Normalized muscle recruitment obtained by stimulation of the radial nerve (n=3 representative animals). (e) Acute median and radial functional selectivity across animals (n=5). (f) Immunological response after 42 days of TIME implantation in the median nerve (Mk-Me_c). (g) Weekly evaluations of the activation charge threshold (10% recruitment) over three active sites (n=2 chronic animals, Mk-Me_c: 42 days, Mk-Ol_c: 58 days). (h) Change in functional selectivity over the course of the experiment (n=2 chronic animals). (i) Number of functional contacts (eliciting visible movements) over the course of the experiment (n=2 chronic animals). Error bars: s.e.m - a.u.: arbitrary units. Abbreviations: palmaris longus (PL), flexor carpi radialis (FCR), flexor digitorum superficialis (FDS), flexor digitorum profundus (FDP), extensor carpi radialis (ECR), extensor digitorum communis (EDC), abductor pollicis longus (APL), first dorsal interosseus (FDI) and abductor pollicis brevis (APB), Choline acetyltransferase (ChAT).

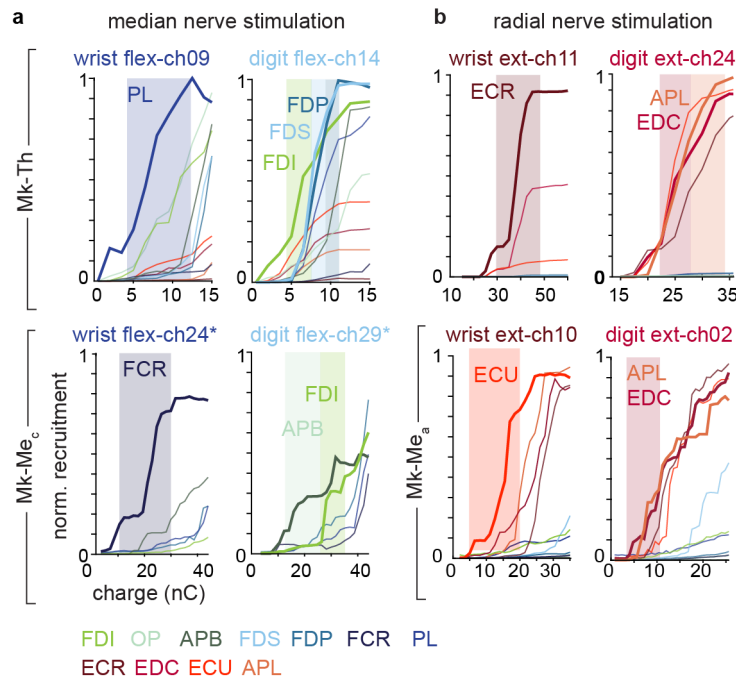


Figure 3.11 – Selective hand muscles recruitment in additional animals. (a) Normalized muscle recruitment obtained by stimulating the median nerve in two additional animals. Channels on the left preferentially recruit wrist flexors (FCR and PL) while channels on the right selectively activate finger flexion (FDS, FDI) and thumb opposition (APB, OP). (b) Normalized muscle recruitment obtained by stimulating the radial nerve in the same two additional animals. Channels on the left preferentially recruit wrist extensors (ECR and ECU) while channels on the right selectively activate finger extension (EDC) and thumb abduction (APL). Abbreviations: palmaris longus (PL), flexor carpi radialis (FCR), flexor digitorum superficialis (FDS), flexor digitorum profundus (FDP), extensor carpi radialis (ECR), extensor digitorum communis (EDC), and abductor pollicis longus (APL), first dorsal interosseous (FDI), opponens pollicis (OP), abductor pollicis brevis (APB).

3.4.3. Intrafascicular stimulation elicits a variety of functional grips

The ability of the TIMEs to selectively recruit different muscles allowed us to generate a rich repertoire of motor functions in awake and anesthetized animals (**Figure 3.12 a-b,h**, **Supp. Video 3.1**, and Methods). In particular, median nerve stimulation elicited flexion of the wrist and the closing of the hand in three stereotypical grips, referred hereafter to 1) cylindrical grip, or hook grip, characterized by the closure of the index, middle, and ring finger; 2) pinch-like grip, or lateral grip, identified as the opposition of the thumb against the index and middle finger; and 3) spherical grip, or whole handgrip, in which all the fingers, including the thumb, were flexed (Feix et al., 2016) (**Figure 3.12 a**, **Figure 3.13 a,b**, and **Supp. Video 3.1**). Similarly, intraneural stimulation of the radial nerve triggered specific hand movements such as ulnar deviation and extension of the wrist, hand opening through finger extension, and abduction of the thumb (**Figure 3.12 h**, **Figure 3.13 b, c**, and **Supp. Video 3.1**). The different hand movements elicited by intraneural stimulation were underlined by different muscle activity and kinematic profiles for the same animal (**Figure 3.12 c-d,i**, and **Figure 3.13 a-c**), while highly similar kinematic features across animals for each movement were observed (**Figure 3.12 c,d,i** and **Figure 3.13 d**).

Importantly, the two monkeys implanted with chronic TIME implants did not exhibit any sign of discomfort or pain during stimulation even for the largest amplitudes of current. No side effect was observed during the several weeks under observation, in the lab or the housing environment.

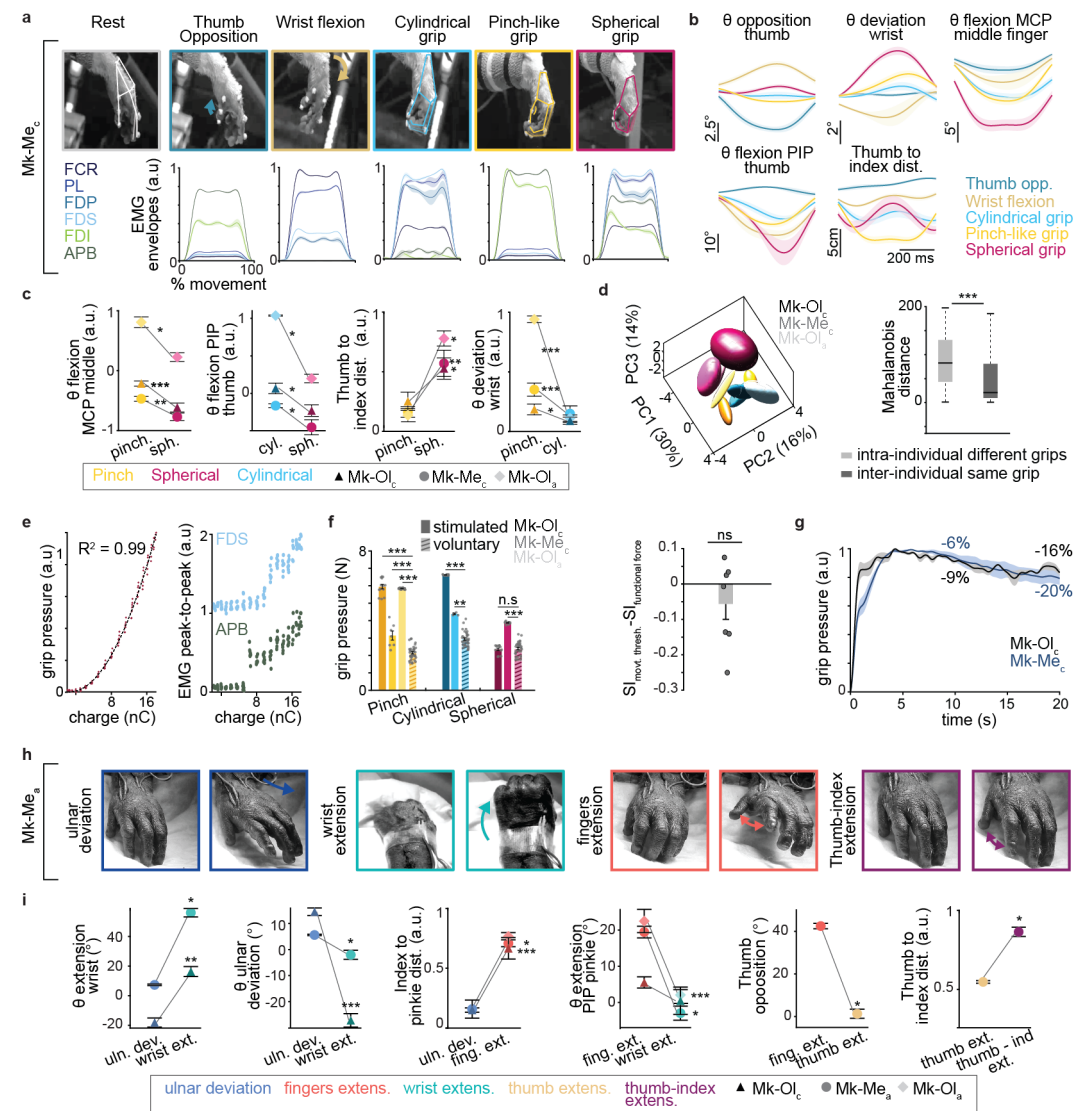


Figure 3.12 – (Continued on the following page.)

Functional grip movements and extension gestures achieved with the TIME. (a) Range of movements obtained by burst stimulation (500 ms) of different channels of the median nerve (awake). Corresponding muscle activation is displayed for each movement. (b) Concurrent kinematic profiles of relevant joint angles and inter-joint distances for each movement over the course of the stimulation burst. (c) Average kinematic features measured during stimulation for each type of grip (cylindrical, pinch and spherical, $n=3$ animals Mk- Ol_c and Mk- Me_c awake, Mk- Ol_a anesthetized). (d) Left: grip movements represented as least-squares ellipsoids in the 3D-space created by the three first principal components (PC) obtained by PC analysis of movement kinematics. Different colors code for different grips, different shades represent different animals. Right: Quantification of 3D distances between different grips of a single animal (intra-individual distance) and between the same grips for different animals (inter-individual distance). (e) Left: Normalized grip pressure as a function of the injected charge (curve fit with 2^{nd} order polynomial, $R^2=0.99$). Right: Corresponding increase in the EMG peak-to-peak for the fingers flexor and thumb abductor muscles ($n=1$ animal). (f) Left: Grip pressure elicited for different grips (full bars, different shades indicate different monkeys) compared to the voluntary force exerted during a behavioral functional task (striped bars). Right: Difference between the SI for the charge at which a grip is observed and the SI measured when injecting enough current to produce functional levels of force observed on the left ($n=7$ data points, one sample t-test $p > 0.05$). (g) Evolution of grip pressure over 20 seconds of tonic stimulation on a single channel of the median nerve ($n=2$ monkeys). (h) Types of movement obtained by stimulating different channels of the radial nerve. (i) Average kinematic features measured during stimulation for each type of extension movement ($n=3$ animals, Mk- Ol_c awake, Mk- Me_a and Mk- Ol_a anesthetized). Contrary to (c), data are not normalized as not all movements were observed in all animals. * $P < 0.05$, ** $P < 0.01$, *** $P < 0.001$, non-parametric Kruskal-Wallis test with Bonferroni correction for $n > 2$ and Wilcoxon rank-sum test for unpaired data, except specified otherwise. Shaded lines: s.e.m - Error bars: s.e.m - a.u: arbitrary units. Abbreviations: proximal interphalangeal (PIP), metacarpal interphalangeal (MCP), palmaris longus (PL), flexor carpi radialis (FCR), flexor digitorum superficialis (FDS), flexor digitorum profundus (FDP), extensor carpi radialis (ECR), extensor digitorum communis (EDC), and abductor pollicis longus (APL), first dorsal interosseous (FDI). Data specifications for each panel are summarized in **Appendix Table A.9**.

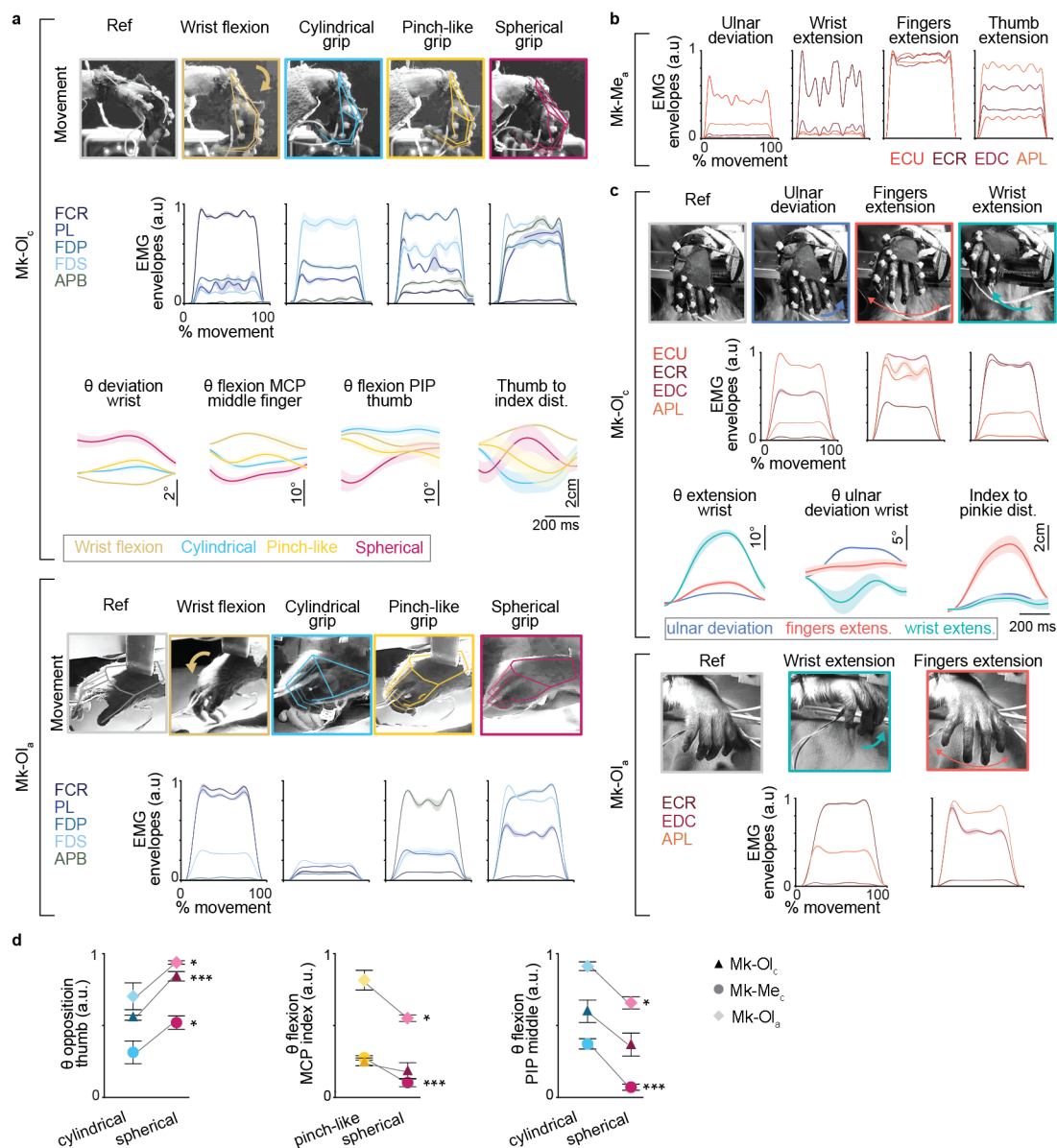


Figure 3.13 – (Continued on the following page.)

Reproducible grips and hand extension movements elicited by intraneural stimulation. (a) Top: snapshots extracted from video recordings illustrating the range of movements obtained by stimulating different channels of the median nerve in Mk-*Ol_c* (12 days post-implantation). Corresponding muscle activation is displayed for each movement (3 repetitions/movement, same intensity of stimulation). Concurrent kinematic profiles are shown for relevant joint angles and distances for each movement over the course of the stimulation burst (500 ms duration). Stimulation intensities eliciting similar range of motion were pooled together (n= 9 repetitions/movement). Bottom: Movement snapshots and EMGs recorded in Mk-*Ol_a* when stimulating the media nerve (acute, n=4 to 5 repetitions per movement). (b) EMG recordings corresponding to extension movements illustrated in Figure 3h (Mk-*Me_a* n=1 repetition per movement). (c) Top: snapshots extracted from video recordings illustrating the range of extension movements obtained by stimulating different channels of the radial nerve in Mk-*Ol_c* (12 days post-implantation). Corresponding muscle activation is displayed for each movement (3 to 4 repetitions/movement, same intensity of stimulation). Concurrent kinematic profiles are shown for relevant joint angles and distances for each movement over the course of the stimulation (500 ms burst). Stimulation intensities eliciting similar range of motion were pooled together (4 to 24 repetitions/movement). Bottom: Movement snapshots and EMGs recorded when stimulating the radial nerve in Mk-*Ol_a* (acute, n=4 repetitions per movement). (d) Average kinematic features measured during stimulation for each type of grip, cylindrical, pinch and spherical, in n=3 animals (Mk-*Me_c*, 33 days post-implantation, 7 repetitions/grip - Mk-*Ol_c*, 12 days post-implantation, 9 repetitions/grip - Mk-*Ol_a*, acute, 4 repetitions/grip). Data are normalized across grip within each animal (see Methods). * $P < 0.05$, *** $P < 0.001$, non-parametric Kruskal-Wallis test with Bonferroni correction. Shaded lines: s.e.m - Error bars: s.e.m - a.u: arbitrary units. Abbreviations: proximal interphalangeal (PIP), metacarpal interphalangeal (MCP, extensor carpi radialis (ECR), extensor digitorum communis (EDC), and abductor pollicis longus (APL).

Modulation of movement amplitude and grasping force induced by intraneural electrodes were assessed by modifying the amplitude and frequency of the stimulation bursts (Valle, Petrini, et al., 2018) (**Figure 3.12 e**, **Figure 3.14 a, c, d**, and **Supp. Video 3.2**). Interestingly, similarly to surface NMES (Kesar et al., 2008), we found that amplitude modulation provided a larger working range of forces and resulted in a reduced force attenuation over time compared to frequency modulation (**Figure 3.14 d-e**). By gradually increasing the stimulation charges of each channel evoking specific grips, we achieved a monotonic force increase reaching values superior or equal to those generated by an intact monkey performing a grasping task (**Figure 3.12 f**, **Figure 3.14 a**, and Methods). More importantly, we did not observe any significant change in selectivity when modulating the stimulation charge to attain these force levels (**Figure 3.12 f**). We also adjusted the stimulation charge to reconstruct smooth sequences of hand movements. Specifically, we reproduced natural patterns of muscular co-activation by alternatively stimulating independent channels of the median and radial nerves. This strategy produced a natural transition between flexion and extension and closing fingers while maintaining a stabilized wrist posture (**Figure 3.14 e** and **Supp. Video 3.2**). Finally, we quantified the ability of the TIME to sustain functional levels of force for extended periods of time by measuring grip pressure and wrist torques during tonic stimulation bursts. Our analysis demonstrated that force levels were only attenuated by 10% after 5 seconds of stimulation and declined by approximately 20 to 50% following 20 seconds bursts at 50Hz (**Figure 3.12 g** and **Figure 3.14 b**). These properties suggest a relatively physiological onset of

fatigue (Danion et al., 2000) conducive to the performance of relevant grasping tasks (Brochier, 2004; Kurillo et al., 2005; Thrasher et al., 2005).

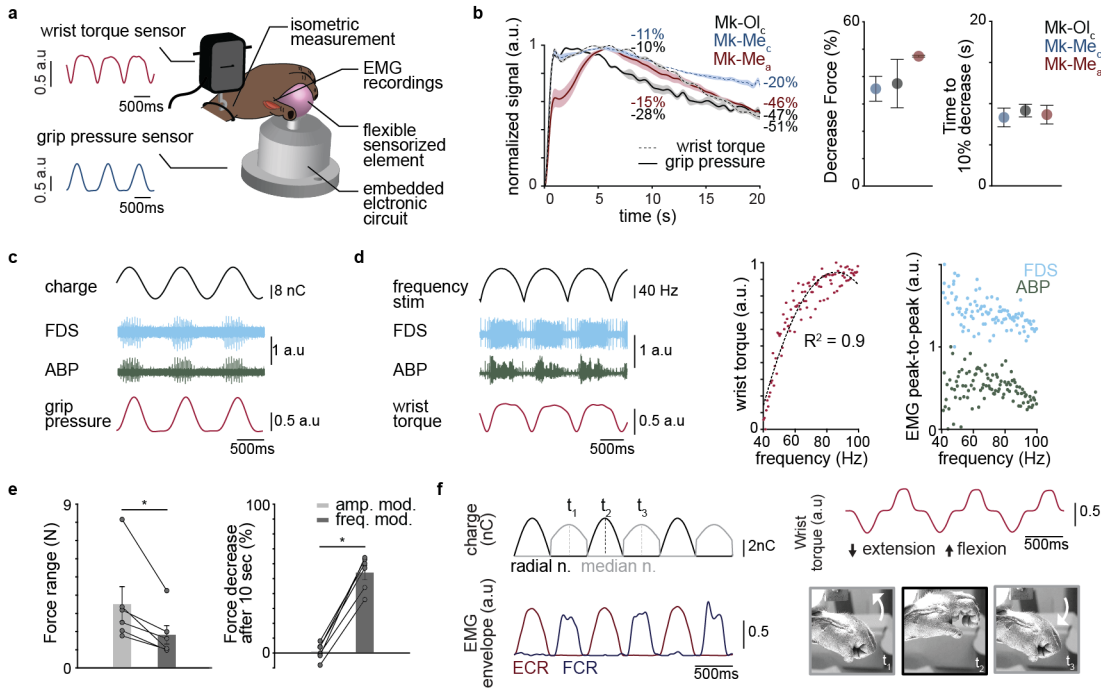


Figure 3.14 – Intraneural stimulation can be modulated to produce functional force levels. (a) Top: Experimental setup used to record the force and muscular activity generated by intraneural stimulation. The wrist torque is recorded in an isometric manner using a dual-range force sensor. Grip pressure is acquired using a custom-designed grip pressure sensor. (b) Left: evolution of the grip pressure and wrist torque over 20 sec of tonic stimulation on single channels of the median nerve in $n=3$ monkeys. Force values recorded after 10 and 20 seconds of stimulation are reported. Right: the first scatter plot reports the amount of fatigue induced by tonic stimulation as the difference between the maximal force and the force generated after 20 seconds of stimulation. The second scatter plot presents the time necessary for the force to decrease of 10% of the maximal value. (Mk-Me_c 14-20 days post-implantation, 3 to 4 repetitions - Mk-Ol_c 37 days post-implantation, 3 repetitions - Mk-Ol_a acute, 3 repetitions). (c) Traces showing the effects of stimulation charge modulation on elicited muscular activity and grip pressure over 3 sinusoidal stimulation cycles (Mk-Me_c 20 days post-implantation). (d) Left: traces showing the effects of stimulation frequency modulation on elicited muscular activity and wrist torque over 3 stimulation cycles (Mk-Me_c, 20 days post-implantation). Middle: the normalized wrist torque is represented as a function of the stimulation frequency. The curve is fitted with a 2nd order polynomial, correlation $R^2=0.9$. Right: corresponding EMG peak to peak values are reported across the whole frequency range (Mk-Me_c 11 stimulation cycles). (e) Left: force range obtained when modulating the amplitude or the frequency of stimulation (Mk-Me_c, 6 repetitions, 10 seconds of stimulation). Force measurements are obtained by converting voltage values to N using calibration curves (see Methods). Right: decrease of force peak after 10 seconds of modulation, expressed in percentage of maximal peak (Mk-Me_c, 6 repetitions, 10 seconds of stimulation per rep). (f) Example of bimodal stimulation achieved by alternatively stimulating one channel from the radial and median nerve respectively. Injected charge is shown over 3 stimulation cycles per electrode. Corresponding EMG envelopes are plotted for the wrist flexor and extensor muscles and normalized wrist torque is reported on the top right. Snapshots extracted from video recordings at different time points during the stimulation display successive closing and opening movements of the hand (Mk-Me_a, acute). * $P < 0.05$, Wilcoxon signed-rank test. Shaded lines: s.e.m - Error bars: s.e.m - a.u.: arbitrary units. Abbreviations: flexor digitorum superficialis (FDS), abductor pollicis brevis (APB).

3.4.4. Cortically driven TIME modulation during a functional grasping task: a proof-of-concept

Finally, we explored the possibility of using the TIME to enable a monkey to perform a voluntary functional task requiring the activation of partially paralyzed muscles. For this experiment, we developed an intuitive control strategy whereby intra-cortical recordings from the primary motor cortex directly adjust the relative stimulation charge delivered through one channel on the radial nerve TIME that produced simultaneous wrist and finger extension (**Figure 3.6** and **Figure 3.16 a**).

To selectively impair hand opening, we engineered a microfluidic system (Pohlmeyer et al., 2009) composed of a silicone cuff wrapped around the nerve, coupled to a thin tube directed to the chronic assembly fixed the skull of the animal (**Figure 3.2**, **Figure 3.3**). The efficacy of the peripheral nerve block was preliminary assessed acutely by delivering lidocaine to the median nerve in one animal (**Figure 3.15 a**). Likewise, in our chronic setup, lidocaine delivery inside the pedestal port progressively induced a selective pharmacological block of the radial nerve, resulting in a specific transient paralysis of the hand extensor muscles (**Figure 3.15 b-c**).

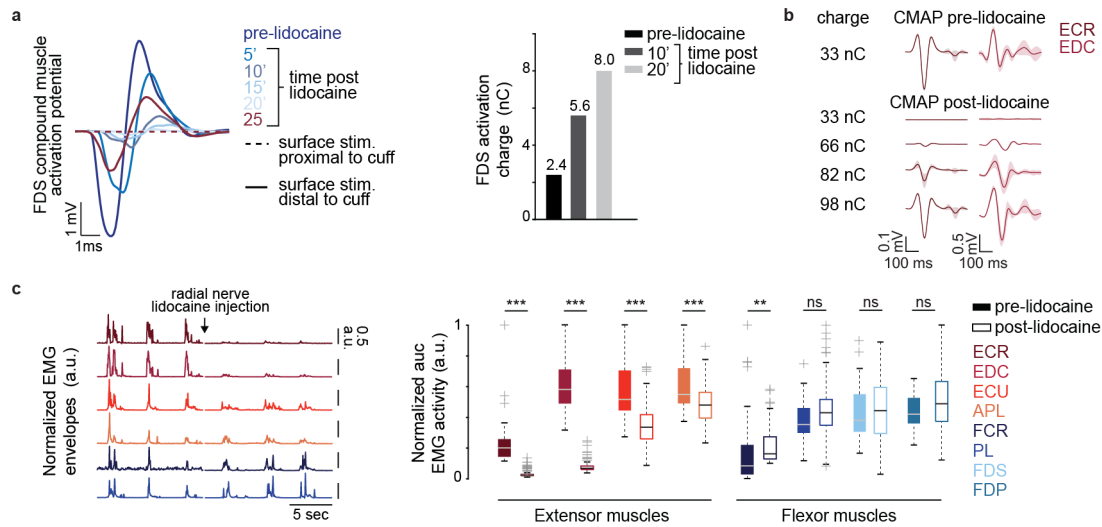


Figure 3.15 – Microfluidic cuff characterization for the selective paralysis of movement. (a) Acute characterization of the paralyzing effects after lidocaine delivery to the median nerve. Left: FDS CMAP elicited by surface stimulation of the nerve were measured before and after lidocaine injection at 5' intervals (1-2 mA bipolar, epineural stimulation, see Methods). After 25', stimulation was applied both proximally and distally to the microfluidic cuff (red color). Right: intraneural activation charge (10% recruitment) was measured before and after lidocaine injection for the FDS muscle (1 recruitment curve per time point, see Methods). (b) Chronic evaluation of the intraneural activation charge thresholds after paralysis of the radial nerve. Extensor muscles CMAPs are illustrated for various injected charges before and after lidocaine injection (Mk-*Ol_c*, 47 days post implantation. 25 repetitions/charge levels, see Methods). (c) Left: normalized EMG envelopes of flexor and extensor muscles across successive trials of the reach-and-pull robotic task before (baseline) and after lidocaine injection. Right: The boxplots report the normalized area under the curve of the EMG envelopes computed across successful trials (dexterous and imprecise reaches). (Mk-*Ol_c* – session 2, 47 days post implantation, n= 264 trials). ** P <0.01, *** P <0.001, non-parametric Kruskal-Wallis test. Shaded lines: s.e.m - a.u: arbitrary units. Boxplot distribution: median with 25th and 75th percentiles.

We monitored the spiking activity in the right primary motor cortex of the monkey while reaching for an object presented by a robotic arm (Barra et al., 2019, and chapter 2). We then used principal component (PC) analysis to compute the main dimensions of variance found in the cortical activity during the task (Gallego et al., 2017). The resulting coefficient matrix, labeled hereafter “neural modes coefficient matrix” (**Figure 3.5**, and Methods) mapped the original brain activity to the linearly transformed PC space. Since hand opening primarily occurs when approaching an object, we anticipated that the PC correlating the most with movement during the reach would provide a simple and effective control variable to drive the stimulation in real-time. Evaluation of the neural activation during movement projected on the first three PCs revealed a preferential tuning along the 2nd PC (PC2) which was preserved throughout months of behavioral recordings (**Figure 3.5** and **Figure 3.17 d-f**).

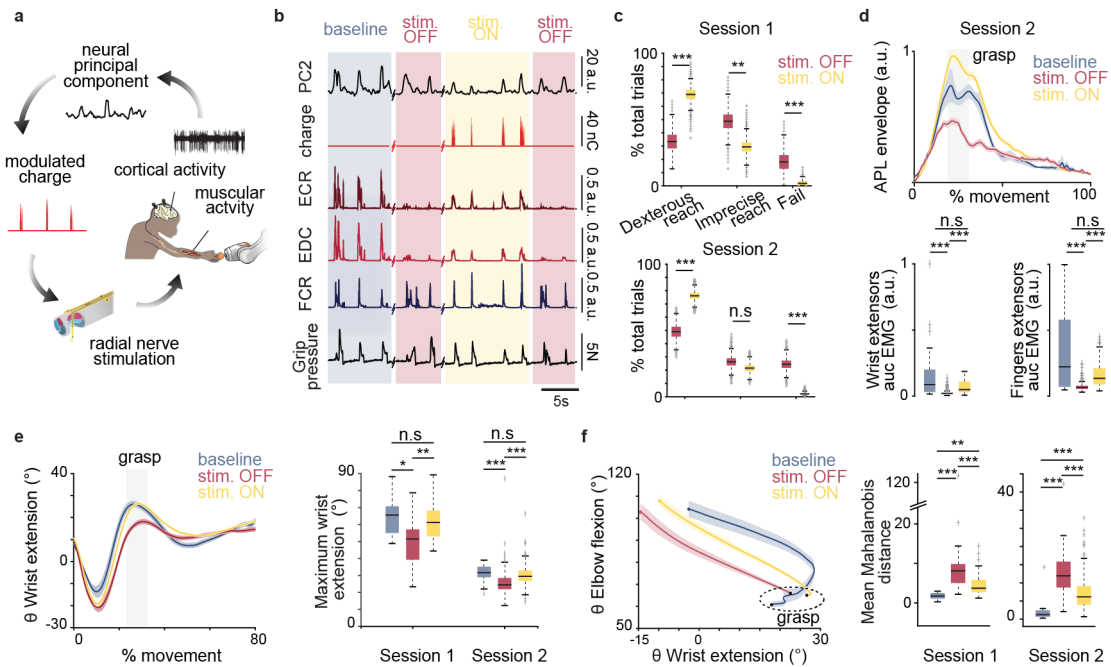


Figure 3.16 – Intraneural stimulation restores hand extension during functional reaching task. (a) Behavioral task setup. (b) Successive reach and grasp movements and corresponding brain, muscle and grip pressure signals recorded during the task before paralysis of the radial nerve (baseline), and after paralysis, with or without radial nerve stimulation (stim. ON vs. stim. OFF). (c) Proportion of dexterous reaches, imprecise reaches and failed trials, performed with or without stimulation of the paralyzed arm. (d) Top: Mean muscular activation of the thumb abductor in all three conditions. Bottom: area under the curve of flexor and extensor EMG activation across the whole movement. (e) Left: Mean wrist extension angle interpolated across the whole movement during baseline trials and trials with or without stimulation (session 2). Right: Maximum wrist extension achieved when approaching the grasping phase of the movement. (f) Left: Average multi-joint coordination of the arm during reach, when approaching the grasping phase during baseline trials and during trials with or without stimulation (session 2). Right: Mean Mahalanobis distance between a given condition and the baseline distribution at time t. Results are averaged along the movement and then across trials. Session 1: 40 days post implantation, session 2: 47 days post implantation. n.s $P > 0.05$, * $P < 0.05$, ** $P < 0.01$, *** $P < 0.001$, non-parametric Kruskal-Wallis test with Bonferroni correction for $n > 2$ or adapted t-test for bootstrapped samples in (a). Shaded lines: s.e.m – Boxplot distribution: median with 25th and 75th percentiles - a.u.: arbitrary units. Data specifications for each panel are summarized in **Appendix Table A.10**.

We computed the modulation depth along PC2 on data acquired before the injection of the paralytic drug through the microfluidic cuff placed proximal to the TIMEs, and evaluated the stimulation charge thresholds after the inactivation of the radial nerve, to calibrate the stimulation controller (**Figure 3.5**). Without preliminary training, the monkey was able to integrate instantaneously the stimulation-induced hand movement to the task behavior. The graded stimulation of the radial nerve based on the PC2-related cortical dynamics potentiated the activation of the wrist and fingers extensors (**Figure 3.16 d** and **Figure 3.17 b**). This approach allowed the animal to efficiently and smoothly reach for the target object presented and complete the task (**Figure 3.16 b-c**, **Figure 3.17 a**, and **Supp. Video 3.3**). Brain-controlled intraneural stimulation applied after paralysis of the hand also restored wrist extension angles comparable to the tonic activation observed during baseline trials (**Figure 3.16 e**). This recovery coincided with an improved kinematic strategy during the execution of the movement. Indeed, the inter-joint coordination (Cirstea et al., 2003) measured in trials executed with intraneural stimulation was found to be markedly closer to the healthy condition than in the trials performed without stimulation (**Figure 3.16 f** and **Figure 3.17 c** and Methods).

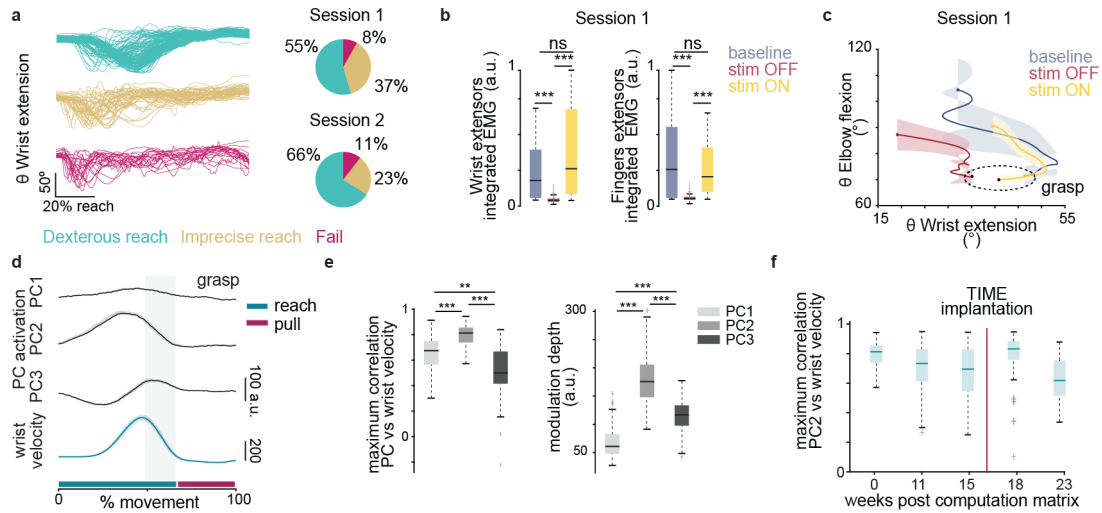


Figure 3.17 – Performance during behavioral task and neural manifold characteristics (a) Left: profiles of wrist extension for each type of reach movement during a representative behavioral session. Right: proportion of each movement type for trials with and without stimulation (session 1: 97 trials and session 2: 295 trials). (b) Area under the curve of the EMG activation across the whole movement. The left and right panel respectively show the values of the extensor and flexor muscles pooled together. Data are normalized to the maximum value for each muscle (session 1: n= 89 trials). (c) Average multi-joint coordination of the arm during reach when approaching the grasping phase during baseline trials and trials with or without stimulation (Mk-OL_c, session 1: n=89). (d) Mean neural activation computed along the first three principal components (PCs) during the behavioral grasping task along with the average wrist velocity (Mk-OL_c, 17 weeks before TIME implantation, n= 54 trials). (e) Maximum cross-correlation coefficient between the neural activation along one of the PCs and the velocity profile of the wrist (left, see Supplementary Info, n= 54 trials). Modulation depth of each neural activation waveform (right, see Supplementary Info, n= 54 trials). Data are computed on the session used to derive the neural modes coefficient (Mk-OL_c, 17 weeks before TIME implantation, see Methods). (f) Evolution of the maximum correlation coefficient between the neural activation along the 2nd PC (PC2) and the wrist velocity during the behavioral grasping task. (n = 54, 155, 48, 62, 27 trials for each time point respectively, see Supplementary Info). ** P < 0.01, *** P < 0.001, non-parametric Kruskal-Wallis test. Shaded lines: s.e.m - a.u.: arbitrary units. Boxplot distribution: median with 25th and 75th percentiles. Abbreviation: principal component (PC).

3.5. Discussion

We introduced a tailored design and implantation paradigm for generating dexterous and functional hand movements using intrafascicular stimulation in a pre-clinical animal model. Our approach displayed the unique ability to selectively engage different motor pools using a single implant inserted in the nerve. This specific activation produced sustained, functionally relevant, and controllable actuation of the wrist and fingers with low amounts of current. The simplicity and efficacy of the system are illustrated by the rich variety of grasps and extension movements evoked from only two TIMEs with monopolar stimulation protocols. While epineural stimulation can potentially achieve similar levels of specificity (Tigra et al., 2020), it requires the implementation of complex multipolar stimulation patterns that strongly depend on the implant location and nerve organization (Brill et al., 2018). On the other hand, intramuscular stimulation calls for the synchronized control of numerous implants, compelling to tedious manual design of stimulation strategies (Ajiboye et al., 2017).

The large collection of movements evoked by intrafascicular stimulation offers promising therapeutic perspectives for those suffering from tetraplegia or stroke. Indeed, rehabilitation studies involving patients affected by ischemic events reported that compensatory mechanisms arising in the subacute phase more efficiently restored gross arm movements than precise fingers motion (Krakauer and Carmichael, 2017; Raghavan et al., 2006; Twitchell, 1951; Xu et al., 2017). Similarly, individuals suffering from spinal cord lesions still lack acceptable solutions for the recovery of fine hand motion and only partially benefit from current rehabilitation strategies (Mangold et al., 2005; M. R. Popovic et al., 2006). In patients affected by spasticity (Gracies, 2005a, 2005b; Sommerfeld Disa K. et al., 2004; Welmer et al., 2010) and in individuals exhibiting a flaccid state of the limb (Borboni et al., 2014; Kwakkel Gert et al., 2003; McDonald and Sadowsky, 2002), the relaxation of the fist and the stable support of the hand present important medical challenges that could potentially be addressed through intrafascicular stimulation of the extensor muscles. As the model of paralysis used in our last functional task did not strictly reproduce these conditions, the clinical translation of our approach would require the validation of its therapeutic benefits in subjects with paralysis.

Importantly, previous anatomical examinations of the upper limb muscles and nerves in monkeys and humans (Brushart, 1991; Delgado-Martínez et al., 2016; Gesslbauer et al., 2017; Johnston et al., 2016; Marin et al., 2009; Stewart, 2003) revealed that the structural organization of the arm is preserved within primates, suggesting that our approach could be efficiently translated to humans. The larger number of fascicles in human median nerve (Delgado-Martínez et al., 2016; Gesslbauer et al., 2017) yet indicates the possible need for additional TIME implants, or denser electrode arrays (Ledbetter et al., 2013), to achieve similar results. Although we showed that simple stimulation patterns could be linked with cortical inputs to provide intuitive low-dimensional control of the implant, numerous challenges remain for the translation of user commands into more dexterous movements such as the need for the decoding of a large repertoire of finger movements. The effective embodiment of this new motor control modalities into the natural sensory-motor schemes of the users must be also investigated. In this regard, the simple synergistic activation of hand muscles triggered by intrafascicular stimulation presents encouraging evidence for its instinctive control through a low number of instructing commands. Our results, together with the recent clinical application of intrafascicular implants to restore sensory feedback in upper (D'Anna et al., 2017; Petrini, Valle, Strauss, et al., 2019; Valle, Petrini, et al., 2018) and lower limb (Petrini, Bumbasirevic, et al., 2019; Petrini, Valle, Bumbasirevic, et al., 2019) amputees, suggest promising opportunities to restore fine hand motor control in subjects with paralysis.

3.6. Contributions

SM, EMR, SW, MB and MC conceived the study. MC, MB, IS, ER, AB designed and implemented the experimental setup. IS and MB programmed the electrophysiology and stimulation control software. PC designed and fabricated the intraneural implants with the support and supervision of TS. MB implemented the computational model. MB and SW performed

neuroanatomy and histological procedures and used the results to dimension the intraneural implants. FF, MB and SW designed the microfluidic cuff system, FF manufactured the system and the encapsulating pedestal with the support and supervision of SL. MB, AB and MD trained the animal. GC, JB, DS, AB, SW, SB, MB and ES performed the surgeries. MB, SW, IS, ER, EL, AB and SB conducted the experiments. MB, SW, ER, EL and SB performed the data analysis. MB, ER and SB pre-processed the data. MB, SW, EL, and ER prepared the figures. SM, MC and EMR supervised the study.

3.7. General Conclusion

In this chapter, I presented an ensemble of anatomical, electrophysiological, and functional data that show, for the first time, the potential of intrafascicular electrodes to restore precise hand movements in a relevant pre-clinical animal model. I demonstrated that the tuned implantation of an anatomically-tailored intraneural interface results in highly specific activation of the extrinsic and intrinsic muscles of the hand. I showed that such activation translated to a large collection of functional grips and extension of the fingers. I provided evidence for the graded control of the force generated by intraneural stimulation, and ultimately applied such control in a proof-of-concept experiment to restore hand extension in a transiently paralyzed monkey performing a functional grasping task. This work represents the main core of this thesis and an important milestone for the translation of intrafascicular electrical stimulation to the clinic.

4 Low-dimensional manifold-based direct cortical control strategy

The success of restorative electrical therapies in paralyzed individuals relies on the possibility of regaining spatial and temporal control over the remnant muscles. In the case of hand paralysis following spinal cord injury or stroke, only residual limb activity remains, undermining the control stimulation through peripheral body signals. Cortically-driven protocols create promising alternatives to achieve natural voluntary control over electrical stimulation. In chapter 3, we showed that intrafascicular peripheral nerve stimulation could produce selective activation of the wrist and fingers in monkeys using only a few stimulation channels. Furthermore, in a proof-of-concept experiment we demonstrated that stimulation amplitude could be coupled to natural brain activation to restore hand movements during a functional grasping task. In this initial implementation, the stimulation was not delivered based on the direct activation of voluntary cortical inputs but was derived from naturally-occurring cortical dynamics. To encourage the translation of intrafascicular implants to the clinic, in this chapter, I propose an intuitive direct control framework for the modulation of peripheral nerve stimulation in monkeys. I developed a direct control algorithm in which the control space was confined to a low-dimensional manifold associated with a hand motor task. I characterized the ability of the monkey to learn and adapt to this new control modality in a two-degrees of freedom brain control task. Ultimately, I evaluated the feasibility of linking low-dimensional cortical inputs to a peripheral nerve implant to trigger flexion and extension movements of the hand.

The content of this chapter recapitulates the results obtained in this preliminary study and suggests key elementary insights for the development of a simple and robust cortical control strategy.

Contributions: Responsible for the project. I trained the animal, designed the experimental protocol, designed and implemented the experimental setup, performed the experiments, supervised a master student, Evgenia Roussinova, for the data analysis, analyzed the data, wrote the text, and prepared the figures.

4.1. Abstract

A potential treatment for people suffering from motor neurological disorders or traumatic lesions rests in bridging control signals from the brain to the underlying functional muscles through artificial connections. Previous studies have relied on brain machine interfaces (BMIs) to link cortical activity to functional electrical stimulation (FES) of the muscles in order to partially restore arm and hand movements in clinical applications (Ajiboye et al., 2017; Bouton et al., 2016). These works have largely relied on biomimetic cortical decoders for improved prediction performance and intuitive use (Carmena et al., 2003; Collinger, Wodlinger, et al., 2013; Hochberg et al., 2012; Irwin et al., 2017). However, these algorithms require complex initial training and frequent re-calibration (Jarosiewicz et al., 2015). In parallel, neural adaptation studies have also demonstrated that animals can learn nearly arbitrary, nonbiomimetic decoders, and create robust neural mapping for the reliable control of a prosthetic device (Fetz, 1969; Ganguly and Carmena, 2009; Koralek et al., 2012; Moritz et al., 2008; Radhakrishnan et al., 2008). In this preliminary work, we investigate the possibility of fixing such arbitrary neuroprosthetic control into an intuitive low-dimensional neural space, derived from the neural ensemble (Gallego et al., 2017) activity recorded during a grasping task. We evaluate the ability of a monkey to adapt to such control modalities over several months, and assess the quality and stability of control in a bi-dimensional task. In a pilot experiment, we test the coupling of neural ensembles commands to a peripheral stimulation interface to elicit opening and closing of the hand. This exploratory study aims at providing basic building blocks for the design of a functional, simple and robust brain-to-nerve interface.

4.2. Introduction

Brain-machine interfaces (BMIs) have emerged as an efficient and instinctive way to control assistive devices in people suffering from upper-limb paralysis. Recent clinical studies have relied on BMI for the reanimation of paralyzed muscles through functional electrical stimulation (Ajiboye et al., 2017; Bouton et al., 2016; Colachis et al., 2018), or the driving of robotic limbs (Collinger, Wodlinger, et al., 2013; Hochberg et al., 2012; Wodlinger et al., 2015). These endeavours employed sophisticated neural decoders, which translate neural activity from the motor cortex into motion commands. They represent important demonstrations in the field of BMI and allow patients with severe paralysis to partially regain motor functions. However, most of these approaches focus on “reaching” arm movements (Collinger, Wodlinger, et al., 2013; Hochberg et al., 2012) or are limited to the decoding and elicitation of simple grasp patterns (Ajiboye et al., 2017; Colachis et al., 2018). Continuous neural decoding of whole hand kinematics has been achieved in monkeys (Irwin et al., 2017) and was later refined for the prediction of single-digit movements (Vaskov et al., 2018). Despite this important proof-of-concept, to date, no BMI has been implemented for the restoration of functional precise hand motion in clinical applications. Critical barriers to the clinical development of this technology include the need to reliably decode a large collection of finger movements for an extended period of time (Gilja et al., 2011), and to efficiently integrate these new motor control paradigms in the natural body scheme of the user. While instabilities in neural recordings can be addressed by using fast calibration algorithms (Brandman et al., 2018), self-calibrating techniques (Jarosiewicz et al., 2015), or stabilization methods (Degenhart et al., 2020), these approaches have not yet been tested for fine motor skills decoding. Additionally, the independent and simultaneous control of fine finger motor commands (Vaskov et al., 2018), as well as the cognitive load imposed on the user, remain to be investigated.

A less natural, yet, more direct way to translate cortical commands into control signals is through direct cortical control. This method involves a direct artificial link between the neural firing rate and the controlled variable (cursor on a screen for example). It relies on the ability of the brain to adapt to new sensorimotor modalities (Shadmehr and Mussa-Ivaldi, 1994; Thach, 1978), and has been employed in paralyzed monkeys to generate bidirectional wrist torque through FES, and to control multiple neuron-muscle pairs simultaneously (Moritz et al., 2008). Other studies have reported successful 3D-control of neuroprosthetic devices using direct cortical control in monkeys (Helms Tillery et al., 2003; D. M. Taylor et al., 2002). Direct control paradigms provide interesting opportunities for the robust, independent and simultaneous control of artificial cortical signals that can be coupled to any output variable. However, researchers have so far relied on single-unit activity to drive the controlled variable, reducing the long-term applicability of this technique (Perge et al., 2013).

Rather than focusing on single-cell activity, recent studies have considered the analysis of neural dynamics to understand motor behavior (Ahrens et al., 2012; Churchland et al., 2012; Churchland and Shenoy, 2007; Churchland et al., 2010; Cunningham and Yu, 2014; Elsayed et al., 2016; Sussillo et al., 2015). In particular, Gallego et al. discussed the existence of low-

dimensional manifolds recapitulating a significant fraction of neural variability (Gallego et al., 2017). They argue that the connectivity of underlying brain networks constrains the patterns of neural population activity, confining it to such low-dimensional spaces. Axes spanning the manifold are linearly independent patterns, called “neural modes”, that reflect the contribution of each neural unit to the motor behavior. Interestingly, Sadtler and colleagues developed a center-out brain-controlled task in monkeys in which the cursor control space was confined to a 10-dimensional intrinsic neural manifold (Sadtler et al., 2014). They linearly mapped the 2-dimensional (2D)-cursor kinematics to the latent variables and demonstrated that, upon learning the task, the monkey more easily adapted to modifications of the decoder requiring the use of existing neural modes than to modifications requiring the acquisition of new neural modes.

Building on these interesting results, we investigated the ability of a monkey to actively learn a direct control paradigm based on a low-dimensional motor manifold. This pilot study aimed at evaluating the level of performance achieved using a fixed, yet intrinsic, neural manifold for the independent control of two degrees of freedom. We inferred that low-dimensional manifold-based direct control would provide robust and long-lasting control properties without the need to adapt to day-to-day neural variability. We computed the neural modes capturing a significant fraction of population covariance during a functional grasping task (see chapter 2 and Barra et al., 2019) and used fixed latent variables to direct the movement of a cursor throughout the training. We evaluated the adaptation of neural dynamics when introducing novel motor control modalities and assessed the direct control performance throughout weeks of training. Finally, we investigated the possibility of using direct control commands for the elicitation of graded hand movements. We modulated the stimulation amplitude of a peripheral nerve implant (see chapter 3) based on the activation of one latent variable, and measured the effects on the direct-control performance.

4.3. Methods

4.3.1. Animal involved in this study

The experiments were conducted on 1 female adult macaque monkey, 5 years of age (*Macaca fascicularis*) and weighing 3.1 kg. The animal was group-housed in an enriched indoor room and had access to water and food ad libitum. The experimental protocol was elaborated in compliance with the national law on animal protection and approved by the Federal and local veterinary authorities (authorization number 2017_03_FR, see chapter 3).

4.3.2. Surgical procedures

All surgical procedures were conducted under aseptic conditions and general anaesthesia (see chapter 3 and Badoud et al., 2017).

Brain array surgery

The monkey was implanted with three microelectrode arrays. One array, with 48 channels was implanted in the right hemisphere in the primary motor cortex (M1) hand region (Blackrock Microsystems, USA, 400 μm pitch, 1.5 mm tip length). Primary somatosensory (S1) and premotor (PMv) cortices were also implanted, but were not analyzed for this study. Implantation procedure is detailed in chapter 3.

Peripheral nerve electrode and intramuscular leads implantation

Two custom-made chronic intrafascicular peripheral nerve implants (TIMES) (Boretius et al., 2010) were inserted in the median and radial nerves of the monkey, as described in chapter 3. The animal also received 8 pairs of Teflon-coated stainless steel wires to chronically record electromyographic (EMG) activity from flexor and extensor muscles of the hand. Implantation procedure is detailed in chapter 3 and chronically implanted muscles are reported in **Appendix Table A.3** under *Mk-OL_c*.

4.3.3. Experimental paradigm

The animal was trained on two different tasks. First, a behavioral grasping task (chapter 2, and Barra et al., 2019), that was used to compute the axes spanning the motor neural manifold, i.e. the “neural modes coefficients matrix”, $U_{weights}$ (**Figure 4.1 a-b**). Second, a direct control task, in which the animal was trained to actuate a computer screen cursor by modulating latent cortical variables within the neural manifold (**Figure 4.1 a-b**). Ultimately, we coupled the latent cortical variables to the stimulation amplitude of a peripheral nerve implant during the direct control task (**Figure 4.1 a,c**).

Behavioral motor task

In brief, several small, custom-molded, silicone objects (cylindrical, spherical, and small triangular objects) were affixed to the end of a robotic arm (Intelligent Industrial Work Assistant, IIWA – KUKA, Augsburg, Germany) with seven degrees of freedom. A C++ custom control software enabled the positioning of the robot in space. The monkey was trained to freely reach for the object, grasp it using only the right hand, and then pull it towards the body. While the object was displaced from its initial position, the robot exerted a force towards the initial position that was proportional to the horizontal displacement. Each trial was deemed successful after the position of the object passed a pre-determined distance threshold. Upon success, the monkey received an automated liquid food reward through a sipper tube. M1 cortical activity recorded during the task was bandpass-filtered (750 to 5000 Hz) and thresholded ($-6.25 \times$ root mean square value) to extract spike events. We computed the firing rate for each channel from 10 ms bins, and applied principal component analysis (PCA) on all channels to derive the

“neural modes coefficient matrix”, $U_{weights}$ such as:

$$Y = U_{weights}^T * X \quad (4.1)$$

where X corresponds to the centered neural firing rates of the 48 M1 channels and Y to the projection of the firing rates in the principal components (PCs) space (**Figure 4.1 b**). Cortical data collected over an entire session were used in the PCA, including data collected in between trial periods. The total number of reaching trials for this initial calibration session consisted of 625 trials.

Following this calibration phase, the computed “neural modes coefficients matrix” was kept constant and used as a linear transformation between firing rates and cortical activity along the main neural modes (Gallego et al., 2017) in subsequent experimental sessions. More precisely, we used $U_{weights}$ to compute the latent cortical variables, S, along the main directions of variance such as:

$$S = X * U_{weights} \quad (4.2)$$

where X corresponds to the centered neural firing rates of the 48 M1 channels and S the latent variables, i.e. the neural activity projected on the columns of the $U_{weights}$ matrix. In this work, we refer to S_2 and S_3 when describing the latent variables along the second and third neural modes (**Figure 4.1 a-b**). These latent variables were used as control signals in the direct control experiments (see next section Methods).

Direct brain control task

The monkey was seated in a custom primate chair (chapter 2, **Figure 2.2 a-b**). The left arm was immobilized using padded plastic restraints to prevent movements of the arm and hand. A large computer screen supplied visual feedback. For a trial to be deemed successful, the monkey first had to maintain latent cortical activity under a baseline level for 500 ms, then up-regulate it to reach a certain threshold within 8 seconds. Latent cortical activity controlled a moving cursor that provided real-time feedback to the animal. Upon initiation of a trial, the baseline target, represented as an empty square, appeared at the bottom of the screen (**Figure 4.3 c**). The animal was required to maintain the cursor within the square for 500 ms. Upon success in this first phase, the baseline square disappeared and a rectangular target appeared on the upper part of the screen (**Figure 4.1 a**). The animal had to displace the cursor into this target and hold it for a fixed time (100-150 ms) to succeed in the task and receive an automated liquid food reward.

Throughout the training, the cursor displacement was variably mapped to cortical activity. Based on the dynamics of latent variables during the behavioral motor task (see Results and **Figure 4.3 a-b**), we chose the neural activity projected along the 2nd and 3rd neural modes (2nd and 3rd columns of $U_{weights}$), S_2 and S_3 , to drive the cursor in the vertical and horizontal directions respectively (**Figure 4.1 a**).

The kinematic components of the cursor were computed as:

$$\begin{aligned} x &= g_3 * S_3 - b_3 \\ y &= g_2 * S_2 - b_2 \end{aligned} \tag{4.3}$$

where x represents the horizontal component of the cursor and y the vertical component. The gains g_2 and g_3 were manually assigned to 0.25 and 0.4 respectively based on the screen dimensions and the amplitude of modulation of latent variables S_2 and S_3 . They were kept constant for the duration of the experiment. The offset values b_2 and b_3 were adjusted for each session based on the neural baseline activity (see **Figure 4.3 c**).

Direct brain control training timeline

The timeline of the direct brain control training is presented in **Figure 4.1 c**. During the first 10 days, the monkey was trained to modulate cortical activity along only one neural mode. The cursor was moved only along the vertical direction based on S_2 activation, to reach a vertical target (**Figure 4.1 c** (1)). We then introduced a horizontal component to the displacement of the cursor, proportional to S_3 activation, forcing the monkey to up-regulate S_2 activity and down-regulate S_3 to successfully reach the vertical target. We then progressively displaced the target along the horizontal axis to promote a simultaneous modulation of S_2 and S_3 (**Figure 4.1 c** (2)). After 1 week, we set the vertical component of the target to zero and retained only the horizontal component to encourage the monkey to exclusively modulate S_3 cortical activity (**Figure 4.1 c** (3)). Once the animal began achieving high rates of success in this task, we started alternating vertical and horizontal targets (**Figure 4.1 c** (4)), and finally introduced a diagonal target. The next 20 days of recordings consisted of the alternation of those 3 different targets (**Figure 4.1 c** (5)). The animal was then implanted with the peripheral nerve interfaces and the EMG implants, and one week was devoted to post-surgery recovery. During the last two weeks of experiments, we evaluated the feasibility of using direct control commands to drive the amplitude of stimulation of the peripheral implants.

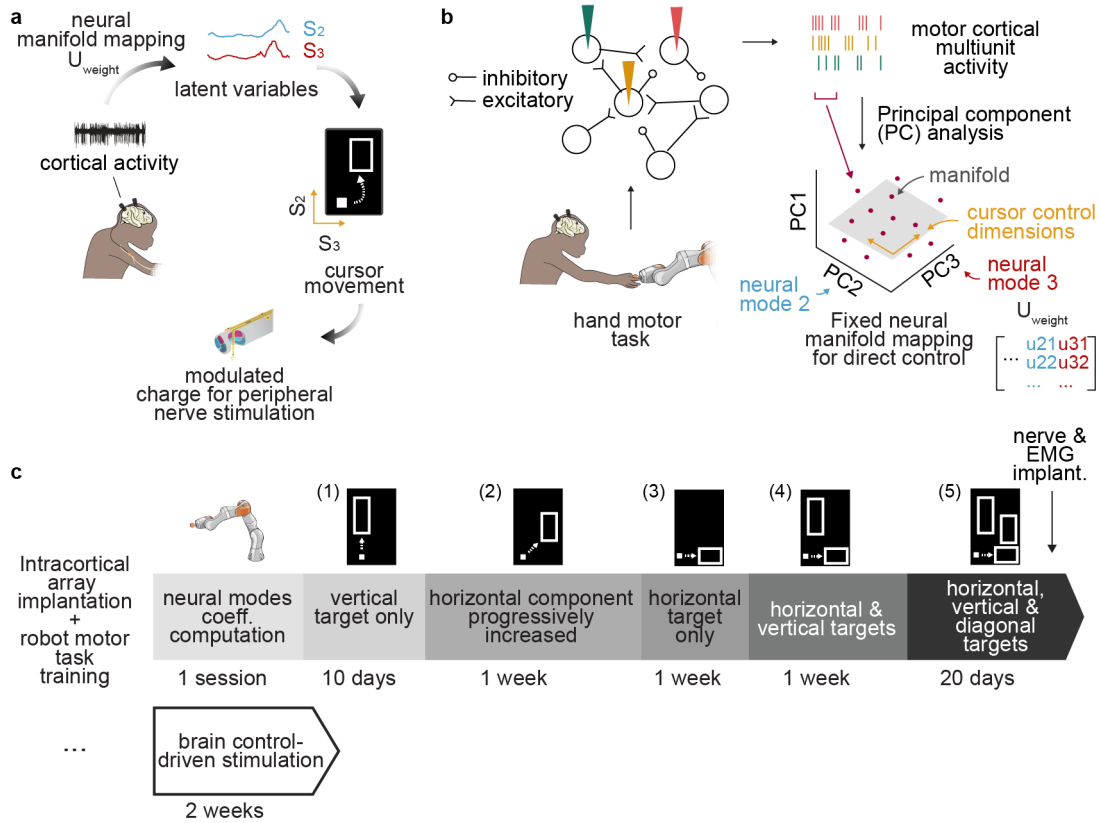


Figure 4.1 – Training of 2D cortical control using cortical manifolds. **a)** Behavioral task setup. The monkey moves a cursor (white square) in two dimensions (orange arrows) by modulating its neural activity. The neural manifold mapping consisted of first mapping the population neural activity to a cortical manifold using PCA, then to vary the vertical and horizontal cursor coordinates based on the variation of the latent variables along the second and third neural modes (S_2 and S_3) respectively. The latent variables were also used to modulate the stimulation amplitude of an intrafascicular peripheral nerve implant after direct control training was completed. **b)** Simplified, conceptual illustration using three recording channels. The firing rate recorded during a hand motor task (Barra et al., 2019 and chapter 2) and observed on each electrode in a brief epoch define a point (pink dots) in the neural space projected along the PCs. Each PC is labelled hereafter as a neural mode. Neural modes coefficients correspond to the column of the PCA coefficient matrix $U_{weights}$. The neural manifold (grey plane) characterizes the prominent patterns of co-modulation along the second and third neural modes. Neural activity maps onto the control space (orange arrows) to specify cursor displacement. **c)** Experimental timeline for the training of the animal on the direct control task. The pictograms illustrate the different targets (empty rectangles) the monkey had to reach with the cursor (white square).

4.3.4. Data acquisition

Neural signals were acquired with a Neural Signal Processor (Blackrock Microsystems, USA) using the Cereplex-E headstage with a sampling frequency of 30 kHz. Multiunit activity was thresholded to extract spike events ($-6.25 \times \text{root mean square value}$). Timings of the spikes were extracted in a control computer through a custom-written C++ routine (Visual Studio®, USA). Artifacts were removed (see next Artifacts removal Methods section) and latent cortical variables were computed in the control computer by projecting the firing rates of each channel

onto the “neural modes coefficient matrix” $U_{weights}$. The latent variables values along the second and third neural modes, S_2 and S_3 , were streamed through UDP to a training computer program developed in MATLAB (Matlab, The MathWorks Inc, MA). This program converted the latent variables into cursor coordinates, managed the placement of the visual targets on the screen and their alternating sequence, and controlled a peristaltic pump delivering the liquid food reward. Timing marking the different steps in the task, such as start an end of trials, success, display of the visual targets, reward tone etc, were sent as digital triggers to the neural signal processor through a synchronization board (National Instruments, US). In the behavioral reaching task, hand and arm kinematics were recorded at 100 Hz using a 14-camera motion capture system (Vicon, Oxford, UK). Markers were placed on the elbow and wrist.

For the sessions in which direct control was used to trigger peripheral nerve stimulation, bipolar EMG were acquired at 12 kHz through the RZ2 processor (RZ2, Tucker David Technologies, USA) after amplification (1000×, PZ5, Tucker David Technologies, USA) using a 16-channels active headstage (LP32CH - 16, Tucker Davis Technologies, USA). Grip pressure was measured using a custom-made sensor (chapter 2 and Barra et al., 2019), and wrist torque was acquired using a commercial dual-range force sensor (Vernier, EducaTEC AG, CH). Pressure and force signals were saved at 1 kHz in the RZ2 processor. Pressure and torque voltage values were converted in Newtons using respective calibration curves (Barra et al., 2019, chapter 2 and ¹).

Artifact removal

During the direct control experiments, movement artifacts in neural recordings were suppressed online by ensuring that if more than 40 channels displayed a firing rate superior to 20 spikes/s, these channels were discarded. During electrophysiology experiments, we removed stimulation artifacts from neural recordings by subtracting from each channel the number of spike events recorded in a reference channel found to be silent outside stimulation bursts.

Hand movement monitoring

We assessed the absence of hand movements or muscle contraction during the direct control task by monitoring kinematics, EMG activity and force exerted at the wrist. While it must be noted that the animal explored the possibility to contract the hand or lower arm during the first sessions of direct control, the EMG-artifacts removal procedure prevented the use of such strategy. After only a few session, the monkey stopped extraneous movements and remained immobile during the task. Hand movements were then nearly non-existent during the direct control trials (data not shown) and should therefore have no effect on learnability or performance during the task. We found no correlation between the residual muscular activity (**Figure 4.2**) and the success in the task, nor did we observe any flexion or extension force applied at the wrist (**Figure 4.2**).

¹Dual-Range Force Sensor User Manual – Vernier. <https://www.vernier.com/manuals/DFS-BTA>

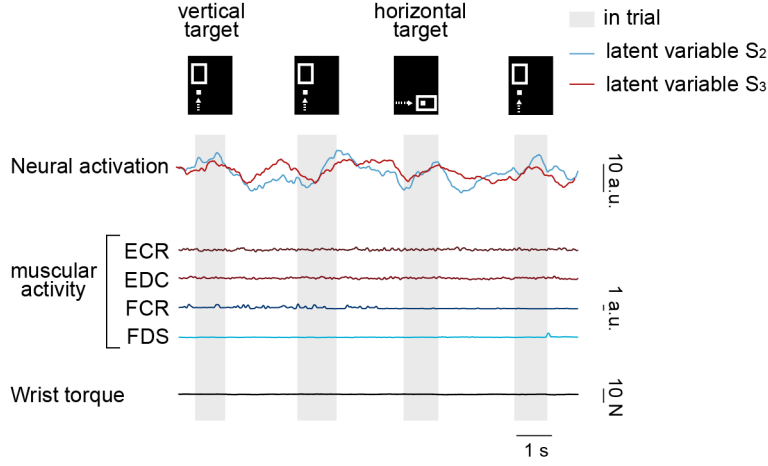


Figure 4.2 – Hand muscular activity during direct control. Representative examples of neural latent variables, muscular activity and isometric wrist force applied by the monkey on the fixated hand during the direct control task for the vertical and horizontal targets.

4.3.5. Direct brain control of peripheral nerve stimulation

The experiment started with a calibration of approximately 10 minutes, during which the animal performed the direct brain-control task with alternating vertical and horizontal targets. This calibration phase was used to determine the range of latent variables modulation achieved by the animal on that day, and to tune the stimulation parameters. Because the baseline cortical activity varied across days, the threshold for initiating the stimulation bursts, together with the gain, had to be adjusted. Namely, we computed S_{max} , the maximum latent variable activation measured during baseline trials and S_{thresh} , representing $\sim 20\%$ of S_{max} . We then derived $[I_{min}, I_{max}]$ the current range to be used for the stimulation with I_{min} corresponding to the minimum amplitude at which movement twitch appeared, and I_{max} , the amplitude at which strong contraction movement was observed.

We then modulated the current injected through the intraneural peripheral nerve implant at time t , $I(t)$ as a function of the neural activation at time t , $S(t)$:

$$I(t) = I_{min} + gain * (S(t) - S_{thresh})$$

$$gain = \frac{I_{max} - I_{min}}{S_{max} - S_{thresh}} \quad (4.4)$$

$$if I > I_{max}, I = I_{max}$$

During stimulation trials, the animal performed the direct brain-control task, while cortical activity drove the cursor movement and the stimulation amplitude. The hand was attached to

a wrist torque transducer (Vernier, EducaTEC AG, CH) or placed on a custom-designed grip pressure sensor (see chapter 2 and Barra et al., 2019), depending on the movement triggered by the stimulation. Stimulation bursts were delivered only when the animal succeeded in the baseline phase of the trial, i.e. during the phase where it had to displace the cursor toward the horizontal or vertical target. Stimulation was interrupted in between trials.

The user could adjust stimulation parameters (amplitude, gain and thresholds) during the experiment using a graphical user interface displayed on the control computer.

Stimulation pulses were delivered as asymmetric charge-balanced cathodic pulse with a pulsewidth of 40 μ s and a frequency of 50 Hz. The stimulation channels were chosen based on observed triggered movements. We used a channel located on the median nerve TIME to recruit the flexor muscles and trigger the closing of the hand; and a channel of the radial nerve implant to recruit the extensor muscles actuating the opening of the hand.

Radial nerve stimulation amplitude was mapped to S_2 latent variable and median nerve stimulation was mapped to S_3 latent variable. Stimulation was delivered only on one channel per session. These two channels were used in independent sessions.

4.3.6. Data analysis

Modulation of latent variables during behavioral task

We assessed the cross-correlation between the cortical activity projected along each neural mode of the manifold and the velocity of the wrist during the behavioral task (**Figure 4.3 a-b**). The wrist marker trajectory was smoothed with a moving average window of 100 ms. The wrist velocity was computed as the speed of the wrist marker component parallel to the reaching movement. The wrist velocity profile was smoothed (moving average window of 100 ms) and cross-correlated with the latent variables along the three first PCs (moving average window of 100 ms) between the start and the end of the movement. The cross-correlation was calculated on z-score signals using the Matlab (Matlab, The MathWorks Inc, MA) function `xcorr` with the normalization option 'normalized'. The cross-correlation for lags in the range [-200 ms, 0 ms] (wrist velocity shifted backwards in time with respect to the latent variable) was analyzed and the maximum cross-correlation index was reported in **Figure 4.3 a-b**. The modulation depth was evaluated along each neural mode by applying a 50 ms moving average and computing the difference in latent variable activation between the maximum value and the average value measured in the baseline box.

Computation of baseline activity

For each trial, the baseline activity of S_2 and S_3 latent variables was computed over a 300 ms window from the last entrance of the cursor in the baseline box (**Figure 4.3 c**).

Calculation of channel and latent variable modulation depth

The modulation depth of latent variables and M1 recording channels (**Figures 4.4, 4.5, 4.6 and 4.7**) was computed as the difference between the maximum activation in the target box and the average activation in the baseline box for each trial. Latent variables were recorded directly through our acquisition system (see data acquisition section), while firing rates were computed from spike events (thresholding at $-6.25 \times$ root mean square value) on bins of 100 ms and smoothed using a 100 ms-centered moving average. The average S_2 trace across trials for the vertical target was computed by interpolating S_2 between the start and the end of each trial and apply a 100 ms centered moving average smoothing (**Figure 4.4 b**).

Perievent time histograms of neural firing rate

Perievent time histograms representing the dynamics of M1 channel activation across the direct control task (**Figures 4.5 c and 4.6 d**) were obtained by normalizing the neural activity on each channel and sorting them in temporal order of maximum activation. We considered a window of 400 ms centered on the maximum activation peak of the latent variable.

Performance assessment in the direct control task

Trials were deemed successful if, in under 8 seconds, the monkey was able to 1) maintain the cursor in the baseline box for 500 ms and, 2) reach the target box and hold the cursor inside for 100-150 ms. "First attempt trials" refer to trials in which the monkey successfully maintained the cursor in the baseline box without error (back and forth outside the box), reached the target box directly, and remained inside for 100-150 ms. The time to successful task completion was computed as the time between the appearance of the baseline box on the screen and the success of the trial (**Figures 4.4 c, 4.5 a, 4.6 b, and 4.8 d**).

Single and dual modulation strategies

For the horizontal target, trials were considered to rely on a dual modulation strategy if the modulation depth of the latent variable S_2 exceeded 30% of the modulation depth of the latent variable S_3 , when reaching for the target. Conversely, for the vertical target, trials were considered to rely on a dual modulation strategy if S_3 modulation depth exceeded 30% of S_2 modulation depth (**Figure 4.7 d**).

Electromyographic signal processing

Differential EMG signals were band-pass filtered offline (50-500 Hz). A Savitzky-Golay filter (2.5 ms smoothing window) was applied to remove stimulation artifacts. The envelope was computed by rectifying the EMG and applying a low-pass filter at 6 Hz. Signals were normalized to the maximal muscle activity obtained across the trials of interest.

Quantification of stimulation trials

We quantified the ability to independently modulate the 2^{nd} and 3^{rd} latent variables when stimulation was delivered to the nerve. For median nerve stimulation based on the activation of the 3^{rd} latent variable S_3 , we considered "stimulation during trials of interest" trials to be those in which stimulation was delivered for the horizontal target and shut down for the vertical target. "Stimulation outside trials of interest" trials constituted trials where stimulation was delivered for the vertical target. Conversely, for the radial nerve stimulation based on the activation of the 2^{nd} latent variable S_2 , we quantified "stimulation during trials of interest" trials as those in which stimulation was delivered for the vertical target and shut down for the horizontal target. "Stimulation outside trials of interest" trials constituted trials where stimulation was delivered for the horizontal target (**Figure 4.8 d**).

Statistics

All computed parameters were quantified and compared between tested groups unless otherwise specified. All data are reported as mean \pm SEM, unless otherwise specified. Significance was analysed using non-parametric Kruskal-Wallis test with Bonferroni correction for multiple comparisons with $n=3$ and Tukey-Kramer correction with $n>3$.

4.4. Results

4.4.1. Calibration of a direct cortical control space based on neural manifold directions

In the initial phase of this study, we derived an intuitive control space for the direct cortical control of two degrees of freedom through latent cortical dynamics. To potentially use this control strategy to drive a stimulation device for the restoration of hand movements, we chose to base the neural control space on neural components associated to a hand motor task. We recorded the cortical activity of a monkey performing various types of grasps (see Methods and Barra et al., 2019) and derived a low-dimensional neural manifold, in which axes represented the directions of most variance in the task (**Figure 4.1**). Namely, we studied the neural activation along the first three axes of the manifold, recapitulating 13%, 8% and 5% of the neural variance, respectively. The activation along the first neural mode was only slightly tuned during the reach (**Figure 4.3 a-c**), while along the second neural mode, we observed a preferential tuning during the reach (**Figure 4.3 a-b**). Conversely, activation along the third neural mode was negatively tuned during the reach and positively tuned during the grasping phase of the movement (**Figure 4.3 a-b**). Modulation depth across the movement was found to be higher along the 2^{nd} and 3^{rd} neural modes than along the 1^{st} , supposing a larger working range to finely tune neural activity along these two components (**Figure 4.3 c**). Altogether, these results motivated the decision to use the 2^{nd} and 3^{rd} latent variables as control signals for the direct control training.

The "neural modes coefficient matrix" computed during the motor task was fixed to evaluate the adaptation of the monkey to a new control modality. The 2nd and 3rd latent variables were used to drive a cursor movement in the vertical and horizontal directions, respectively, to reach a target box on a screen, following a period of resting activity (see Methods). The gains mapping the latent variables to the cursor displacement in two directions were kept constant across sessions. However, baseline activation levels were adapted throughout the sessions to account for variations in neural recordings (Dickey et al., 2009; Jackson and Fetz, 2007; Perge et al., 2013) (**Figure 4.3 c**).

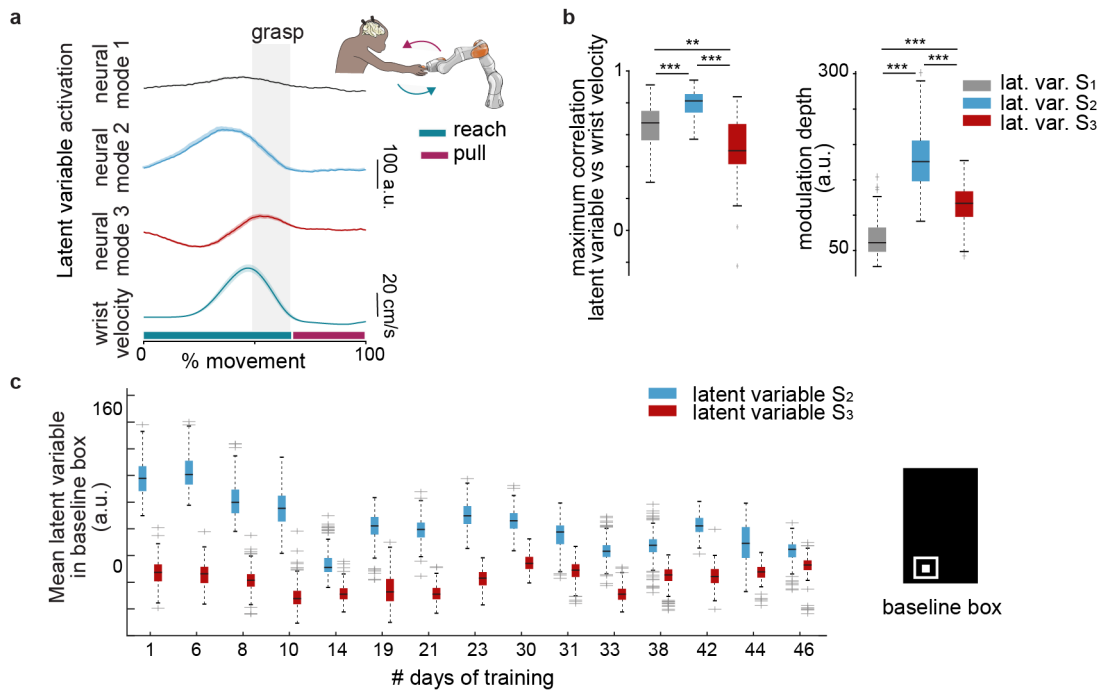


Figure 4.3 – Choice of control space and baseline activity drift. **a)** Mean latent variable activity computed along the first three neural modes during the behavioral grasping task along with the average wrist velocity ($n = 54$ trials) **b)** Left: maximum cross-correlation coefficient between the latent variable along one of the neural modes and the velocity profile of the wrist ($n = 54$ trials). Right: modulation depth of each latent variable activation waveform (right $n = 54$ trials). Data are computed on the session used to derive the neural modes coefficient. **c)** Mean latent variable activation in baseline box throughout the training for S_2 and S_3 variables. Because of changes in baseline levels of cortical activity, baseline and target boxes had to be slightly adjusted during the training. The gains for moving the cursor vertically and horizontally were kept fixed. ** $P < 0.01$, *** $P < 0.001$ - a.u. : arbitrary units

4.4.2. Rapid learning of a one-dimensional direct control through neural mode activation

During the first 10 days of training, we tested the ability of the monkey to adapt to fixed weights employing a single latent variable. To this aim, we presented a visual task to the animal in which it was required to maintain neural activity at rest for 500 ms, then modulate the neural activation along the 2nd neural mode to operate the vertical movement of the cursor and reach

a vertical target on the screen. Within the first few days of training, the monkey successfully learned to modulate the firing rate of channels associated with high neural weights to steer the cursor (Figure 4.4 a) in a reliable manner (Figure 4.4 b). Throughout the training, the number of targets attained at the first attempt monotonically increased, while the time necessary to succeed in a trial decreased (Figure 4.4 c-d). Interestingly, the overall modulation depth did not increase during this first training phase, suggesting that a higher success rate was more likely linked to the speed of execution than to the ability to more strongly tune latent cortical activity (Figure 4.4 d-e).

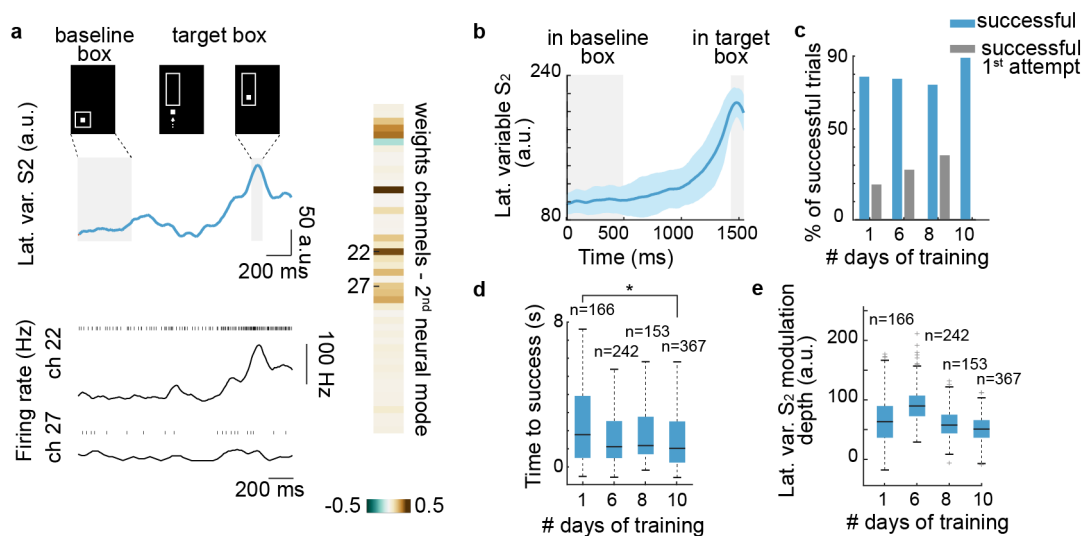


Figure 4.4 – Rapid learning of one-dimensional control of the cursor. **a)** Modulation of the latent cortical activity along the second neural mode, labeled S_2 , drives the vertical displacement of the cursor (white square). The monkey first learned to maintain neural activity low for 500 ms thereby keeping the cursor in a baseline box (empty square), then modulated neural activity to steer the cursor towards a vertical target. Representative trial from training day # 6. **b)** Mean neural activity along the second neural mode during the vertical target task ($n=166$ trials, first training day). Shaded area represents standard deviation. **c)** Proportion of successful trials (i.e. completed in < 8 seconds) during the first 10 days of training on the vertical task. **d)** Duration of a trial from the appearance of the baseline box on the screen to the successful completion of the trial. **e)** Modulation depth of the latent variable along the second neural mode S_2 throughout the first 10 days of training. * $P < 0.05$ - a.u. : arbitrary units

4.4.3. Progressive adaptation to a second degree of freedom of direct cortical control

After successfully training the monkey on the control of one degree of freedom, we introduced a horizontal component to the cursor's displacement associated with the neural activation along the 3rd neural mode. We then progressively shifted the target displayed on the screen to the right, to promote the modulation of this new cortical variable, in addition to the neural activation of the 2nd neural mode (Figure 4.5 a). Following the introduction of this new component, we observed a drop in performance, consistent with the disruption of a previously learned strategy (Figure 4.5 a). The performance then gradually increased to reach

levels comparable to the ones obtained at the end of the first days of training (**Figure 4.5 a**, day 19).

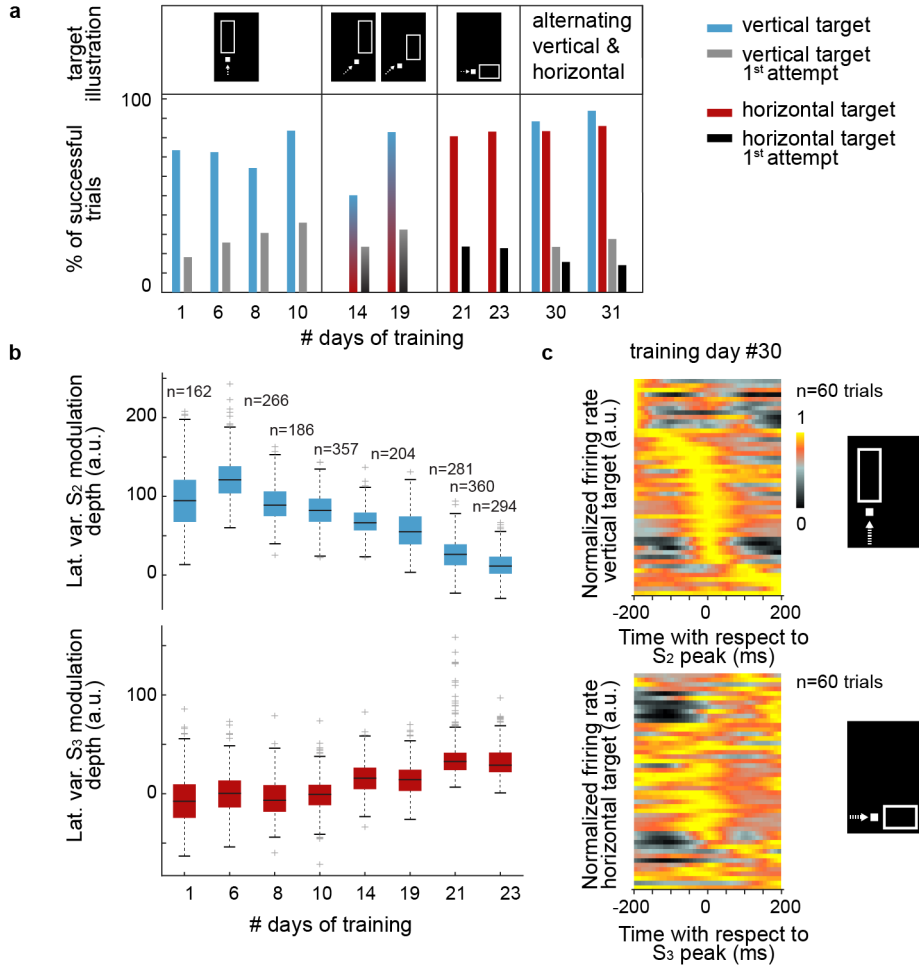


Figure 4.5 – Progressive adaptation to a second degree of freedom of cortical control. **a)** Proportion of successful trials (i.e. completed in <8 seconds) for the vertical target task and for tasks involving a second degree of freedom to the cursor. From day 1 to day 10, the cursor moved only vertically as a function of the latent variable along the second neural mode (S₂). On day 12 we introduced a horizontal component, driven by the modulation of the latent variable along the third neural mode (S₃). The target was progressively displaced to the right of the screen to promote S₃ activation. **b)** Modulation depth of the latent variable along the second and third neural modes throughout the training. **c)** Average normalized M1 firing rate during the vertical target (top) and horizontal target (bottom) tasks. The reference condition for aligning neural signals is the vertical target task. a.u. : arbitrary units

We then evaluated the ability of the animal to modulate the neural activity along the 3rd cortical mode only and demonstrated levels of performance superior to 80%. However, the capacity to reach the target at the first attempt was reduced compared to the vertical case (**Figure 4.5 a**, day 21 to 31). After 1 month of training, the animal was able to consistently alternate between the vertical and horizontal targets and exploit different patterns of neural activation for the two targets (**Figure 4.5 c**). This second training phase was characterized by a

reduction of variance in the modulation depth of the the 2^{nd} and 3^{rd} latent variables (**Figure 4.5 b**). The modulation depth of the 2^{nd} latent variable (steering the vertical cursor's motion) progressively decreased while the modulation depth of the 3^{rd} latent variable (controlling the horizontal cursor's displacement) increased (**Figure 4.5 b**).

4.4.4. Successful independent and simultaneous modulation of two degrees of freedom

Following the training on the vertical and horizontal targets, we introduced a third diagonal target and randomly presented these three conditions on the screen, each with equal probability. Reaching the diagonal target required the displacement of the cursor along the horizontal and vertical components simultaneously. We measured the modulation depth along the 2^{nd} and 3^{rd} neural mode for each of the three targets.

Our results demonstrate a significantly higher modulation of the 2^{nd} latent variable when the animal was presented with the vertical target, as compared to the horizontal condition. Conversely, activation of the 3^{rd} latent variable prevailed for the horizontal target (**Figure 4.6 a**).

Furthermore, in the trials featuring the diagonal target, we observed that the modulation depth of the 2^{nd} latent variable was comparable to the modulation obtained for the vertical target. Similarly, diagonal target presentation resulted in modulation depth values close to the horizontal target for the 3^{rd} latent variable. These findings are coherent with the joint activation of the two neural modes needed to attain the diagonal target (**Figure 4.6 a**).

Regarding the performance during the task, the introduction of the diagonal target did not impede the ability of the monkey to reach the two other targets (**Figure 4.6 b**). This observation potentially reflects the fact that no change in activation strategy was required to account for this novel condition. The proportion of successful trials fluctuated throughout the 3-targets training but generally remained above 80% for each target (**Figure 4.6 b**).

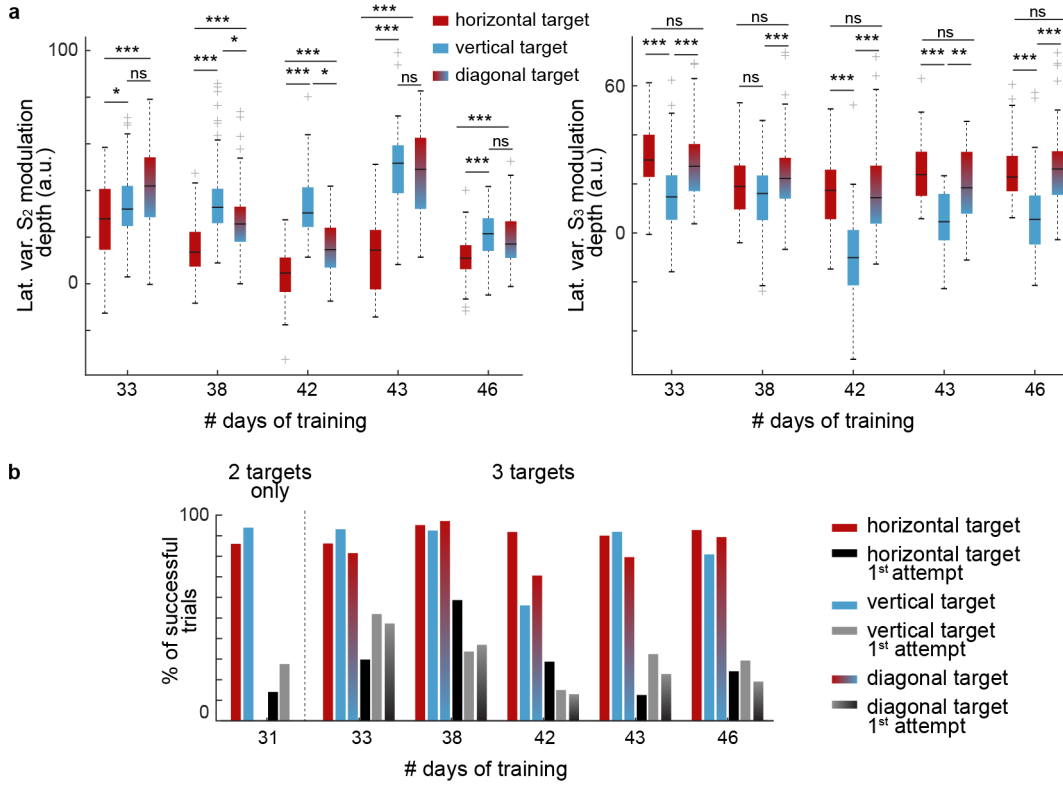


Figure 4.6 – Successful simultaneous modulation of two degrees of freedom. **a)** Evolution of the mean modulation depth of the latent variables along the second (left) and third (right) neural modes in sessions in which the monkey was presented with vertical, horizontal, and diagonal targets, alternatively. **b)** Proportion of successful trials (i.e. completed in <8 seconds) for the vertical, horizontal and diagonal targets, throughout the training. n.s P > 0.05, ** P < 0.01, *** P < 0.001 - a.u. : arbitrary units

4.4.5. Evolving strategies for the activation of two degrees of freedom via fixed cortical mapping

To evaluate the dynamic and continuous adaptation to fixed weights imposed on the commands of the cursor, we quantified the mean modulation depth of M1 intracortical channels during the various phases of the training (**Figure 4.1** and **Figure 4.7**). We first evaluated the firing rate modulation during the vertical target task (**Figure 4.7**, (1)), in which only the weights along the 2nd neural mode had an impact on the cursor. We then measured the average modulation depth when introducing a horizontal component to the cursor's displacement, driven by the neural activation of the 3rd neural mode (**Figure 4.7**, (2) and (3)). Finally, we investigated the cortical modulation depth when different targets were alternatively presented, and explored the strategy employed for each target (**Figure 4.7**, (4) and (5)).

Our results show that during the one-dimensional control towards the vertical target, the monkey strongly activated the channels associated with large neural weights along the 2nd neural mode, namely channels #3, 13, 16, 20 and 22 (**Figure 4.7 a** (1) (i)). Upon the introduction of the horizontal control component (**Figure 4 a** (2)), the animal reduced the activation of

channels #13 and #22, associated with a negative weight along the 3rd neural mode (**Figure 4.7 a** (2) (ii) and **Figure 4.7 b**).

Steering of the cursor in the horizontal direction (**Figure 4.7 b** (3)) was achieved by the concomitant activation of channel #20, associated with positive weights in both neural modes, and channels #25 and #27, linked to high positive coefficients in the 3rd neural mode (**Figure 4.7 a** and **Figure 4.7 b** (3) (iii)) .

After the monkey learned to modulate the brain activity in two directions, we alternatively presented the vertical and horizontal targets (**Figure 4.7 a-b** (4)) . Interestingly, in these sessions, the modulation of channels #13 and #16 completely vanished in the vertical condition (**Figure 4.7 a** (4) (iv)), potentially due to their negative weights on the 3rd neural mode (**Figure 4.7 b**), which resulted in task failure in the horizontal condition.

In the last phase of the training, we alternated between vertical, horizontal, and diagonal targets (**Figure 4.7 a-c** (5)). The monkey seemed to preferentially activate channel #22 having a positive coefficient along the 2nd neural mode, and negative coefficients along the 3rd neural mode in order to steer the cursor to the vertical target (**Figure 4.7 a** (5) (v)). Conversely, the completion of the horizontal task was achieved by the joint activation of several channels associated to positive weights along the 3rd mode, namely channels #20, 25 and 27 (**Figure 4.7 b** (5) (vi)). The diagonal target was efficiently reached by the combination of the two strategies, namely the activation of activation of channels used for both the vertical and horizontal targets simultaneously **Figure 4.7 c** (5) (vii)).

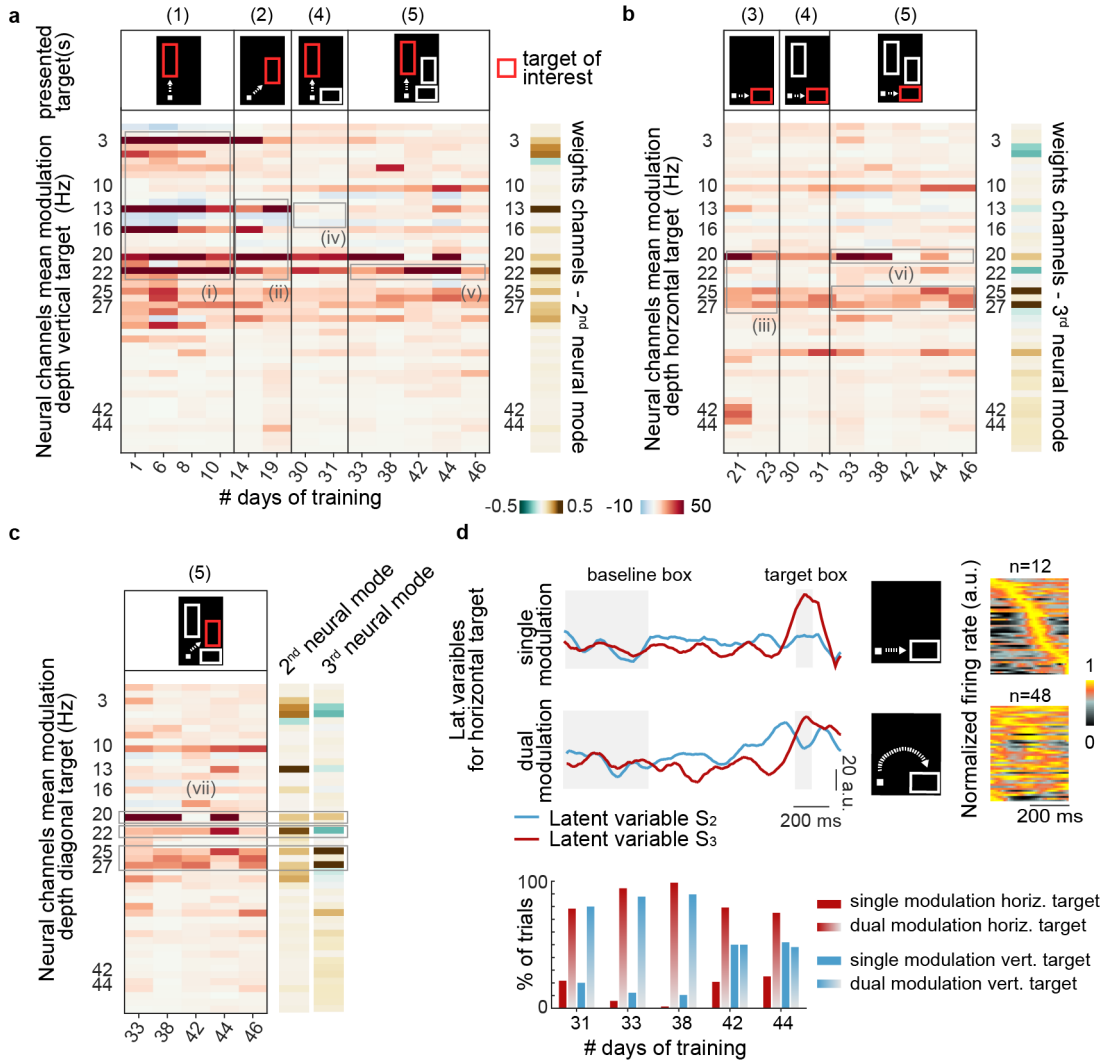


Figure 4.7 – Evolving strategies for the driving of 2D cursor using fixed cortical mapping. **a**) Evolution of the mean neural modulation depth of intracortical channels for the vertical target throughout the training. Different phases of the training are illustrated on top, with all the targets presented during the task (white empty rectangles) and the target to which modulation data corresponds (red rectangle). Numbering refers to the training phases reported in **Figure 4.1 c**. On the right, representation of the contribution weights for each channel along the 2nd neural mode. Grey rectangles with roman numerals highlight channels of interest (see Results). **b**) Evolution of the mean neural modulation depth of intracortical channels for the horizontal target throughout the training. Data are presented as in **a**). On the right, representation of the contribution weights for each channel along the 3rd neural mode. **c**) Evolution of the mean neural modulation depth of intracortical channels for the diagonal target throughout the training. Data are presented as in **a**) and **b**). **d**) Top left: representative latent variables (S_2 and S_3) for two different trials of the horizontal target. Single modulation refers to the strategy in which the monkey modulated only one latent variable to reach the target, while dual modulation refers to the asynchronous modulation of the two latent variables. Top right: normalized sorted average neural firing rates. The reference condition for aligning neural signals is the single modulation strategy. Bottom: proportion of trials in which the monkey used the single or the dual modulation strategy for the horizontal and vertical target trials throughout the training.

While patterns of activation could be extracted from individual channels throughout the

training, modulation depth varied from one session to the other, possibly due to instabilities in recorded units (Perge et al., 2013).

However, a subset of this modulation variability was also found to be associated with changes in strategy across sessions. Indeed, because the path towards a given target was not imposed, we observed different patterns of neural activation leading to the success of a trial. For the horizontal target, for example, the monkey completed the task either by up-regulating only the 3rd latent variable, thus generating a straight trajectory (single modulation, **Figure 4.7 d**), or by co-activating channels driving the 2nd and 3rd latent variables to create a curvilinear path towards the target (dual modulation, **Figure 4.7 d**). In the latter, the cursor first moved upwards, following modulation of the 2nd neural mode, was then shifted to the right by the up-regulation of the 3rd neural mode, and finally landed in the target after attenuation along the 2nd neural mode. The dynamics of neural firing rates in these two cases were found to be very different (**Figure 4.7 d**). Interestingly, the dual modulation strategy was mostly employed at the beginning of the training, when alternating vertical and horizontal targets were first introduced. Later on, the number of trials exploiting direct cursor trajectories (single modulation) progressively increased, reflecting a better control over the two degrees of freedom.

4.4.6. Direct low-dimensional control of peripheral nerve stimulation: a demonstration

Finally, we explored the possibility of using low-dimensional manifold-based direct control to modulate the amplitude of stimulation of a peripheral nerve implant.

For this experiment, the animal was implanted with two intrafascicular electrodes, one in the median nerve and one in the radial nerve, to trigger flexion and extension of the hand, respectively. We linearly mapped the neural activity along the 2nd or the 3rd neural modes to the stimulation amplitude of channels of the radial and median electrode respectively (see Methods). Each electrode was modulated in distinct experimental sessions, to avoid unnatural co-contraction of the muscles.

Modulating the median nerve stimulation amplitude according to the activation of the 3rd neural mode efficiently potentiated the activity of the flexor muscles of the hand and produced graded levels of grip pressure (**Figure 4.8 a**). Conversely, the modulation of the radial nerve stimulation amplitude following the activation of the 2nd neural mode led to the specific activation of the extensor muscles and the enhancement of the wrist extension torque (**Figure 4.8 b**).

In 63% of the trials, median nerve stimulation was successfully delivered for the horizontal target and silenced for the vertical target (**Figure 4.8 c**). However, in 37% of cases, stimulation was also triggered when the monkey directed the cursor towards the vertical target.

Conversely, radial nerve stimulation preferentially happened during the vertical target trials

and was shut down for horizontal targets (78%, **Figure 4.8 c**). Yet, in 22% of the cases, stimulation also occurred when moving the cursors towards the horizontal target (**Figure 4.8 c**). This unspecific delivery of stimulation reflects a co-activation of the two latent variables in a subset of trials (**Figure 4.7 d**), i.e. the latent variable responsible for triggering the stimulation was up-regulated outside the trials of interest, leading to the crossing of the stimulation threshold.

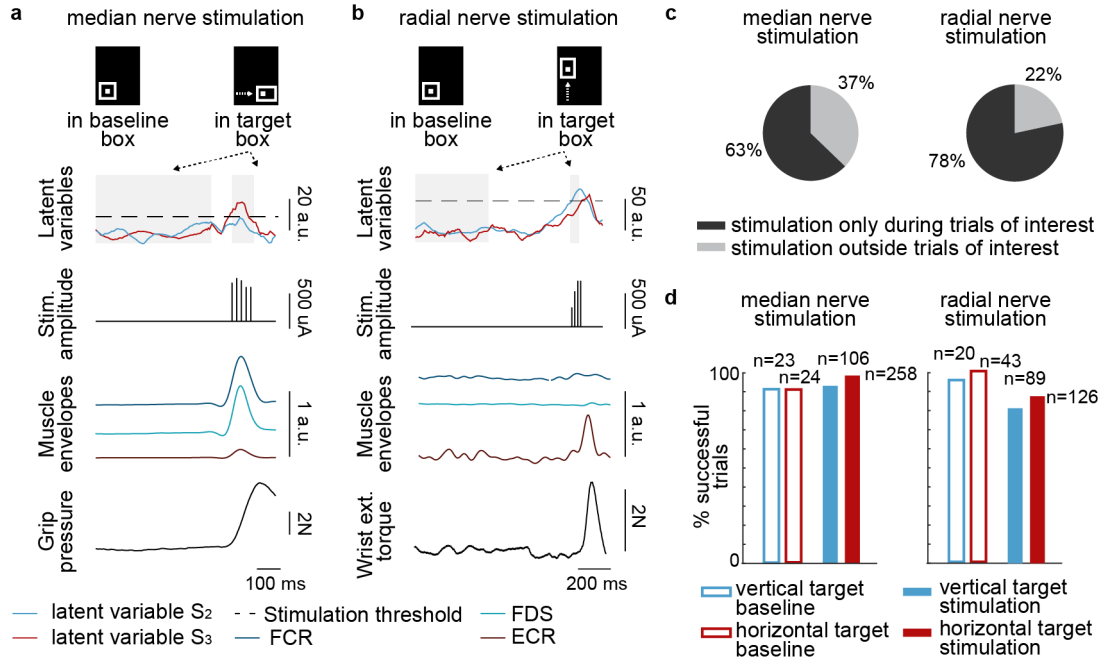


Figure 4.8 – Direct low-dimensional control of peripheral nerve stimulation. **a)** Representative successful trial of direct control-driven median nerve electrical stimulation. The neural activation along the 3rd neural mode was used to modulate the stimulation amplitude of electrode site recruiting the flexor muscles of the hand. Stimulation was delivered in the healthy monkey performing a visual direct control task alternating between horizontal and vertical targets. **b)** Representative successful trial of direct control-driven radial nerve electrical stimulation. The neural activation along the 2nd neural mode was used to modulate the stimulation amplitude of an electrode site recruiting the extensor muscles of the hand. As in **a)**, the stimulation was delivered in the healthy monkey performing a visual direct control task alternating between horizontal and vertical targets. **c)** Proportion of trials in which the nerve was stimulated only within trials of interest and outside trials of interest. For median nerve stimulation, trials of interest were the ones presenting the horizontal target. For radial nerve stimulation, trials of interest were the ones presenting the vertical target. **d)** Proportion of successful trials (i.e. completed in <8 seconds) for the vertical and horizontal targets during the baseline phase of the direct control experiment (without stimulation), and for the stimulation condition. In the stimulation condition, median nerve stimulation amplitude was modulated by the 3rd latent variable, while the radial nerve was modulated based on the 2nd latent variable. The two nerves were stimulated independently, in 2 different sessions.

For both median and radial nerve stimulation, the success rate during the task was above 80% during the baseline, i.e. without stimulation, and during the direct-control-driven stimulation trials (**Figure 4.8 d**). The percentage of successful trials did not decrease upon median nerve stimulation, and trials in which the stimulation most frequently occurred, i.e. horizontal target trials (**Figure 4.8 c**), did not exhibit any reduction in success rate as compared to the vertical target trials **Figure 4.8 d** . During radial nerve stimulation, the proportion of successful trials

was slightly higher for the less-stimulated horizontal condition (87%, **Figure 4.8 d**) than for the vertical target (81%). This marginally higher performance for the horizontal target was also observable during median nerve stimulation.

4.5. Discussion

Several studies have exploited direct control strategies for the multidimensional control of external devices (Moritz et al., 2008; D. M. Taylor et al., 2002). These works have mapped the firing rates of single cells to output command variables, but the application of this method to neural ensembles has not been demonstrated. Here, we investigated the possibility to use multiunit activity for direct bi-dimensional cortical control. Based on previous neural ensembles studies (Sadtlir et al., 2014), we fixed the direct cortical control space within an intrinsic neural manifold to promote easy learning and long term consolidation in the task.

We showed that a monkey could readily learn and adapt to new control modalities confined within a planar manifold plane, and could independently and conjointly modulate multiple latent variables over an extended period of time. In a pilot experiment, we demonstrated that direct cortical control of peripheral nerve stimulation produced graded levels of force, and that latent variables activation could partially tune the independent delivery of stimulation bursts. We critically discuss our findings in terms of functional considerations, long-term usability, and perspectives for BMI applications.

4.5.1. Controllability of neural dynamics based direct-control

In this work, we showed that the monkey was able to efficiently modulate its cortical activity along a fixed neural mode from the first days of training, suggesting that mapping the control space to an intrinsic motor manifold provided intuitive control modalities. The execution speed of the task increased over the first ten training days, indicating an improved ability to tune the activation of the latent variable on command. Ten days after introducing a horizontal component to the cursor movement, the animal efficiently adapted to this new control property, and multiunit activity in M1 channels changed accordingly. The rapid adjustments of cortical channels to the dynamic cursor control space possibly results from the "ecological" strategy used to build the fixed control map (Sadtlir et al., 2014). By anchoring the control into neural modes corresponding to already acquired tasks, learning could be facilitated (Braun et al., 2009; Thoroughman and Taylor, 2005). While it is complex to study the evolution of multiunit cortical activity on individual brain channels due to the day-to-day variability in recorded neurons (Perge et al., 2013), we observed variations in the mean modulation depth of the most modulated channels conducive of an adaptation to the contribution weights of this new neural mode. After 33 days of training, the monkey was able to efficiently alternate between the three different targets by independently and conjointly modulating two latent variables. However, during the training, we did not impose the trajectory of the cursor, leading to the emergence of different co-activation strategies to reach a given target. Such mixed

activations resulted in a partially unspecific stimulation of the nerve in our last experiment. Exploitation of dual modulation strategies may arise from underlying network connectivity constraining spatiotemporal patterns of neural activity (Gallego et al., 2017; Okun et al., 2015; Sadtler et al., 2014; Tsodyks et al., 1999), but may also correspond to the optimal strategy attained by the monkey in the absence of additional instructions during the task. Alternative to such traditional "point-to-point" tasks, research groups have developed "intructed-path" tasks, or "pursuit tracking" tasks in which the user has to follow a specified path (Sadtler et al., 2015), or pursuit a moving target respectively (Hochberg et al., 2006; Wu et al., 2006). Such approaches efficiently decreased BMI cursor movement variability, provided finer control and more precise knowledge of the user's intention and progresses. In our case, a more confined task could promote the independent modulation of multiple degrees of freedom and a finer tuning of simultaneous activation patterns, thereby improving the performance of brain-controlled stimulation.

4.5.2. Functionality of neural dynamics based direct-control

While recent studies have relied on low-dimensional manifold for the stabilization of brain decoders (Degenhart et al., 2020; Gallego, Perich, Chowdhury, et al., 2018), this work is the first to demonstrate the direct cortical control of latent variables confined to a low-dimensional space. Here, we showed that a monkey rapidly learned to control two degrees of freedom, and that each control variable could be coupled to a peripheral nerve interface for the delivery of graded stimulation patterns in the arm nerves. By encouraging the animal to keep neural activity at rest for a certain period and to up-regulate latent neural dynamics in a timely fashion, our approach provided a robust triggering of the stimulation and a sufficient working range to modulate the stimulation amplitude and create graded fingers and wrist force. Importantly, electrical stimulation delivered to the healthy nerves, did not impede the performance in the direct control task, despite almost surely triggering sensory percepts (Oddo et al., 2016; Petrini, Bumbasirevic, et al., 2019; Raspopovic et al., 2014). However, due to the co-modulation of the two control variables in a subset of trials, the delivery of the stimulation in each nerve was not limited to one type of target, preventing us from triggering the two types of stimulation in a single session. As mentioned earlier, a more constrained training (Sadtler et al., 2015) could help decoupling the control commands to successfully combine different stimulation patterns.

Although the control of only two degrees of freedom may seem insufficient for the restoration of precise hand movements, the number of control variables required for a functional output highly depends on the stimulating interface and the movement one intends to produce. As we showed in chapter 3, intrafascicular interfaces can elicit specific and natural patterns of muscular co-activation through the stimulation of only two channels positioned in different nerves. Such technology represents an interesting option to elicit graded open-and-close movement of the hand, where the timing of activation could be entirely controlled by the user through direct cortical inputs. Alternatively, combination of thumb opposition and

finger flexion through the activation of a few stimulation channels could reconstruct a large repertoire of grips with only two to three control dimensions (chapter 3). In this regard, researchers argued that one to two postural synergies were necessary to capture most of the human grip variance (Mason et al., 2001; Santello et al., 1998). A more recent study conducted on a large dataset comprising multiple subjects has shown that 50% of the total variance of hand grasp kinematics was summarized by the three first synergies, namely flexion and abduction of the middle and fourth fingers, flexion of the wrist, and opposition of the thumb (Jarque-Bou et al., 2019). A direct control approach robustly controlling two to three (D. M. Taylor et al., 2002) degrees of freedom would present exciting opportunities for the control of a few relevant postures. Moreover, the synergistic representation of movements provides an interesting ground for the use of low-dimensional spaces in cortical control. Indeed, studies linking brain activity to muscle and kinematic synergies suggested that the motor cortex executes complex skills using spatiotemporal motor primitives confined to low-dimensional neural manifolds (Giszter, 2015; Overduin et al., 2015; Shenoy et al., 2013; Thoroughman and Shadmehr, 2000). The proper coupling of neural modes spanning these manifolds to stimulation commands eliciting relevant muscle synergies could thus significantly improve the efficacy and functionality of neuroprosthetic devices.

4.5.3. Long-term stability of neural dynamics-based direct control

One of the major challenges limiting the translation of BMI to the clinic is that neural activity recorded by implanted cortical electrodes can vary over time (Perge et al., 2013). If not corrected for, these instabilities in neural signal can impede the performance of a decoder even after very short time periods (Nuyujukian et al., 2018). In this study, we reported high levels of performance in the direct control task more than 80 days after computing the static matrix translating brain activity into latent motor variables. Previous direct control studies have largely relied on single-unit activity calibrated on a day-to-day basis and none of them has, to the best of our knowledge, quantified the control performance over extended time periods (Moritz et al., 2008; D. M. Taylor et al., 2002). Alternatively, BMI control in monkeys has shown that a fixed decoder algorithm applied on stable recordings from an ensemble of 15 M1 neurons across 19 days led to long-term consolidation of control skills (Ganguly and Carmena, 2009). In our experiment, the process of untangling the degree of stability provided by the low-dimensional control space from the adaptive mechanisms learned by the monkey to succeed in the task is a delicate one. The contribution of the low-dimensional manifold mapping to the efficacy and stability of the direct control should be assessed by comparing the performance obtained to the one achieved in a similar task using single-cells activity modulation. Additionally, while we showed that neuronal modulation depth varied over time, it would be interesting to study adaptations at the single-unit level, together with the temporal dynamics of channel activation from one session to another.

Recent work has shed light on the stable nature of neural correlates associated to consistent motor behaviors (Gallego et al., 2020). Data demonstrated that dynamics of neural latent

activity, which capture the dominant co-variation patterns within the neural population are preserved over long-term and can be aligned from one recording day to the other through linear transformations. Building on these properties, researchers have shown that alignment of low-dimensional spaces can be used to stabilize static decoders in a center-out brain control task, thereby alleviating the need for regular re-calibration procedures (Sadtlir et al., 2015). In the framework of this study, it would be interesting to study the effects of low-dimensional neural manifold realignment techniques on direct control performance. Indeed, adaptive low-dimensional space-based direct control could provide a good trade-off between providing intuitive modalities of control and allowing innate learning mechanisms to optimize this control (Shenoy and Carmena, 2014).

4.5.4. Limitations and perspectives

Critical challenges in the development of BMIs for the restoration of motor and, in particular, fine hand function, consist of achieving functional levels of performance for extended periods of time (Gilja et al., 2011). In this preliminary study, we designed a fixed control framework based on inherent motor neural dynamics to engage neural adaptation and achieve consolidation of the learned strategy over 3 months. We hypothesized that a few degrees of freedom controlled in a robust and reliable way could serve as stable commands for driving a stimulating implant. While we showed that modulation of neural ensemble activity can readily be learned by a monkey and used to drive a peripheral nerve interface to produce graded movements of the hand, the voluntary control of the stimulation in a functional task remains to be demonstrated. For instance, the monkey could be trained to maintain a certain level of grip pressure in healthy condition, be transiently paralyzed for the flexion of the fingers (chapter 3), and probed to reach the same level of grip force through direct-control-driven stimulation. Another important aspect for the functional recovery of hand movements is the spatiotemporal combination of multiple stimulation patterns to activate different subsets of muscles. Hence, it would be critical to investigate the scaling of this technique to additional degrees of freedom (D. M. Taylor et al., 2002) and ensure the decoupling of neural commands for an independent control of stimulation channels. Although the comparison of our approach with traditional direct control methods was out of the scope of this study, it would be crucial to evaluate the benefits of low-dimensional space-based direct control with respect to single-unit activity based techniques (Moritz et al., 2008). As previously discussed, the changes occurring at the neuronal population levels also need to be characterized (Ganguly and Carmena, 2009) and potential stabilization or refined calibration procedures introduced to improve the efficacy of the control (Gilja et al., 2012). Such adaptive algorithms will likely be necessary to ensure stable performance over several months or years (Chestek et al., 2011; Gilja et al., 2015). Ultimately, the translation of this approach to people suffering from paralysis does not always allow for the computation of a low-dimensional manifold in motor tasks. Other brain areas such the sensory or premotor cortices could provide an interesting alternative to derive stable low-dimensional spaces associated with motor control (Perich et al., 2020; Perich et al., 2018) and possibly include sensorimotor modalities to the BMI, thus enhancing the

user's performance. In the same line, building the control space on a much larger repertoire of complex natural behaviors (Gallego, Perich, Naufel, et al., 2018) may bring more generalized ways to modulate neural dynamics in people suffering from limb paralysis and accurately command neuroprosthetic devices.

4.6. General Conclusion

Throughout this chapter, I explored a novel approach for the voluntary operation of a neuroprosthesis by leveraging the learning properties of direct cortical control and the inherent neural dynamics of motor control. I developed a direct control algorithm based on low-dimensional neural manifolds and preliminarily assessed the performance achieved by a monkey during a bi-dimensional task. My findings demonstrate the feasibility and the potential of low-dimensional space-based control and could represent a paradigm shift towards more intuitive direct control mappings. While still in the early exploratory phase, the approach provides basic insights to the exploitation of the complementary properties of adaptive learning and intrinsic neural spaces to design robust and efficient cortical control paradigms. I advocate that this method could positively impact the control of stimulating interfaces for the restoration of hand movements (see chapter 3) after paralysis.

5 Perspectives on the translation of intraneural prostheses to restore hand movements

The work presented in this thesis provides a solid basis to deploy intraneural peripheral nerve neuroprosthetics for the restoration of dexterous hand movements after a paralyzing injury. While intrafascicular arrays have been clinically implanted in subjects with limb amputation for the restoration of somatosensory feedback (D’Anna et al., 2019; Petrini, Bumbasirevic, et al., 2019; Petrini, Valle, Bumbasirevic, et al., 2019; Raspopovic et al., 2014), their ability to restore hand motor functions had not yet been determined before this project. I believe the collection of data presented here brings compelling evidence that intrafascicular implants bear the potential to reproduce fine and selective hand movements after paralysis, and can be intuitively controlled through cortical inputs. In this last chapter, I first discuss important functional and technical considerations for the clinical testing of this device in terms of patient criteria, experimental setup, and control paradigms. I then review a variety of opportunities for the refinement of peripheral nerve stimulation protocols to enhance selectivity and functional outcomes. In the third part, I discuss the necessity for complementary interventions aimed at integrating somatosensory information into neuroprosthetic devices for enhancing recovery of dexterous finger movements.

Contributions: I wrote this chapter and generated the experimental data presented in the figures. I implemented the computational model presented for bipolar stimulation. Elena Losanno, a Ph.D. student working under my co-supervision analyzed the data, generated the modeled bipolar curves, and implemented the Gaussian Process search algorithm. I prepared the figures.

5.1. Functional and technical considerations for the clinical application of intrafascicular stimulation targeting motor functions

5.1.1. Clinical application for hand paralysis: challenges and prospects

As discussed in the introduction of this work, stroke and cervical spinal cord injury stand amongst the major neurological disorders leading to the impediment of hand functions. Most studies exploring rehabilitation mechanisms in individuals affected by ischemic events reported that subjects were able to partially recover arm function and rudimentary grasp abilities, but often failed at producing dexterous finger movements (Krakauer and Carmichael, 2017; Raghavan et al., 2006). Similarly, individuals affected by spinal cord lesions still lack sustainable solutions for the recovery of fine hand motion, and only partially benefit from current rehabilitation strategies (Mangold et al., 2005; M. R. Popovic et al., 2006). Experimental approaches, involving the electrical stimulation of the cervical spinal cord, have investigated the feasibility of restoring upper limb movements (Kasten et al., 2013; Lu et al., 2016; Nishimura et al., 2013). While a variety of responses could be elicited to generate arm movements or improve their execution, data suggests that selectivity in distal muscle recruitment (digits, wrist) was insufficient to project restoring dexterous and usable control of the hand (Kaesler et al., 2013; Sunshine et al., 2013).

The selectivity provided by intrafascicular stimulation has the potential to address these limitations and creates promising opportunities for reproducing fine hand movements after paralysis. In patients afflicted by velocity-dependent spasticity (Gracies, 2005a, 2005b; Sommerfeld Disa K. et al., 2004; Welmer et al., 2010) and in individuals presenting flaccid hand condition (Borboni et al., 2014; Kwakkel et al., 2003; McDonald and Sadowsky, 2002), the relaxation of the co-contracted hand muscles and the stable support of the grasp are important medical challenges that could be addressed with intrafascicular stimulation.

In chapter 3, we demonstrated the potential of intraneural stimulation to restore the extension of the fingers and wrist after a transient paresis of the muscles. However, our paralysis model induced by pharmacological block did not formally mimic the clinical condition of patients affected by stroke or tetraplegia. The characterization of intraneural stimulation effects in relevant clinical conditions represents a critical step to validate its functionality in terms of evoked movements and somatosensory mechanisms.

Indeed, we need to consider that peripheral nerve stimulation recruits underlying muscles either via direct muscle engagement through the alpha-motor fibers, or indirect spinal reflexes mediated by the activation of afferent fibers (Mezzarane et al., 2013). In subjects affected by spinal cord lesions, the functional impact of direct and indirect muscular responses may vary with the level of injury. Similarly, the amplitude of elicited compound muscle action potential (CMAP) may be impacted by the over-activation of spinal and supra-spinal circuitries in spastic individuals (Gracies, 2005b). The ability to elicit functional and selective muscle responses under these conditions must therefore be investigated.

5.1 Functional and technical considerations for the clinical application of intrafascicular stimulation targeting motor functions

Another key point to evaluate is the nature of somatosensory percepts evoked via intraneural stimulation. It is clear that stimulation of the nerves simultaneously engages motor, sensory and proprioceptive fibers (Petrini, Bumbasirevic, et al., 2019; Raspopovic et al., 2014) but the influence of this mixed activation on movement control is yet undefined. The assessment of constructive, destructive, or neutral interactions between somatosensory and motor fibers recruitment remains a crucial issue to explore for the application of intraneural implants in subjects retaining somatosensory function.

5.1.2. Development of tailored experimental paradigms in humans

Intraneural interfaces present interesting opportunities for the personalization of therapeutic paradigms in people with paralysis. One of the main advantages is the high degree of modularity they provide in terms of the number of contacts, implantation sites, and stimulation protocols. For instance, in a tetraplegic individual suffering from spinal lesion at the C8 segment, fingers flexion will be impeded but most of the extension of the hand will remain intact. Multiple intrafascicular implants inserted in the median nerve could promote the restoration of a large collection of grasps and act in synergy with residual extensor muscles function. Such individualized approach could also be focused on the patient's needs. For example, in individuals affected by spastic contraction of the fingers, the relaxation of the hand by activating the extensor muscles could be prioritized over individual finger flexion.

Additionally, peripheral nerve implants could be combined with robotic devices to target a larger set of upper limb movements. In people affected by cervical spinal cord injury or stroke, upper arm muscles responsible for the support of the shoulder and arm (deltoid) and the actuation of the elbow (biceps and triceps) are often impeded, rendering necessary gravity-assistive devices to support the arm. Hybrid neuroprosthetic systems integrating robotic or exoskeleton braces withstanding the arm, with peripheral nerve stimulation, could favor the simultaneous restoration of arm lifting, extension and flexion, and fine finger movements. Such arm support has already been tested in combination with surface FES in a tetraplegic patient (Ajiboye et al., 2017), and its application to peripheral nerve stimulation opens new avenues for the production of fine, yet, fully-functional reaching and grasping movements, in individuals suffering from complete upper-limb paralysis.

Another way to adjust intrafascicular stimulation to individual patients' needs is through targeted rehabilitation protocols. In people suffering from stroke, peripheral nerve stimulation could address very specific movement impairments, creating new prospects for the long-term recovery of dexterous finger movements. For instance, during the rehabilitative phase (Langhorne et al., 2009), intraneural implants could be used to generate functional activation focused on the most impaired hand functions, therefore improving the outcomes of rehabilitative paradigms. Although they require surgical intervention, intrafascicular implants inserted in the nerves for up to six months (Petrini, Valle, Strauss, et al., 2019) could provide substantial benefits, as compared to current, state-of-the-art, non-invasive approaches (Shin

et al., 2018), justifying the cost for the patient. Over the long term, intraneural devices could bridge the gap between rehabilitated functions and unmet recovery goals, and remain implanted upon the termination of rehabilitation protocols to reproduce movements that have not been fully recovered.

These strategies fit into a new direction in neuroprosthetics that aims at designing individualized neurorehabilitation programs based on patient-specific circuitopathies and their potential for recovery (Borton et al., 2013). Ultimately, tailored neuroprostheses may have an important impact on functional restoration after paralysis, owing to their capacity to comprehensively address patient-specific impairments.

5.1.3. Technical prospects for the clinical use of intrafascicular implants

We showed in chapter 3 that intrafascicular stimulation presents interesting properties for the engagement of selective hand muscles, and the production of a large collection of hand movements. Here, I discuss a few elements I believe to be critical to transfer intrafascicular stimulation into clinical applications targeting fine motor control of the hand (**Figure 5.1**).

Modular stimulation device

As reported in chapter 3, the spatiotemporal combination of multiple intrafascicular stimulation channels allows the generation of complex and natural grip postures, as well as smooth transitions between the opening and closing of the hand. The fine-tuning of spatiotemporal activation patterns for the precise co-activation of muscles requires stimulating devices operating at high temporal resolution (20-50 ms-scale). Moreover, while only one intrafascicular implant per nerve was sufficient to trigger different grips in monkeys (chapter 3), the larger number of fascicles in the human median nerve (Delgado-Martínez et al., 2016; Gesslbauer et al., 2017) suggests that additional implants or denser electrode arrays will likely be needed to achieve similar results. In light of these considerations, two intrafascicular interfaces inserted in the median nerve and one interface implanted in the radial nerve probably constitute a reasonable trade-off for the restoration of functional opening and closing hand movements (chapter 3). Because it is intricate to decide intra-operatively which combination of channels will be used in the clinical protocol, the resulting 48 channels will likely have to be coupled, *post hoc*, to a multiplexer device operating 6 to 8 independent channels on a medical-grade stimulator (**Figure 5.1**). Additionally, a fully implantable stimulation tool integrating similar features should be developed in parallel with early clinical trials to promote the successful translation of this approach to wide clinical practice and home users. These requirements raise substantial engineering challenges and will require the manufacturing of high-density connectors to interface between the implant and the stimulator, long-lasting, yet compact rechargeable batteries for the integration into fully-implantable designs (Zanos et al., 2011), energy-saving stimulation paradigms (Almeida et al., 2016), and low-power architectures (Shoaran et al., 2014).

5.1 Functional and technical considerations for the clinical application of intrafascicular stimulation targeting motor functions

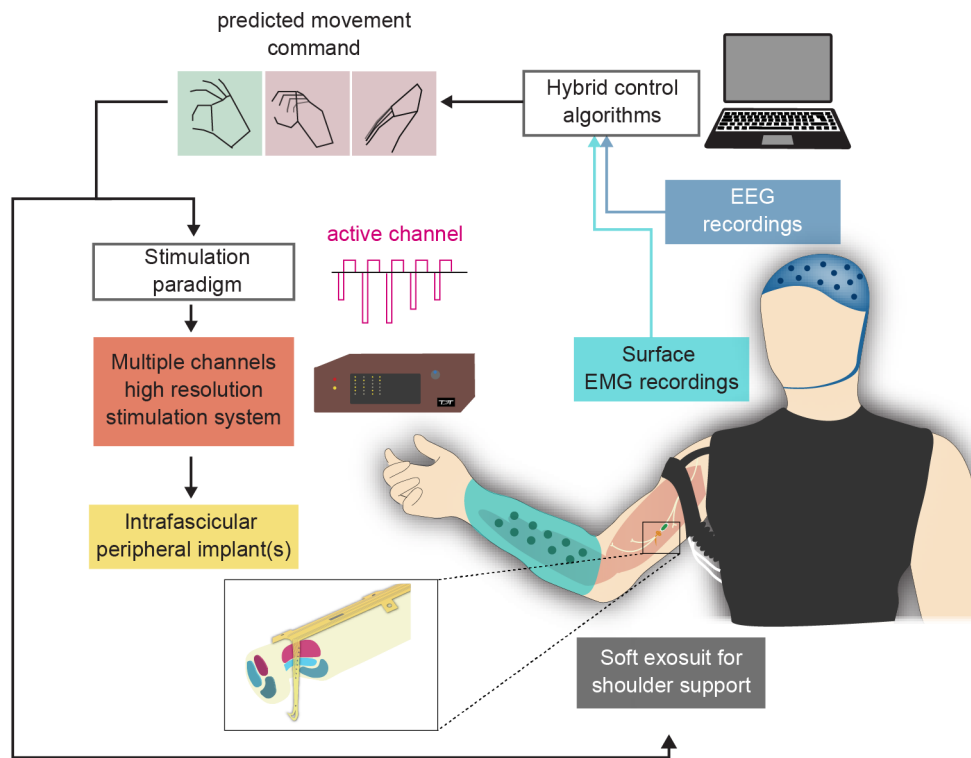


Figure 5.1 – Proposed experimental setup for the preliminary clinical testing of intrafascicular stimulation targeting hand motor functions. Important components for the early clinical assessment of intrafascicular implants in paralyzed subjects. This framework includes 1) high-density surface EMG for recording myoelectric commands from residual muscles contraction, 2) EEG for the monitoring of beta-waves associated with motor inputs, 3) a multi-channel stimulation system operating at high temporal resolution for the closed-loop control of the intrafascicular implants, and 4) a soft exoskeleton for the support of the arm at the shoulder and elbow level. Hybrid algorithms integrating EEG-based classifiers and myoelectric triggering are used for selecting the intended movement and initiating pre-determined stimulation bursts on individual intrafascicular electrode channels. Because of increased intrafascicular selectivity, a single active site can be used to elicit a functional grasp pattern (see chapter 3). Simultaneously, exosuit actuators are controlled based on incoming brain and muscle commands to promote the correct positioning of the arm and elbow and facilitate reaching and/or pulling movements.

Light-weight support exoskeleton

Another strategic element for the refinement of stimulation paradigms to recover hand function is the development of a light-weight, supportive exoskeleton for the arm. Over the past few years, numerous light exoskeletons and exosuits have been developed to assist patients during motor control of all joints of the upper limb, from the shoulder to the hand. Particular attention has been given to hand exoskeletons, in which actuation and control units were housed in the wheelchairs. These devices have been tested with disabled patients using non-invasive human-robot interfaces (In et al., 2015; Soekadar et al., 2015). Recently, the team of Prof. Conor Walsh has developed a novel exosuit for shoulder-bearing in individuals impacted by spinal cord injury (O'Neill et al., 2017). Adjusting such soft-actuators designs to shoulder and elbow joints would likely provide a compliant and safe support of the arm in users (**Figure**

5.1), comply with peripheral nerve stimulation, and further improve the functional clinical outcomes in grasp-and-release tasks.

Simple functional closed-control paradigm

Typical FES-based neuroprostheses rely on open-loop or finite-state controls, kinematics signals from unimpaired limbs, residual EMG activity, or manual commands to activate stimulation paradigms (R. Hart et al., 1998). However, the adoption of the devices by the users has been undermined by the poorly intuitive nature of these control strategies, the insufficient functional benefits, and the cumbersome technical setups.

In the work presented in this thesis the delivery of intrafascicular stimulation was based on the activation of cortical ensembles dynamics, either naturally associated with a reaching movement (chapter 3), or “voluntarily” modulated by a monkey through adaptive learning (chapter 4). These closed-loop paradigms rely on invasive intracortical signals and could potentially be applied to accurately and robustly decode multi-joint arm and hand movements (Chestek et al., 2011; Collinger, Wodlinger, et al., 2013; Gilja et al., 2012; Gilja et al., 2015; Vaskov et al., 2018; Wodlinger et al., 2015), or artificially control several degrees of freedom (Fetz, 1969; Moritz et al., 2008; D. M. Taylor et al., 2002).

While I concede that the development of invasive cortical closed-loop strategy is important for the future autonomous and high-performance use of BMIs, I argue that peripheral body signals and non-invasive neural recordings present considerable advantages for the early application of peripheral nerve stimulation in clinical trials. To reduce the burden imposed on subjects, and limit the number of surgical procedures, we should preliminarily investigate the use of high-density surface EMG signals and electroencephalograms (EEG) to control stimulation patterns of intraneural implants (**Figure 5.1**). Several studies have demonstrated the usability of myoelectric control to operate external devices (R. L. Hart et al., 2011; Ison and Artemiadis, 2014; Kilgore et al., 2008). Additionally, EEG-driven activation of surface electrical stimulation has shown interesting perspectives for the actuation of simple grasp and release hand movements (Lauer et al., 1999; Mueller-Putz et al., 2005; Pfurtscheller et al., 2003). While non-invasive neural recordings typically allow control over only a few degrees of freedom, the transverse intrafascicular multichannel electrodes (TIMEs) have been able to elicit different grips with only a limited number of channels (see chapter 3), suggesting that the low information content of EEG could be functionally-relevant for preliminary testings. Finally, the combination of EEG-based and myoelectric control into hybrid algorithms (**Figure 5.1**) could substantially improve the performance of the decoding (Lalitharatne et al., 2013; Ruhunage et al., 2019). For instance, beta-band EEG signals could be used to predict the grasp type through classification algorithms (linear discriminant analysis, support vector machine, etc...), while activation and relaxation of residual muscles could be used to activate and interrupt the stimulation. As such, the recordings of one flexor and one extensor muscle coupled to the classification of three different EEG activation patterns could potentially provide up to 6 combinations of stimulating channels, i.e. 6 evoked movements using intrafascicular

implants. Up-scaling the number of muscles we record from and optimizing the EEG classifier could potentially increase the dimensions and stability of the control, and improve functional outcomes.

Along with providing more intuitive and time-lock control of the stimulation, closed-loop paradigms hold great potential for the enhancement of functional benefits through activity-dependent neuroplasticity (Daly and Wolpaw, 2008; Ethier et al., 2015; Jackson and Zimmermann, 2012; Soekadar et al., 2015). Several studies have demonstrated that coupling brain signals to the control of FES in stroke rehabilitation protocols improved functional motor outputs (Ramos-Murguialday et al., 2013), and resulted in increased functional connectivity between motor areas in the affected hemisphere (Biasiucci et al., 2018). Likewise, recent studies unveiled that brain-controlled neuromodulation therapies augmented recovery of locomotor functions in spinal cord injured rats (Bonizzato et al., 2018), and paraplegic patients (Shokur et al., 2018). In this framework, closed-loop control paradigms linking natural and spontaneous voluntary commands to the stimulation of specific muscles could significantly improve the functional recovery in paralyzed subjects.

5.2. Opportunities for the refinement of peripheral nerve stimulation

In chapter 3 of this thesis, I implemented an anatomically realistic computational model of the median nerve based on previous works (McIntyre and Grill, 2000; Raspopovic et al., 2011; Romeni et al., 2020) to predict the optimal level of implantation of an intrafascicular implant. This computational approach delivered critical *a priori* insights for refining the surgical intervention, and maximizing the functional outcomes of the intraneural implant in monkeys. While we applied this model to optimize the implant location, computational techniques also offer tremendous opportunities to derive novel stimulation paradigms and harvest the full potential of peripheral nerve interfaces for the restoration of motor functions (Capogrosso and Lempka, 2020).

5.2.1. Realistic computational frameworks for the design and optimization of stimulation strategies

With the growing accessibility to fast computers and powerful processing units, computational approaches have taken a large leap forward in neuroscience and neuroprosthetic applications (Capogrosso and Lempka, 2020). In the particular field of neuromuscular stimulation, several computational-based studies have brought interesting insights into new ways to interface with the peripheral nervous system.

Inspired by the early work of McIntyre and Grill on the stimulation of mammalian nerve fibers (McIntyre et al., 2002), our group has published several studies in which computational models have been used to refine stimulation paradigms. Namely, Valle and colleagues (Valle, Mazzoni,

et al., 2018) have derived frequency neuromodulation approaches based on a biomimetic model, able to reproduce nerve activation patterns arising from skin mechanoreceptors (Saal and Bensmaia, 2015; Saal et al., 2017). By implementing stimulation strategies that mimicked the firing rate of sensory nerve fibers, they reported an increased feeling of “naturalness” in individuals with amputation operating an artificial sensorized hand. In the same line, another study demonstrated the possibility to induce asynchronous stochastic neural activity through the use of high-frequency bursts with promising potential for the reduction of muscle fatigue (Formento et al., 2020).

Other works have successfully employed computational models to design multipolar configurations improving the selectivity of muscular recruitment (Raspopovic et al., 2017). This method has been applied to cuff implants to optimize the three-dimensional configuration of anodes and cathodes (Dali et al., 2018), and created focused electrical fields, eliciting single-digit movements in anesthetized tetraplegic patients (Tigra et al., 2020).

Using the experimental setup described in chapter 3, we preliminarily evaluated the performance of bipolar configurations during intrafascicular stimulation in monkeys. In two animals, we tested multiple combinations of cathode and anode and observed a global increase in selectivity for the flexor and extensor muscles of the hand (**Figure 5.2 a**). However, the degree of selectivity improvement differed between animals and did not generalize for similar bipolar configurations (data not shown).

5.2 Opportunities for the refinement of peripheral nerve stimulation

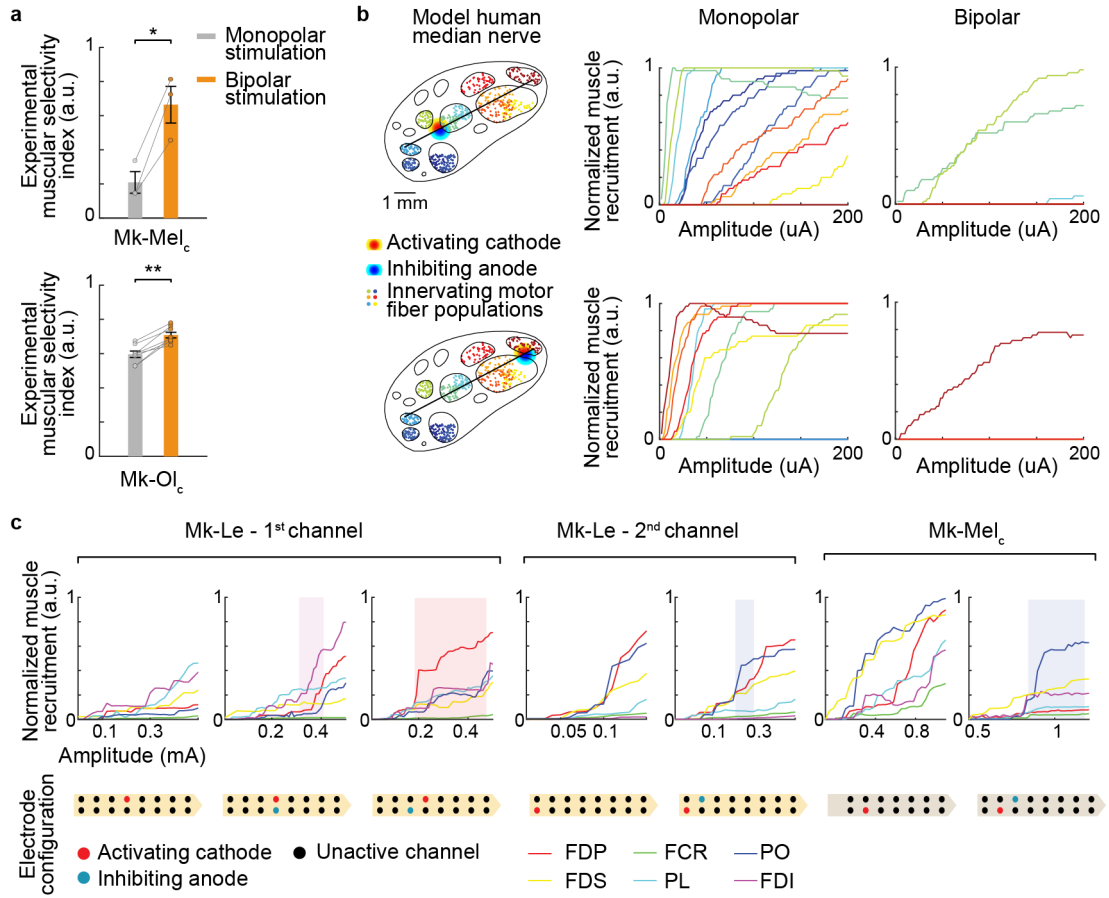


Figure 5.2 – Bipolar intrafascicular stimulation increases muscular selectivity. **a)** Normalized selectivity index for monopolar and bipolar configurations for radial (top) and median (bottom) nerve stimulation (n=2 animals, only channels combinations leading to more than 10% of muscle activity were considered). **b)** Left: anatomically realistic computational model of the human median nerve (methods described in chapter 3, data from Delgado-Martínez et al., 2016). Neural fibers innervating different muscles are represented in different colors. Cathode and anode configuration is overlapped on the intrafascicular implant. Right: muscle recruitment curves obtained for different amplitudes (methods described in chapter 3) for monopolar and bipolar stimulation. **c)** Recruitment curves obtained *in vivo* (methods described in chapter 3) when stimulating channels of the median nerve electrode in close vicinity (n=2 animals). Abbreviations: a.u. : arbitrary units; FDP: flexor digitorum pollicis; FDS: flexor digitorum superficialis; FCR: flexor carpi radialis, PL: palmaris longus, PO: pollicis opposens; 1DI: first dorsal interosseous. *P<0.05, **P<0.05, paired Wilcoxon signed-rank test. Mk-Me_c and Mk-Ol_c reported in **Appendix Table A.3**, Mk-Le: acute, 3.8 kg, 3 years old, license number: 2017_22_FR.

As reported in chapter 3, motor fibers in arm nerves are heterogeneously distributed in the fascicles and their organization is not conserved across individuals. Besides, the number of fascicles, as well as the placement of the intrafascicular electrode shaft varies from one monkey to the other. This variability makes it difficult to generalize bipolar stimulation patterns based on experimental data only. Interestingly, our computational model of the median revealed that when the cathodic and anodic poles were located in close vicinity (~a maximum of one to two contacts distance), on opposite sides of the electrode shaft, they consistently improved the selectivity of fiber recruitment (**Figure 5.2 b**). Preliminary experimental findings collected

in two monkeys seem to confirm these results (**Figure 5.2 c**), thus highlighting the advantage of *in-silico* approaches for the understanding and exploration of the stimulation parameter space.

Realistic and biomimetic models allow for a more transparent and systematic search than manual experimental screening. Ultimately, implementing generalized computational tools and testing the outcomes of bipolar electrode configurations on a larger dataset of simulated fiber populations (Raspopovic et al., 2017) could help derive generic relationships between intraneural implants and the surrounding nervous system, further improving the reliability and predictability of this interface for clinical use.

5.2.2. Machine learning approaches to improve parameter search

A second approach for the optimization of functional benefits in peripheral nerve stimulation is the use of unsupervised machine learning algorithms. As discussed earlier, novel clinical neuroprostheses will likely integrate numerous implants, each featuring several stimulation channels that can be combined in a myriad of spatiotemporal stimulation patterns. For human use, the exploration of motor maps engaged through electrical stimulation needs to be fast and efficient. The tedious exhaustive search that has so far represented the clinical standard will not reasonably scale to increasingly larger sets of parameters. Recently, researchers have proposed to use active learning algorithms for the automatic and optimized selection of stimulation parameters for neuroprosthetic applications (Desautels et al., 2015; Laferriere et al., 2019). In 2019, Laferriere and colleagues implemented a Gaussian Process (GP) based hierarchical Bayesian Optimization (BO) approach to build priors for stimulation-to-EMG mappings (Laferriere et al., 2019). They showed that the algorithm succeeded in rapidly learning relationships between complex stimulation patterns of the primary motor cortex (including several stimulation sites), and evoked muscle activity. Their method efficiently unveiled nonlinear circuit-level mechanisms, suggesting exciting opportunities for the prediction of motor outputs resulting from multipolar intrafascicular stimulation. In our particular case, while it is very complex to model non-linear voltages distributions emanating from voltage drops around nerve sub-structures, it may be possible to search the parameter space of intraneural implants by drawing a few assumptions on the stimulation-to-EMG mapping. To test this hypothesis, we implemented a similar algorithm and maximized the activity of a fixed number of hand muscles known to contribute to specific grip patterns (see chapter 3). Briefly, we used a GP-BO search to find the stimulation parameters, i.e. contact location and amplitude of stimulation that minimized the following function:

$$OBJ = \min \left\{ \sum_{i=1}^M w_i \mu_i - \sum_{j=1}^N w_j \mu_j \right\} \quad (5.1)$$

5.2 Opportunities for the refinement of peripheral nerve stimulation

With μ_i the average normalized EMG envelope of muscle i during the stimulation phase ($0 < \mu_i < 1$), M the number of muscles to minimize (dysfunctional for the given movement), N the number of muscles to maximize (functionally-relevant for the given movement), and $w > 0$ the corresponding weights. In our preliminary implementation, the input space of the GP was a two-dimensional space where the first dimension represented the stimulation channel and the second dimension represented the monopolar stimulation amplitude of this channel. Because we tested this algorithm using TIME-triggered muscle activation (see chapter 3). Channels were identified through a distance-based map to take into account any similarities arising from spatial proximity. Namely, channels closely located on the electrode shaft were closely related in the parameter space, while channel located farther apart were assumed to evoke more distant EMG patterns. The output motor response was represented by the average normalized EMG envelopes of the hand muscles.

While very preliminary, the testing of our approach on median nerve intrafascicular stimulation protocols in monkeys (see Methods chapter 3) resulted in the successful screening of the parameter space and the maximization of muscles of interest (**Figure 5.3 a**). The algorithm was found to converge (**Figure 5.3 b**), and in the case of the thumb opposition and wrist flexion, the optimized channel/amplitude combination elicited the expected movements (**Figure 5.3 c**). However, for complex grasp patterns, such as spherical or cylindrical grips, the maximization of a few muscles of interest did not always result in functionally-relevant hand motion (data not shown).

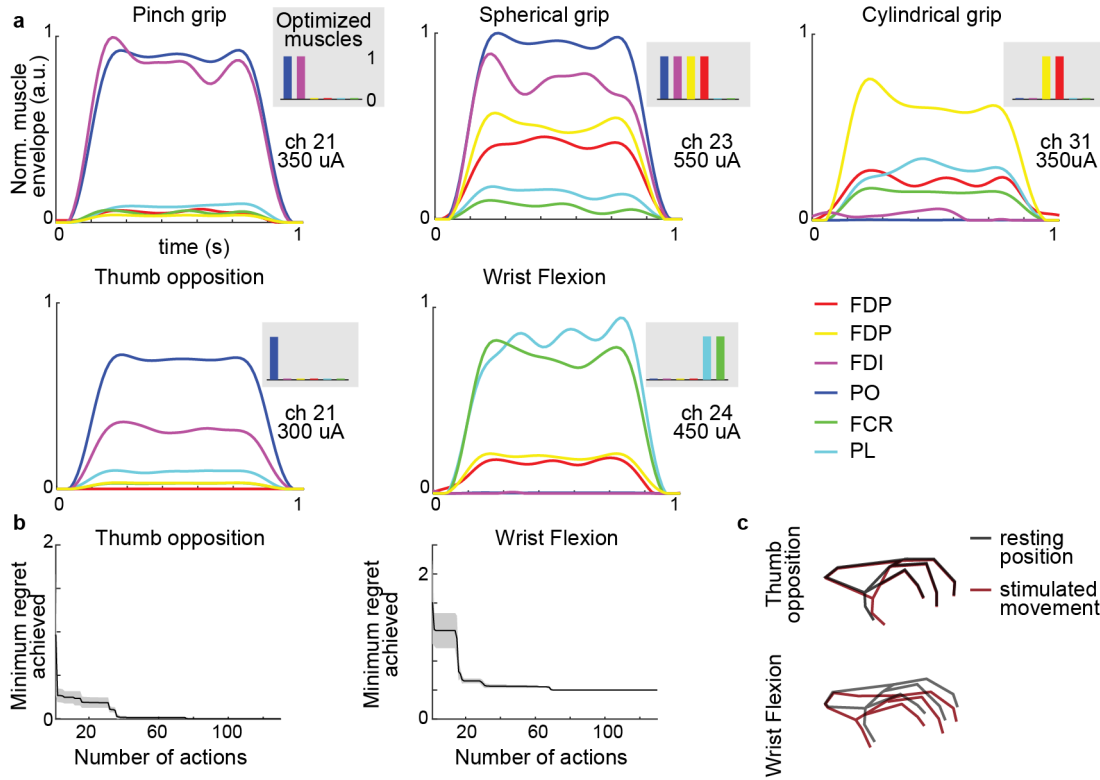


Figure 5.3 – Gaussian process-based Bayesian Optimization algorithm for intraneural stimulation paradigms. **a)** EMG envelopes obtained for the optimal combination of channel and stimulation amplitude for different types of movement. Muscles whose activity is maximized by the algorithm are indicated in the grey inset. Channel and stimulation amplitude outputted by the algorithm are reported next to the plots. **b)** Minimum regret achieved through the optimization procedure for the thumb opposition and wrist flexion movements. This value reflects the convergence of the algorithm over the number of optimization steps. **c)** Hand kinematics elicited by intraneural stimulation (median nerve) using the parameters optimized by the GP-BO algorithm for the thumb opposition and wrist flexion (see chapter 3). Monkey: $Mk - Me_c$, see **Appendix Table A.3**.

While this method would likely scale to multipolar configurations, the optimization of stimulation parameters based on EMG activation provides limited functional outcomes, especially for dexterous hand movements. Indeed, it is impossible to monitor the activity of every single muscle of the hand during the generation of a specific movement. Besides, the generation of certain grips may be associated with muscle activation patterns that vary from one individual to the next. This incomplete characterization of muscular contributions results in under-defined targets for the optimization algorithm, and a perfect fit between expected and observed muscle activity does not necessarily result in a relevant nor functional hand movement. To tackle this issue, one option would be to optimize the GP based on kinematic outputs. Indeed, kinematic features are more easily generalizable across subjects and directly reflect functional motor outputs. Recent advances in marker-less kinematic tracking (Mathis et al., 2018; Nath et al., 2019) will likely promote the online implementation of such learning-based frameworks, making them applicable in experimental paradigms and clinical settings.

5.3 Merging motor and somatosensory restoration for the recovery of fine hand function

In the long run, combining active learning algorithms with prior knowledge built on anatomically realistic computational models could provide powerful tools for the design of large scale generalizable routines and the extraction of meaningful stimulation paradigms to restore specific motor functions.

5.3. Merging motor and somatosensory restoration for the recovery of fine hand function

We have considered here some of the important aspects underlying the clinical applicability of peripheral nerve implants together with relevant optimization strategies for the restoration of hand movements after paralysis. Another question to examine is the incorporation of sensorimotor modalities into the neuroprosthetic scheme of the patient. Given its importance for object manipulation, the restoration of somatosensory feedback has been identified as one of the key requirements for motor recovery (Bensmaia and Miller, 2014; Fagg et al., 2007; Lebedev and Nicolelis, 2006). Indeed, most of the motor tasks we perform in our daily life, such as reaching (Gordon et al., 1995), fine grasping (Johansson et al., 1992; Richardson et al., 2016; Rothwell et al., 1982), object manipulation (Johansson and Flanagan, 2009) or walking (Petrini, Valle, Bumbasirevic, et al., 2019; Shokur et al., 2016), rely on tactile and proprioceptive information.

Typical BMI paradigms depend on visual feedback only for creating accurate motor outputs (Ajiboye et al., 2017; Bouton et al., 2016; Carmena et al., 2003; Chestek et al., 2013; Collinger, Wodlinger, et al., 2013; Irwin et al., 2017; Moritz et al., 2008; D. M. Taylor et al., 2002; Vaskov et al., 2018; Velliste et al., 2008). However, the efficacy of BMIs for the precise control of movement depends on the integration of somatosensory modalities that supplies touch and kinesthetic feedback to the operator (Gilja et al., 2011). In the case of patients suffering from cervical spinal cord injury, dorsal column tract damages and subsequent somatosensory deprivation (Pons et al., 1985) is very likely to undermine the performance of a hand prosthetic system.

While some studies have employed vibrotactile arrays to interface with sensate skin and restore somatosensory feedback after spinal lesions (Ganzer et al., 2020), larger attention has been given to the electrical stimulation of somatosensory cortices. Over the last decade, researchers have shown that monkeys can discriminate between intracortical microstimulation stimuli delivered at different intensity (Kim et al., 2015; Tabot et al., 2013) and frequency (Callier et al., 2020; O'Doherty et al., 2011; Romo et al., 1998). Similar studies conducted in humans provided a more precise insight into the type of sensation produced by cortical stimulation. They reported natural pressure-like percepts on the palm and index (Flesher et al., 2019), together with the apparition of both tactile and proprioceptive sensations on the phalanges and arm, depending on the intensity of stimulation (Salas et al., 2018).

Cortical stimulation techniques offer promising ways to restore somatosensory percepts and

complement motor neuroprostheses for subjects with neurological sensorimotor disorders. However, to date, very little is known on how precisely sensory afferent signals are perceived by the brain and most importantly, how we can faithfully reproduce this neural activation through artificial stimulation. Open questions remain on the characterization of the sensations elicited through stimulation, the bodily integration of those percepts into the control scheme of the user, and the effects on performance during motor tasks. In particular, the encoding of proprioception has been only rarely reported in human subjects (Armenta Salas et al., 2018), or achieved via non-homologous approaches (Dadarlat et al., 2015). While proprioceptive feedback will surely improve the performance of motor neuroprosthetic systems (D’Anna et al., 2019; Tomlinson and Miller, 2016), the multimodal aspect of proprioception necessitates a better understanding of its cortical encoding, and the possibility for reliable multichannel stimulation. In light of these considerations, the experimental platform described in chapter 2 provides meaningful tools for the investigation of sensorimotor integration mechanisms in primates and the implementation of translational stimulation protocols to include “natural” and functional somatosensory information in motor neuroprostheses (Badi et al., 2020).

6 General conclusion

This thesis summarizes the incremental steps necessary for the development of a peripheral neuroprosthesis in the preclinical primate model. It provides a vast body of evidence demonstrating the functionality of intrafascicular peripheral stimulation for producing precise hand movements in monkeys, and explores promising ways of controlling such stimulation using an intuitive brain-control paradigm.

Current strategies to restore hand function after paralyzing neurological disorders have investigated the use of surface, epimysial or intramuscular stimulation, but have shown limited benefit owing to limited movement specificity, high technical complexity, and the fast generation of fatigue (Ajiboye et al., 2017; Ethier et al., 2012; Kapadia et al., 2020; P. Peckham et al., 2002). Alternatively, research groups have used epineural (Brill et al., 2018; Memberg et al., 2014; Tigra et al., 2020) as well as intrafascicular stimulation (Ledbetter et al., 2013), but none of these approaches has yet been implemented in clinical applications. In this thesis, I advocate that intrafascicular devices, tailored to a specific experimental model, can be employed to restore selective muscle activation, thus representing an interesting option for the recovery of functional fine hand movement in clinical applications.

In the first part of this thesis, I presented a versatile robotic platform for the design of natural reaching and grasping tasks in monkeys. This framework enables a comprehensive characterization of the neural, kinematic, as well as kinetic components of hand movements in monkeys, and provides a vast collection of tools for designing customized experimental paradigms for many different applications. Our open-source platform will hopefully facilitate and empower the implementation of experimental protocols for fundamental, as well as translational studies, in the monkey research community.

In the second part of this thesis, I leveraged this modular experimental platform and adapted it to functionally assess the performance of intrafascicular stimulation in recruiting specific muscles of the hand. I first conducted an extensive anatomical characterization of the monkey's median and radial nerves and built computational models predicting the optimal implantation

site for the intrafascicular interface. I then tailored the interface and optimized the surgical implantation to maximize the functional outcomes of the stimulation. This personalized approach resulted in highly specific activation of the hand's extrinsic and intrinsic muscles, engaging the flexion and extension of the wrist, fingers, and thumb. The chronic implantation of intrafascicular electrodes enabled the production of a large collection of grasps and extension movements. Additionally, I showed that intrafascicular stimulation could be finely tuned to modulate muscle contraction and grip force across functionally-relevant time periods. Finally, I demonstrated in a proof-of-concept study that stimulation amplitude could be modulated based on intracortical signals to enable a transiently paralyzed animal to perform a functional grasping task. The data presented highlight the functional applicability of intrafascicular technologies for the restoration of fine hand movement after paralysis, and have important implications for the translation of this approach to the clinic. This work provides the building blocks for scaling such implants to motor applications in patients, hopefully paving the way to a novel generation of peripheral nerve neuroprostheses for dexterous hand control.

In the third part of this thesis, I explored the feasibility of using low-dimensional motor cortical dynamics for the direct control of a prosthetic device. This very preliminary study provided encouraging evidence for the control of a bidimensional cursor using this strategy. I demonstrated that over a few weeks of training, a monkey readily learned to modulate neural activity along fixed neural modes to actuate a moving cursor in two independent directions. I also demonstrated that coupling voluntary activation of neural latent variables to the stimulation amplitude of an intrafascicular implant generated graded levels of force, without impeding the quality of the control. These results provide intriguing investigation routes for the design of intuitive, robust, and efficient control paradigms permitting the volitional operation of a neuroprosthetic device.

In the last part of this thesis, I examined several technical and scientific aspects I believe to be instrumental for the safe and efficient translation of peripheral neuroprostheses to the clinic. I also discussed various computational tools and experimental strategies that could effectively improve functional outcomes in people afflicted by hand paralysis.

To conclude, the work presented in this thesis presents a solid basis for the development of intrafascicular implants and the engineering of peripheral nerve electrical therapies targeting neurological disorders of the upper-limbs. Future systems inspired by these results may provide accurate control of the arm and hand, and promote the restoration of a wide range of functional activities resulting in increased autonomy and quality of life.

A Appendix

A.1. Animals involved in the study

Table A.1 – Animals used for neuro-anatomy

Name	f/m	Age (y)	Weight (kg)
Mk-Ca	f	12	4.5
Mk-Ce	f	8	4.4
Mk-Li	m	16	8.0
Mk-Lo	f	9	4.1
Mk-Ls	f	13	4.0
Mk-Xe	f	7	4.3

Table A.2 – Animals used for acute electrophysiology

Name	f/m	Age (y)	Weight (kg)
Mk-Lo	f	9	4.1
Mk-Li	m	16	8.0
Mk-Th	f	13	5.7
Mk- Me_a	f	9	3.9
Mk- Ol_a	f	5	3.1

Table A.3 – Animals used for chronic electrophysiology

Name	f/m	Age (y)	Weight (kg)
Mk- Me_c	f	9	3.9
Mk- Ol_c	f	5	3.1

Table A.4 – Veterinary license numbers

License number	Animals
2017_03_FR	Mk-Lo, Mk-Li, Mk-Me (Mk- Me_a & Mk- Me_c), Mk-Ol (Mk- Ol_a , Mk- Ol_c)
2014_42E_FR	Mk-Ca, Mk-Th, Mk-Lo
2017_04_FR	Mk-Ce
2016_09_FR	Mk-Xe

A.2. Computational models tensor values

Table A.5 – Electrical conductivities of the materials and tissues included in our volume conductor representing the NHP median nerve

Material	Conductivity ($S.m^{-1}$)	Reference
Epineurium	0.0826	Raspopovic et al., 2011; Schiefer et al., 2008
Perineurium	0.00088	Raspopovic et al., 2017
Endoneurium	0.571 longitud. / 0.0826 transv.	Raspopovic et al., 2011; Schiefer et al., 2008
Saline bath	2	Capogrosso et al., 2013
Polyimide	6.67×10^{-14}	Raspopovic et al., 2017
Active sites	8.9×10^6	Raspopovic et al., 2017

A.3. Detailed muscular implants

Abbreviations: palmaris longus (PL), flexor carpi radialis (FCR), flexor digitorum superficialis (FDS), flexor digitorum profundus (FDP), extensor carpi radialis (ECR), extensor digitorum communis (EDC), abductor pollicis longus (APL), first dorsal interosseous (FDI), pollicis opponens (PO) and abductor pollicis brevis (APB)

A.3 Detailed muscular implants

Table A.6 – Implanted muscles and nerves for electrophysiology in each animal

-	Mk-Lo	Mk-Li	Mk-Th	Mk- Me_a	Mk- Ol_a	Mk- Me_c	Mk- Ol_c
Median nerve implantation (# days functional)	Acute	Acute	Acute	Acute	Acute	Chronic (42)	Chronic (30)
Radial nerve implantation (# days functional)	Acute	Acute	Acute	Acute	Acute	Chronic (<7)	Chronic (58)
Implanted arm	left	left	left	right	right	left	left
Implanted arm	left	left	left	right	right	left	left
	PL	PL	PL	PL	PL	PL	PL
	FCR	FCR	FCR	FCR	FCR	FCR	FCR
Flexor muscles implanted	FDS	FDS	FDS	FDS	FDS	FDS	FDS
	-	FDP	FDP	FDP	FDP	FDP	FDP
	APB	APB	APB	APB	APB	APB	APB
	PO	PO	PO	-	PO	-	-
	FDI	FDI	FDI	FDI	FDI	FDI	FDI
	ECR	ECR	ECR	ECR	ECR	ECR	ECR
Extensor muscles implanted	EDC	EDC	EDC	EDC	EDC	EDC	EDC
	ECU	ECU	ECU	ECU	ECU	ECU	ECU
	APL	APL	APL	APL	APL	APL	APL

A.4. Kinematic features characterizing hand movements in 2D

Table A.7 – Kinematic features computed to characterize flexion movements

Flexion movements median nerve stimulation	Computation from 2D kinematic
PIP index angle PIP pinkie angle PIP thumb angle PIP middle finger angle	Adapted from Barra et al., 2019 in 2D
MCP pinkie angle MCP middle finger angle	\vec{v}_1 : vector from right wrist to MCP pinkie joint \vec{v}_f : vector along the MCP segment of the finger Θ_{MCP_f} : angle between $\perp \vec{v}_1$ and \vec{v}_f $\perp \vec{v}_1$ is a vector normal to the palm
MCP index angle	\vec{v}_2 : vector from left wrist to MCP index joint \vec{v}_f : vector along the MCP segment of the finger Θ_{MCP_f} : angle between $\perp \vec{v}_2$ and \vec{v}_f $\perp \vec{v}_2$ is a vector normal to the palm
MCP thumb angle	\vec{v}_3 : vector from left wrist to MCP joint thumb \vec{v}_f : vector along the MCP segment of the finger Θ_{MCP_f} : angle between \vec{v}_3 and \vec{v}_f
Thumb opposition	\vec{v}_4 : vector from left wrist to MCP joint index Θ_{Opp} : angle between $\perp \vec{v}_4$ and \vec{v}_3 $\perp \vec{v}_4$ is a vector normal to the palm
Abduction pinkie angle	\vec{v}_5 : vector from the MCP index joint to the MCP pinkie joint \vec{v}_f : vector along the MCP segment of the finger Θ_{Abd} : angle between \vec{v}_5 and \vec{v}_f \vec{v}_5 is a vector horizontal to the palm
Wrist flexion angle	\vec{v}_1 : vector from right wrist to MCP pinkie joint \vec{v}_6 : vector from right wrist to midline of the posterior forearm (5cm) $\Theta_{Flexion_{wrist}}$: angle between \vec{v}_1 and \vec{v}_6
Wrist deviation angle	\vec{v}_1 : vector from right wrist to MCP pinkie joint \vec{v}_7 : vector from right to left wrist $\Theta_{Dev_{wrist}}$: angle between \vec{v}_1 and \vec{v}_7
Distance from thumb tip to index tip	Euclidean distance between tip of the thumb and tip of the index in 2D

A.4 Kinematic features characterizing hand movements in 2D

Table A.8 – Kinematic features computed to characterize extension movements

Extension movements radial nerve stimulation	Computation from 2D kinematic
PIP pinkie angle	Adapted from Barra et al., 2019 in 2D
Thumb opposition	\vec{v}_8 : vector along the MCP segment of the index \vec{v}_9 : vector from MCP joint to tip of the thumb θ_{Opp} : angle between \vec{v}_8 and \vec{v}_9
Wrist extension angle	same as flexion
Wrist ulnar deviation angle	\vec{v}_{10} : vector from MCP pinkie joint to MCP thumb joint $\vec{v}_h : \begin{pmatrix} 0 \\ 1 \end{pmatrix}$ $\theta_{Dev_{wrist}}$: angle between \vec{v}_{10} and \vec{v}_h
Distance from index tip to pinkie tip	Euclidean distance between tip of the index and tip of the pinkie in 2D
Distance from thumb tip to index tip	Euclidean distance between tip of the thumb and tip of the index in 2D

A.5. Data specifications

Table A.9 – Data specifications for Figure 3.12 - Analysis of functional grip movements and extension gestures achieved with the TIME

Figure panel	Data specificity
Figure 3.12a top: Video snapshots median nerve stimulation	Mk- Me_c , 33 days post-implantation
Figure 3.12a bottom: Corresponding muscle activation envelopes	Mk- Me_c , 33 days post-implantation, 3-4 repetitions per movement, same stimulation intensity
Figure 3.12b top: Corresponding kinematic profiles	Mk- Me_c , 33 days post-implantation, 7 repetitions/movement
Figure 3.12c: Average kinematic features during stimulation of each grip type across animals	Mk- Me_c , 33 days post-implantation, 7 repetitions/grip - Mk- Ol_c , 12 days post-implantation, 9 repetitions/grip - Mk- Ol_a , acute, 4 repetitions/grip. Data are normalized across grips within each animal (see Methods)
Figure 3d: PCA	Same data
Figure 3e: Grip pressure vs charge	Mk- Me_c , 6 stimulation cycles
Figure 3.12f left: Grip pressure for different stimulated grips compared to voluntary grip pressure exerted during functional task	n=1 voluntary monkey Mk- Ol_c 36 trials/grip, n=3 stimulated monkeys, Mk- Ol_c , 13 trials/grip, Mk- Me_c , 4 to 11 trials/grip, Mk- Ol_a 15 trials/grip
Figure 3.12f right: SI corresponding to the charge at which the grip pressure was measured vs. maximal SI computed from the most recent recruitment curves	Mk- Ol_c : 4 days before, Mk- Me_c : 5 days after and Mk- Ol_a : on the same day, 7 data points ,i.e 3 different grips for Mk- Ol_c (pinch, cylinder, sphere), and 2 different grips for Mk- Ol_a and Mk- Me_c (cylinder, sphere)
Figure 3.12g: evolution of grip pressure over 20 seconds of stimulation	Mk- Me_c 29 days post-implantation, 2 repetitions - Mk- Ol_c 23 days post-implantation, 2 repetitions
Figure 3.12h: Video snapshots radial nerve stimulation	Mk- Me_a , acute
Figure 3.12h: Average kinematic features during stimulation of extension movements across animals	Mk- Ol_c , 33 days post-implantation, 4 repetitions/movement - Mk- Me_a , acute, 4 repetitions/grip - Mk- Ol_a , acute, 12 repetitions for finger extension and 4 for ulnar wrist deviation

Table A.10 – Data specifications for 3.16 – Intraneural stimulation restores hand extension during functional reaching task

Figure panel	Data specificity
Figure 3.16b: example traces of brain and EMG signals, delivered stimulation and recorded grip pressure before (baseline, blue) and after lidocaine injections	3 trials baseline, 2 trials stim. OFF, 6 consecutive trials with 4 stim. ON and 2 stim. OFF
Figure 3.16c: performance quantification during the different conditions during session 1 (top) and session 2 (bottom)	Mk- Ol_c , session 1: 97 trials, session 2: 295 trials, 40 and 47 days post-implantation respectively. Statistics are computed on bootstrapped populations (100'000 samples with replacement – see Methods).
Figure 3.16d top: Representative thumb abductor activation for each condition throughout full movement	Mk- Ol_c , session 2, n=278 trials (27 baseline, 175 stim. ON, 76 stim. OFF)
Figure 3.16d bottom: quantification of flexor vs. extensor muscle activation	The left and right panel respectively show the values of the extensor and flexor muscles pooled together. Data are normalized to the maximum value for each muscle (session 2: n=278).
Figure 3.16e left: mean wrist extension angle for each condition during session 2	Mk- Ol_c , session 2, session 2: n=271 (27 baseline, 175 stim. ON, 76 stim. OFF)
Figure 3.16e right: max wrist extension angle before grasping for each condition	see Methods - Mk- Ol_c , session 1: n=89 trials (9 baseline, 51 stim. ON, 29 stim. OFF), session 2: n=278 (27 baseline, 175 stim. ON, 76 stim. OFF)
Figure 3.16f left: multi-joint coordination	Mk- Ol_c , session 2: n=278 (27 baseline, 175 stim. ON, 76 stim. OFF)
Figure 3.16f right: 2d distance	Mk- Ol_c , session 1: n= 89 trials (9 baseline, 51 stim. ON, 29 stim. OFF), session 2: n=278 (27 baseline, 175 stim. ON, 76 stim. OFF)

A.6. Supplementary videos captions

Supplementary video 1.1 shows the operation of the robotic arm by a human user, in different configurations and for different paradigms.

Supplementary video 3.1 shows the different flexion and extension movements elicited by intraneural stimulation of the median and radial nerve respectively, in anesthetized and awake animals. Together with video recordings, corresponding stimulation triggers and filtered EMG signals are displayed. In case of experiments performed in awake conditions, 3D marker position and relevant kinematic features are also presented. Data are normalized to the maximum obtained across the trials shown for each animal. When available, three consecutive trials per movement are displayed, elicited by the same active site at the same or

similar stimulation intensities (eliciting similar movement range). When not available, the same trial is looped three times. In case of short stimulation bursts (i.e. 500 ms), the speed of the video is decreased by 50% during the stimulation phase to better visualize the generated movement.

Supplementary video 3.2 shows force modulation experiments. The first part of the video displays the flexion movements elicited in Mk-Mec over 5 cycles of sine-wave modulation of the stimulation amplitude of three median active sites evoking respectively a spherical, cylindrical and pinch-like grip. The second part shows the movement achieved by alternatively stimulating one channel from the radial nerve and one channel from the median nerve with shifted sinusoidal amplitude waves. For Mk-Mea the radial and median active sites are chosen to open the hand and perform a spherical or a cylindrical grip, while for Mk-Ola to extend and flex the wrist joint. Together with video recordings, stimulation amplitude wave, filtered force and EMG signals are presented. Data are normalized to the maximum of each trial.

Supplementary video 3.3 shows the restoration of hand extension during functional reaching tasks through brain-controlled stimulation of the radial nerve. Baseline trials, and trial with or without stimulation (stim. ON and stim. OFF respectively) are displayed. The raster plot shows M1 activity after artefact removal (see Methods). The second neural principal component, stimulation triggers, filtered grip pressure and EMG signals are also presented. Data are normalized to the maximum obtained across all the trials shown. In case of trials with stimulation, the speed of the video is decreased by 50% during the grasping phase to better visualize the performed movement.

Bibliography

- Accornero, N., Bini, G., Lenzi, G. L., & Manfredi, M. (1977). Selective activation of peripheral nerve fibre groups of different diameter by triangular shaped stimulus pulses. [eprint: <https://physoc.onlinelibrary.wiley.com/doi/pdf/10.1113/jphysiol.1977.sp012109>]. *The Journal of Physiology*, 273(3), 539–560. <https://doi.org/10.1113/jphysiol.1977.sp012109>
- Aflalo, T., Kellis, S., Klaes, C., Lee, B., Shi, Y., Pejsa, K., Shanfield, K., Hayes-Jackson, S., Aisen, M., Heck, C., Liu, C., & Andersen, R. A. (2015). Decoding motor imagery from the posterior parietal cortex of a tetraplegic human. *Science*, 348(6237), 906–910. <https://doi.org/10.1126/science.aaa5417>
- Ahrens, M. B., Li, J. M., Orger, M. B., Robson, D. N., Schier, A. F., Engert, F., & Portugues, R. (2012). Brain-wide neuronal dynamics during motor adaptation in zebrafish. *Nature*, 485(7399), 471–477. <https://doi.org/10.1038/nature11057>
- Ajiboye, A. B., Willett, F. R., Young, D. R., Memberg, W. D., Murphy, B. A., Miller, J. P., Walter, B. L., Sweet, J. A., Hoyen, H. A., Keith, M. W., Et al. (2017). Restoration of reaching and grasping movements through brain-controlled muscle stimulation in a person with tetraplegia: a proof-of-concept demonstration. *The Lancet*, 389(10081), 1821–1830.
- Almeida, L., Rawal, P. V., Ditty, B., Smelser, B. L., Huang, H., Okun, M. S., Guthrie, B. L., & Walker, H. C. (2016). Deep brain stimulation battery longevity: comparison of monopolar versus bipolar stimulation modes. *Movement Disorders Clinical Practice*, 3(4), 359–366. <https://doi.org/10.1002/mdc3.12285>
- Anderson, K. D. (2004). Targeting recovery: priorities of the spinal cord-injured population [Publisher: Mary Ann Liebert, Inc., publishers]. *Journal of Neurotrauma*, 21(10), 1371–1383. <https://doi.org/10.1089/neu.2004.21.1371>
- Andlin-Sobocki, P., Jönsson, B., Wittchen, H.-U., & Olesen, J. (2005). Cost of disorders of the brain in europe. *European Journal of Neurology*, 12 Suppl 1, 1–27. <https://doi.org/10.1111/j.1468-1331.2005.01202.x>
- Armenta Salas, M., Bashford, L., Kellis, S., Jafari, M., Jo, H., Kramer, D., Shanfield, K., Pejsa, K., Lee, B., Liu, C. Y., & Andersen, R. A. (2018). Proprioceptive and cutaneous sensations in humans elicited by intracortical microstimulation. *eLife*, 7, e32904. <https://doi.org/10.7554/eLife.32904>

-
- Armour, B. S., Courtney-Long, E. A., Fox, M. H., Fredine, H., & Cahill, A. (2016). Prevalence and causes of paralysis-united states, 2013. *American Journal of Public Health*, 106(10), 1855–1857. <https://doi.org/10.2105/AJPH.2016.303270>
- Badi, M., Borgognon, S., O'Doherty, J. E., & Shokur, S. (2020). Cortical stimulation for somatosensory feedback: translation from nonhuman primates to clinical applications. *somatosensory feedback for neuroprosthetics*.
- Badia, J., Boretius, T., Andreu, D., Azevedo-Coste, C., Stieglitz, T., & Navarro, X. (2011). Comparative analysis of transverse intrafascicular multichannel, longitudinal intrafascicular and multipolar cuff electrodes for the selective stimulation of nerve fascicles. *Journal of Neural Engineering*, 8(3), 036023. <https://doi.org/10.1088/1741-2560/8/3/036023>
- Badia, J., Raspopovic, S., Carpaneto, J., Micera, S., & Navarro, X. (2016). Spatial and functional selectivity of peripheral nerve signal recording with the transversal intrafascicular multichannel electrode (TIME). *IEEE Transactions on Neural Systems and Rehabilitation Engineering*, 24(1), 20–27. <https://doi.org/10.1109/TNSRE.2015.2440768>
- Badoud, S., Borgognon, S., Cottet, J., Chatagny, P., Moret, V., Fregosi, M., Kaeser, M., Fortis, E., Schmidlin, E., Bloch, J., Brunet, J. E., & Rouiller, E. M. (2017). Effects of dorsolateral prefrontal cortex lesion on motor habit and performance assessed with manual grasping and control of force in macaque monkeys. *Brain Structure and Function*, 222(3), 1193–1206. <https://doi.org/10.1007/s00429-016-1268-z>
- Barra, B., Badi, M., Perich, M. G., Conti, S., Salehian, S. S. M., Moreillon, F., Bogaard, A., Wurth, S., Kaeser, M., Passeraub, P., Milekovic, T., Billard, A., Micera, S., & Capogrosso, M. (2019). A versatile robotic platform for the design of natural, three-dimensional reaching and grasping tasks in monkeys. *Journal of Neural Engineering*, 17(1), 016004. <https://doi.org/10.1088/1741-2552/ab4c77>
- Barrett, E. F., & Barrett, J. N. (1982). Intracellular recording from vertebrate myelinated axons: mechanism of the depolarizing afterpotential. *The Journal of Physiology*, 323(1), 117–144. <https://doi.org/10.1113/jphysiol.1982.sp014064>
- Bensmaia, S. J., & Miller, L. E. (2014). Restoring sensorimotor function through intracortical interfaces: progress and looming challenges. *Nature Reviews. Neuroscience*, 15(5), 313–325. <https://doi.org/10.1038/nrn3724>
- Bhadra, N., Peckham, P. H., Keith, M. W., Kilgore, K. L., Montague, F., Gazdik, M., & Stage, T. (2002). Implementation of an implantable joint-angle transducer, 39(3), 12.
- Biasiucci, A., Leeb, R., Iturrate, I., Perdakis, S., Al-Khodairy, A., Corbet, T., Schnider, A., Schmidlin, T., Zhang, H., Bassolino, M., Viceic, D., Vuadens, P., Guggisberg, A. G., & Millán, J. d. R. (2018). Brain-actuated functional electrical stimulation elicits lasting arm motor recovery after stroke [Number: 1 Publisher: Nature Publishing Group]. *Nature Communications*, 9(1), 2421. <https://doi.org/10.1038/s41467-018-04673-z>
- Binder-Macleod, S. A., & Snyder-Mackler, L. (1993). Muscle fatigue: clinical implications for fatigue assessment and neuromuscular electrical stimulation [Publisher: Oxford Academic]. *Physical Therapy*, 73(12), 902–910. <https://doi.org/10.1093/ptj/73.12.902>

-
- Blight, A. R., & Someya, S. (1985). Depolarizing afterpotentials in myelinated axons of mammalian spinal cord. *Neuroscience*, 15(1), 1–12. [https://doi.org/10.1016/0306-4522\(85\)90118-6](https://doi.org/10.1016/0306-4522(85)90118-6)
- Bonizzato, M., Pidpruzhnykova, G., DiGiovanna, J., Shkorbatova, P., Pavlova, N., Micera, S., & Courtine, G. (2018). Brain-controlled modulation of spinal circuits improves recovery from spinal cord injury [Number: 1 Publisher: Nature Publishing Group]. *Nature Communications*, 9(1), 3015. <https://doi.org/10.1038/s41467-018-05282-6>
- Borboni, A., Faglia, R., & Mor, M. (2014, October 23). Compliant device for hand rehabilitation of stroke patient. ASME 2014 12th Biennial Conference on Engineering Systems Design and Analysis, American Society of Mechanical Engineers Digital Collection. <https://doi.org/10.1115/ESDA2014-20081>
- Boretius, T., Badia, J., Pascual-Font, A., Schuettler, M., Navarro, X., Yoshida, K., & Stieglitz, T. (2010). A transverse intrafascicular multichannel electrode (TIME) to interface with the peripheral nerve. *Biosensors and Bioelectronics*, 26(1), 62–69. <https://doi.org/10.1016/j.bios.2010.05.010>
- Boretius, T., Yoshida, K., Badia, J., Harreby, K., Kundu, A., Navarro, X., Jensen, W., & Stieglitz, T. (2012). A transverse intrafascicular multichannel electrode (TIME) to treat phantom limb pain—towards human clinical trials, In *Biomedical robotics and biomechatronics (BioRob)*, 2012 4th IEEE RAS & EMBS international conference on, IEEE.
- Borton, D., Micera, S., Millán, J. d. R., & Courtine, G. (2013). Personalized neuroprosthetics [Publisher: American Association for the Advancement of Science Section: Review]. *Science Translational Medicine*, 5(210), 210rv2–210rv2. <https://doi.org/10.1126/scitranslmed.3005968>
- Bostock, H., Baker, M., & Reid, G. (1991). Changes in excitability of human motor axons underlying post-ischaemic fasciculations: evidence for two stable states. *The Journal of Physiology*, 441, 537–557. Retrieved September 17, 2020, from <https://www.ncbi.nlm.nih.gov/pmc/articles/PMC1180213/>
- Bourbeau, D. J., Hokanson, J. A., Rubin, J. E., & Weber, D. J. (2011). A computational model for estimating recruitment of primary afferent fibers by intraneural stimulation in the dorsal root ganglia. *Journal of neural engineering*, 8(5), 056009. <https://doi.org/10.1088/1741-2560/8/5/056009>
- Bouton, C. E., Shaikhouni, A., Annetta, N. V., Bockbrader, M. A., Friedenberg, D. A., Nielson, D. M., Sharma, G., Sederberg, P. B., Glenn, B. C., Mysiw, W. J., Morgan, A. G., Deogaonkar, M., & Rezai, A. R. (2016). Restoring cortical control of functional movement in a human with quadriplegia. *Nature*, 533(7602), 247–250. <https://doi.org/10.1038/nature17435>
- Brandman, D., Hosman, T., Saab, J., Burkhart, M., Shanahan, B., Ciancibello, J., Sarma, A., Milstein, D., Vargas-Irwin, C., Franco, B., Kelemen, J., Blabe, C., Murphy, B., Young, D., Willett, F., Pandarinath, C., Stavisky, S., Kirsch, R., Walter, B., & Hochberg, L. (2018). Rapid calibration of an intracortical brain–computer interface for people with tetraplegia. *Journal of Neural Engineering*, 15, 026007. <https://doi.org/10.1088/1741-2552/aa9ee7>

-
- Branner, A., Stein, R. B., Fernandez, E., Aoyagi, Y., & Normann, R. A. (2004). Long-term stimulation and recording with a penetrating microelectrode array in cat sciatic nerve. *IEEE transactions on bio-medical engineering*, 51(1), 146–157. <https://doi.org/10.1109/TBME.2003.820321>
- Branner, A., Stein, R. B., & Normann, R. A. (2001). Selective stimulation of cat sciatic nerve using an array of varying-length microelectrodes [Publisher: American Physiological Society]. *Journal of Neurophysiology*, 85(4), 1585–1594. <https://doi.org/10.1152/jn.2001.85.4.1585>
- Braun, D., Mehring, C., & Wolpert, D. (2009). Structure learning in action. *Behavioural brain research*, 206, 157–65. <https://doi.org/10.1016/j.bbr.2009.08.031>
- Brill, N. A., Naufel, S. N., Polasek, K., Ethier, C., Cheesborough, J., Agnew, S., Miller, L. E., & Tyler, D. J. (2018). Evaluation of high-density, multi-contact nerve cuffs for activation of grasp muscles in monkeys. *Journal of Neural Engineering*, 15(3), 036003. <https://doi.org/10.1088/1741-2552/aa8735>
- Brochier, T. (2004). Patterns of muscle activity underlying object-specific grasp by the macaque monkey. *Journal of Neurophysiology*, 92(3), 1770–1782. <https://doi.org/10.1152/jn.00976.2003>
- Brushart, T. M. (1991). Central course of digital axons within the median nerve of macaca mulatta. *Journal of Comparative Neurology*, 311(2), 197–209.
- Buma, F., Kwakkel, G., & Ramsey, N. (2013). Understanding upper limb recovery after stroke. *Restorative Neurology and Neuroscience*, 31(6), 707–722. <https://doi.org/10.3233/RNN-130332>
- Callier, T., Brantly, N. W., Caravelli, A., & Bensmaia, S. J. (2020). The frequency of cortical microstimulation shapes artificial touch [Publisher: National Academy of Sciences Section: Biological Sciences]. *Proceedings of the National Academy of Sciences*, 117(2), 1191–1200. <https://doi.org/10.1073/pnas.1916453117>
- Capogrosso, M., Wenger, N., Raspopovic, S., Musienko, P., Beauparlant, J., Bassi Luciani, L., Courtine, G., & Micera, S. (2013). A computational model for epidural electrical stimulation of spinal sensorimotor circuits. *Journal of Neuroscience*, 33(49), 19326–19340. <https://doi.org/10.1523/JNEUROSCI.1688-13.2013>
- Capogrosso, M., Gandar, J., Greiner, N., Moraud, E. M., Wenger, N., Polina Shkorbatova, Musienko, P., Minev, I., Lacour, S., & Courtine, G. (2018). Advantages of soft subdural implants for the delivery of electrochemical neuromodulation therapies to the spinal cord. *Journal of Neural Engineering*, 15(2), 026024. <https://doi.org/10.1088/1741-2552/aaa87a>
- Capogrosso, M., & Lempka, S. F. (2020). A computational outlook on neurostimulation. *Bio-electronic Medicine*, 6(1), 10. <https://doi.org/10.1186/s42234-020-00047-3>
- Capogrosso, M., Milekovic, T., Borton, D., Wagner, F., Moraud, E. M., Mignardot, J.-B., Buse, N., Gandar, J., Barraud, Q., Xing, D., Rey, E., Duis, S., Jianzhong, Y., Ko, W. K. D., Li, Q., Detemple, P., Denison, T., Micera, S., Bezaud, E., ... Courtine, G. (2016). A brain–spine interface alleviating gait deficits after spinal cord injury in primates. *Nature*, 539(7628), 284–288. <https://doi.org/10.1038/nature20118>

-
- Capogrosso, M., Wagner, F. B., Gandar, J., Moraud, E. M., Wenger, N., Milekovic, T., Shkorbatova, P., Pavlova, N., Musienko, P., Bezard, E., Bloch, J., & Courtine, G. (2018). Configuration of electrical spinal cord stimulation through real-time processing of gait kinematics. *Nature Protocols*, 13(9), 2031–2061. <https://doi.org/10.1038/s41596-018-0030-9>
- Carmena, J. M., Lebedev, M. A., Crist, R. E., O'Doherty, J. E., Santucci, D. M., Dimitrov, D. F., Patil, P. G., Henriquez, C. S., & Nicolelis, M. A. L. (2003). Learning to control a brain–machine interface for reaching and grasping by primates. *PLOS Biology*, 1(2), e42. <https://doi.org/10.1371/journal.pbio.0000042>
- Carroll, S., Cooper, C., Brown, D., Sormann, G., Flood, S., & Denison, M. (2000). Australian experience with the freehand system for restoring grasp in quadriplegia. *The Australian and New Zealand Journal of Surgery*, 70(8), 563–568. <https://doi.org/10.1046/j.1440-1622.2000.01899.x>
- Chae, J., & Hart, R. (1998). Comparison of discomfort associated with surface and percutaneous intramuscular electrical stimulation for persons with chronic hemiplegia. *American Journal of Physical Medicine & Rehabilitation*, 77(6), 516–522. <https://doi.org/10.1097/00002060-199811000-00013>
- Chen, R., Corwell, B., Yaseen, Z., Hallett, M., & Cohen, L. G. (1998). Mechanisms of cortical reorganization in lower-limb amputees [Publisher: Society for Neuroscience Section: ARTICLE]. *Journal of Neuroscience*, 18(9), 3443–3450. <https://doi.org/10.1523/JNEUROSCI.18-09-03443.1998>
- Cheney, P. D., & Fetz, E. E. (1980). Functional classes of primate corticomotoneuronal cells and their relation to active force [Publisher: American Physiological Society]. *Journal of Neurophysiology*, 44(4), 773–791. <https://doi.org/10.1152/jn.1980.44.4.773>
- Chestek, C. A., Gilja, V., Blabe, C. H., Foster, B. L., Shenoy, K. V., Parvizi, J., & Henderson, J. M. (2013). Hand posture classification using electrocorticography signals in the gamma band over human sensorimotor brain areas. *Journal of neural engineering*, 10(2), 026002. <https://doi.org/10.1088/1741-2560/10/2/026002>
- Chestek, C. A., Gilja, V., Nuyujukian, P., Foster, J. D., Fan, J. M., Kaufman, M. T., Churchland, M. M., Rivera-Alvidrez, Z., Cunningham, J. P., Ryu, S. I., & Shenoy, K. V. (2011). Long-term stability of neural prosthetic control signals from silicon cortical arrays in rhesus macaque motor cortex. *Journal of neural engineering*, 8(4), 045005. <https://doi.org/10.1088/1741-2560/8/4/045005>
- Choi, A., Cavanaugh, J., & Durand, D. (2001). Selectivity of multiple-contact nerve cuff electrodes: a simulation analysis [Conference Name: IEEE Transactions on Biomedical Engineering]. *IEEE Transactions on Biomedical Engineering*, 48(2), 165–172. <https://doi.org/10.1109/10.909637>
- Christensen, M. B., Pearce, S. M., Ledbetter, N. M., Warren, D. J., Clark, G. A., & Tresco, P. A. (2014). The foreign body response to the utah slant electrode array in the cat sciatic nerve. *Acta Biomaterialia*, 10(11), 4650–4660. <https://doi.org/10.1016/j.actbio.2014.07.010>

-
- Churchland, M. M., Cunningham, J. P., Kaufman, M. T., Foster, J. D., Nuyujukian, P., Ryu, S. I., & Shenoy, K. V. (2012). Neural population dynamics during reaching. *Nature*, 487(7405), 51–56. <https://doi.org/10.1038/nature11129>
- Churchland, M. M., & Shenoy, K. V. (2007). Temporal complexity and heterogeneity of single-neuron activity in premotor and motor cortex. *Journal of Neurophysiology*, 97(6), 4235–4257. <https://doi.org/10.1152/jn.00095.2007>
- Churchland, M. M., Yu, B. M., Cunningham, J. P., Sugrue, L. P., Cohen, M. R., Corrado, G. S., Newsome, W. T., Clark, A. M., Hosseini, P., Scott, B. B., Bradley, D. C., Smith, M. A., Kohn, A., Movshon, J. A., Armstrong, K. M., Moore, T., Chang, S. W., Snyder, L. H., Lisberger, S. G., ... Shenoy, K. V. (2010). Stimulus onset quenches neural variability: a widespread cortical phenomenon. *Nature neuroscience*, 13(3), 369–378. <https://doi.org/10.1038/nn.2501>
- Cirstea, M. C., Mitnitski, A. B., Feldman, A. G., & Levin, M. F. (2003). Interjoint coordination dynamics during reaching in stroke. *Experimental Brain Research*, 151(3), 289–300. <https://doi.org/10.1007/s00221-003-1438-0>
- Colachis, S. C. I., Bockbrader, M. A., Zhang, M., Friedenberg, D. A., Annetta, N. V., Schwemmer, M. A., Skomrock, N. D., Mysiw, W. J., Rezai, A. R., Bresler, H. S., & Sharma, G. (2018). Dexterous control of seven functional hand movements using cortically-controlled transcutaneous muscle stimulation in a person with tetraplegia [Publisher: Frontiers]. *Frontiers in Neuroscience*, 12. <https://doi.org/10.3389/fnins.2018.00208>
- Collinger, J. L., Boninger, M. L., Bruns, T. M., Curley, K., Wang, W., & Weber, D. J. (2013). Functional priorities, assistive technology, and brain-computer interfaces after spinal cord injury. *Journal of rehabilitation research and development*, 50(2), 145–160. Retrieved September 14, 2020, from <https://www.ncbi.nlm.nih.gov/pmc/articles/PMC3684986/>
- Collinger, J. L., Wodlinger, B., Downey, J. E., Wang, W., Tyler-Kabara, E. C., Weber, D. J., McMorland, A. J., Velliste, M., Boninger, M. L., & Schwartz, A. B. (2013). High-performance neuroprosthetic control by an individual with tetraplegia. *The Lancet*, 381(9866), 557–564. [https://doi.org/10.1016/S0140-6736\(12\)61816-9](https://doi.org/10.1016/S0140-6736(12)61816-9)
- Cornwall, R., & Hausman, M. R. (2004). Implanted neuroprostheses for restoration of hand function in tetraplegic patients. *JAAOS - Journal of the American Academy of Orthopaedic Surgeons*, 12(2), 72–79. Retrieved September 16, 2020, from https://journals.lww.com/jaaos/Fulltext/2004/03000/Implanted_Neuroprostheses_for_Restoration_of_Hand.2.aspx
- Cunningham, J. P., & Yu, B. M. (2014). Dimensionality reduction for large-scale neural recordings [Number: 11 Publisher: Nature Publishing Group]. *Nature Neuroscience*, 17(11), 1500–1509. <https://doi.org/10.1038/nn.3776>
- Cutrone, A., Valle, J. D., Santos, D., Badia, J., Filippeschi, C., Micera, S., Navarro, X., & Bossi, S. (2015). A three-dimensional self-opening intraneural peripheral interface (SELINe). *Journal of Neural Engineering*, 12(1), 016016. <https://doi.org/10.1088/1741-2560/12/1/016016>
- Čvančara, P., Valle, G., Müller, M., Guiho, T., Hiairassary, A., Petrini, F., Raspopovic, S., Strauss, I., Granata, G., Fernandez, E., Rossini, P. M., Barbaro, M., Yoshida, K., Jensen, W., Di-

-
- voux, J.-L., Guiraud, D., Micera, S., & Stieglitz, T. (2019). On the reliability of chronically implanted thin-film electrodes in human arm nerves for neuroprosthetic applications [Publisher: Cold Spring Harbor Laboratory Section: New Results]. *bioRxiv*, 653964. <https://doi.org/10.1101/653964>
- Čvančara, P., Boretius, T., López-Álvarez, V. M., Maciejasz, P., Andreu, D., Raspopovic, S., Petrini, F., Micera, S., Granata, G., Fernandez, E., Rossini, P. M., Yoshida, K., Jensen, W., Divoux, J.-L., Guiraud, D., Navarro, X., & Stieglitz, T. (2020). Stability of flexible thin-film metallization stimulation electrodes: analysis of explants after first-in-human study and improvement of in vivo performance [Publisher: IOP Publishing]. *Journal of Neural Engineering*, 17(4), 046006. <https://doi.org/10.1088/1741-2552/ab9a9a>
- Dadarlat, M. C., O'Doherty, J. E., & Sabes, P. N. (2015). A learning-based approach to artificial sensory feedback leads to optimal integration [Number: 1 Publisher: Nature Publishing Group]. *Nature Neuroscience*, 18(1), 138–144. <https://doi.org/10.1038/nn.3883>
- Dali, M., Rossel, O., Andreu, D., Laporte, L., Hernandez, A., Laforet, J., Marijon, E., Hagège, A., Clerc, M., Henry, C., & Guiraud, D. (2018). Model based optimal multipolar stimulation without a priori knowledge of nerve structure: application to vagus nerve stimulation. *Journal of Neural Engineering*. <https://doi.org/10.1088/1741-2552/aabeb9>
- Daly, J. J., & Wolpaw, J. R. (2008). Brain–computer interfaces in neurological rehabilitation. *The Lancet Neurology*, 7(11), 1032–1043. [https://doi.org/10.1016/S1474-4422\(08\)70223-0](https://doi.org/10.1016/S1474-4422(08)70223-0)
- Dana Reeve Foundation. (2020). *Paralysis statistics* [Reeve foundation]. Retrieved September 30, 2020, from <https://www.christopherreeve.org/living-with-paralysis/stats-about-paralysis>
- Danion, F., Latash, M. L., Li, Z. M., & Zatsiorsky, V. M. (2000). The effect of fatigue on multifinger co-ordination in force production tasks in humans. *The Journal of Physiology*, 523, 523–532. <https://doi.org/10.1111/j.1469-7793.2000.00523.x>
- D'Anna, E., Petrini, F. M., Artoni, F., Popovic, I., Simanić, I., Raspopovic, S., & Micera, S. (2017). A somatotopic bidirectional hand prosthesis with transcutaneous electrical nerve stimulation based sensory feedback. *Scientific Reports*, 7(1), 10930. <https://doi.org/10.1038/s41598-017-11306-w>
- D'Anna, E., Valle, G., Mazzoni, A., Strauss, I., Iberite, F., Patton, J., Petrini, F. M., Raspopovic, S., Granata, G., Iorio, R. D., Controzzi, M., Cipriani, C., Stieglitz, T., Rossini, P. M., & Micera, S. (2019). A closed-loop hand prosthesis with simultaneous intraneural tactile and position feedback [Publisher: Science Robotics Section: Research Article]. *Science Robotics*, 4(27). <https://doi.org/10.1126/scirobotics.aau8892>
- Davis, T. S., Wark, H. A. C., Hutchinson, D. T., Warren, D. J., O'Neill, K., Scheinblum, T., Clark, G. A., Normann, R. A., & Greger, B. (2016). Restoring motor control and sensory feedback in people with upper extremity amputations using arrays of 96 microelectrodes implanted in the median and ulnar nerves [Publisher: IOP Publishing]. *Journal of Neural Engineering*, 13(3), 036001. <https://doi.org/10.1088/1741-2560/13/3/036001>
- de Haan, M. J., Brochier, T., Grün, S., Riehle, A., & Barthélemy, F. V. (2018). Real-time visuomotor behavior and electrophysiology recording setup for use with humans and monkeys

-
- [Publisher: American Physiological Society]. *Journal of Neurophysiology*, 120(2), 539–552. <https://doi.org/10.1152/jn.00262.2017>
- Degenhart, A. D., Bishop, W. E., Oby, E. R., Tyler-Kabara, E. C., Chase, S. M., Batista, A. P., & Yu, B. M. (2020). Stabilization of a brain–computer interface via the alignment of low-dimensional spaces of neural activity. *Nature Biomedical Engineering*, 4(7), 672–685. <https://doi.org/10.1038/s41551-020-0542-9>
- Delgado-Martínez, I., Badia, J., Pascual-Font, A., Rodríguez-Baeza, A., & Navarro, X. (2016). Fascicular topography of the human median nerve for neuroprosthetic surgery. *Frontiers in Neuroscience*, 10. <https://doi.org/10.3389/fnins.2016.00286>
- Desautels, T. A., Choe, J., Gad, P., Nandra, M. S., Roy, R. R., Zhong, H., Tai, Y.-C., Edgerton, V. R., & Burdick, J. W. (2015). An active learning algorithm for control of epidural electrostimulation. *IEEE Transactions on Biomedical Engineering*, 62(10), 2443–2455. <https://doi.org/10.1109/TBME.2015.2431911>
- Dickey, A. S., Suminski, A., Amit, Y., & Hatsopoulos, N. G. (2009). Single-unit stability using chronically implanted multielectrode arrays. *Journal of Neurophysiology*, 102(2), 1331–1339. <https://doi.org/10.1152/jn.90920.2008>
- Dobkin, B. H. (2005). Rehabilitation after stroke [Publisher: Massachusetts Medical Society _eprint: <https://doi.org/10.1056/NEJMcp043511>]. *New England Journal of Medicine*, 352(16), 1677–1684. <https://doi.org/10.1056/NEJMcp043511>
- Donoghue, J. P. (2002). Connecting cortex to machines: recent advances in brain interfaces [Number: 11 Publisher: Nature Publishing Group]. *Nature Neuroscience*, 5(11), 1085–1088. <https://doi.org/10.1038/nn947>
- Durand, D., Yoo, P., & Lertmanorat, Z. (2004, September). Neural interfacing with the peripheral nervous system, In *The 26th annual international conference of the IEEE engineering in medicine and biology society*. The 26th Annual International Conference of the IEEE Engineering in Medicine and Biology Society. <https://doi.org/10.1109/IEMBS.2004.1404488>
- Edgerton, V. R., Courtine, G., Gerasimenko, Y. P., Lavrov, I., Ichiyama, R. M., Fong, A. J., Cai, L. L., Otsoshi, C. K., Tillakaratne, N. J. K., Burdick, J. W., & Roy, R. R. (2008). Training locomotor networks [Publisher: NIH Public Access]. *Brain research reviews*, 57(1), 241. <https://doi.org/10.1016/j.brainresrev.2007.09.002>
- Elsayed, G. F., Lara, A. H., Kaufman, M. T., Churchland, M. M., & Cunningham, J. P. (2016). Reorganization between preparatory and movement population responses in motor cortex. *Nature Communications*, 7, 13239. <https://doi.org/10.1038/ncomms13239>
- Ethier, C., Gallego, J., & Miller, L. (2015). Brain-controlled neuromuscular stimulation to drive neural plasticity and functional recovery. *Current opinion in neurobiology*, 33, 95–102. <https://doi.org/10.1016/j.conb.2015.03.007>
- Ethier, C., Oby, E., Bauman, M., & Miller, L. (2012). Restoration of grasp following paralysis through brain-controlled stimulation of muscles. *Nature*, 485(7398), 368–371. <https://doi.org/10.1038/nature10987>
- Fagg, A. H., Hatsopoulos, N. G., Lafuente, V. d., Moxon, K. A., Nemati, S., Rebesco, J. M., Romo, R., Solla, S. A., Reimer, J., Tkach, D., Pohlmeier, E. A., & Miller, L. E. (2007).

-
- Biomimetic brain machine interfaces for the control of movement [Publisher: Society for Neuroscience Section: Symposia and Mini-Symposia]. *Journal of Neuroscience*, 27(44), 11842–11846. <https://doi.org/10.1523/JNEUROSCI.3516-07.2007>
- Fang, Z.-P., & Mortimer, J. (1991). Selective activation of small motor axons by quasitrapezoidal current pulses [Conference Name: IEEE Transactions on Biomedical Engineering]. *IEEE Transactions on Biomedical Engineering*, 38(2), 168–174. <https://doi.org/10.1109/10.76383>
- Feigin, V. L., Nichols, E., Alam, T., Bannick, M. S., Beghi, E., Blake, N., Culpepper, W. J., Dorsey, E. R., Elbaz, A., Ellenbogen, R. G., Fisher, J. L., Fitzmaurice, C., Giussani, G., Glennie, L., James, S. L., Johnson, C. O., Kassebaum, N. J., Logroscino, G., Marin, B., ... Vos, T. (2019). Global, regional, and national burden of neurological disorders, 1990–2016: a systematic analysis for the global burden of disease study 2016 [Publisher: Elsevier]. *The Lancet Neurology*, 18(5), 459–480. [https://doi.org/10.1016/S1474-4422\(18\)30499-X](https://doi.org/10.1016/S1474-4422(18)30499-X)
- Feix, T., Romero, J., Schmiedmayer, H.-B., Dollar, A. M., & Kragic, D. (2016). The GRASP taxonomy of human grasp types. *IEEE Transactions on Human-Machine Systems*, 46(1), 66–77. <https://doi.org/10.1109/THMS.2015.2470657>
- Fetz, E. E. (1969). Operant conditioning of cortical unit activity [Publisher: American Association for the Advancement of Science Section: Reports]. *Science*, 163(3870), 955–958. <https://doi.org/10.1126/science.163.3870.955>
- Fitzhugh, R. (1962). Computation of impulse initiation and saltatory conduction in a myelinated nerve fiber. *Biophysical Journal*, 2(1), 11–21. Retrieved September 17, 2020, from <https://www.ncbi.nlm.nih.gov/pmc/articles/PMC1366385/>
- Fitzpatrick, D., Struijk, J., & Andrews, B. (1991, October). A nerve cuff design for the selective activation and blocking of myelinated nerve fibres, In *Proceedings of the annual international conference of the IEEE engineering in medicine and biology society volume 13: 1991*. Proceedings of the Annual International Conference of the IEEE Engineering in Medicine and Biology Society Volume 13: 1991. <https://doi.org/10.1109/IEMBS.1991.684255>
- Fitzsimmons, N., Lebedev, M., Peikon, I., & Nicolelis, M. A. L. (2009). Extracting kinematic parameters for monkey bipedal walking from cortical neuronal ensemble activity [Publisher: Frontiers]. *Frontiers in Integrative Neuroscience*, 3. <https://doi.org/10.3389/neuro.07.003.2009>
- Flesher, S. N., Downey, J. E., Weiss, J. M., Hughes, C. L., Herrera, A. J., Tyler-Kabara, E. C., Boninger, M. L., Collinger, J. L., & Gaunt, R. A. (2019). Restored tactile sensation improves neuroprosthetic arm control [Publisher: Cold Spring Harbor Laboratory Section: New Results]. *bioRxiv*, 653428. <https://doi.org/10.1101/653428>
- Fonseca, L., Tigra, W., Navarro, B., Guiraud, D., Fattal, C., Bó, A., Fachin-Martins, E., Leynaert, V., Gélis, A., & Azevedo-Coste, C. (2019). Assisted grasping in individuals with tetraplegia: improving control through residual muscle contraction and movement. *Sensors (Basel, Switzerland)*, 19(20). <https://doi.org/10.3390/s19204532>

-
- Formento, E., D'Anna, E., Gribo, S., Lacour, S. P., & Micera, S. (2020). A biomimetic electrical stimulation strategy to induce asynchronous stochastic neural activity [Publisher: IOP Publishing]. *Journal of Neural Engineering*, 17(4), 046019. <https://doi.org/10.1088/1741-2552/aba4fc>
- Formento, E., Minassian, K., Wagner, F., Mignardot, J. B., Le Goff-Mignardot, C. G., Rowald, A., Bloch, J., Micera, S., Capogrosso, M., & Courtine, G. (2018). Electrical spinal cord stimulation must preserve proprioception to enable locomotion in humans with spinal cord injury [Number: 12 Publisher: Nature Publishing Group]. *Nature Neuroscience*, 21(12), 1728–1741. <https://doi.org/10.1038/s41593-018-0262-6>
- Friedenberg, D. A., Schwemmer, M. A., Landgraf, A. J., Annetta, N. V., Bockbrader, M. A., Bouton, C. E., Zhang, M., Rezai, A. R., Mysiw, W. J., Bresler, H. S., & Sharma, G. (2017). Neuroprosthetic-enabled control of graded arm muscle contraction in a paralyzed human. *Scientific Reports*, 7(1). <https://doi.org/10.1038/s41598-017-08120-9>
- Frijns, J. H. M., & ten Kate, J. H. (1994). A model of myelinated nerve fibres for electrical prosthesis design. *Medical and Biological Engineering and Computing*, 32(4), 391–398. <https://doi.org/10.1007/BF02524690>
- Gaillet, V., Cutrone, A., Artoni, F., Vagni, P., Mega Pratiwi, A., Romero, S. A., Lipucci Di Paola, D., Micera, S., & Ghezzi, D. (2020). Spatially selective activation of the visual cortex via intraneural stimulation of the optic nerve [Number: 2 Publisher: Nature Publishing Group]. *Nature Biomedical Engineering*, 4(2), 181–194. <https://doi.org/10.1038/s41551-019-0446-8>
- Gallego, J. A., Perich, M. G., Chowdhury, R. H., Solla, S. A., & Miller, L. E. (2018, October 18). *A stable, long-term cortical signature underlying consistent behavior* (preprint). Neuroscience. <https://doi.org/10.1101/447441>
- Gallego, J. A., Perich, M. G., Chowdhury, R. H., Solla, S. A., & Miller, L. E. (2020). Long-term stability of cortical population dynamics underlying consistent behavior [Number: 2 Publisher: Nature Publishing Group]. *Nature Neuroscience*, 23(2), 260–270. <https://doi.org/10.1038/s41593-019-0555-4>
- Gallego, J. A., Perich, M. G., Miller, L. E., & Solla, S. A. (2017). Neural manifolds for the control of movement. *Neuron*, 94(5), 978–984. <https://doi.org/10.1016/j.neuron.2017.05.025>
- Gallego, J. A., Perich, M. G., Naufel, S. N., Ethier, C., Solla, S. A., & Miller, L. E. (2018). Cortical population activity within a preserved neural manifold underlies multiple motor behaviors [Number: 1 Publisher: Nature Publishing Group]. *Nature Communications*, 9(1), 4233. <https://doi.org/10.1038/s41467-018-06560-z>
- Gandolfo, F., Li, C.-S. R., Benda, B. J., Schioppa, C. P., & Bizzi, E. (2000). Cortical correlates of learning in monkeys adapting to a new dynamical environment. *Proceedings of the National Academy of Sciences of the United States of America*, 97(5), 2259–2263. Retrieved September 23, 2020, from <https://www.ncbi.nlm.nih.gov/pmc/articles/PMC15788/>
- Ganguly, K., & Carmena, J. M. (2009). Emergence of a stable cortical map for neuroprosthetic control [Publisher: Public Library of Science]. *PLOS Biology*, 7(7), e1000153. <https://doi.org/10.1371/journal.pbio.1000153>

-
- Ganong, W. F. (2013, January 15). *Review of medical physiology* [Accepted: 2015-01-14T00:01:31Z]. McGraw-Hill. Retrieved September 28, 2020, from <http://116.206.63.139:8080/xmlui/handle/123456789/425>
- Ganzer, P. D., Colachis, S. C., Schwemmer, M. A., Friedenber, D. A., Dunlap, C. F., Swiftney, C. E., Jacobowitz, A. F., Weber, D. J., Bockbrader, M. A., & Sharma, G. (2020). Restoring the sense of touch using a sensorimotor demultiplexing neural interface. *Cell*, 181(4), 763–773.e12. <https://doi.org/10.1016/j.cell.2020.03.054>
- Garrett, A. L., Perry, J., & Nickel, V. L. (1964). Traumatic quadriplegia: many of these patients can become self-sufficient through the use of orthotic devices and by means of resistance exercises [Publisher: American Medical Association]. *JAMA*, 187(1), 7–11. <https://doi.org/10.1001/jama.1964.03060140013003>
- Gaunt, R., Hokanson, J., & Weber, D. (2009). Microstimulation of primary afferent neurons in the l7 dorsal root ganglia using multielectrode arrays in anesthetized cat: thresholds and recruitment properties. *Journal of neural engineering*, 6(5), 055009. <https://doi.org/10.1088/1741-2560/6/5/055009>
- George, J. A., Kluger, D. T., Davis, T. S., Wendelken, S. M., Okorokova, E. V., He, Q., Duncan, C. C., Hutchinson, D. T., Thumser, Z. C., Beckler, D. T., Marasco, P. D., Bensmaia, S. J., & Clark, G. A. (2019). Biomimetic sensory feedback through peripheral nerve stimulation improves dexterous use of a bionic hand [Publisher: Science Robotics Section: Research Article]. *Science Robotics*, 4(32). <https://doi.org/10.1126/scirobotics.aax2352>
- Georgopoulos, A., Schwartz, A., & Kettner, R. (1986). Neuronal population coding of movement direction. *Science*, 233(4771), 1416–1419. <https://doi.org/10.1126/science.3749885>
- Gesslbauer, B., Hruby, L. A., Roche, A. D., Farina, D., Blumer, R., & Aszmann, O. C. (2017). Axonal components of nerves innervating the human arm: axonal components of human upper limb nerves. *Annals of Neurology*. <https://doi.org/10.1002/ana.25018>
- Gilja, V., Chestek, C. A., Diester, I., Henderson, J. M., Deisseroth, K., & Shenoy, K. V. (2011). Challenges and opportunities for next-generation intracortically based neural prostheses. *IEEE Transactions on Biomedical Engineering*, 58(7), 1891–1899. <https://doi.org/10.1109/TBME.2011.2107553>
- Gilja, V., Nuyujukian, P., Chestek, C. A., Cunningham, J. P., Yu, B. M., Fan, J. M., Churchland, M. M., Kaufman, M. T., Kao, J. C., Ryu, S. I., & Shenoy, K. V. (2012). A high-performance neural prosthesis enabled by control algorithm design. *Nature neuroscience*, 15(12), 1752–1757. <https://doi.org/10.1038/nn.3265>
- Gilja, V., Pandarinath, C., Blabe, C. H., Nuyujukian, P., Simeral, J. D., Sarma, A. A., Sorice, B. L., Perge, J. A., Jarosiewicz, B., Hochberg, L. R., Shenoy, K. V., & Henderson, J. M. (2015). Clinical translation of a high-performance neural prosthesis [Number: 10 Publisher: Nature Publishing Group]. *Nature Medicine*, 21(10), 1142–1145. <https://doi.org/10.1038/nm.3953>
- Gilman, S., & Arbor, A. (1983). Handbook of physiology. section 1: the nervous system, vol II. motor control, parts 1 and 2. section editors: john m. brookhart and vernon b. mountcastle volume editor: vernon b. brooks bethesda, MD, american physiological

-
- society, 1981 1480 pp, illustrated. *Annals of Neurology*, 13(1), 111–111. <https://doi.org/10.1002/ana.410130130>
- Giszter, S. F. (2015). Motor primitives—new data and future questions. *Current Opinion in Neurobiology*, 33, 156–165. <https://doi.org/10.1016/j.conb.2015.04.004>
- Glen E. Gresham, W. B. (2004, August 30). *Post-stroke rehabilitation* [Google-Books-ID: 5GgQYAP-WyLAC]. DIANE Publishing.
- Goldman, L., & Albus, J. S. (1968). Computation of impulse conduction in myelinated fibers; theoretical basis of the velocity-diameter relation. *Biophysical Journal*, 8(5), 596–607. Retrieved September 17, 2020, from <https://www.ncbi.nlm.nih.gov/pmc/articles/PMC1367402/>
- Gordon, J., Ghilardi, M. F., & Ghez, C. (1995). Impairments of reaching movements in patients without proprioception. i. spatial errors [Publisher: American Physiological Society]. *Journal of Neurophysiology*, 73(1), 347–360. <https://doi.org/10.1152/jn.1995.73.1.347>
- Gracies, J.-M. (2005a). Pathophysiology of spastic paresis. i: paresis and soft tissue changes [eprint: <https://onlinelibrary.wiley.com/doi/pdf/10.1002/mus.20284>]. *Muscle & Nerve*, 31(5), 535–551. <https://doi.org/10.1002/mus.20284>
- Gracies, J.-M. (2005b). Pathophysiology of spastic paresis. II: emergence of muscle overactivity [eprint: <https://onlinelibrary.wiley.com/doi/pdf/10.1002/mus.20285>]. *Muscle & Nerve*, 31(5), 552–571. <https://doi.org/10.1002/mus.20285>
- Greiner, N., Barra, B., Schiavone, G., James, N., Fallegger, F., Borgognon, S., Lacour, S., Bloch, J., Courtine, G., & Capogrosso, M. (2020, February 18). *Recruitment of upper-limb motoneurons with epidural electrical stimulation of the primate cervical spinal cord* (preprint). Bioengineering. <https://doi.org/10.1101/2020.02.17.952796>
- Grüsser, O.-J. (1994). Early concepts on efference copy and reafference [Publisher: Cambridge University Press]. *Behavioral and Brain Sciences*, 17(2), 262–265. <https://doi.org/10.1017/S0140525X00034415>
- Halter, J. A., & Clark, J. W. (1991). A distributed-parameter model of the myelinated nerve fiber. *Journal of Theoretical Biology*, 148(3), 345–382. [https://doi.org/10.1016/S0022-5193\(05\)80242-5](https://doi.org/10.1016/S0022-5193(05)80242-5)
- Handa, Y., Yagi, R., & Hoshimiya, N. (1998). Application of functional electrical stimulation to the paralyzed extremities. *Neurologia Medico-Chirurgica*, 38(11), 784–788. <https://doi.org/10.2176/nmc.38.784>
- Handa, Y., & Hoshimiya, N. (1987). Functional electrical stimulation for the control of the upper extremities (K. Atsumi, F. Kajiya, T. Tsuji, & K. Tsujioka, Eds.). In K. Atsumi, F. Kajiya, T. Tsuji, & K. Tsujioka (Eds.), *Medical progress through technology: medical engineering in japan research and development*. Dordrecht, Springer Netherlands. https://doi.org/10.1007/978-94-009-3361-3_6
- Hart, R., Kilgore, K., & Peckham, P. (1998). A comparison between control methods for implanted FES hand-grasp systems. *IEEE Transactions on Rehabilitation Engineering*, 6(2), 208–218. <https://doi.org/10.1109/86.681187>
- Hart, R. L., Bhadra, N., Montague, F. W., Kilgore, K. L., & Peckham, P. H. (2011). Design and testing of an advanced implantable neuroprosthesis with myoelectric control. *IEEE*

-
- Transactions on Neural Systems and Rehabilitation Engineering*, 19(1), 45–53. <https://doi.org/10.1109/TNSRE.2010.2079952>
- Hastie, T., Tibshirani, R., & Friedman, J. (2009). Boosting and additive trees (T. Hastie, R. Tibshirani, & J. Friedman, Eds.). In T. Hastie, R. Tibshirani, & J. Friedman (Eds.), *The elements of statistical learning: data mining, inference, and prediction*. New York, NY, Springer. https://doi.org/10.1007/978-0-387-84858-7_10
- Helms Tillery, S., Taylor, D., & Schwartz, A. (2003, September). The general utility of a neuroprosthetic device under direct cortical control [ISSN: 1094-687X], In *Proceedings of the 25th annual international conference of the IEEE engineering in medicine and biology society (IEEE cat. no.03ch37439)*. Proceedings of the 25th Annual International Conference of the IEEE Engineering in Medicine and Biology Society (IEEE Cat. No.03CH37439). ISSN: 1094-687X. <https://doi.org/10.1109/IEMBS.2003.1280137>
- Henneman, E. (1985). The size-principle: a deterministic output emerges from a set of probabilistic connections [Publisher: The Company of Biologists Ltd Section: Journal Articles]. *Journal of Experimental Biology*, 115(1), 105–112. Retrieved September 17, 2020, from <https://jeb.biologists.org/content/115/1/105>
- Herter, T. M., Korbelt, T., & Scott, S. H. (2009). Comparison of neural responses in primary motor cortex to transient and continuous loads during posture. *Journal of Neurophysiology*, 101(1), 150–163. <https://doi.org/10.1152/jn.90230.2008>
- Hesse, S., Schmidt, H., Werner, C., & Bardeleben, A. (2003). Upper and lower extremity robotic devices for rehabilitation and for studying motor control. *Current opinion in neurology*. <https://doi.org/10.1097/00019052-200312000-00010>
- Hobby, J., Taylor, P. N., & Esnouf, J. (2001). Restoration of tetraplegic hand function by use of the neurocontrol freehand system. *Journal of Hand Surgery*, 26(5), 459–464. <https://doi.org/10.1054/jhsb.2001.0587>
- Hochberg, L. R., Bacher, D., Jarosiewicz, B., Masse, N. Y., Simeral, J. D., Vogel, J., Haddadin, S., Liu, J., Cash, S. S., van der Smagt, P., & Donoghue, J. P. (2012). Reach and grasp by people with tetraplegia using a neurally controlled robotic arm. *Nature*, 485(7398), 372–375. <https://doi.org/10.1038/nature11076>
- Hochberg, L. R., Serruya, M. D., Friehs, G. M., Mukand, J. A., Saleh, M., Caplan, A. H., Branner, A., Chen, D., Penn, R. D., & Donoghue, J. P. (2006). Neuronal ensemble control of prosthetic devices by a human with tetraplegia. *Nature*, 442(7099), 164–171. <https://doi.org/10.1038/nature04970>
- Hohenfellner, M., Schultz-Lampel, D., Dahms, S., Matzel, K., & Thuroff, J. W. (1998). Bilateral chronic sacral neuromodulation for treatment for lower urinary tract dysfunction. *The Journal of Urology*, 160(3), 821–824. [https://doi.org/10.1016/S0022-5347\(01\)62795-2](https://doi.org/10.1016/S0022-5347(01)62795-2)
- Hu, K., Jamali, M., Moses, Z. B., Ortega, C. A., Friedman, G. N., Xu, W., & Williams, Z. M. (2018). Decoding unconstrained arm movements in primates using high-density electrocorticography signals for brain-machine interface use. *Scientific Reports*, 8. <https://doi.org/10.1038/s41598-018-28940-7>
- Hugosdottir, R., Jónasson, S. Þ., Sigþórsson, H., & Helgason, Þ. (2014). Feasibility study of a novel electrode concept for a neuroprosthesis for augmentation of impaired finger

-
- functions. *European Journal of Translational Myology*, 24(3). <https://doi.org/10.4081/ejtm.2014.4671>
- In, H., Kang, B. B., Sin, M., & Cho, K. (2015). Exo-glove: a wearable robot for the hand with a soft tendon routing system [Conference Name: IEEE Robotics Automation Magazine]. *IEEE Robotics Automation Magazine*, 22(1), 97–105. <https://doi.org/10.1109/MRA.2014.2362863>
- Irwin, Z., Schroeder, K., Vu, P., Bullard, A., Tat, D., Nu, C., Vaskov, A., Nason, S., Thompson, D., Bentley, J., Patil, P., & Chestek, C. (2017). Neural control of finger movement via intracortical brain-machine interface. *Journal of neural engineering*, 14(6), 066004. <https://doi.org/10.1088/1741-2552/aa80bd>
- Ison, M., & Artemiadis, P. (2014). The role of muscle synergies in myoelectric control: trends and challenges for simultaneous multifunction control. *Journal of Neural Engineering*, 11(5), 051001. <https://doi.org/10.1088/1741-2560/11/5/051001>
- Jackson, A., & Fetz, E. E. (2007). Compact movable microwire array for long-term chronic unit recording in cerebral cortex of primates. *Journal of Neurophysiology*, 98(5), 3109–3118. <https://doi.org/10.1152/jn.00569.2007>
- Jackson, A., & Zimmermann, J. B. (2012). Neural interfaces for the brain and spinal cord—restoring motor function [Number: 12 Publisher: Nature Publishing Group]. *Nature Reviews Neurology*, 8(12), 690–699. <https://doi.org/10.1038/nrneurol.2012.219>
- Jarosiewicz, B., Sarma, A. A., Bacher, D., Masse, N. Y., Simeral, J. D., Sorice, B., Oakley, E. M., Blabe, C., Pandarinath, C., Gilja, V., Cash, S. S., Eskandar, E. N., Friehs, G., Henderson, J. M., Shenoy, K. V., Donoghue, J. P., & Hochberg, L. R. (2015). Virtual typing by people with tetraplegia using a self-calibrating intracortical brain-computer interface. *Science translational medicine*, 7(313), 313ra179. <https://doi.org/10.1126/scitranslmed.aac7328>
- Jarque-Bou, N. J., Scano, A., Atzori, M., & Müller, H. (2019). Kinematic synergies of hand grasps: a comprehensive study on a large publicly available dataset. *Journal of NeuroEngineering and Rehabilitation*, 16(1), 63. <https://doi.org/10.1186/s12984-019-0536-6>
- Johansson, R. S., & Flanagan, J. R. (2009). Coding and use of tactile signals from the fingertips in object manipulation tasks [Number: 5 Publisher: Nature Publishing Group]. *Nature Reviews Neuroscience*, 10(5), 345–359. <https://doi.org/10.1038/nrn2621>
- Johansson, R. S., Häger, C., & Bäckström, L. (1992). Somatosensory control of precision grip during unpredictable pulling loads. *Experimental Brain Research*, 89(1), 204–213. <https://doi.org/10.1007/BF00229017>
- Johnston, J. M., Cohen, Y. E., Shirley, H., Tsunada, J., Bennur, S., Christison-Lagay, K., & Veeder, C. L. (2016). Recent refinements to cranial implants for rhesus macaques (macaca mulatta). *Lab animal*, 45(5), 180–186. <https://doi.org/10.1038/labon.997>
- Kaesler, M., Wannier, T., Brunet, J.-F., Wyss, A., Bloch, J., & Rouiller, E. M. (2013). Representation of motor habit in a sequence of repetitive reach and grasp movements performed by macaque monkeys: evidence for a contribution of the dorsolateral prefrontal cortex. *Cortex*, 49(5), 1404–1419. <https://doi.org/10.1016/j.cortex.2012.05.025>

-
- Kapadia, N., Moineau, B., & Popovic, M. R. (2020). Functional electrical stimulation therapy for retraining reaching and grasping after spinal cord injury and stroke [Publisher: Frontiers]. *Frontiers in Neuroscience*, 14. <https://doi.org/10.3389/fnins.2020.00718>
- Kasten, M. R., Sunshine, M. D., Secrist, E. S., Horner, P. J., & Moritz, C. T. (2013). Therapeutic intraspinal microstimulation improves forelimb function after cervical contusion injury. *Journal of Neural Engineering*, 10(4), 044001. <https://doi.org/10.1088/1741-2560/10/4/044001>
- Keith, M. W., Kilgore, K. L., Peckham, P. H., Wuolle, K. S., Creasey, G., & Lemay, M. (1996). Tendon transfers and functional electrical stimulation for restoration of hand function in spinal cord injury. *The Journal of Hand Surgery*, 21(1), 89–99.
- Kesar, T., Chou, L.-W., & Binder-Macleod, S. A. (2008). Effects of stimulation frequency versus pulse duration modulation on muscle fatigue. *Journal of Electromyography and Kinesiology*, 18(4), 662–671. <https://doi.org/10.1016/j.jelekin.2007.01.001>
- Kilgore, K. L., Hoyen, H. A., Bryden, A. M., Hart, R. L., Keith, M. W., & Peckham, P. H. (2008). An implanted upper-extremity neuroprosthesis using myoelectric control. *The Journal of Hand Surgery*, 33(4), 539–550. <https://doi.org/10.1016/j.jhsa.2008.01.007>
- Kim, S., Callier, T., Tabot, G. A., Gaunt, R. A., Tenore, F. V., & Bensmaia, S. J. (2015). Behavioral assessment of sensitivity to intracortical microstimulation of primate somatosensory cortex. *Proceedings of the National Academy of Sciences of the United States of America*, 112(49), 15202–15207. <https://doi.org/10.1073/pnas.1509265112>
- Koralek, A. C., Jin, X., Long, J. D., Costa, R. M., & Carmena, J. M. (2012). Corticostriatal plasticity is necessary for learning intentional neuroprosthetic skills. *Nature*, 483(7389), 331–335. <https://doi.org/10.1038/nature10845>
- Krakauer, J. W., & Carmichael, S. T. (2017, November 3). *Broken movement: the neurobiology of motor recovery after stroke*. MIT Press.
- Kurillo, G., Gregorič, M., Goljar, N., & Bajd, T. (2005). Grip force tracking system for assessment and rehabilitation of hand function. *Technology and Health Care*, 13(3), 137–149. <https://doi.org/10.3233/THC-2005-13301>
- Kwakkel Gert, Kollen Boudewijn J., van der Grond Jeroen, & Prevo Arie J.H. (2003). Probability of regaining dexterity in the flaccid upper limb [Publisher: American Heart Association]. *Stroke*, 34(9), 2181–2186. <https://doi.org/10.1161/01.STR.0000087172.16305.CD>
- Kwakkel, G., Kollen, B. J., Grond, J. v. d., & Prevo, A. J. H. (2003). Probability of regaining dexterity in the flaccid upper limb [Publisher: Lippincott Williams & Wilkins]. *Stroke*. <https://doi.org/10.1161/01.STR.0000087172.16305.CD>
- Laferriere, S., Bonizzato, M., Dancause, N., & Lajoie, G. (2019). Learning to evoke complex motor outputs with spatiotemporal neurostimulation using a hierarchical and adaptive optimization algorithm. *BioRxiv*, 662072.
- Lalitharatne, T., Teramoto, K., Hayashi, Y., & Kiguchi, K. (2013). Towards hybrid EEG-EMG-based control approaches to be used in bio-robotics applications: current status, challenges and future directions. *Paladyn, Journal of Behavioral Robotics*, 4, 147–154. <https://doi.org/10.2478/pjbr-2013-0009>

-
- Langhorne, P., Coupar, F., & Pollock, A. (2009). Motor recovery after stroke: a systematic review. *The Lancet Neurology*, 8(8), 741–754. [https://doi.org/10.1016/S1474-4422\(09\)70150-4](https://doi.org/10.1016/S1474-4422(09)70150-4)
- Lauer, Peckham, & Kilgore. (1999). EEG-based control of a hand grasp neuroprosthesis. *Neuroreport*.
- Lawlor, P. N., Perich, M. G., Miller, L. E., & Kording, K. P. (2018). Linear-nonlinear-time-warp-poisson models of neural activity. *Journal of Computational Neuroscience*, 45(3), 173–191. <https://doi.org/10.1007/s10827-018-0696-6>
- Lebedev, M. A., Carmena, J. M., O'Doherty, J. E., Zacksenhouse, M., Henriquez, C. S., Principe, J. C., & Nicolelis, M. A. L. (2005). Cortical ensemble adaptation to represent velocity of an artificial actuator controlled by a brain-machine interface [Publisher: Society for Neuroscience Section: Behavioral/Systems/Cognitive]. *Journal of Neuroscience*, 25(19), 4681–4693. <https://doi.org/10.1523/JNEUROSCI.4088-04.2005>
- Lebedev, M. A., & Nicolelis, M. A. L. (2006). Brain-machine interfaces: past, present and future. *Trends in Neurosciences*, 29(9), 536–546. <https://doi.org/10.1016/j.tins.2006.07.004>
- Ledbetter, N. M., Ethier, C., Oby, E. R., Hiatt, S. D., Wilder, A. M., Ko, J. H., Agnew, S. P., Miller, L. E., & Clark, G. A. (2013). Intrafascicular stimulation of monkey arm nerves evokes coordinated grasp and sensory responses. *Journal of Neurophysiology*, 109(2), 580–590. <https://doi.org/10.1152/jn.00688.2011>
- Levy, W., Amassian, V., Traad, M., & Cadwell, J. (1990). Focal magnetic coil stimulation reveals motor cortical system reorganized in humans after traumatic quadriplegia. *Brain Research*. [https://doi.org/10.1016/0006-8993\(90\)90738-W](https://doi.org/10.1016/0006-8993(90)90738-W)
- Liu, P., Peng, J., Han, G.-H., Ding, X., Wei, S., Gao, G., Huang, K., Chang, F., & Wang, Y. (2019). Role of macrophages in peripheral nerve injury and repair [Publisher: Wolters Kluwer – Medknow Publications]. *Neural Regeneration Research*, 14(8), 1335. <https://doi.org/10.4103/1673-5374.253510>
- Loeb, G. E., & Peck, R. A. (1996). Cuff electrodes for chronic stimulation and recording of peripheral nerve activity. *Journal of Neuroscience Methods*, 64(1), 95–103. [https://doi.org/10.1016/0165-0270\(95\)00123-9](https://doi.org/10.1016/0165-0270(95)00123-9)
- London, B. M., & Miller, L. E. (2013). Responses of somatosensory area 2 neurons to actively and passively generated limb movements. *Journal of Neurophysiology*, 109(6), 1505–1513. <https://doi.org/10.1152/jn.00372.2012>
- Long, C. (1963). An electrophysiologic splint for the hand. *Archives of Physical Medicine and Rehabilitation*, 44, 499–503.
- Lu, D. C., Edgerton, V. R., Modaber, M., AuYong, N., Morikawa, E., Zdunowski, S., Sarino, M. E., Sarrafzadeh, M., Nuwer, M. R., Roy, R. R., & Gerasimenko, Y. (2016). Engaging cervical spinal cord networks to reen able volitional control of hand function in tetraplegic patients. *Neurorehabilitation and Neural Repair*, 30(10), 951–962. <https://doi.org/10.1177/1545968316644344>
- Mangold, S., Keller, T., Curt, A., & Dietz, V. (2005). Transcutaneous functional electrical stimulation for grasping in subjects with cervical spinal cord injury [Number: 1 Publisher: Nature Publishing Group]. *Spinal Cord*, 43(1), 1–13. <https://doi.org/10.1038/sj.sc.3101644>

-
- Marin, K. A., Silva, F. O. C. e., Carvalho, A. A. V. d., do Nascimento, G. N. L., do Prado, Y. C. L., & Aversi-Ferreira, T. A. (2009). Anatomy of the nervous of forearm and hand of cebus libidinosus (rylands, 2000). *International Journal of Morphology*, 27(3). <https://doi.org/10.4067/S0717-95022009000300003>
- Markram, H., Muller, E., Ramaswamy, S., Reimann, M. W., Abdellah, M., Sanchez, C. A., Ailamaki, A., Alonso-Nanclares, L., Antille, N., Arsever, S., Kahou, G. A. A., Berger, T. K., Bilgili, A., Buncic, N., Chalimourda, A., Chindemi, G., Courcol, J.-D., Delalandre, F., Delattre, V., ... Schürmann, F. (2015). Reconstruction and simulation of neocortical microcircuitry. *Cell*, 163(2), 456–492. <https://doi.org/10.1016/j.cell.2015.09.029>
- Mason, C. R., Gomez, J. E., & Ebner, T. J. (2001). Hand synergies during reach-to-grasp. *Journal of Neurophysiology*, 86(6), 2896–2910. <https://doi.org/10.1152/jn.2001.86.6.2896>
- Mathis, A., Mamidanna, P., Cury, K. M., Abe, T., Murthy, V. N., Mathis, M. W., & Bethge, M. (2018). DeepLabCut: markerless pose estimation of user-defined body parts with deep learning [Number: 9 Publisher: Nature Publishing Group]. *Nature Neuroscience*, 21(9), 1281–1289. <https://doi.org/10.1038/s41593-018-0209-y>
- McDonald, J. W., & Sadowsky, C. (2002). Spinal-cord injury. *The Lancet*, 359(9304), 417–425. [https://doi.org/10.1016/S0140-6736\(02\)07603-1](https://doi.org/10.1016/S0140-6736(02)07603-1)
- Mcintyre, C. C., & Foutz, T. J. (2013). Computational modeling of deep brain stimulation [Publisher: NIH Public Access]. *Handbook of clinical neurology*, 116, 55. <https://doi.org/10.1016/B978-0-444-53497-2.00005-X>
- McIntyre, C. C., & Grill, W. M. (2000). Selective microstimulation of central nervous system neurons. *Annals of Biomedical Engineering*, 28(3), 219–233. <https://doi.org/10.1114/1.262>
- McIntyre, C. C., & Grill, W. M. (2002). Extracellular stimulation of central neurons: influence of stimulus waveform and frequency on neuronal output. *Journal of neurophysiology*, 88(4), 1592–1604.
- McIntyre, C. C., Richardson, A. G., & Grill, W. M. (2002). Modeling the excitability of mammalian nerve fibers: influence of afterpotentials on the recovery cycle. *Journal of Neurophysiology*, 87(2), 995–1006. <https://doi.org/10.1152/jn.00353.2001>
- McNeal. (1976). Analysis of a model for excitation of myelinated nerve. *IEEE Transactions on Biomedical Engineering*.
- Memberg, W. D., Polasek, K. H., Hart, R. L., Bryden, A. M., Kilgore, K. L., Nemunaitis, G. A., Hoen, H. A., Keith, M. W., & Kirsch, R. F. (2014). Implanted neuroprosthesis for restoring arm and hand function in people with high level tetraplegia. *Archives of Physical Medicine and Rehabilitation*, 95(6), 1201–1211.e1. <https://doi.org/10.1016/j.apmr.2014.01.028>
- Mezzarane, R., Elias, L., Magalhães, F., Martins, V., & Kohn, A. (2013, May 22). Experimental and simulated EMG responses in the study of the human spinal cord [Journal Abbreviation: Electrodiagnosis in New Frontiers of Clinical Research], In *Electrodiagnosis in new frontiers of clinical research*. Journal Abbreviation: Electrodiagnosis in New Frontiers of Clinical Research. <https://doi.org/10.5772/54870>

-
- Micera, S., Carpaneto, J., & Raspopovic, S. (2010). Control of hand prostheses using peripheral information. *IEEE Reviews in Biomedical Engineering*, 3, 48–68. <https://doi.org/10.1109/RBME.2010.2085429>
- Micera, S., Navarro, X., Carpaneto, J., Citi, L., Tonet, O., Rossini, P. M., Carrozza, M. C., Hoffmann, K. P., Vivo, M., Yoshida, K., & Dario, P. (2008). On the use of longitudinal intrafascicular peripheral interfaces for the control of cybernetic hand prostheses in amputees [Conference Name: IEEE Transactions on Neural Systems and Rehabilitation Engineering]. *IEEE Transactions on Neural Systems and Rehabilitation Engineering*, 16(5), 453–472. <https://doi.org/10.1109/TNSRE.2008.2006207>
- Milekovic, T., Ball, T., Schulze-Bonhage, A., Aertsen, A., & Mehring, C. (2013). Detection of error related neuronal responses recorded by electrocorticography in humans during continuous movements [Publisher: Public Library of Science]. *PLOS ONE*, 8(2), e55235. <https://doi.org/10.1371/journal.pone.0055235>
- Milekovic, T., Sarma, A., Bacher, D., Donoghue, J., & Hochberg, L. (2013). Stable asynchronous BCIs based on field potentials for communication. *Paper presented at: BCCN ConferencePLOS ONE*.
- Milekovic, T., Sarma, A. A., Bacher, D., Simeral, J. D., Saab, J., Pandarinath, C., Sorice, B. L., Blabe, C., Oakley, E. M., Tringale, K. R., Eskandar, E., Cash, S. S., Henderson, J. M., Shenoy, K. V., Donoghue, J. P., & Hochberg, L. R. (2018). Stable long-term BCI-enabled communication in ALS and locked-in syndrome using LFP signals [Publisher: American Physiological Society]. *Journal of Neurophysiology*, 120(1), 343–360. <https://doi.org/10.1152/jn.00493.2017>
- Milekovic, T., Truccolo, W., Grün, S., Riehle, A., & Brochier, T. (2015). Local field potentials in primate motor cortex encode grasp kinetic parameters. *NeuroImage*, 114, 338–355. <https://doi.org/10.1016/j.neuroimage.2015.04.008>
- Mizrahi, J. (1997). Fatigue in muscles activated by functional electrical stimulation [Publisher: Begel House Inc.]. *Critical Reviews™ in Physical and Rehabilitation Medicine*, 9(2). <https://doi.org/10.1615/CritRevPhysRehabilMed.v9.i2.10>
- Moore, D. S., McCabe, G. P., & Craig, B. A. (2014, February 7). *Introduction to the practice of statistics* [Google-Books-ID: pX1_AwAAQBAJ]. W. H. Freeman.
- Moore, J. W., Joyner, R. W., Brill, M. H., Waxman, S. D., & Najar-Joa, M. (1978). Simulations of conduction in uniform myelinated fibers. relative sensitivity to changes in nodal and internodal parameters. *Biophysical Journal*, 21(2), 147–160. Retrieved September 17, 2020, from <https://www.ncbi.nlm.nih.gov/pmc/articles/PMC1473353/>
- Moraud, E. M., Capogrosso, M., Formento, E., Wenger, N., DiGiovanna, J., Courtine, G., & Micera, S. (2016). Mechanisms underlying the neuromodulation of spinal circuits for correcting gait and balance deficits after spinal cord injury. *Neuron*, 89(4), 814–828. <https://doi.org/10.1016/j.neuron.2016.01.009>
- Moritz, C. T., Lucas, T. H., Perlmutter, S. I., & Fetz, E. E. (2007). Forelimb movements and muscle responses evoked by microstimulation of cervical spinal cord in sedated monkeys. *Journal of Neurophysiology*, 97(1), 110–120. <https://doi.org/10.1152/jn.00414.2006>

-
- Moritz, C. T., Perlmutter, S. I., & Fetz, E. E. (2008). Direct control of paralysed muscles by cortical neurons. *Nature*, 456(7222), 639–642. <https://doi.org/10.1038/nature07418>
- Mueller-Putz, G. R., Scherer, R., Pfurtscheller, G., & Rupp, R. (2005). EEG-based neuroprosthesis control: a step towards clinical practice. *Neuroscience Letters*, 382(1), 169–174. <https://doi.org/10.1016/j.neulet.2005.03.021>
- Mulcahey, M. J., Betz, R. R., Smith, B. T., Weiss, A. A., & Davis, S. E. (1997). Implanted functional electrical stimulation hand system in adolescents with spinal injuries: an evaluation. *Archives of Physical Medicine and Rehabilitation*, 78(6), 597–607. [https://doi.org/10.1016/S0003-9993\(97\)90425-1](https://doi.org/10.1016/S0003-9993(97)90425-1)
- Nath, T., Mathis, A., Chen, A. C., Patel, A., Bethge, M., & Mathis, M. W. (2019). Using DeepLabCut for 3d markerless pose estimation across species and behaviors [Number: 7 Publisher: Nature Publishing Group]. *Nature Protocols*, 14(7), 2152–2176. <https://doi.org/10.1038/s41596-019-0176-0>
- National Spinal Cord Injury Statistical Center. (2020). Facts and figures at a glance. Retrieved September 15, 2020, from uab.edu/NSCISC
- Nishimura, Y., Perlmutter, S. I., & Fetz, E. E. (2013). Restoration of upper limb movement via artificial corticospinal and musculoskeletal connections in a monkey with spinal cord injury. *Frontiers in Neural Circuits*, 7. <https://doi.org/10.3389/fncir.2013.00057>
- Noback, C. R., Ruggiero, D. A., Demarest, R. J., & Strominger, N. L. (2005). *The human nervous system: structure and function* [Google-Books-ID: UnRO3A_cS44C]. Springer Science & Business Media.
- Nudo, R. J., Milliken, G. W., Jenkins, W. M., & Merzenich, M. M. (1996). Use-dependent alterations of movement representations in primary motor cortex of adult squirrel monkeys [Publisher: Society for Neuroscience Section: Articles]. *Journal of Neuroscience*, 16(2), 785–807. <https://doi.org/10.1523/JNEUROSCI.16-02-00785.1996>
- Nuyujukian, P., Kao, J. C., Fan, J. M., Stavisky, S. D., Ryu, S. I., & Shenoy, K. V. (2014). Performance sustaining intracortical neural prostheses. *Journal of Neural Engineering*, 11(6), 066003. <https://doi.org/10.1088/1741-2560/11/6/066003>
- Nuyujukian, P., Sanabria, J. A., Saab, J., Pandarinath, C., Jarosiewicz, B., Blabe, C. H., Franco, B., Mernoff, S. T., Eskandar, E. N., Simeral, J. D., Hochberg, L. R., Shenoy, K. V., & Henderson, J. M. (2018). Cortical control of a tablet computer by people with paralysis [Publisher: Public Library of Science]. *PLOS ONE*, 13(11), e0204566. <https://doi.org/10.1371/journal.pone.0204566>
- Oddo, C. M., Raspopovic, S., Artoni, F., Mazzoni, A., Spigler, G., Petrini, F., Giambattistelli, F., Vecchio, F., Miraglia, F., & Zollo, L. (2016). Intraneural stimulation elicits discrimination of textural features by artificial fingertip in intact and amputee humans. *Elife*, 5, e09148.
- O'Doherty, J. E., Lebedev, M. A., Ifft, P. J., Zhuang, K. Z., Shokur, S., Bleuler, H., & Nicolelis, M. A. L. (2011). Active tactile exploration using a brain-machine-brain interface [Number: 7372 Publisher: Nature Publishing Group]. *Nature*, 479(7372), 228–231. <https://doi.org/10.1038/nature10489>

-
- Okorokova, E. V., Goodman, J. M., Hatsopoulos, N. G., & Bensmaia, S. J. (2020). Decoding hand kinematics from population responses in sensorimotor cortex during grasping [Publisher: IOP Publishing]. *Journal of Neural Engineering*, 17(4), 046035. <https://doi.org/10.1088/1741-2552/ab95ea>
- Okun, M., Steinmetz, N., Cossell, L., Iacaruso, M. F., Ko, H., Barthó, P., Moore, T., Hofer, S. B., Mrcic-Flogel, T. D., Carandini, M., & Harris, K. D. (2015). Diverse coupling of neurons to populations in sensory cortex. *Nature*, 521(7553), 511–515. <https://doi.org/10.1038/nature14273>
- Omrani, M., Murnaghan, C. D., Pruszynski, J. A., & Scott, S. H. (2016). Distributed task-specific processing of somatosensory feedback for voluntary motor control (R. M. Costa, Ed.). *eLife*, 5, e13141. <https://doi.org/10.7554/eLife.13141>
- O'Neill, C. T., Phipps, N. S., Cappello, L., Paganoni, S., & Walsh, C. J. (2017, July). A soft wearable robot for the shoulder: design, characterization, and preliminary testing [ISSN: 1945-7901], In *2017 international conference on rehabilitation robotics (ICORR)*. 2017 International Conference on Rehabilitation Robotics (ICORR). ISSN: 1945-7901. <https://doi.org/10.1109/ICORR.2017.8009488>
- Overduin, S. A., d'Avella, A., Roh, J., Carmena, J. M., & Bizzi, E. (2015). Representation of muscle synergies in the primate brain [Publisher: Society for Neuroscience Section: Articles]. *Journal of Neuroscience*, 35(37), 12615–12624. <https://doi.org/10.1523/JNEUROSCI.4302-14.2015>
- Peckham, P. H., Keith, M. W., Kilgore, K. L., Grill, J. H., Wuolle, K. S., Thrope, G. B., Gorman, P., Hobby, J., Mulcahey, M. J., Carroll, S., Hentz, V. R., & Wiegner, A. (2001). Efficacy of an implanted neuroprosthesis for restoring hand grasp in tetraplegia: a multicenter study. *Archives of Physical Medicine and Rehabilitation*, 82(10), 1380–1388. <https://doi.org/10.1053/apmr.2001.25910>
- Peckham, P. H., & Knutson, J. S. (2005). Functional electrical stimulation for neuromuscular applications. *Annual Review of Biomedical Engineering*, 7(1), 327–360. <https://doi.org/10.1146/annurev.bioeng.6.040803.140103>
- Peckham, P. H., Marsolais, E. B., & Mortimer, J. T. (1980). Restoration of key grip and release in the c6 tetraplegic patient through functional electrical stimulation. *The Journal of Hand Surgery*, 5(5), 462–469. [https://doi.org/10.1016/S0363-5023\(80\)80076-1](https://doi.org/10.1016/S0363-5023(80)80076-1)
- Peckham, P., Kilgore, K. L., Keith, M. W., Bryden, A. M., Bhadra, N., & Montague, F. W. (2002). An advanced neuroprosthesis for restoration of hand and upper arm control using an implantable controller. *The Journal of Hand Surgery*, 27(2), 265–276. <https://doi.org/10.1053/jhsu.2002.30919>
- Perge, J. A., Homer, M. L., Malik, W. Q., Cash, S., Eskandar, E., Friebs, G., Donoghue, J. P., & Hochberg, L. R. (2013). Intra-day signal instabilities affect decoding performance in an intracortical neural interface system. *Journal of Neural Engineering*, 10(3), 036004. <https://doi.org/10.1088/1741-2560/10/3/036004>
- Perich, M. G., Conti, S., Badi, M., Bogaard, A., Barra, B., Wurth, S., Bloch, J., Courtine, G., Micera, S., Capogrosso, M., & Milekovic, T. (2020). Motor cortical dynamics are shaped by multiple distinct subspaces during naturalistic behavior [Publisher: Cold Spring

-
- Harbor Laboratory Section: New Results]. *bioRxiv*, 2020.07.30.228767. <https://doi.org/10.1101/2020.07.30.228767>
- Perich, M. G., Gallego, J. A., & Miller, L. E. (2018). A neural population mechanism for rapid learning. *Neuron*, 100(4), 964–976.e7. <https://doi.org/10.1016/j.neuron.2018.09.030>
- Petrini, F. M., Valle, G., Strauss, I., Granata, G., Iorio, R. D., D’Anna, E., Čvančara, P., Mueller, M., Carpaneto, J., Clemente, F., Controzzi, M., Bioni, L., Carboni, C., Barbaro, M., Iodice, F., Andreu, D., Hiairassary, A., Divoux, J.-L., Cipriani, C., ... Micera, S. (2019). Six-month assessment of a hand prosthesis with intraneural tactile feedback [eprint: <https://onlinelibrary.wiley.com/doi/pdf/10.1002/ana.25384>]. *Annals of Neurology*, 85(1), 137–154. <https://doi.org/10.1002/ana.25384>
- Petrini, F. M., Bumbasirevic, M., Valle, G., Ilic, V., Mijović, P., Čvančara, P., Barberi, F., Katic, N., Bortolotti, D., Andreu, D., Lechler, K., Lesic, A., Mazic, S., Mijović, B., Guiraud, D., Stieglitz, T., Alexandersson, A., Micera, S., & Raspopovic, S. (2019). Sensory feedback restoration in leg amputees improves walking speed, metabolic cost and phantom pain [Number: 9 Publisher: Nature Publishing Group]. *Nature Medicine*, 25(9), 1356–1363. <https://doi.org/10.1038/s41591-019-0567-3>
- Petrini, F. M., Valle, G., Bumbasirevic, M., Barberi, F., Bortolotti, D., Cvancara, P., Hiairassary, A., Mijovic, P., Sverrisson, A. Ö., Pedrocchi, A., Divoux, J.-L., Popovic, I., Lechler, K., Mijovic, B., Guiraud, D., Stieglitz, T., Alexandersson, A., Micera, S., Lesic, A., & Raspopovic, S. (2019). Enhancing functional abilities and cognitive integration of the lower limb prosthesis [Publisher: American Association for the Advancement of Science Section: Research Article]. *Science Translational Medicine*, 11(512). <https://doi.org/10.1126/scitranslmed.aav8939>
- Pfurtscheller, G., Müller, G. R., Pfurtscheller, J., Gerner, H. J., & Rupp, R. (2003). ‘thought’ – control of functional electrical stimulation to restore hand grasp in a patient with tetraplegia. *Neuroscience Letters*, 351(1), 33–36. [https://doi.org/10.1016/S0304-3940\(03\)00947-9](https://doi.org/10.1016/S0304-3940(03)00947-9)
- Pillow, J. W., Shlens, J., Paninski, L., Sher, A., Litke, A. M., Chichilnisky, E. J., & Simoncelli, E. P. (2008). Spatio-temporal correlations and visual signalling in a complete neuronal population. *Nature*, 454(7207), 995–999. <https://doi.org/10.1038/nature07140>
- Pirondini, E., Coscia, M., Marcheschi, S., Roas, G., Salsedo, F., Frisoli, A., Bergamasco, M., & Micera, S. (2016). Evaluation of the effects of the arm light exoskeleton on movement execution and muscle activities: a pilot study on healthy subjects. *Journal of NeuroEngineering and Rehabilitation*, 13. <https://doi.org/10.1186/s12984-016-0117-x>
- Pohlmeyer, E. A., Jordon, L. R., Kim, P., & Miller, L. E. (2009). A fully implanted drug delivery system for peripheral nerve blocks in behaving animals. *Journal of Neuroscience Methods*, 182(2), 165–171. <https://doi.org/10.1016/j.jneumeth.2009.06.006>
- Pons, T. P., Garraghty, P. E., Cusick, C. G., & Kaas, J. H. (1985). The somatotopic organization of area 2 in macaque monkeys. *Journal of Comparative Neurology*, 241(4), 445–466. <https://doi.org/10.1002/cne.902410405>

-
- Popović, D., Stojanović, A., Pjanović, A., Radosavljević, S., Popović, M., Jović, S., & Vulović, D. (1999). Clinical evaluation of the bionic glove. *Archives of Physical Medicine and Rehabilitation*, 80(3), 299–304. [https://doi.org/10.1016/S0003-9993\(99\)90141-7](https://doi.org/10.1016/S0003-9993(99)90141-7)
- Popovic, M. R., Thrasher, T. A., Adams, M. E., Takes, V., Zivanovic, V., & Tonack, M. I. (2006). Functional electrical therapy: retraining grasping in spinal cord injury [Number: 3 Publisher: Nature Publishing Group]. *Spinal Cord*, 44(3), 143–151. <https://doi.org/10.1038/sj.sc.3101822>
- Popovic, M., Keller, T., Papas, I., Dietz, V., & Morari, M. (2001). Surface-stimulation technology for grasping and walking neuroprostheses. *IEEE Engineering in Medicine and Biology Magazine*, 20(1), 82–93. <https://doi.org/10.1109/51.897831>
- Prochazka, A., Gauthier, M., Wieler, M., & Kenwell, Z. (1997). The bionic glove: an electrical stimulator garment that provides controlled grasp and hand opening in quadriplegia. *Archives of physical medicine and rehabilitation*, 78(6), 608–614.
- Prud'homme, M. J., & Kalaska, J. F. (1994). Proprioceptive activity in primate primary somatosensory cortex during active arm reaching movements [Publisher: American Physiological Society]. *Journal of Neurophysiology*, 72(5), 2280–2301. <https://doi.org/10.1152/jn.1994.72.5.2280>
- Radhakrishnan, S. M., Baker, S. N., & Jackson, A. (2008). Learning a novel myoelectric-controlled interface task. *Journal of Neurophysiology*, 100(4), 2397–2408. <https://doi.org/10.1152/jn.90614.2008>
- Raghavan, P., Krakauer, J. W., & Gordon, A. M. (2006). Impaired anticipatory control of fingertip forces in patients with a pure motor or sensorimotor lacunar syndrome [Publisher: Oxford Academic]. *Brain*, 129(6), 1415–1425. <https://doi.org/10.1093/brain/awl070>
- Ramos-Murguialday, A., Broetz, D., Rea, M., Lärer, L., Yilmaz, Ö., Brasil, F. L., Liberati, G., Curado, M. R., Garcia-Cossio, E., Vyziotis, A., Cho, W., Agostini, M., Soares, E., Soekadar, S., Caria, A., Cohen, L. G., & Birbaumer, N. (2013). Brain-machine-interface in chronic stroke rehabilitation: a controlled study. *Annals of neurology*, 74(1), 100–108. <https://doi.org/10.1002/ana.23879>
- Ranck, J. B., & BeMent, S. L. (1965). The specific impedance of the dorsal columns of cat: an anisotropic medium. *Experimental Neurology*, 11(4), 451–463. [https://doi.org/10.1016/0014-4886\(65\)90059-2](https://doi.org/10.1016/0014-4886(65)90059-2)
- Raspopovic, S., Capogrosso, M., Badia, J., Navarro, X., & Micera, S. (2012). Experimental validation of a hybrid computational model for selective stimulation using transverse intrafascicular multichannel electrodes. *IEEE Transactions on Neural Systems and Rehabilitation Engineering*, 20(3), 395–404. <https://doi.org/10.1109/TNSRE.2012.2189021>
- Raspopovic, S., Capogrosso, M., & Micera, S. (2011). A computational model for the stimulation of rat sciatic nerve using a transverse intrafascicular multichannel electrode. *IEEE Transactions on Neural Systems and Rehabilitation Engineering*, 19(4), 333–344. <https://doi.org/10.1109/TNSRE.2011.2151878>
- Raspopovic, S., Capogrosso, M., Petrini, F. M., Bonizzato, M., Rigosa, J., Di Pino, G., Carpaneto, J., Controzzi, M., Boretius, T., Fernandez, E., Granata, G., Oddo, C. M., Citi, L., Ciano, A. L., Cipriani, C., Carrozza, M. C., Jensen, W., Guglielmelli, E., Stieglitz, T., ... Micera, S.

-
- (2014). Restoring natural sensory feedback in real-time bidirectional hand prostheses. *Science Translational Medicine*, 6(222), 222ra19–222ra19. <https://doi.org/10.1126/scitranslmed.3006820>
- Raspopovic, S., Petrini, F. M., Zelechowski, M., & Valle, G. (2017). Framework for the development of neuroprostheses: from basic understanding by sciatic and median nerves models to bionic legs and hands. *Proceedings of the IEEE*, 105(1), 34–49. <https://doi.org/10.1109/JPROC.2016.2600560>
- Rattay, F. (1989). Analysis of models for extracellular fiber stimulation [Conference Name: IEEE Transactions on Biomedical Engineering]. *IEEE Transactions on Biomedical Engineering*, 36(7), 676–682. <https://doi.org/10.1109/10.32099>
- Rattay, F. (1986). Analysis of models for external stimulation of axons. *IEEE transactions on biomedical engineering*, (10), 974–977.
- Rea, P. (2016, January 1). Chapter 3 - neck (P. Rea, Ed.). In P. Rea (Ed.), *Essential clinically applied anatomy of the peripheral nervous system in the head and neck*. Academic Press. <https://doi.org/10.1016/B978-0-12-803633-4.00003-X>
- Richardson, A. G., McIntyre, C. C., & Grill, W. M. (2000). Modelling the effects of electric fields on nerve fibres: influence of the myelin sheath. *Medical and Biological Engineering and Computing*, 38(4), 438–446.
- Richardson, A. G., Attiah, M. A., Berman, J. I., Chen, H. I., Liu, X., Zhang, M., Van der Spiegel, J., & Lucas, T. H. (2016). The effects of acute cortical somatosensory deafferentation on grip force control. *Cortex*, 74, 1–8. <https://doi.org/10.1016/j.cortex.2015.10.007>
- Rijkhoff, N., Koldewijn, E., van Kerrebroeck, P., Debruyne, F., & Wijkstra, H. (1993, October). Sacral root stimulation in the dog: reduction of urethral resistance, In *Proceedings of the 15th annual international conference of the IEEE engineering in medicine and biology societ*. Proceedings of the 15th Annual International Conference of the IEEE Engineering in Medicine and Biology Societ. <https://doi.org/10.1109/IEMBS.1993.979123>
- Rodríguez, F. J., Ceballos, D., Schüttler, M., Valero, A., Valderrama, E., Stieglitz, T., & Navarro, X. (2000). Polyimide cuff electrodes for peripheral nerve stimulation. *Journal of Neuroscience Methods*, 98(2), 105–118. [https://doi.org/10.1016/S0165-0270\(00\)00192-8](https://doi.org/10.1016/S0165-0270(00)00192-8)
- Romeni, S., Valle, G., Mazzoni, A., & Micera, S. (2020). Tutorial: a computational framework for the design and optimization of peripheral neural interfaces. *Nature Protocols*, 15(10), 3129–3153. <https://doi.org/10.1038/s41596-020-0377-6>
- Romo, R., Hernández, A., Zainos, A., & Salinas, E. (1998). Somatosensory discrimination based on cortical microstimulation [Number: 6674 Publisher: Nature Publishing Group]. *Nature*, 392(6674), 387–390. <https://doi.org/10.1038/32891>
- Rothwell, J. C., Traub, M. M., Day, B. L., Obeso, J. A., Thomas, P. K., & Marsden, C. D. (1982). Manual motor performance in a deafferented man [Publisher: Oxford Academic]. *Brain*, 105(3), 515–542. <https://doi.org/10.1093/brain/105.3.515>
- Rubinstein, J. T. (1991). Analytical theory for extracellular electrical stimulation of nerve with focal electrodes. II. passive myelinated axon. *Biophysical Journal*, 60(3), 538–555.

-
- Retrieved September 17, 2020, from <https://www.ncbi.nlm.nih.gov/pmc/articles/PMC1260098/>
- Ruhunage, I., Mallikarachchi, S., Chinthaka, D., Sandaruwan, J., & Lalitharatne, T. (2019, March 1). Hybrid EEG-EMG signals based approach for control of hand motions of a transhumeral prosthesis. <https://doi.org/10.1109/LifeTech.2019.8883865>
- Saal, H. P., & Bensmaia, S. J. (2015). Biomimetic approaches to bionic touch through a peripheral nerve interface. *Neuropsychologia*, 79, 344–353. <https://doi.org/10.1016/j.neuropsychologia.2015.06.010>
- Saal, H. P., Delhay, B. P., Rayhaun, B. C., & Bensmaia, S. J. (2017). Simulating tactile signals from the whole hand with millisecond precision. *Proceedings of the National Academy of Sciences of the United States of America*, 114(28), E5693–E5702. <https://doi.org/10.1073/pnas.1704856114>
- Sadtler, P. T., Ryu, S. I., Tyler-Kabara, E. C., Yu, B. M., & Batista, A. P. (2015). Brain–computer interface control along instructed paths [Publisher: IOP Publishing]. *Journal of Neural Engineering*, 12(1), 016015. <https://doi.org/10.1088/1741-2560/12/1/016015>
- Sadtler, P. T., Quick, K. M., Golub, M. D., Chase, S. M., Ryu, S. I., Tyler-Kabara, E. C., Yu, B. M., & Batista, A. P. (2014). Neural constraints on learning [Number: 7515 Publisher: Nature Publishing Group]. *Nature*, 512(7515), 423–426. <https://doi.org/10.1038/nature13665>
- Salas, M. A., Bashford, L., Kellis, S., Jafari, M., Jo, H., Kramer, D., Shanfield, K., Pejisa, K., Lee, B., & Liu, C. Y. (2018). Proprioceptive and cutaneous sensations in humans elicited by intracortical microstimulation. *eLife*, 7, e32904.
- Santello, M., Flanders, M., & Soechting, J. F. (1998). Postural hand synergies for tool use. *The Journal of Neuroscience*, 18(23), 10105–10115. <https://doi.org/10.1523/JNEUROSCI.18-23-10105.1998>
- Saxena, S. (1995). An EMG-controlled grasping system for tetraplegics, 8.
- Schaffelhofer, S., & Scherberger, H. (2016). Object vision to hand action in macaque parietal, premotor, and motor cortices (S. Kastner, Ed.) [Publisher: eLife Sciences Publications, Ltd]. *eLife*, 5, e15278. <https://doi.org/10.7554/eLife.15278>
- Schiefer, M., Triolo, R., & Tyler, D. (2008). A model of selective activation of the femoral nerve with a flat interface nerve electrode for a lower extremity neuroprosthesis. *IEEE Transactions on Neural Systems and Rehabilitation Engineering*, 16(2), 195–204. <https://doi.org/10.1109/TNSRE.2008.918425>
- Schwartz, A. B. (2004). CORTICAL NEURAL PROSTHETICS. *Annual Review of Neuroscience*, 27(1), 487–507. <https://doi.org/10.1146/annurev.neuro.27.070203.144233>
- Schwartz, A. B., Kettner, R. E., & Georgopoulos, A. P. (1988). Primate motor cortex and free arm movements to visual targets in three-dimensional space. i. relations between single cell discharge and direction of movement. *Journal of Neuroscience*, 8(8), 2913–2927.
- Scott, S. H. (1999). Apparatus for measuring and perturbing shoulder and elbow joint positions and torques during reaching. *Journal of Neuroscience Methods*, 89(2), 119–127. [https://doi.org/10.1016/s0165-0270\(99\)00053-9](https://doi.org/10.1016/s0165-0270(99)00053-9)

-
- Seáñez-González, I., Pierella, C., Farshchiansadegh, A., Thorp, E. B., Wang, X., Parrish, T., & Mussa-Ivaldi, F. A. (2016). Body-machine interfaces after spinal cord injury: rehabilitation and brain plasticity. *Brain Sciences*, 6(4). <https://doi.org/10.3390/brainsci6040061>
- Seki, K., Perlmuter, S. I., & Fetz, E. E. (2003). Sensory input to primate spinal cord is presynaptically inhibited during voluntary movement. *Nature Neuroscience*, 6(12), 1309–1316. <https://doi.org/10.1038/nn1154>
- Serruya, M. D., Hatsopoulos, N. G., Paninski, L., Fellows, M. R., & Donoghue, J. P. (2002). Brain-machine interface: instant neural control of a movement signal. *Nature*, 416(6877), 141–142.
- Shadmehr, R., & Mussa-Ivaldi, F. A. (1994). Adaptive representation of dynamics during learning of a motor task [Publisher: Society for Neuroscience Section: Articles]. *Journal of Neuroscience*, 14(5), 3208–3224. <https://doi.org/10.1523/JNEUROSCI.14-05-03208.1994>
- Shenoy, K. V., & Carmena, J. M. (2014). Combining decoder design and neural adaptation in brain-machine interfaces [Publisher: Elsevier]. *Neuron*, 84(4), 665–680. <https://doi.org/10.1016/j.neuron.2014.08.038>
- Shenoy, K. V., Sahani, M., & Churchland, M. M. (2013). Cortical control of arm movements: a dynamical systems perspective [Publisher: Annual Reviews]. *Annual Review of Neuroscience*, 36(1), 337–359. <https://doi.org/10.1146/annurev-neuro-062111-150509>
- Shin, H., Zheng, Y., & Hu, X. (2018). Variation of finger activation patterns post-stroke through non-invasive nerve stimulation [Publisher: Frontiers]. *Frontiers in Neurology*, 9. <https://doi.org/10.3389/fneur.2018.01101>
- Shoaran, M., Kamal, M. H., Pollo, C., Vanderghelynst, P., & Schmid, A. (2014). Compact low-power cortical recording architecture for compressive multichannel data acquisition [Conference Name: IEEE Transactions on Biomedical Circuits and Systems]. *IEEE Transactions on Biomedical Circuits and Systems*, 8(6), 857–870. <https://doi.org/10.1109/TBCAS.2014.2304582>
- Shokur, S., Donati, A. R. C., Campos, D. S. F., Gitti, C., Bao, G., Fischer, D., Almeida, S., Braga, V. A. S., Augusto, P., Petty, C., Alho, E. J. L., Lebedev, M., Song, A. W., & Nicolelis, M. A. L. (2018). Training with brain-machine interfaces, visuo-tactile feedback and assisted locomotion improves sensorimotor, visceral, and psychological signs in chronic paraplegic patients [Publisher: Public Library of Science]. *PLOS ONE*, 13(11), e0206464. <https://doi.org/10.1371/journal.pone.0206464>
- Shokur, S., Gallo, S., Moioli, R. C., Donati, A. R. C., Morya, E., Bleuler, H., & Nicolelis, M. A. L. (2016). Assimilation of virtual legs and perception of floor texture by complete paraplegic patients receiving artificial tactile feedback [Number: 1 Publisher: Nature Publishing Group]. *Scientific Reports*, 6(1), 32293. <https://doi.org/10.1038/srep32293>
- Snoek, G. J., IJzerman, M. J., Hermens, H. J., Maxwell, D., & Biering-Sorensen, F. (2004). Survey of the needs of patients with spinal cord injury: impact and priority for improvement in hand function in tetraplegics [Number: 9 Publisher: Nature Publishing Group]. *Spinal Cord*, 42(9), 526–532. <https://doi.org/10.1038/sj.sc.3101638>

-
- Snoek, G. J., IJzerman, M. J., Groen, F. A. C. G. i. ', Stoffers, T. S., & Zilvold, G. (2000). Use of the NESS handmaster to restore handfunction in tetraplegia: clinical experiences in ten patients. *Spinal cord*, 38(4), 244–249.
- Soekadar, S. R., Birbaumer, N., Slutzky, M. W., & Cohen, L. G. (2015). Brain–machine interfaces in neurorehabilitation of stroke. *Neurobiology of Disease*, 83, 172–179. <https://doi.org/10.1016/j.nbd.2014.11.025>
- Sommerfeld Disa K., Eek Elsy U.-B., Svensson Anna-Karin, Holmqvist Lotta Widén, & von Arbin Magnus H. (2004). Spasticity after stroke [Publisher: American Heart Association]. *Stroke*, 35(1), 134–139. <https://doi.org/10.1161/01.STR.0000105386.05173.5E>
- Spalletti, C., Alia, C., Lai, S., Panarese, A., Conti, S., Micera, S., & Caleo, M. (2017). Combining robotic training and inactivation of the healthy hemisphere restores pre-stroke motor patterns in mice (H. Johansen-Berg, Ed.) [Publisher: eLife Sciences Publications, Ltd]. *eLife*, 6, e28662. <https://doi.org/10.7554/eLife.28662>
- Spalletti, C., Lai, S., Mainardi, M., Panarese, A., Ghionzoli, A., Alia, C., Gianfranceschi, L., Chisari, C., Micera, S., & Caleo, M. (2014). A robotic system for quantitative assessment and poststroke training of forelimb retraction in mice [Publisher: SAGE Publications Inc STM]. *Neurorehabilitation and Neural Repair*, 28(2), 188–196. <https://doi.org/10.1177/1545968313506520>
- Stephanova, D. I., & Bostock, H. (1995). A distributed-parameter model of the myelinated human motor nerve fibre: temporal and spatial distributions of action potentials and ionic currents. *Biological Cybernetics*, 73(3), 275–280. <https://doi.org/10.1007/BF00201429>
- Stewart, J. D. (2003). Peripheral nerve fascicles: anatomy and clinical relevance. *Muscle & nerve*, 28(5), 525–541. Retrieved June 2, 2017, from <http://onlinelibrary.wiley.com/doi/10.1002/mus.10454/full>
- Stieglitz, T., Beutel, H., & Meyer, J. .-.-U. (2000). microflex”—a new assembling technique for interconnects. *Journal of Intelligent Material Systems and Structures*, 11(6), 417–425. <https://doi.org/10.1106/R7BV-511B-21RJ-R2FA>
- Stieglitz, T., Schuettler, M., Rubehn, B., Boretius, T., Badia, J., & Navarro, X. (2011, April). Evaluation of polyimide as substrate material for electrodes to interface the peripheral nervous system [ISSN: 1948-3554], In *2011 5th international IEEE/EMBS conference on neural engineering*. 2011 5th International IEEE/EMBS Conference on Neural Engineering. ISSN: 1948-3554. <https://doi.org/10.1109/NER.2011.5910602>
- Sunshine, M. D., Cho, F. S., Lockwood, D. R., Fechko, A. S., Kasten, M. R., & Moritz, C. T. (2013). Cervical intraspinal microstimulation evokes robust forelimb movements before and after injury. *Journal of Neural Engineering*, 10(3), 036001. <https://doi.org/10.1088/1741-2560/10/3/036001>
- Sussillo, D., Churchland, M. M., Kaufman, M. T., & Shenoy, K. V. (2015). A neural network that finds a naturalistic solution for the production of muscle activity. *Nature Neuroscience*, 18(7), 1025–1033. <https://doi.org/10.1038/nn.4042>

-
- Sweeney, J., Mortimer, J. T., & Durand, D. (1987). *Modeling of mammalian myelinated nerve for functional neuromuscular stimulation*. Retrieved September 17, 2020, from /paper/MODELING-OF-MAMMALIAN-MYELINATED-NERVE-FOR-Sweeney-Mortimer/bfdf15aa4281adb3638f2c373f94ac4972c0767f
- Tabot, G. A., Dammann, J. F., Berg, J. A., Tenore, F. V., Boback, J. L., Vogelstein, R. J., & Bensmaia, S. J. (2013). Restoring the sense of touch with a prosthetic hand through a brain interface. *Proceedings of the National Academy of Sciences of the United States of America*, 110(45), 18279–18284. <https://doi.org/10.1073/pnas.1221113110>
- Tanagho, Richard, & Bradley. (1989). Neural stimulation for control of voiding dysfunction: a preliminary report in 22 patients with voiding disorders. *THE JOURNAL OF UROLOGY*.
- Taylor, D. M., Tillery, S. I. H., & Schwartz, A. B. (2002). Direct cortical control of 3d neuroprosthetic devices. *Science*, 296(5574), 1829–1832.
- Taylor, P., Esnouf, J., & Hobby, J. (2002). The functional impact of the freehand system on tetraplegic hand function. clinical results [Number: 11 Publisher: Nature Publishing Group]. *Spinal Cord*, 40(11), 560–566. <https://doi.org/10.1038/sj.sc.3101373>
- Terzis, J. K., Smith, K. L., & Orgel, M. G. (1991). The peripheral nerve: structure, function, reconstruction. *Plastic and Reconstructive Surgery*, 87(6), 1138–1139. Retrieved September 28, 2020, from https://journals.lww.com/plasreconsurg/Citation/1991/06000/The_Peripheral_Nerve__Structure,_Function,.27.aspx
- Teulings, H. L., Contreras-Vidal, J. L., Stelmach, G. E., & Adler, C. H. (1997). Parkinsonism reduces coordination of fingers, wrist, and arm in fine motor control [Publisher: Academic Press Inc.]. *Experimental Neurology*, 146(1), 159–170. <https://doi.org/10.1006/exnr.1997.6507>
- Thach, W. T. (1978). Correlation of neural discharge with pattern and force of muscular activity, joint position, and direction of intended next movement in motor cortex and cerebellum [Publisher: American Physiological Society]. *Journal of Neurophysiology*, 41(3), 654–676. <https://doi.org/10.1152/jn.1978.41.3.654>
- Thoroughman, K. A., & Shadmehr, R. (2000). Learning of action through adaptive combination of motor primitives. *Nature*, 407(6805), 742–747. <https://doi.org/10.1038/35037588>
- Thoroughman, K. A., & Taylor, J. A. (2005). Rapid reshaping of human motor generalization. *The Journal of Neuroscience*, 25(39), 8948–8953. <https://doi.org/10.1523/JNEUROSCI.1771-05.2005>
- Thorp, E. B., Abdollahi, F., Chen, D., Farshchiansadegh, A., Lee, M.-H., Pedersen, J. P., Pierella, C., Roth, E. J., Seáñez Gonzáles, I., & Mussa-Ivaldi, F. A. (2016). Upper body-based power wheelchair control interface for individuals with tetraplegia [Conference Name: IEEE Transactions on Neural Systems and Rehabilitation Engineering]. *IEEE Transactions on Neural Systems and Rehabilitation Engineering*, 24(2), 249–260. <https://doi.org/10.1109/TNSRE.2015.2439240>
- Thorsen, Ferrarin, Spadone, & Frigo. (1999). Functional control of the hand in tetraplegics based on residual synergistic EMG activity. *Artificial Organs*, 23(5).
- Thrasher, A., Graham, G. M., & Popovic, M. R. (2005). Reducing muscle fatigue due to functional electrical stimulation using random modulation of stimulation parameters [eprint:

-
- <https://onlinelibrary.wiley.com/doi/pdf/10.1111/j.1525-1594.2005.29076.x>]. *Artificial Organs*, 29(6), 453–458. <https://doi.org/10.1111/j.1525-1594.2005.29076.x>
- Tigra, W., Dali, M., William, L., Fattal, C., Gélis, A., Divoux, J.-L., Coulet, B., Teissier, J., Guiraud, D., & Azevedo Coste, C. (2020). Selective neural electrical stimulation restores hand and forearm movements in individuals with complete tetraplegia. *Journal of Neuro-Engineering and Rehabilitation*, 17(1), 66. <https://doi.org/10.1186/s12984-020-00676-4>
- Timmermans, A. A. A., Seelen, H. A. M., Willmann, R. D., Bakx, W., de Ruyter, B., Lanfermann, G., & Kingma, H. (2009). Arm and hand skills: training preferences after stroke. *Disability and Rehabilitation*, 31(16), 1344–1352. <https://doi.org/10.1080/09638280902823664>
- Tomlinson, T., & Miller, L. E. (2016). Toward a proprioceptive neural interface that mimics natural cortical activity (J. Laczko & M. L. Latash, Eds.). In J. Laczko & M. L. Latash (Eds.), *Progress in motor control*. Cham, Springer International Publishing. https://doi.org/10.1007/978-3-319-47313-0_20
- Topka, H., Cohen, L. G., Cole, R. A., & Hallett, M. (1991). Reorganization of corticospinal pathways following spinal cord injury. *Neurology*, 41(8), 1276–1276. <https://doi.org/10.1212/WNL.41.8.1276>
- Tsodyks, M., Kenet, T., Grinvald, A., & Arieli, A. (1999). Linking spontaneous activity of single cortical neurons and the underlying functional architecture [Publisher: American Association for the Advancement of Science Section: Report]. *Science*, 286(5446), 1943–1946. <https://doi.org/10.1126/science.286.5446.1943>
- Turton, A. J., Cunningham, P., Heron, E., van Wijck, F., Sackley, C., Rogers, C., Wheatley, K., Jowett, S., Wolf, S. L., & van Vliet, P. (2013). Home-based reach-to-grasp training for people after stroke: study protocol for a feasibility randomized controlled trial. *Trials*, 14, 109. <https://doi.org/10.1186/1745-6215-14-109>
- Twitchell, T. E. (1951). The restoration of motor function following hemiplegia in man [Publisher: Oxford Academic]. *Brain*, 74(4), 443–480. <https://doi.org/10.1093/brain/74.4.443>
- Tyler, D., & Durand, D. (1993, October). Design and acute test of a radially penetrating interfascicular nerve electrode, In *Proceedings of the 15th annual international conference of the IEEE engineering in medicine and biology societ*. Proceedings of the 15th Annual International Conference of the IEEE Engineering in Medicine and Biology Societ. <https://doi.org/10.1109/IEMBS.1993.979118>
- Tyler, D., & Durand, D. (1997). A slowly penetrating interfascicular nerve electrode for selective activation of peripheral nerves. *IEEE Transactions on Rehabilitation Engineering*, 5(1), 51–61. <https://doi.org/10.1109/86.559349>
- Tyler, & Durand. (2002). Functionally selective peripheral nerve stimulation with a flat interface nerve electrode [Conference Name: IEEE Transactions on Neural Systems and Rehabilitation Engineering]. *IEEE Transactions on Neural Systems and Rehabilitation Engineering*, 10(4), 294–303. <https://doi.org/10.1109/TNSRE.2002.806840>

-
- Umeda, T., Koizumi, M., Katakai, Y., Saito, R., & Seki, K. (2019). Decoding of muscle activity from the sensorimotor cortex in freely behaving monkeys. *NeuroImage*, 197, 512–526. <https://doi.org/10.1016/j.neuroimage.2019.04.045>
- Ushiki, T., & Ide, C. (1990). Three-dimensional organization of the collagen fibrils in the rat sciatic nerve as revealed by transmission- and scanning electron microscopy. *Cell and Tissue Research*, 260(1), 175–184. <https://doi.org/10.1007/BF00297503>
- Valle, G., Petrini, F. M., Strauss, I., Iberite, F., D'Anna, E., Granata, G., Controzzi, M., Cipriani, C., Stieglitz, T., Rossini, P. M., Mazzoni, A., Raspopovic, S., & Micera, S. (2018). Comparison of linear frequency and amplitude modulation for intraneural sensory feedback in bidirectional hand prostheses [Number: 1 Publisher: Nature Publishing Group]. *Scientific Reports*, 8(1), 16666. <https://doi.org/10.1038/s41598-018-34910-w>
- Valle, G., Mazzoni, A., Iberite, F., D'Anna, E., Strauss, I., Granata, G., Controzzi, M., Clemente, F., Rognini, G., Cipriani, C., Stieglitz, T., Petrini, F. M., Rossini, P. M., & Micera, S. (2018). Biomimetic intraneural sensory feedback enhances sensation naturalness, tactile sensitivity, and manual dexterity in a bidirectional prosthesis. *Neuron*, 100(1), 37–45.e7. <https://doi.org/10.1016/j.neuron.2018.08.033>
- Vansteensel, M. J., Pels, E. G. M., Bleichner, M. G., Branco, M. P., Denison, T., Freudenburg, Z. V., Gosselaar, P., Leinders, S., Ottens, T. H., Van Den Boom, M. A., Van Rijen, P. C., Aarnoutse, E. J., & Ramsey, N. F. (2016). Fully implanted brain-computer interface in a locked-in patient with ALS. *The New England Journal of Medicine*, 375(21), 2060–2066. <https://doi.org/10.1056/NEJMoal608085>
- Varga, I., & Mravec, B. (2015, January 1). Chapter 8 - nerve fiber types (R. S. Tubbs, E. Rizk, M. M. Shoja, M. Loukas, N. Barbaro, & R. J. Spinner, Eds.). In R. S. Tubbs, E. Rizk, M. M. Shoja, M. Loukas, N. Barbaro, & R. J. Spinner (Eds.), *Nerves and nerve injuries*. San Diego, Academic Press. <https://doi.org/10.1016/B978-0-12-410390-0.00008-1>
- Vargas-Irwin, C. E., Shakhnarovich, G., Yadollahpour, P., Mislow, J. M. K., Black, M. J., & Donoghue, J. P. (2010). Decoding complete reach and grasp actions from local primary motor cortex populations. *Journal of Neuroscience*, 30(29), 9659–9669. <https://doi.org/10.1523/JNEUROSCI.5443-09.2010>
- Vaskov, A. K., Irwin, Z. T., Nason, S. R., Vu, P. P., Nu, C. S., Bullard, A. J., Hill, M., North, N., Patil, P. G., & Chestek, C. A. (2018). Cortical decoding of individual finger group motions using ReFIT kalman filter. *Frontiers in Neuroscience*, 12. <https://doi.org/10.3389/fnins.2018.00751>
- Velliste, M., Perel, S., Spalding, M. C., Whitford, A. S., & Schwartz, A. B. (2008). Cortical control of a prosthetic arm for self-feeding. *Nature*, 453(7198), 1098–1101. <https://doi.org/10.1038/nature06996>
- Veltink, P. H., van Veen, B. K., Struijk, J. J., Holsheimer, J., & Boom, H. B. (1989). A modeling study of nerve fascicle stimulation. *IEEE transactions on bio-medical engineering*, 36(7), 683–692. <https://doi.org/10.1109/10.32100>
- Veltink, P. H., Alste, J. A. v., & Boom, H. B. K. (1989). Multielectrode intrafascicular and extraneural stimulation [Publisher: Springer]. *Medical & biological engineering & computing*, 27(1), 19–24. <https://doi.org/10.1007/BF02442165>

-
- Vodovnik, L., Long, C., Reswick, J. B., Lippay, A., & Starbuck, D. (1965). Myo-electric control of paralyzed muscles. *IEEE transactions on bio-medical engineering*, 12(3), 169–172. <https://doi.org/10.1109/tbme.1965.4502374>
- Wagner, F. B., Mignardot, J.-B., Goff-Mignardot, C. G. L., Demesmaeker, R., Komi, S., Capogrosso, M., Rowald, A., Seáñez, I., Caban, M., Pirondini, E., Vat, M., McCracken, L. A., Heimgartner, R., Fodor, I., Watrin, A., Seguin, P., Paoles, E., Keybus, K. V. D., Eberle, G., ... Courtine, G. (2018). Targeted neurotechnology restores walking in humans with spinal cord injury. *Nature*, 563(7729), 65–71. <https://doi.org/10.1038/s41586-018-0649-2>
- Wark, H. A. C., Mathews, K. S., Normann, R. A., & Fernandez, E. (2014). Behavioral and cellular consequences of high-electrode count Utah arrays chronically implanted in rat sciatic nerve [Publisher: IOP Publishing]. *Journal of Neural Engineering*, 11(4), 046027. <https://doi.org/10.1088/1741-2560/11/4/046027>
- Waxman, S. G. (1980). Determinants of conduction velocity in myelinated nerve fibers. *Muscle & Nerve*, 3(2), 141–150. <https://doi.org/10.1002/mus.880030207>
- Weerasuriya, A., Spangler, R., Rapoport, S., & Taylor, R. (1984). AC impedance of the perineurium of the frog sciatic nerve. *Biophysical Journal*, 46(2), 167–174. [https://doi.org/10.1016/S0006-3495\(84\)84009-6](https://doi.org/10.1016/S0006-3495(84)84009-6)
- Weiler, J., Gribble, P. L., & Pruszynski, J. A. (2019). Spinal stretch reflexes support efficient hand control [Number: 4 Publisher: Nature Publishing Group]. *Nature Neuroscience*, 22(4), 529–533. <https://doi.org/10.1038/s41593-019-0336-0>
- Welmer, A.-K., Holmqvist, L. W., & Sommerfeld, D. K. (2010). Location and severity of spasticity in the first 1–2 weeks and at 3 and 18 months after stroke. *European Journal of Neurology*, 17(5), 720–725. <https://doi.org/10.1111/j.1468-1331.2009.02915.x>
- Wodlinger, B., Downey, J. E., Tyler-Kabara, E. C., Schwartz, A. B., Boninger, M. L., & Collinger, J. L. (2015). Ten-dimensional anthropomorphic arm control in a human brain-machine interface: difficulties, solutions, and limitations. *Journal of Neural Engineering*, 12(1), 016011. <https://doi.org/10.1088/1741-2560/12/1/016011>
- Wolpaw, J. R., Birbaumer, N., McFarland, D. J., Pfurtscheller, G., & Vaughan, T. M. (2002). Brain-computer interfaces for communication and control. *Clinical Neurophysiology: Official Journal of the International Federation of Clinical Neurophysiology*, 113(6), 767–791. [https://doi.org/10.1016/s1388-2457\(02\)00057-3](https://doi.org/10.1016/s1388-2457(02)00057-3)
- Wu, W., Gao, Y., Bienenstock, E., Donoghue, J. P., & Black, M. J. (2006). Bayesian population decoding of motor cortical activity using a kalman filter [Publisher: MIT Press]. *Neural Computation*, 18(1), 80–118. <https://doi.org/10.1162/089976606774841585>
- Wurth, S., Capogrosso, M., Raspopovic, S., Gandar, J., Federici, G., Kinany, N., Cutrone, A., Piersigilli, A., Pavlova, N., Guiet, R., Taverni, G., Rigosa, J., Shkrobatova, P., Navarro, X., Barraud, Q., Courtine, G., & Micera, S. (2017). Long-term usability and bio-integration of polyimide-based intra-neural stimulating electrodes. *Biomaterials*, 122, 114–129. <https://doi.org/10.1016/j.biomaterials.2017.01.014>
- Xu, J., Ejaz, N., Hertler, B., Branscheidt, M., Widmer, M., Faria, A. V., Harran, M. D., Cortes, J. C., Kim, N., Celnik, P. A., Kitago, T., Luft, A. R., Krakauer, J. W., & Diedrichsen, J. (2017). Separable systems for recovery of finger strength and control after stroke [Publisher:

- American Physiological Society]. *Journal of Neurophysiology*, 118(2), 1151–1163. <https://doi.org/10.1152/jn.00123.2017>
- Yoshida, K., & Horch, K. (1993). Selective stimulation of peripheral nerve fibers using dual intrafascicular electrodes [Conference Name: IEEE Transactions on Biomedical Engineering]. *IEEE Transactions on Biomedical Engineering*, 40(5), 492–494. <https://doi.org/10.1109/10.243412>
- Zanos, S., Richardson, A. G., Shupe, L., Miles, F. P., & Fetz, E. E. (2011). The neurochip-2: an autonomous head-fixed computer for recording and stimulating in freely behaving monkeys [Conference Name: IEEE Transactions on Neural Systems and Rehabilitation Engineering]. *IEEE Transactions on Neural Systems and Rehabilitation Engineering*, 19(4), 427–435. <https://doi.org/10.1109/TNSRE.2011.2158007>
- Zimmermann, J. B., & Jackson, A. (2014). Closed-loop control of spinal cord stimulation to restore hand function after paralysis. *Frontiers in Neuroscience*, 8. <https://doi.org/10.3389/fnins.2014.00087>

Glossary of abbreviations

APB: Abductor pollicis brevis
APL: Abductor pollicis longus
BMI: Brain-machine interface
BRC: Brachioradialis
CMAP: Compound muscle action potential
DAC: Digital-to-analog converter
Dors. cut.: Dorsal cutaneous branch
ECR: Extensor carpi radialis
ECU: Extensor carpi ulnaris
EDC: Extensor digitorum communis
EMG: Electromyogram
FCR: Flexor carpi radialis
FCU: Flexor carpi ulnaris
FDI: First dorsal interosseous
FDP: Flexor digitorum profundus
FDS: Flexor digitorum superficialis
FEA: Front-end amplifier
FEM: Finite element model
FES: Functional electrical stimulation
FPB: Flexor pollicis brevis
FR: Firing rate
Lat. cut. : Lateral cutaneous branch
LUM: lumbricals
M1: Primary motor cortex
MCP: Metacarpophalangeal
Med. cut. : Median cutaneous branch
NMES: Neuromuscular electrical stimulation
PC: Principal component
PCA: Principal component analysis
PIP: Proximal interphalangeal
PL: Palmaris longus
PO: Pollicis Opponens
PW: Pulse-width
S1: Primary somatosensory cortex
SCI: Spinal cord injury
SI: Selectivity index
SP: Supinator muscle
THE: Thenar eminence
TIME: Transverse intrafascicular multichannel electrode
TRI: Triceps

Marion Badi

Swiss Federal Institute of Technology (EPFL)
Center for Neuroprosthetics B3.4
Chemin des Mines 9, 1202 Geneva, Switzerland
marion.badi-dubois@epfl.ch

EDUCATION

- 2016-present **PhD in Electrical Engineering** - Swiss Federal Institute of Technology, EPFL, Lausanne, Switzerland
- 2014-2016 **Master in Biomedical Engineering** - Swiss Federal Institute of Technology, EPFL, Lausanne, Switzerland
- 2011-2014 **Bachelor in Life Sciences and Technology** - Swiss Federal Institute of Technology, EPFL, Lausanne, Switzerland

RESEARCH EXPERIENCE

- 2016-present **PhD Thesis in Electrical Engineering – Translational Neuroengineering Lab**, EPFL, Switzerland Laboratory of Silvestro Micera
Research: *Intraneural stimulation for the restoration of fine grasping in NHP.*
Worked performed at the University of Fribourg, Switzerland, laboratory of Eric Rouiller.
- 2015-2016 **Master Thesis – Neuroregeneration Institute**, Harvard Medical School, United States
Laboratory of Ole Isacson
Research: *Restorative cell technology for Parkinson's disease.*
- 2015 **Project – Translational neural engineering lab**, EPFL, Switzerland
Laboratory of Silvestro Micera
Research: *Functional electrical stimulation for hand movement restoration in paralyzed patients.*
- 2014 **Internship – CERN**, Geneva, Switzerland
Laboratory of Paul Lecoq
Research: *Optimization of scintillators spatial resolution in PET for cancer imaging.*
- 2014 **Bachelor thesis - Chair in non-invasive brain-machine interface**, EPFL, Switzerland
Laboratory of José del R. Millán
Research: *Brain-computer interface for automated error correction.*

PUBLICATIONS

- [1] Barra B.*, **Badi M.***, Perich M. G., Conti S., Mirrazavi Salehian S. S., Moreillon F., Bogaard A., Wurth S., Kaeser M., Passeraub P., Milekovic T., Billard A., Micera S.** & Capogrosso M.**, (2019). A versatile robotic platform for the design of natural, three-dimensional reaching and grasping tasks in monkeys. **Journal of Neural Engineering**, 17(1), 016004.
- [2] **Badi M.***, Wurth S.*, Kaeser M., Čvančara P., Stieglitz T., Courtine G., Bloch J., Capogrosso M., Rouiller EM., Micera S. # (2018). Development of an Intraneural Peripheral Stimulation Paradigm for the Restoration of Fine Hand Control in Non-human Primates. **In Converging Clinical and Engineering Research on Neurorehabilitation III** (Vol. 21, pp. 112–116).
- [3] **Badi M.***, Wurth S.*, Scarpato I., Roussinova E., Losanno E., Bogaard A., Delacombaz M., Borgognon S., Čvančara P., Fallegger F., Su D.K., Schmidlin E., Courtine G., Bloch J., Lacour S.P., Stieglitz T., Rouiller E.M., Capogrosso M., Micera S. # (*in Review*) Intrafascicular peripheral nerve stimulation produces fine functional hand movements in primates.
- [4] **Badi M.***, Borgognon S. *, O'Doherty J. E., Shokur S. # (*in Review*). Cortical stimulation for somatosensory feedback: translation from nonhuman primates to clinical applications. Somatosensory Feedback for Neuroprosthetics.
*co-first authors, # corresponding author, **co-senior authors

PRESENTATIONS

- [1] An implanted neuroprosthesis based on peripheral intraneural electrodes to restore grasping functions (2020) – poster and oral – Center for Neuroprosthetics Retreat, Lavey-Les-Bains, Switzerland
- [2] Neuroanatomical, computational, and experimental evidences for the use of intraneural peripheral nerve stimulation to induce fine hand movements (2018) – poster – Society for Neuroscience (SfN) – San Diego (CA), USA
- [3] Development of an intraneural peripheral stimulation paradigm for the restoration of fine hand control in non-human primates (2018) – poster – 4th International Conference on NeuroRehabilitation – Pisa, Italy
- [4] Grasp restoration in non-human primates (2018) – oral – Cognition day University of Fribourg – Fribourg, Switzerland
- [5] Development of an intraneural peripheral stimulation paradigm for reversing hand paralysis in non-human primates (2017) – poster – Society for Neuroscience (SfN) – Washington, D.C., USA
- [6] An implanted peripheral nerve prosthesis to restore grasping functions in NHP (2017) – poster and oral – Summer School on Neurorehabilitation – Baiona, Spain

AWARDS AND SCHOLARSHIPS

2020	1 st place winner - Poster prize at Center for Neuroprosthetics Retreat, Lavey-Les-Bains, Switzerland
2018	Finalist - Poster prize at International Conference on NeuroRehabilitation, Pisa, Italy
2016	Best GPA Biomedical Engineering Master studies EPFL
2015-2016	Bertarelli Fellowship in Translational Neuroscience and Neuroengineering – 20'000 USD

TEACHING EXPERIENCES

2016-2019	Teaching Assistant - Swiss Federal Institute of Technology, EPFL, Switzerland <i>Fundamentals of Neural Engineering – master engineering students</i>
2016-2018	Teaching Assistant – University of Fribourg, Switzerland <i>Bio-statistics course – bachelor biomedical students</i>

RESEARCH SUPERVISIONS

PhD students

2019-Present Elena Losanno, PhD candidate, Scuola superior Sant'Anna Pisa, Italy

Master students

2019-2020	Evgenia Roussinova, Swiss Federal Institute of Technology (EPFL), Lausanne, Switzerland
2018-2020	Ilaria Scarpato, Politecnico di Milano, Milan, Italy
2019	Gaia Carparelli, Swiss Federal Institute of Technology (EPFL), Lausanne, Switzerland
2019	Giovanna Aiello, Swiss Federal Institute of Technology (EPFL), Lausanne, Switzerland
2018	Aurelien Touzain, ECE Engineering School, Paris, France
2017	Sebastian Savidan, Swiss Federal Institute of Technology (EPFL), Lausanne, Switzerland
2016	Sherida M. de Leeuw's, Harvard Medical School, Boston, United States

Bachelor students

2018	Clea Kunz, Swiss Federal Institute of Technology (EPFL), Lausanne, Switzerland
2018	Federica Furfaro, University of Fribourg, Fribourg, Switzerland
2017	Diego Canton, Swiss Federal Institute of Technology (EPFL), Lausanne, Switzerland

EXTRACURRICULAR ACTIVITIES

2014-2015	Organizer of the Lausanne Technologies and Innovation Forum (STIL) – Lausanne, Switzerland
2012-2018	Member of Ingénieurs du Monde - EPFL - Committee promoting North-South scientific

LANGUAGES AND SKILLS

Languages

French: Native, English: Fluent, German: Basics, Russian: Basics

IT skills

Matlab, C++, Python, html, java, LabVIEW, COMSOL, Neuron, LaTeX, CAD design (SolidWorks, Autocad), OpenEx

Engineering skills

Mathematics, Physics, Electrical engineering, Robotics, Neural engineering, Neuroprosthetics, BCI, Machine learning, Deep learning, Biomicroscopy, Bioelectronis, Fluid mechanics, Biomaterials, BioMEMS, Tissue engineering

Life Sciences skills

Neurosciences, Molecular Biology, Immunology, Physiology, Microbiology, Regenerative Medicine

Laboratory

Animal models (rodents & primates), animals training, electrophysiology, surgery, microscopy, cellular culture, immunohistochemistry

